Magnetic control over supramolecular polymerization

Michaela Schicho

UNIVERSITÉ DE STRASBOURG

ÉCOLE DOCTORALE 222

UMR 7140 Chimie de la Matière Complexe

THÈSE présentée par :

Michaela SCHICHO

soutenue le : **16 Novembre 2021**

pour obtenir le grade de : **Docteur de l'Université de Strasbourg**

Discipline/Spécialité : Chimie Supramoléculaire

Magnetic Control over Supramolecular Polymerization

THÈSE dirigée par :

M HERMANS Thomas Professeur, UMR 7140, Université de Strasbourg, France

RAPPORTEURS :

M GONZÁLEZ RODRÍGUEZ David Professeur, Universidad Autónoma de Madrid, Espagne

Mme MARCHESAN Silvia Professeur, Università degli Studi di Trieste, Italie

---

AUTRES MEMBRES DU JURY :

Mme FERLAY-CHARITAT Sylvie Professeur, UMR 7140, Université de Strasbourg, France

Table of contents

Table of contents 1
Résumé (version française) 4
Références 8
Summary (English version) 9
References 13
List of abbreviations 14
List of symbols 17
List of constants 20
List of SI-derived and CGS units 20
Chapter 1. General introduction 21
1.1 Controlling supramolecular polymerization 22
1.1.1 Supramolecular chemistry: self-organization and self-assembly 22
1.1.2 Supramolecular polymerization 23
1.1.3 Stimuli-responsive supramolecular polymers 25
1.2 Magnetism 32
1.2.1 History and global impact 32
1.2.2 Magnetic fields 33
1.2.3 Magnetic materials 35
1.2.3.1 Characterization 35
1.2.3.2 Classification 36
1.2.3.3 Lanthanides 39
1.3 Magnetic control over soft matter 41
1.3.1 Magnetic energies and forces 41
1.3.1.1 Magnetic energy in constant fields 42
1.3.1.2 Magnetic forces in gradient fields 42
1.3.1.3 Dipolar coupling 43
1.3.1.4 Energetic significance 43
1.3.2 Effects in constant fields 45
1.3.2.1 Diamagnetic alignment 45

1.3.2.2 Paramagnetic alignment 49
1.3.2.3 Magneto-crystalline anisotropy in paramagnetic alignment 51
1.3.3 Effects in gradient fields 52
1.3.3.1 Deformation of fluids 52
1.3.3.2 Magnetophoresis 54
1.3.4 Dipolar coupling 55
1.3.5 Dually controlled systems 57
1.3.6 Non-trivial observations 60
1.4 Aims and contents of this thesis 64
1.5 Appendix 65
1.6 References 68

Chapter 2. Thermodynamics of the supramolecular assembly of lanthanide containing NDI derivatives 75

2.1 Introduction 76
2.2 Molecular design 77
2.3 Synthesis and chemical characterization 78
2.4 Magnetic characterization 81
2.5 Spectroscopic characterization 83
2.6 Thermodynamics of supramolecular polymerization 84
2.7 Conclusions 90
2.8 Author contributions 90
2.9 Appendix 91
2.10 References 114

Chapter 3. Magnetophoresis in colloidal assemblies of lanthanide containing NDI derivatives 117

3.1 Introduction 118
3.2 Solvent induced colloid formation 119
3.3 Colloid morphology and size 120
3.4 Magnetophoresis 121
3.5 Force considerations 126
3.6 Conclusions 128

3.7 Author contributions 128
3.8 Appendix 129
3.9 References 133

Chapter 4. Magnetic control over the fractal dimension of supramolecular BTA networks 135

4.1 Introduction 136
4.2 Network characterization 137
4.3 Magnetically controlled network topology 140
4.4 Energetic considerations 142
4.5 Conclusions 143
4.6 Author contributions 143
4.7 Appendix 144
4.8 References 152

Chapter 5. Magnetic control over supramolecular gelation kinetics 155

5.1 Introduction 156
5.2 Lanthanide-containing supramolecular hydrogels 157
5.3 Magnetically controlled gelation kinetics 159
5.4 Magneto-response of an organic supramolecular hydrogel 164
5.5 Conclusions 167
5.6 Author contributions 168
5.7 Appendix 169
5.8 References 178

Chapter 6. Overall conclusions and outlook 181

References 186

Acknowledgements 187

Résumé

Cette thèse résumée ci-dessous s'intitule « Contrôle Magnétique sur la Polymérisation Supramoléculaire ». Elle fournit un aperçu général sur les possibilités qu'un stimulus magnétique peut offrir pour le contrôle de systèmes supramoléculaires. L'objectif final est de savoir si des modes d'action magnétiques peuvent venir enrichir l'ensemble d'interactions non-covalentes de la chimie supramoléculaire.

Les polymères supramoléculaires sont des structures polymériques composées de motifs moléculaires répétés qui sont liés par des interactions secondaires non-covalentes. Grâce à la nature réversible de ces liaisons, les matériaux supramoléculaires sont intrinsèquement dynamiques, ce qui les rend réactifs vis-à-vis de stimuli externes et capables de s'auto-guérir. Leur capacité à s'adapter aux conditions de leur environnement est habituellement exploitée pour contrôler leurs propriétés par des stimuli externes[1] comme la température, le pH, la lumière, le potentiel redox, la force mécanique, ou encore les enzymes. L'utilisation du magnétisme comme stimulus est rare, alors qu'il offre de nombreux avantages qui ne sont pas permis par ces alternatives plus conventionnelles. Il s'agit d'une méthode non-invasive et non-destructive, qui est facilement modulable en termes d'intensité, de portée spatiale et temporelle. Elle tolère également une large gamme de matériaux et d'environnements. Ces avantages sont couramment exploités dans des systèmes de nanoparticules et de colloïdes. À cette échelle, il suffit d'appliquer un champ magnétique faible, inférieur ou égal à 2 T, pour contrôler leur auto-assemblage. Au niveau (supra-)moléculaire, en revanche, des champs forts de l'ordre de 10 à 30 T sont nécessaires pour atteindre des effets observables en conditions douces, c'est-à-dire à faibles concentrations et à pression et température ambiantes.[2] La raison en est que dans ces conditions, l'énergie magnétique $E_{mag} = -\frac{1}{2}\, mB$ rentre en compétition avec les fluctuations thermiques, autrement dit l'énergie du mouvement Brownien $E_{therm} = -\frac{3}{2}\, k_B T$, où m est le moment magnétique de la particule, B la densité de flux magnétique, k_B la constante de Boltzmann et T la température absolue.[3,4]

Néanmoins, plusieurs études récentes rapportent des observations inattendues dans ce contexte. La plupart de ces phénomènes non-triviaux manquent d'une compréhension satisfaisante.[5–9] Polarz et ses collaborateurs ont observé un assemblage complexe d'un tensioactif chélatant des ions de Dy^{3+}, en forme d'haltères de plusieurs micromètres. Cet assemblage n'a pas été formé quand un analogue diamagnétique avec du Lu^{3+} a été utilisé à la place du Dy^{3+}.[5] Zhu et ses collaborateurs ont réussi à diriger l'auto-assemblage de copolymères à blocs contenant des tétrabromoferrates vers la formation de nanostructures à microphases séparées dans un champ de seulement 0,35 T.[10] Dans un système de polysaccharides enrichis en ions ferriques, Mezzenga et ses collaborateurs ont montré un changement de conformation, passant de pelotes aléatoires à des hélices dans un champ constant de 1,1 T.[11]

Inspirés par ces rapports récents, nous avons cherché à mieux comprendre comment s'effectue l'incorporation d'ions magnétiques dans les systèmes supramoléculaires, et comment ces matériaux répondent aux champs magnétiques faibles. Pour cela, quatre systèmes ont été étudiés, chacun se focalisant sur un aspect différent du domaine. Afin de fournir une mise en œuvre simple et un montage expérimental accessible, nous nous limitons à l'utilisation de champs magnétiques de faible intensité (≤ 2 T).

Dans un premier temps (**Chapitre 2**), nous avons étudié si l'incorporation d'ions paramagnétiques de terres rares dans des dérivés de naphtalène diimide (NDI) était susceptible d'influencer leur auto-assemblage. Afin d'effectuer une étude systématique, une bibliothèque de complexes de coordination (**M-NDI**) à base d'un dérivé de NDI et de différents ions magnétiques ($\mathbf{M}^{3+}$ = Tb^{3+}, Dy^{3+}, Gd^{3+}, Ho^{3+}, Er^{3+}) ou diamagnétiques ($\mathbf{M}^{3+}$ = Y^{3+}, La^{3+}, Lu^{3+}) a été préparée. Les cinq ions magnétiques ont été choisis pour leur moment magnétique élevé ainsi que leurs distributions variées de densité électronique. Il a été démontré que cette dernière est décisive pour les propriétés magnétiques de complexes de lanthanides en état cristallin.[12] L'unité centrale de NDI, dont les dérivés sont très utilisés et bien étudiés, induit l'auto-assemblage par effet hydrophobique et par interactions π-π. Elle a été sélectionnée dans cette étude pour sa faible enthalpie de polymérisation comparée aux alternatives connues (perylène diimides, benzènetricarboxamides, porphyrines, ou pyridines). Cela permettrait d'assurer que de possibles interactions magnétiques ne soient pas supplantées par un assemblage trop dominant du ligand.

L'auto-assemblage de **M-NDI** dans l'eau a été analysé par spectroscopie UV-visible en suivant les absorptions spécifiques du noyau aromatique. Grâce à un modèle théorique pour un mécanisme de polymérisation isodesmique, l'énergie libre de Gibbs ΔG et ses composantes, l'enthalpie ΔH et la contribution entropique $T\Delta S$ de polymérisation supramoléculaire ont été déterminées pour tous les membres de la famille **M-NDI**. Les énergies libres ont été obtenues avec une haute précision et ont des valeurs comprises entre –14 et –12 $kJ \cdot mol^{-1}$ pour tous les composés étudiés. Cependant, la balance entre les contributions enthalpiques et entropiques à cette énergie libre identique subit un changement en fonction de la nature de l'ion **M**. Ainsi, les valeurs de l'enthalpie négative sont jusqu'à 60 % plus élevées pour **Dy-NDI** par rapport au **Y-NDI** diamagnétique. La croissance de l'enthalpie négative suit le moment magnétique des ions pour nos huit monomères. Des mesures magnétométriques au SQUID révèlent un couplage antiferromagnétique considérable entre les ions magnétiques de lanthanides dans le **M-NDI** à l'état solide. Ces résultats nous mènent à la conclusion qu'il y a en effet des interactions significatives entre les ions magnétiques incorporés dans les monomères. Par conséquent, l'état polymérique est stabilisé ce qui s'exprime par une enthalpie de polymérisation supramoléculaire plus importante. Comme on observe une compensation de l'enthalpie par la contribution entropique, la constante d'équilibre et l'énergie libre de Gibbs globales ne sont pas affectées.

Le **Chapitre 3** présente l'auto-assemblage du monomère **M-NDI** dans un système binaire eau/THF. Dans ce milieu, la formation de colloïdes de plusieurs micromètres est observée à des fractions volumiques élevées de THF φ_{THF}. Ce deuxième type de polymérisation a ainsi été suivi par spectroscopie UV-visible pour des proportions volumiques φ_{THF} de THF allant de 0,65 à 0,95, révélant un mécanisme de polymérisation isodesmique. Les tailles des colloïdes obtenus ont été estimées par diffusion de la lumière dynamique. Les mesures exposent que le rayon hydrodynamique des colloïdes augmente de 1 à 5 µm avec une proportion de THF φ_{THF} croissante.

Lorsqu'on applique un gradient de champ magnétique à l'aide d'un aimant commercial de NdFeB cubique de 0,5 cm à des dispersions de **Dy-NDI** à $\varphi_{THF} \geq 0{,}80$, on observe en 4 h la formation d'une couche organique sur la surface le long des bords de l'aimant. La couche est d'une centaine de micromètres d'épaisseur et de la couleur orange caractéristique du NDI et de ses dérivés. Le mouvement dirigé des colloïdes a pu être visualisé par microscopie confocale.

Selon la théorie, la force magnétique surpasse la force thermique du mouvement Brownien à partir d'une certaine taille de colloïdes. En effet, à susceptibilité magnétique et viscosité dynamique constantes, le volume des particules est directement lié à leur moment magnétique.[13] La prédominance de la force magnétique sur la force thermique mène au transport de matière à travers l'espace. Ce phénomène est appelé magnétophorèse.

Suivant ce raisonnement, la formation de couche observée peut être corrélée à la taille des colloïdes et au degré de polymérisation des dispersions respectives de **Dy-NDI** à différentes fractions volumiques. Tous les composés **M-NDI** à base d'ions magnétiques ($\mathbf{M}^{3+} = Gd^{3+}$, Dy^{3+}, Tb^{3+}, Ho^{3+}, Er^{3+}) forment une couche à $\varphi_{THF} = 0{,}95$. Aucune accumulation de colloïdes près de l'aimant n'est observée pour les contrôles diamagnétiques ($\mathbf{M}^{3+} = Y^{3+}$, La^{3+}, Lu^{3+}). Une fois formée, la couche peut être enlevée facilement en ajoutant de l'eau pour réduire le pourcentage de THF.

À notre connaissance, ceci est le premier exemple de magnétophorèse dans un système supramoléculaire. La simplicité et la réversibilité du système offre un nouveau degré de contrôle spatiotemporel magnétique sur la matière molle.

Le **Chapitre 4** présente l'auto-assemblage d'un réseau supramoléculaire en solution, ayant comme base un dérivé de 1,3,5-benzènetricraboxamide (BTA) incorporant des ions magnétiques de Gd^{3+}. Des expériences de diffusion de lumière dynamique et statique nous ont permis d'analyser la topologie de l'assemblage. La fonction de relaxation enregistrée est bimodale, ce qui indique la présence de deux populations différentes **P1** et **P2**. On suppose donc une polymérisation en deux étapes : un premier assemblage du monomère en bâtons (**P1**) puis un assemblage de ces derniers en réseau supramoléculaire (**P2**). Les rayons hydrodynamiques correspondants sont d'environ 30 nm pour **P1** et 350 nm pour **P2**. Un équivalent diamagnétique, où le Gd^{3+} est remplacé par l'Y^{3+} diamagnétique (**Y-BTA**), montre un comportement similaire.

Ayant cette nouvelle perception de la structure du réseau, la réponse d'une solution de **Gd-BTA** soumise à un champ magnétique uniforme de 1 ou 2 T a été analysée. Pour cela, l'échantillon a été placé dans le champ pendant une heure, puis analysé par diffusion de la lumière statique pendant une heure. Ce cycle expérimental a été répété 6 ou 7 fois par échantillon pour une durée totale d'expérience de 12 à 14 heures. Après 14 h d'exposition du **Gd-BTA**, des augmentations de 20 % et 35 % du ratio de Rayleigh $R(q)$ (qui est dérivé de l'intensité de la lumière diffusée) ont été respectivement observées pour le processus **P2** dans 1 et 2 T. Ces résultats impliquent qu'il s'agit d'une densification du réseau avec le temps. Pour **P1**, il n'y a pas de changement du ratio de Rayleigh avec le temps. De plus, le facteur de forme des structures d_F a été déterminé, mettant notamment en lumière un changement spontané de la morphologie de type bâtonnet ($d_F = 1{,}7$) pour une structure aléatoirement ramifiée ($d_F = 2{,}6$ pour 2 T) en moins d'une heure. Quand le champ magnétique est supprimé, le système revient à son état initial. Une étude analogue du **Y-BTA** ne montre aucun changement de topologie.

Des mesures au SQUID montrent que la susceptibilité magnétique d'une solution de **Gd-BTA** diminue de 2 % par rapport à la valeur initiale après 12 heures. L'échelle de temps correspond bien au changement de topologie trouvé par diffusion de la lumière. Des calculs de l'état fondamental magnétique mettent en évidence que l'énergie libre anisotropique du système est la force motrice du phénomène observé.

On peut donc en conclure que, réversiblement, l'application d'un champ magnétique perturbe l'équilibre thermodynamique du système. Il apparait que le stimulus magnétique favorise l'auto-assemblage entropiquement par un alignement (partiel) des bâtons. La dépendance mutuelle de l'alignement et l'élongation du polymère fournit une boucle de rétroaction positive.

Le **Chapitre 5** décrit nos efforts pour le développement de matériaux magnéto-réactifs. Nous introduisons un hydrogel à base de *N*,*N*'-bis(5-acide isophthalique)naphthalène diimide (**BINDI**) et d'ions magnétiques de Dy^{3+}. La gélification s'effectue par coordination des carboxylates libres du **BINDI** aux ions de lanthanides et par une baisse de pH contrôlée déclenchée par l'hydrolyse de glucono-δ-lactone (GdL). L'impact d'un champ magnétique uniforme sur la gélification et les propriétés mécaniques des gels formés ont été étudiés par magnéto-rhéologie. Les mesures cinétiques montrent que la gélification se déroule environ deux fois plus vite sous un champ magnétique de 0,78 T qu'en absence de champ magnétique. Le temps de gélification diminue de 650 à 340 min. Dans les deux cas, la rigidité mécanique finale est d'environ 1,3 kPa. Sous un champ plus faible de 0,13 T, le temps de gélification est réduit de 14 %. En déclenchant le champ magnétique à différents moments de la gélification, le profil cinétique peut être adapté à mesure. La microscopie électronique à balayage en transmission (STEM) sur les gels de **Dy-BINDI** révèle une microstructure de fibrilles d'une épaisseur d'environ 10 nm.

Si le Dy^{3+} est remplacé par d'autres ions magnétiques de lanthanides (Gd^{3+}, Er^{3+}), on retrouve des tendances similaires. Dans le cas du La^{3+} diamagnétique, le temps de gélification est accéléré de 48 %, ce qui est surprenant car qu'il s'agit d'un système purement diamagnétique. Il est donc supposé qu'il y ait une influence diamagnétique venant de l'anisotropie diamagnétique du système π du **BINDI** assemblé. Pour vérifier cette hypothèse, un gel de **BINDI** a été préparé sans ions de lanthanide. Pour cela, la concentration du GdL a dû être augmentée. Cet ajustement suggère que les structures des deux gels diffèrent significativement. En effet, l'imagerie STEM du gel **BINDI** sans lanthanides montre des fibres plus larges, d'environ 50 nm de diamètre. Étonnamment, l'application d'un champ de 0,78 T sur ce second système empêche complètement la gélification. En effet, le système collapse après avoir atteint environ la moitié de la rigidité finale du gel formé à 0 T.

En se basant sur ces résultats, nous supposons qu'un alignement partiel des fibres, soit paramagnétique ou diamagnétique, favorise la polymérisation supramoléculaire entropiquement. C'est-à-dire qu'un alignement d'unités, même partiel, réduirait le nombre de leurs degrés de liberté, ce qui modérerait la perte d'entropie lors de leur assemblage. Cependant, nous n'avons pas encore pu prouver l'alignement supposé des fibres par microscopie ou par biréfringence du matériau.

Même si le mécanisme de gélification reste à éclaircir pour les deux systèmes, ces résultats sont prometteurs en vue de la conception de matériaux magnétiquement contrôlables. Considérant la faible intensité du champ magnétique et les susceptibilités magnétiques basses des composantes du système, il est surprenant d'observer des changements si importants et contrôlables avec autant de précision.

Le **Chapitre 6** conclut finalement sur les connaissances acquises et les intègre dans un contexte plus général.

Globalement, le travail présenté montre nos efforts pour esquisser l'impact qu'un stimulus magnétique peut exercer sur les systèmes supramoléculaires, ce qui reste un domaine très peu

étudié à ce jour. Dans quatre systèmes différents, à savoir, un polymère unidimensionnel solubilisé (**Chapitre 2**), un système colloïdal en dispersion (**Chapitre 3**), un réseau de fibres en solution (**Chapitre 4**) et un hydrogel (**Chapitres 5**), les possibilités et les limites du contrôle magnétique ont été démontrées. Nous dévoilons la thermodynamique d'un auto-assemblage magnétique et présentons de nouvelles approches pour guider la formation de structures supramoléculaires. En tenant compte de la nouveauté du sujet de recherche, les connaissances acquises peuvent servir de base solide pour de futurs études. Celles-ci peuvent s'étendre de la chimie supramoléculaire aux matériaux intelligents.

Références

1. Aida, T., Meijer, E. W. & Stupp, S. I. Functional Supramolecular Polymers. *Science* **335**, 813–817 (2012).
2. Shklyarevskiy, I. O., Jonkheijm, P., Christianen, P. C. M., Schenning, A. P. H. J., Meijer, E. W., Henze, O., Kilbinger, A. F. M., Feast, W. J., Del Guerzo, A., Desvergne, J.-P. & Maan, J. C. Magnetic Deformation of Self-Assembled Sexithiophene Spherical Nanocapsules. *J. Am. Chem. Soc.* **127**, 1112–1113 (2005).
3. Coey, J. M. D. *Magnetism and Magnetic Materials*. (Cambridge University Press, 2010).
4. Atkins, P. W. & De Paula, J. *Atkins' Physical Chemistry*. (Oxford University Press, 2014).
5. Polarz, S., Bährle, C., Landsmann, S. & Klaiber, A. Panoscopic Structures by Hierarchical Cascade Self-Assembly of Inorganic Surfactants with Magnetic Heads Containing Dysprosium Ions. *Angew. Chem. Int. Ed.* **52**, 13665–13670 (2013).
6. Sander Langereis, de Lussanet, Q. G., van Genderen, M. H. P., Backes, W. H. & Meijer, E. W. Multivalent Contrast Agents Based on Gadolinium−Diethylenetriaminepentaacetic Acid-Terminated Poly(propylene imine) Dendrimers for Magnetic Resonance Imaging. *Macromolecules* **37**, 3084–3091 (2004).
7. Fujiwara, M., Kodoi, D., Duan, W. & Tanimoto, Y. Separation of Transition Metal Ions in an Inhomogeneous Magnetic Field. *J. Phys. Chem. B* **105**, 3343–3345 (2001).
8. Fujiwara, M., Chie, K., Sawai, J., Shimizu, D. & Tanimoto, Y. On the Movement of Paramagnetic Ions in an Inhomogeneous Magnetic Field. *J. Phys. Chem. B* **108**, 3531–3534 (2004).
9. Fujiwara, M., Mitsuda, K. & Tanimoto, Y. Movement and Diffusion of Paramagnetic Ions in a Magnetic Field. *J. Phys. Chem. B* **110**, 13965–13969 (2006).
10. Yue, B., Jin, X., Zhao, P., Zhu, M. & Zhu, L. Directed Self-Assembly of Templatable Block Copolymers by Easily Accessible Magnetic Control. *Small* **15**, 1804572 (2019).
11. Schefer, L., Bulant, A., Zeder, C., Saha, A. & Mezzenga, R. Magnetic Control of Macromolecular Conformations in Supramolecular Anionic Polysaccharide–Iron Complexes. *Angew. Chem.* **127**, 13487–13490 (2015).
12. Briganti, M., Garcia, G. F., Jung, J., Sessoli, R., Le Guennic, B. & Totti, F. Covalency and Magnetic Anisotropy in Lanthanide Single Molecule Magnets: The DyDOTA Archetype. *Chem. Sci.* **10**, 7233–7245 (2019).
13. Suwa, M. Magnetoanalysis of Micro/Nanoparticles: A review. *Anal. Chim. Acta* **690**, 137–147 (2011).

Summary

This thesis, entitled "Magnetic control over supramolecular polymerization", provides a general overview over the possibilities a magnetic stimulus can offer to control supramolecular systems. The final goal is to identify whether magnetic effects can complete the toolbox of non-covalent interactions in supramolecular self-assembly.

Supramolecular polymers are composed of non-covalently linked repeating units. These reversible interactions make supramolecular materials inherently dynamic, enabling self-repair and stimuli-responsiveness.[1] Their ability to adapt to their environment is commonly exploited to control their properties by external stimuli[1] such as temperature, pH, light, redox potential, mechanical force, or enzymes. Magnetism is rarely used as a trigger, even though it offers many benefits, that cannot be provided by the more conventional alternatives. It is non-invasive and non-destructive, easily tunable in intensity, spatial range, and time, and compatible with most types of materials and atmospheres. In colloidal systems, weak magnetic fields of ≤ 2 T are sufficient to control and direct self-assembly. On a (supra-) molecular scale, in contrast, strong fields in the order of 10 to 30 T are required to achieve observable effects in mild conditions—that is at low concentration, atmospheric pressure, and room temperature.[2] This is because the magnetic energy $E_{mag} = -\frac{1}{2} mB$ is in competition with the thermal energy of Brownian motion $E_{therm} = -\frac{3}{2} k_B T$, where m is the magnetic moment of the particle, B the magnetic flux density, k_B Boltzmann's constant, and T the absolute temperature.[3,4]

Nevertheless, several recent studies report observations that are unexpected in this context. Most of these non-trivial phenomena lack a satisfactory understanding.[5–9] Polarz and coworkers observed a complex, multi-step supramolecular assembly of a Dy^{3+}-chelating surfactant to mm-sized dumbbells, which did not form when using a diamagnetic analog with Lu^{3+}.[5] Zhu and coworkers were able to direct the self-assembly of tetrabromoferrate containing block-copolymers to microphase-segregated nanostructures in low-intensity fields of only 0.35 T.[10] For a polysaccharide enriched with ferric ions, Mezzenga and coworkers have shown a magnetically triggered change of the polymer chain conformation from random coils to helices in a 1.1 T constant field.[11]

Inspired by these recent reports, we aimed to get a deeper understanding of how the incorporation of magnetic ions influences supramolecular systems, and how these materials respond to weak magnetic fields. To this end, four systems have been studied, which all concentrate on a separate aspect of the field. With a special focus on a simple and accessible experimental setup, the use of magnetic fields will be restricted to weak fields of ≤ 2 T.

Firstly (**Chapter 2**), and most fundamentally, we have studied whether the incorporation of paramagnetic lanthanide ions into naphthalene diimide (NDI) derivatives influences their self-assembly. Therefore, a library of isostructural coordination complexes **M-NDI** was prepared using five different paramagnetic (**M**$^{3+}$ = Tb^{3+}, Dy^{3+}, Gd^{3+}, Ho^{3+}, Er^{3+}) and three diamagnetic (**M**$^{3+}$ = Y^{3+}, La^{3+}, Lu^{3+}) lanthanide ions. The five paramagnetic ions were selected for to their elevated magnetic moments, and their different electron density distributions. The latter has been shown to be decisive for the magnetic properties of lanthanide complexes in the crystal state.[12] The NDI core unit induces supramolecular polymerization through π-π stacking and the hydrophobic effect. As NDI derivatives are typically weak assemblers—with enthalpies of supramolecular polymerization inferior to those of common alternatives such as perylene diimides, benzenetricaboxamides, porphyrines, or pyridines—it was chosen for this study to

ensure that possible magnetic effects are not outcompeted by an overly dominant self-organization process.

The self-assembly of **M-NDI** in water was analyzed by UV-Vis spectroscopy, following the characteristic absorption bands of the aromatic core. By applying described theoretical models for an isodesmic polymerization mechanism, the Gibbs free energy of supramolecular polymerization ΔG and its components, the enthalpy ΔH and the entropic contribution $T\Delta S$, could be determined. The free energies were obtained with high precision, with values between –14 and –12 kJ·mol^{-1} for all members of the family **M-NDI**. The enthalpy/entropy balance, however, shifts significantly depending on the incorporated ion **M**. Namely, the negative enthalpy increases by up to 60 % for **Dy-NDI** as compared to the diamagnetic control **Y-NDI**. The trend of the enthalpy follows the magnetic moment of the respective ions over the whole scope of eight monomers. SQUID measurements of the bulk compounds reveal a sizeable antiferromagnetic coupling between the magnetic lanthanide ions in **M-NDI**. These results lead to the conclusion that there are in fact significant magnetic interactions between the ions. These stabilize the assembled state of **M-NDI,** which reflects in larger negative enthalpies of supramolecular polymerization. Owing to enthalpy-entropy compensation, the overall equilibrium constant and the free Gibbs energy remain unaffected.

Chapter 3 presents the self-assembly of the same monomer **M-NDI** in a binary water/THF system. At elevated volume fractions φ_{THF} of THF, the monomers assemble to micrometer-sized spherical colloids, as evidenced by atomic force microscopy. The strong solvent dependence indicates that this second type of self-assembly is driven by solvophobic interactions. The polymerization was equally followed by UV-Vis spectroscopy. Therefore, the THF volume fraction was screened from 0.60 to 0.95 for 0.1 mM **Dy-NDI**. A sigmoidal increase of the absorbance at 395 nm suggests an isodesmic polymerization mechanism. The corresponding colloid sizes were measured by dynamic light scattering (DLS), which reveal an increase of the average hydrodynamic particle radius from 1 to 5 µm with increasing values of φ_{THF}.

When applying the gradient magnetic field of a commercial, 0.5 cm NdFeB cube magnet to dispersions of **Dy-NDI** at $\varphi_{THF} \geq 0.80$ for 4 h, an organic layer is formed at the surface of the magnet. It is around 100 µm thick and exhibits the characteristic orange NDI color. The magnetically directed movement of the colloids towards the magnet surface could be visualized by confocal microscopy.

Theory predicts that the magnetic force surpasses the thermal force of Brownian motion at a certain critical colloid size, as the particle volume correlates directly with its magnetic moment at constant magnetic susceptibility and dynamic viscosity.[13] If the magnetic force is predominant, matter can be transported through space. This phenomenon is known as magnetophoresis.

Following this reasoning, we can correlate the observed layer formation with the colloid size and the degree of polymerization of the respective **Dy-NDI** dispersions at different THF volume fractions. All compounds **M-NDI** incorporating magnetic ions (**M**$^{3+}$ = Gd^{3+}, Dy^{3+}, Tb^{3+}, Ho^{3+}, Er^{3+}) form a layer at $\varphi_{THF} = 0.95$, whereas diamagnetic control molecules (**M**$^{3+}$ = Y^{3+}, La^{3+}, Lu^{3+}) do not. Once the layer is formed, it can be removed fast and easily by adding water to decrease φ_{THF}.

To our knowledge, this is the first report of magnetophoresis in a supramolecular system. The simplicity and reversibility of this approach offers a new degree of spatiotemporal control over soft matter.

Chapter 4 presents the self-assembly of a 1,3,5-benzenetricarboxamide (BTA) derivative, decorated with paramagnetic Gd^{3+} ions in solution. Using dynamic and static light scattering, we could analyze the topology of the system. The recorded correlation function is bimodal, which indicates the coexistence of two different populations **P1** and **P2**. Thus, we assume that **Gd-BTA** assembles in a two-step process: a first assembly of the monomers into rods (**P1**), which then assemble further into networks of rods (**P2**). The corresponding hydrodynamic radii are of around 30 nm for **P1**, and 350 nm for **P2**. The diamagnetic analog **Y-BTA**, where Gd^{3+} is replaced by Y^{3+}, shows similar behavior.

With this new insight into the network structure, the response of a **Gd-BTA** solution to a uniform magnetic field of 1 or 2 T was investigated. Therefore, the sample was placed in the field for one hour, then removed from the field and analyzed by static light scattering for one hour. This cycle was repeated 6 to 7 times, adding up to a total measuring time of 12 to 14 h per experiment. Upon 14 h of exposure to a magnetic field, the Rayleigh ratio $R(q)$ (which is derived from the scattering intensity) of the **Gd-BTA** rod network (**P2**) increases by 20 and 35 % for 1 and 2 T, respectively. These results imply a densification of the rod network over time. The Rayleigh ratio of the **P1** process remains unchanged. Moreover, the evolution of the fractal dimension d_F was followed over time, revealing a spontaneous transformation of the network morphology from rod-like ($d_F = 1.7$) to randomly branched structures ($d_F = 2.6$ for 2 T) within one hour. If the magnetic field is removed, the system relaxes back to its initial state. A control experiment with diamagnetic **Y-BTA** shows that the assembly of the latter does not undergo any topological change.

SQUID measurements show that the magnetic susceptibility of the **Gd-BTA** solution decreases by around 2 % over 12 h. The time scale is in good agreement with the densification process we observe by static light scattering. Magnetic ground state calculations demonstrate that the anisotropic free energy of the system is the driving force of the observed phenomenon.

We can thus conclude that the application of a magnetic field perturbs the thermodynamic equilibrium of the system reversibly. It appears that the magnetic stimulus drives the self-assembly entropically through (partial) alignment of the rods. Thereby, the mutual dependence of alignment and polymer growth provides positive feedback.

Chapter 5 describes our efforts towards the development of magneto-responsive materials. We introduce a hydrogel based on *N*,*N*′-bis (5-aminoisophthalic acid)naphthalene diimide (**BINDI**) and magnetic Dy^{3+} ions. The gel network emerges from coordination of the free carboxylates of **BINDI** to the lanthanide ions, and a controlled pH decrease triggered by glucono-δ-lactone (GdL). We studied the impact of a uniform magnetic field on the gelation process and the mechanical properties of the formed gels using magnetorheology. Kinetic measurements show that the gelation of **Dy-BINDI** proceeds almost twice as fast in a 0.78 T field than in the absence of a magnetic field. The gelation time is reduced from 650 to 340 min. In both cases, the final mechanical stiffness of the gel is of around 1.3 kPa. In a weaker field of 0.13 T, the gelation is still significantly reduced, by 14 %. Switching the field on at different times during gelation allows to fine-tune the kinetic profile. Scanning transmission electron microscopy (STEM) of

Dy-BINDI gels reveals a fibrillar microstructure with an average fiber thickness of around 10 nm.

If Dy^{3+} is replaced by other magnetic lanthanides (Gd^{3+}, Er^{3+}), we find similar trends. In the case of diamagnetic La^{3+}, the gelation is accelerated by 48 %, which is surprising considering the purely diamagnetic nature of the system. Hence, we assume a diamagnetic contribution stemming from the diamagnetic anisotropy of the large π-system in assembled **BINDI**. To verify this hypothesis, a lanthanide-free **BINDI** gel was prepared, which required increasing the GdL concentration. This adjustment of the gelation conditions suggests that the gel structures of the two systems differ significantly. Indeed, STEM imaging of the lanthanide-free **BINDI** gel shows thicker fibers of around 50 nm in diameter. Surprisingly, the application of a 0.78 T field to this second system prevents gelation entirely. The system collapses after having reached around half of the final stiffness of the gel formed in 0 T.

Based on these results, we suppose that partial alignment, diamagnetic or paramagnetic, of the fibers favors supramolecular polymerization entropically. Even partially aligned building blocks would possess a reduced number of degrees of freedom, which would moderate the entropy loss upon their assembly. So far, we have not been able to confirm fiber alignment by microscopy or birefringence of the material.

Even though the gelation mechanisms of both systems remain to be elucidated in more detail, these results are promising regarding the conception of magnetically controllable materials. Considering the low intensity of the applied magnetic fields as well as the small magnetic susceptibilities of the components, the extent and precision of control over the bulk material is striking.

Chapter 6 concludes the main findings and integrates these in the larger picture.

Overall, the presented work shows our efforts to sketch the impact of a magnetic stimulus on supramolecular systems. The possibilities and limits are demonstrated in four different scenarios, namely a 1D polymer in solution (**Chapter 2**), a colloidal polymer in dispersion (**Chapter 3**), a fiber network in solution (**Chapter 4**), and a hydrogel (**Chapter 5**). We give insight into the thermodynamics of magnetic self-assembly and present new approaches to guide structure formation. Considering the novelty of the field, the obtained findings lay a solid foundation for future studies, which can range from fundamental supramolecular polymerization to the development of smart materials.

References

1. Aida, T., Meijer, E. W. & Stupp, S. I. Functional Supramolecular Polymers. *Science* **335**, 813–817 (2012).
2. Shklyarevskiy, I. O., Jonkheijm, P., Christianen, P. C. M., Schenning, A. P. H. J., Meijer, E. W., Henze, O., Kilbinger, A. F. M., Feast, W. J., Del Guerzo, A., Desvergne, J.-P. & Maan, J. C. Magnetic Deformation of Self-Assembled Sexithiophene Spherical Nanocapsules. *J. Am. Chem. Soc.* **127**, 1112–1113 (2005).
3. Coey, J. M. D. *Magnetism and Magnetic Materials*. (Cambridge University Press, 2010).
4. Atkins, P. W. & De Paula, J. *Atkins' Physical Chemistry*. (Oxford University Press, 2014).
5. Polarz, S., Bährle, C., Landsmann, S. & Klaiber, A. Panoscopic Structures by Hierarchical Cascade Self-Assembly of Inorganic Surfactants with Magnetic Heads Containing Dysprosium Ions. *Angew. Chem. Int. Ed.* **52**, 13665–13670 (2013).
6. Sander Langereis, de Lussanet, Q. G., van Genderen, M. H. P., Backes, W. H. & Meijer, E. W. Multivalent Contrast Agents Based on Gadolinium−Diethylenetriaminepentaacetic Acid-Terminated Poly(propylene imine) Dendrimers for Magnetic Resonance Imaging. *Macromolecules* **37**, 3084–3091 (2004).
7. Fujiwara, M., Kodoi, D., Duan, W. & Tanimoto, Y. Separation of Transition Metal Ions in an Inhomogeneous Magnetic Field. *J. Phys. Chem. B* **105**, 3343–3345 (2001).
8. Fujiwara, M., Chie, K., Sawai, J., Shimizu, D. & Tanimoto, Y. On the Movement of Paramagnetic Ions in an Inhomogeneous Magnetic Field. *J. Phys. Chem. B* **108**, 3531–3534 (2004).
9. Fujiwara, M., Mitsuda, K. & Tanimoto, Y. Movement and Diffusion of Paramagnetic Ions in a Magnetic Field. *J. Phys. Chem. B* **110**, 13965–13969 (2006).
10. Yue, B., Jin, X., Zhao, P., Zhu, M. & Zhu, L. Directed Self-Assembly of Templatable Block Copolymers by Easily Accessible Magnetic Control. *Small* **15**, 1804572 (2019).
11. Schefer, L., Bulant, A., Zeder, C., Saha, A. & Mezzenga, R. Magnetic Control of Macromolecular Conformations in Supramolecular Anionic Polysaccharide–Iron Complexes. *Angew. Chem.* **127**, 13487–13490 (2015).
12. Briganti, M., Garcia, G. F., Jung, J., Sessoli, R., Le Guennic, B. & Totti, F. Covalency and Magnetic Anisotropy in Lanthanide Single Molecule Magnets: The DyDOTA Archetype. *Chem. Sci.* **10**, 7233–7245 (2019).
13. Suwa, M. Magnetoanalysis of Micro/Nanoparticles: A review. *Anal. Chim. Acta* **690**, 137–147 (2011).

List of abbreviations

1D, 2D, 3D	1-dimensional, 2-dimensional, 3-dimensional
ACN	acetonitrile
ACQ	aggregation caused quenching
ADP	adenosine diphosphate
AFM	atomic force microscopy
AIC	Akaike Information Criterion
ATP	adenosine triphosphate
BCP	block copolymer
Boc	*tert*-butyl oxyl carbonyl
BTA	1,3,5-benzene tricraboxamide
CD	circular dichroism
CHCA	cyano-4-hydroxy cinnamic acid
CMC	critical micelle concentration
CN	coordination number
COSY	correlation spectroscopy
cryo-TEM	cryogenic transmission electron microscopy
CW	clockwise
CCW	counterclockwise
DCM	dichloromethane
DIPEA	*N*,*N*-diisopropylethylamine
DLS	dynamic light scattering
DMF	dimethyl formamide
DMSO	dimethyl sulfoxide
DNA	deoxyribonucleic acid
DOTA	1,4,7,10-tetraazacyclododecane-1,4,7,10-tetraacetic acid, tetraxetan
DOSY	diffusion ordered spectroscopy
DTPA	diethylenetriaminepentaacetic acid
DSC	differential scanning calorimetry
EPR	electron paramagnetic resonance
ESI	electron spray ionization

EtOH	ethanol
FC	field cooling
FDA	Food and Drug Association (USA)
Fmoc	fluorenyl methoxy carbonyl
FTIR	Fourier transform infrared (-spectroscopy)
GdL	glucono-δ-lactone
HBTU	(2-(1*H*-benzotriazol-1-yl)-1,1,3,3-tetramethyluronium hexafluorophosphate
HFIP	hexafluoro-2-propanol
HMBC	heteronuclear multiple bond correlation
HPLC	high performance liquid chromatography
HSQC	heteronuclear spin quantum coherence
IL	ionic liquid
IO-NP	iron oxide nanoparticle
IR	infrared
ITC	isothermal titration calorimetry
IUPAC	International Unit of Pure and Applied Chemistry
LC-MS	liquid chromatography - mass spectrometry
LD	linear dichroism
LVER	linear viscoelastic region
MCH	methylcyclohexane
MeOH	methanol
MALDI	matrix-assisted laser desorption / ionization
MRI	magnetic resonance imaging
MS	mass spectrometry
NDI	naphthalene diimide
NMR	nuclear magnetic resonance
NP	nanoparticle
PDA	photo diode array
PDI	perylene diimide
rpm	revolutions per minute
RSS	residual sum of squares

SEM	scanning electron microscopy
SANS	small angle neutron scattering
SAXS	small angle X-ray scattering
SLS	static light scattering
SMM	single molecule magnet
SQUID	Superconducting Quantum Interference Device
STEM	scanning transmission electron microscopy
*t*Bu	*tert*-butyl
TEM	transmission electron microscopy
TEMPO	(2,2,6,6-tetramethylpiperidin-1-yl)oxyl
TFA	trifluoroacetic acid
TGA	thermogravimetric analysis
THF	tetrahydrofuran
TIC	total ion count
TOF	time-of-flight
TLC	thin layer chromatography
UV-Vis	ultraviolet-visible
XRD	X-ray diffraction
ZFC	zero field cooling

List of symbols

A	absorbance	(-)
	amplitude	(-)
B	magnetic flux density	(T)
	baseline correction factor	(-)
c	molar concentration	($mol \cdot L^{-1}$)
C	Curie constant	(K)
C_p	molar heat capacity	($J \cdot mol^{-1} \cdot K^{-1}$)
d	distance	(m)
d_F	fractal dimension	(-)
D_t	translational diffusion coefficient	(m^{-1})
E	energy	(J)
E_{mag}	magnetic energy	(J)
E_{therm}	thermal energy	(J)
F	force	(N)
F_{mag}	magnetic force	(N)
F_{therm}	thermal force	(N)
g^1	electric field correlation function	(-)
Δg	dissymmetry factor	(-)
G	Schulz distribution function	(-)
G'	storage modulus	(Pa)
G''	loss modulus	(Pa)
G_n	normal gravitation	(N)
G_{eff}	effective gravitation	(N)
ΔG	Gibbs free energy of supramolecular polymerization	($J \cdot mol^{-1}$)
ΔH	enthalpy of supramolecular polymerization	($J \cdot mol^{-1}$)
I	electric current	(A)
	intensity	(-)
K_{eq}	equilibrium constant	(variable, here M^{-1})
K_e	elongation constant	(variable, here M^{-1})
K_{nuc}	nucleation constant	(variable, here -)

m	magnetic dipole moment	(μ_B, Am^2, or $J \cdot T^{-1}$)
	denaturation potential	($J \cdot mol^{-1}$)
m/z	mass over charge ratio	(-)
M	(volume) magnetization	($A \cdot m^{-1}$)
M_S	magnetization saturation	($A \cdot m^{-1}$)
n	refractive index	(-)
N	demagnetization factor	(-)
	number of foreground pixels *(box counting)*	(-)
R	S_0-S_1(0-1) / S_0-S_1(0-0) absorbance ratio	(-)
R or r	radius	(m)
R_H	hydrodynamic radius	(m)
$R(q)$ or R	Rayleigh ratio	(-)
ΔS	entropy change	($J \cdot mol^{-1}$)
t	time	(s, min, or h)
$t_{1/2}$	half time of gelation	(min)
t_g	time of full gelation	(min)
t_s	starting time of gelation	(min)
t_{tr}	trigger time	(min)
T	temperature	(°C or K)
T_C	Curie temperature	(°C or K)
T_m	melting temperature	(°C or K)
T_N	Néel temperature	(°C or K)
T_r	reduced temperature	(°C or K)
q	scattering vector	(m^{-1})
V	volume	(m^3)
v_{mag}	average magnetophoretic velocity	($\mu m \cdot s^{-1}$)
x	mole fraction	(-)
z	Schulz distribution parameter	(-)

α	degree of supramolecular polymerization	(-)
β	$E_{mag} \cdot E_{therm}^{-1}$ or $F_{mag} \cdot F_{therm}^{-1}$	(-)
Γ	decay rate	(s^{-1})
δ	chemical shift	(ppm)
ε	molar absorption coefficient	($mol^{-1} \cdot cm^{-1}$)
	caliber	(m^2)
η	dynamic viscosity	(Pa·s)
θ	reference temperature	(K)
ϑ	angle	(° or rad)
λ	wavelength	(m)
μ	magnetic moment	(μ_B, Am^2, or $J \cdot T^{-1}$)
	magnetic permeability	($H \cdot m^{-1}$ or $N \cdot A^{-2}$)
	central moment	(-)
ν	wave number	(cm^{-1})
ρ	density	($kg \cdot m^{-3}$)
σ	cooperativity	constant (-)
	normalized standard deviation	(-)
τ	relaxation time	(s)
φ	volume fraction	(-)
χ or χ_V	volumetric magnetic susceptibility	(-)
χ_m	massic magnetic susceptibility	($m^3 \cdot kg^{-1}$)
χ_n	molar magnetic susceptibility	($m^3 \cdot mol^{-1}$)
$\omega(t)$	Gaussian white noise operator	(-)

List of constants

k_B	Boltzmann constant	$1.381 \cdot 10^{23}$ J·K^{-1}
N_A	Avogadro constant	$6.022 \cdot 10^{23}$ mol^{-1}
μ_B	Bohr magneton	$9.274 \cdot 10^{-24}$ A·m^2 = $9.274 \cdot 10^{-24}$ J·T^{-1}
μ_0	vacuum permeability	$1.256 \cdot 10^{-6}$ N·A^{-2}
R	gas constant	8.314 J·mol^{-1}·K^{-1}

List of SI-derived and CGS units

°C	degree Celsius	(x – 273.15) K
Å	Ångström	10^{-10} m
emu	electromagnetic units	A·m^2
F	Farad	s^4·A^2·m^{-2}·kg^{-2}
Gs	Gauss	10^{-4} T = 10^{-4} kg·s^{-1}·A^{-1} = μ_0 Oe
Hz	Hertz	s^{-1}
J	Joule	kg·m^2·s^{-2}
M	molar	mol·dm^{-3}
N	Newton	kg·m·s^{-2}
Oe	Oersted	Gs·μ_0^{-1} = 10^{-4} T ·μ_0^{-1}
Pa	Pascal	kg·m^{-1}·s^{-2}
T	Tesla	kg·s^{-1}·A^{-1}
W	Watt	kg·m^1·s^{-3}

Chapter 1. General introduction

Abstract

Supramolecular polymers are inherently dynamic and reversible, enabling stimuli-responsiveness, and self-healing.[1] Controlling them by external stimuli has been in the focus of research ever since they were first developed in the late 1980s, envisioning the application of these smart materials in electronics, biomedical applications, and a more sustainable use of polymers.[2] So far, magnetism is rather rarely utilized as a stimulus, because in standard conditions the magnetic energies and forces are often insignificant as compared to thermal fluctuations. It withholds, however, many opportunities considering that magnetic fields are non-invasive, easily tunable in field strength and direction, and tolerate many conditions and atmospheres. Starting with the basic principles of supramolecular polymerization and magnetism, this chapter will lay out the state of the art of magnetic control over soft matter, with a special focus on self-assembled materials.

1.1. Controlling supramolecular polymerization

1.1.1 Supramolecular chemistry: self-organization and self-assembly

Described as "chemistry beyond the molecule" by Nobel laureate Jean-Marie Lehn, supramolecular chemistry studies non-covalent interactions between building blocks of variable structures and sizes, forming multi-component assembled structures.[3] With impressive precision, supramolecular interactions guide the self-assembly of natural compounds to specific arrangements and conformations. As the interactions are non-covalent, the assembly processes are dynamic and reversible, which allows biological systems to perform vital functions such as reproduction, growth, self-repair, biosynthesis, and homeostasis.[4]

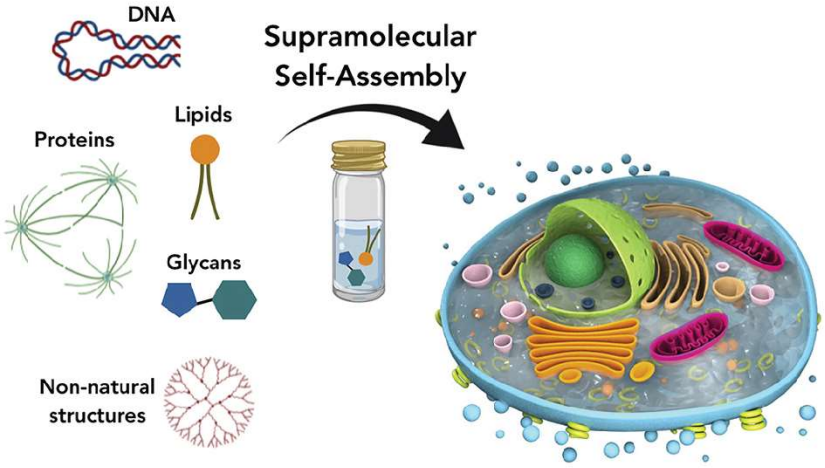

Figure 1.1 | Self-assembly from single compounds to a living cell. Schematic representation of the self-assembly of various (non-) natural compounds forming a cell. Figure reproduced from reference [4] with permission from Elsevier.

Famous examples of natural, self-assembled structures are proteins, the DNA double helix, cell walls, or viruses. As illustrated in Figure 1.2 for collagen (a) and the human DNA (b), self-assembly can occur hierarchically at many different scales. For instance, the polypeptide chains of omnipresent collagen self-assemble into α–chains, which in turn assemble into triple helices (collagen fibrils), and those finally form macro-sized collagen fibers. Similarly, the DNA strains first assemble to a double helix, and further to chromosomes in three more steps.

The self-assembly of molecules can be driven by various interactions: van der Waals forces (London forces), H-bonding, π-π interactions, electrostatic interactions (charge-charge, charge-dipole, dipole-dipole, charge-induced dipole, dipole-induced dipole), and coordination bonding, to name only the most common ones. All of these are unique in their binding energies, spatial range, and directionality. An interplay of different types of interactions can lead to the formation of well-ordered and highly complex structures.

The first synthetic examples of molecular recognition are cryptands[5], spherands[6], clathrates[7], and crown ethers (1973-1979). The pioneering work of Lehn[8], Pedersen[9], and Cram[10] was awarded the Nobel prize in 1987. Since then, a vast number of increasingly diverse and complex supramolecular systems have been developed, such as well-defined nanostructures[11], crystalline networks[12], or monolayers[13].[1]

1.1.2 Supramolecular polymerization

Supramolecular polymers are one class of self-assembled structures. They are polymeric arrays composed of non-covalently and reversibly bound repeating units.[14] Inspired by natural supramolecular polymers, like the previous examples collagen and DNA (Figure 1.2a,b), scientists have mimicked their assembly in synthetic systems. Stupp and coworkers have developed supramolecular polymers based on polypeptides, which assemble through hydrogen bonding to fibrous structures (Figure 1.2c).[15] Figure 1.2d shows an example by the group of Würthner, based on an aromatic perylenediimide (PDI) core, inducing supramolecular assembly through hydrophobic effects and π-π stacking.

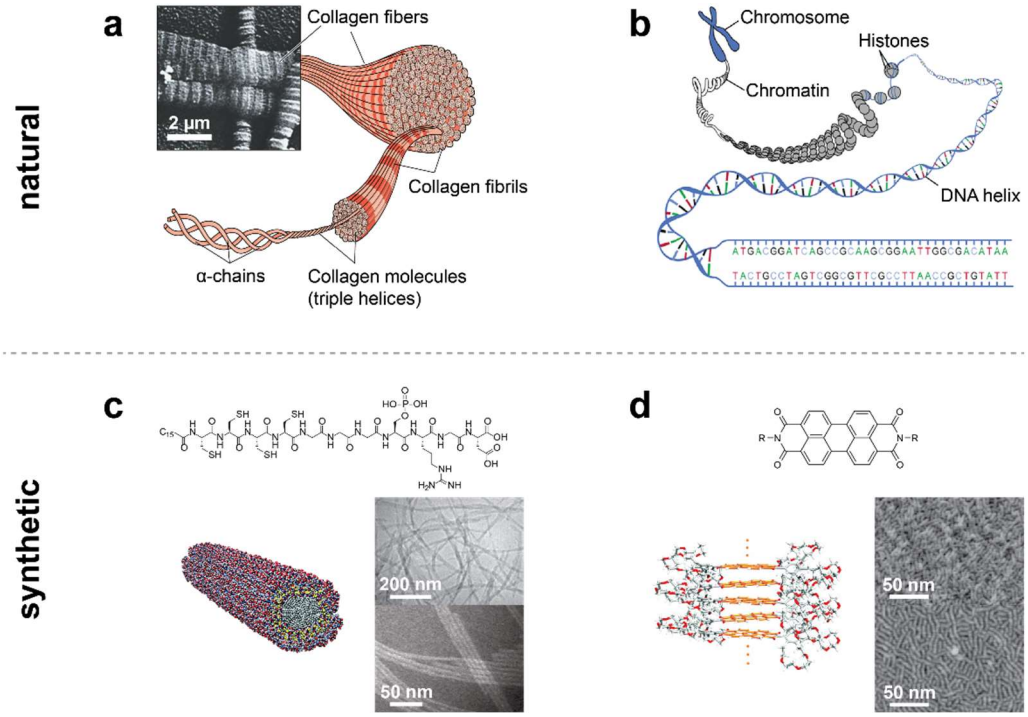

Figure 1.2 | Natural and synthetic supramolecular polymers. (a) Illustration and SEM image of hierarchically self-assembled collagen fibers.[16] (b) Illustration of the hierarchical self-assembly of the human DNA strains to a chromosome.[17] (c) Self-assembled supramolecular fibers of a polypeptide, reported by Stupp and coworkers.[15] The supramolecular polymerization is driven by hydrogen bonding. (d) Self-assembly of a perylene diimide-derivatives into fiber networks, reported by Würthner and coworkers.[18] The polymerization is driven by π-π stacking and hydrophobic interactions. Figure adapted from references [16–18] with permission from Wiley.

The interactions between the monomers determine the arrangement of the monomers with respect to each other, and the final structure of the polymer. Generally, the formed structure will be more regular and ordered, the more the interactions are directional. For regular one-dimensional molecular arrangements, we can find J- or H-type aggregation. In so-called J-aggregates, after Edwin Jelley[19], the monomers are aligned end-to-end. The absorption spectra of J–aggregates exhibit a characteristic, narrow J-band with a bathochromic shift (red-shift) with respect to the monomer absorption, and a nearly resonant fluorescence with small Stokes-shifts. Possible constellations are brick-wall like, ladder-like, or staircase-like. In an H-aggregate, on the other hand, they are joined face-to-face, showing a broader, hypsochromic shift (blue shift), and in most cases low or no fluorescence. The characteristic hypsochromic shift gave the aggregates their name. The observed energy shifts can be explained by excitation theory. If the monomers are considered as dipoles, their interaction leads to a splitting of the

excitonic states in two levels. In an end-to-end arrangement, the parallelly aligned dipoles are stabilized at the lower energy state. Opposed dipoles repel each other, destabilizing the assembly. In the case of face-to-face assemblies (H-aggregate), the opposite is the case. Parallel dipoles repel each other, and antiparallel dipoles attract each other, favoring the latter state energetically. For both cases, only the excitation to parallel alignment is allowed according to selection rules, as the transition dipole moment is zero, and thus forbidden, for antiparallel arrangement. For monomers with a flat structure, as typically found in aromatic moieties, absorbance (and emission) is often weakened or quenched upon aggregation (ACQ, aggregation caused quenching), which leads to a deviation from the Lambert-Beer law.[20,21]

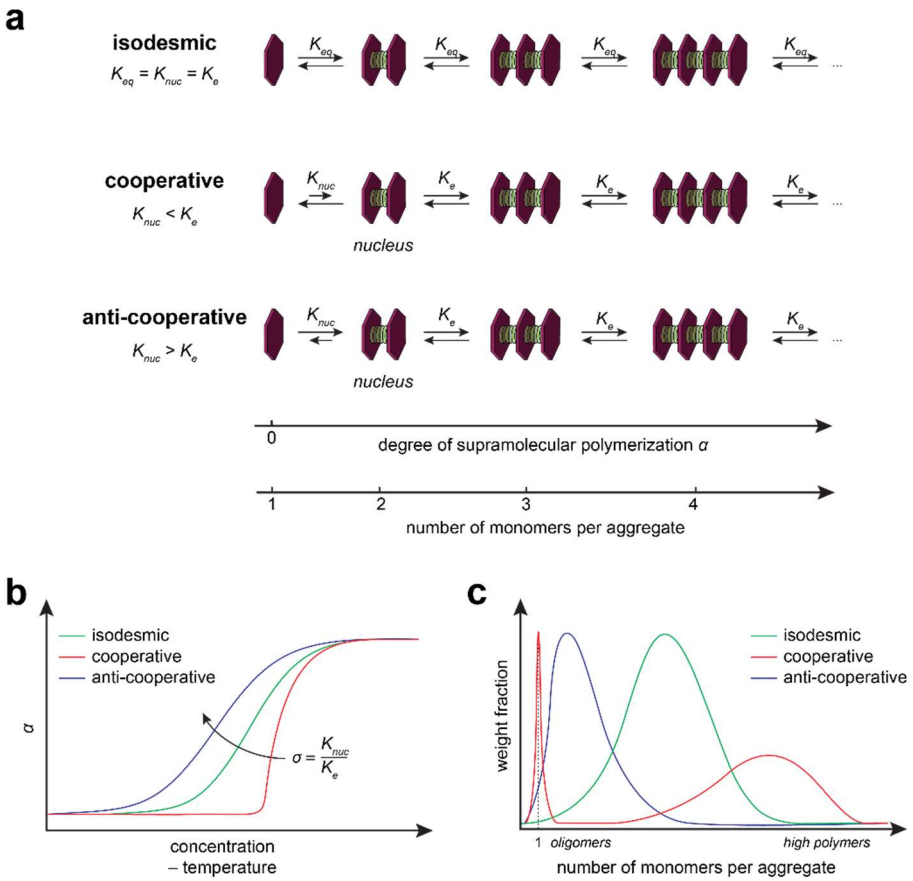

Figure 1.3 | Supramolecular polymerization mechanisms. (a) Scheme depicting stepwise chain growth following an isodesmic (top), cooperative (middle), and anti-cooperative mechanism (bottom). The processes are described by the equilibrium constants K_{eq}, the nucleation constant K_{nuc}, and the elongation constant K_e. In an isodesmic polymerization, K_{nuc} and K_e are equal. Consequently, there is a single equilibrium constant K_{eq}. In this scheme, the nucleus is a dimer. The number of monomers in the nucleus was arbitrarily chosen and is system specific. (b) Schematic illustration of the concentration- and temperature dependent supramolecular polymerization for isodesmic, cooperative, and anti-cooperative mechanisms. σ is the cooperativity constant, giving the ratio of K_{nuc} and K_e. (c) Schematic illustration of the polymer size distributions, expressed as number of monomers per aggregate, for isodesmic, cooperative, and anti-cooperative mechanisms.[22–24]

Different polymerization mechanisms can be distinguished by means of the thermodynamics and kinetics of the assembly process (Figure 1.3). In the simplest case, every addition of a monomer to a single or already assembled species is energetically equivalent, with a single equilibrium constant K_{eq}. Such a polymerization is called isodesmic. Cooperative

polymerization, in contrast, follows a nucleation–elongation mechanism. First, few monomers assemble to a nucleus, which triggers the elongation of the nucleus to a polymer. Thereby, the nucleation process is thermodynamically less favorable and slower than the elongation process ($K_{nuc} < K_e$). If the nucleation step is favored ($K_{nuc} < K_e$), the polymerization is called anti-cooperative.[23,25]

1.1.3 Stimuli-responsive supramolecular polymers

Their dynamic nature and reversibility represent the main advantage of supramolecular polymers as compared to their covalent counterparts. External stimuli to direct and control the mechanism, size, and shape of the assembly are thus important tools to exploit the potential of supramolecular polymers. The thermodynamics and kinetics of the assembly have been successfully controlled by a number of physical and chemical stimuli, allowing for the formation of diverse topologies using different pathways.[26] To present an overview over the vast possibilities, few selected examples will be discussed for the different triggers.

Temperature. Supramolecular polymers at their thermodynamic equilibrium are inherently temperature dependent. In the Gibbs free energy $\Delta G = \Delta H – T\Delta S$, the temperature is considered in the entropic term $T\Delta S$ alongside the enthalpy ΔH. The assembly of most supramolecular polymers is enthalpy-driven ($\Delta H < 0$), leading to disassembly upon heating, and assembly upon cooling. One example is the assembly of perylene diimide (PDI) derivatives reported by, among others, the group of Meijer[27]. Even though supramolecular assembly is in principle entropically disfavored, as the number of (supra)molecules is reduced in the process, this trend can be reversed, if the assembly induces a release of a large number of molecules from the solvation sphere of a monomer. One example of this kind has been reported for naphthalene diimides (NDIs) functionalized with ethylene glycol chains.[28]

These general trends can be evaded to achieve more precise control, as shown by Aida and coworkers.[29] Starting from a metalloporphyrin bearing amide-containing side chains, the authors observe a what they call “thermally bisignate” assembly behavior (Figure 1.4). The monomer assembles in dodecane and depolymerizes upon heating to 110 °C at a concentration of 10 μM. When 1-hexanol is used as a scavenger, the monomer is locked in a non-assembling form at around 50 °C (Phase 2), because the hydrogen bonding between the amide bond and the scavenger is favored as compared to amide-amide H-bonding. Cooling, on the other hand, favors self-aggregation of the scavenger (Phase 1), and further heating disrupts the alcohol-amide interactions, unlocking the monomers for polymerization (Phase 3).

The groups of Lee and Stupp have developed temperature-responsive liquid crystalline gels, which degenerate upon cooling.[1,30] These systems are specifically interesting, because cells can be encapsulated and aligned in a gel matrix under physiological conditions.

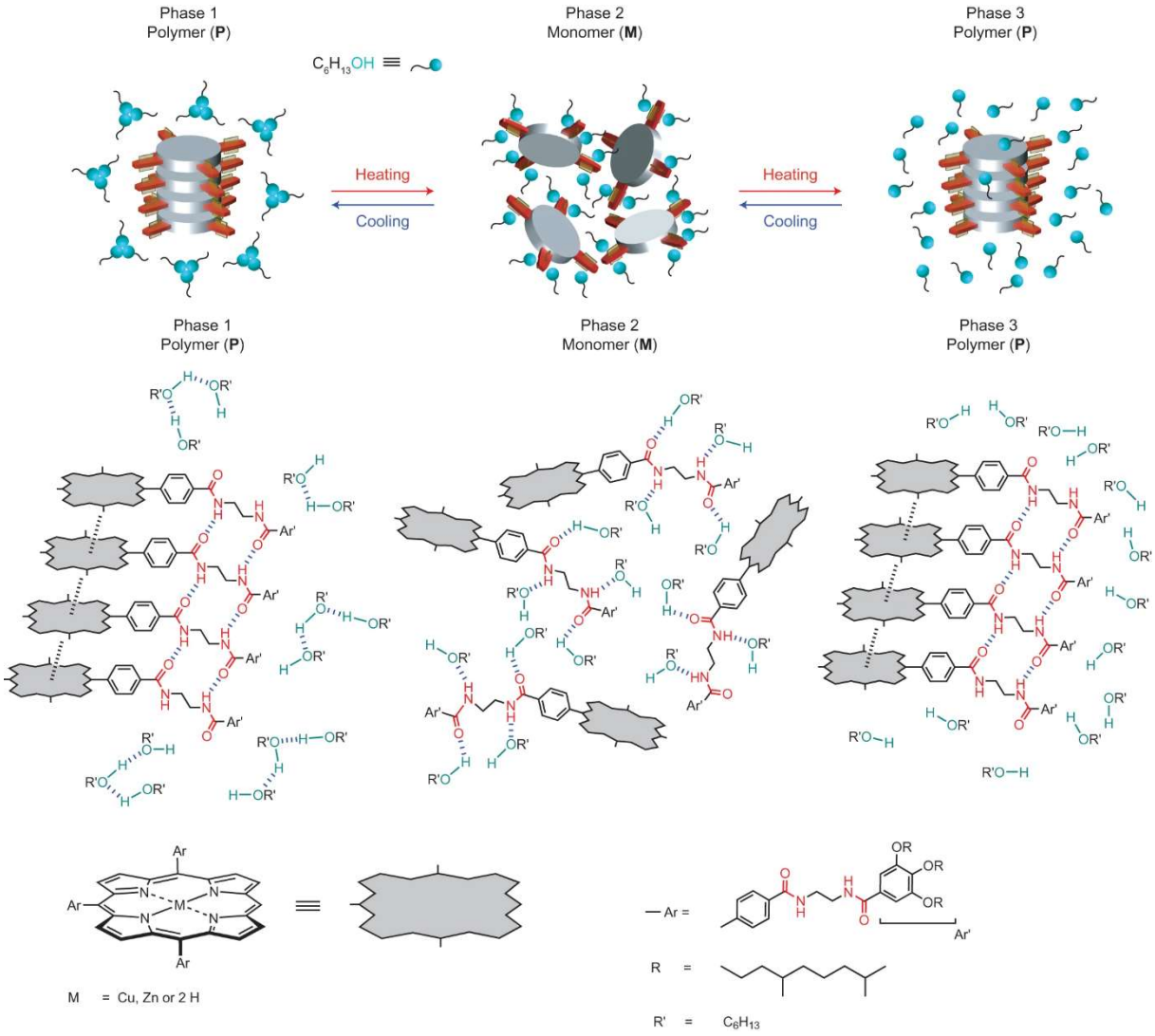

Figure 1.4 | Thermally bisignate metalloporphyrin assembly. Schematic (top) and structural (bottom) representation of the metalloporphyrin assemblies. The monomer (Phase 2) polymerizes upon both cooling (transition to phase 1) and heating (transition to phase 3), mediated by variable hydrogen bonding of the alcohol moieties in the scavenger. Amide groups are highlighted/ illustrated in red, alcohols in turquoise. Blue, dashed bonds represent hydrogen bonding. Black, dashed bonds represent π-π stacking. Reprinted from reference [29] with permission from Springer Nature.

Concentration. Alongside temperature, a concentration increase of the monomer is one of the most common factors to favor assembly. As the molecules are more likely to come in closer contact, short-range supramolecular interactions are more likely to be developed and stabilized. Let us revisit the temperature-controlled system of Meijer and collaborators as one of many possible examples. The *N*-tridodecyloxybenzyl functionalized PDI assembles to J-aggregates upon a concentration increase of 100 nM to 3 mM in methylcyclohexane.[27]

Zhao and coworkers reported multi-dimensional morphology changes of supramolecular assemblies based on a host-guest complex between a star-shaped pillar[5]arene trimer and a biviologen guest upon a change of concentration (Figure 1.5).[31] The assembly undergoes reversible transformation from spherical structures of about 400 nm at a concentration of 1 mM, to around 50 nm thick dendritic tubular fibers at 2 mM, and microscopic, regularly stacked layers at 5 mM.

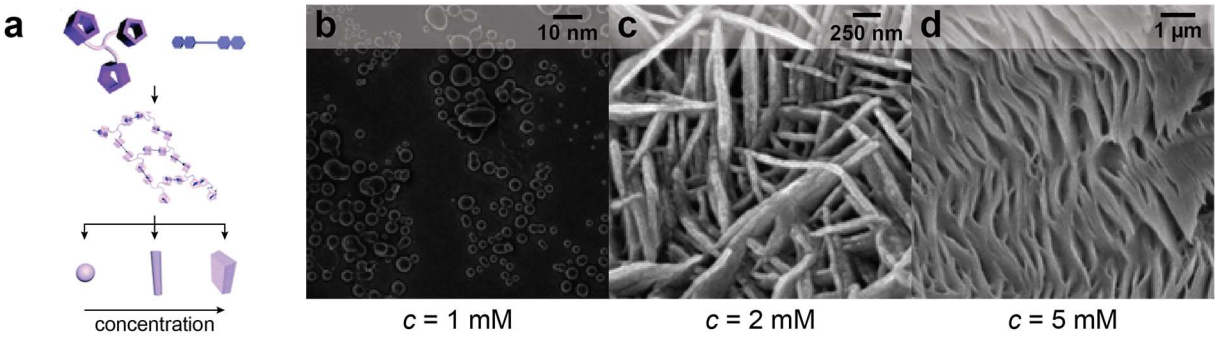

Figure 1.5 | Concentration-dependent, dynamic supramolecular self-assembly. (a) Schematic illustration of the self-assembly of a pillar[5]arene–biviologen (purple and blue, respectively) host-guest complex. (b-d) SEM images of assemblies at different concentrations of the guest–host complex: (b) spherical structures, with diameters of around 40 nm, at a concentration of 1mM, (c) dendritic tubular fibers, around 50 nm thick, in 2 mM. (d) regularly stacked layers, around 50 nm thick, in 5 mM. Figure adapted from reference [31] with permission of the Royal Society of Chemistry.

In the context of micellar self-assembly, the critical micelle concentration (CMC) is one of the main characteristics of a system. It refers to the concentration above which an amphiphile starts to from micelles. As pointed out by Hui and coworkers, this parameter is particularly important when it comes to drug delivery, as micellar assemblies dissociate upon dilution in *in vivo* conditions.[32] While this disassembly can be exploited for intended, therapeutic release, degradation or premature drug release can occur if the system is not adapted to the altered concentration.

Solvent. The molecular structure and polarity of the solvent system influences supramolecular assembly. Thereby it is decisive, whether the interactions of a building block are more favorable with the solvent molecule (good solvent) or with another building block (bad solvent). Increasing the fraction of good solvent in a system will thus lead to disassembly of a polymer, and vice versa, polymerization will be favored upon the addition of bad solvent. Testing the assembly behavior of a certain building block in different solvents often represents one of the initial experiments with a new system. De Greef, Meijer, and coworkers have studied the influence of a variable proportion of good (chloroform) and bad solvent (methylcyclohexane) for a range of different monomers and mechanisms.[33] For examples following a cooperative mechanism, complete disassembly is reached upon the addition of good solvent to a polymer in bad solvent from a critical solvent composition on. In the case of an isodesmic mechanism, the disassembly happens more gradually.

The influence of the solvent on the assembly can go so far as to allow the transition from solution to gel, which is commonly exploited to induce and reinforce supramolecular gelation.[34] One example is reported by the group of Ghosh, who studied the assembly of a core- and bay substituted naphthalene diimide (NDI, Figure 1.6).[35] Atomic force microscopy shows micrometer-scale entangled fibers of the polymer in linear hydrocarbons, of what is macroscopically a free standing gel. In the cyclic methylcyclohexane, in contrast, there is no gelation and the NDI forms spherical aggregates. UV-Vis spectroscopy confirms that the monomer assembles into well-ordered J-aggregates in hexane, with a typical bathochromic shift in absorbance. The UV-Vis spectrum in methylcyclohexane is broad and exhibits no significant shifts in wavelength, indicating another, less ordered state.

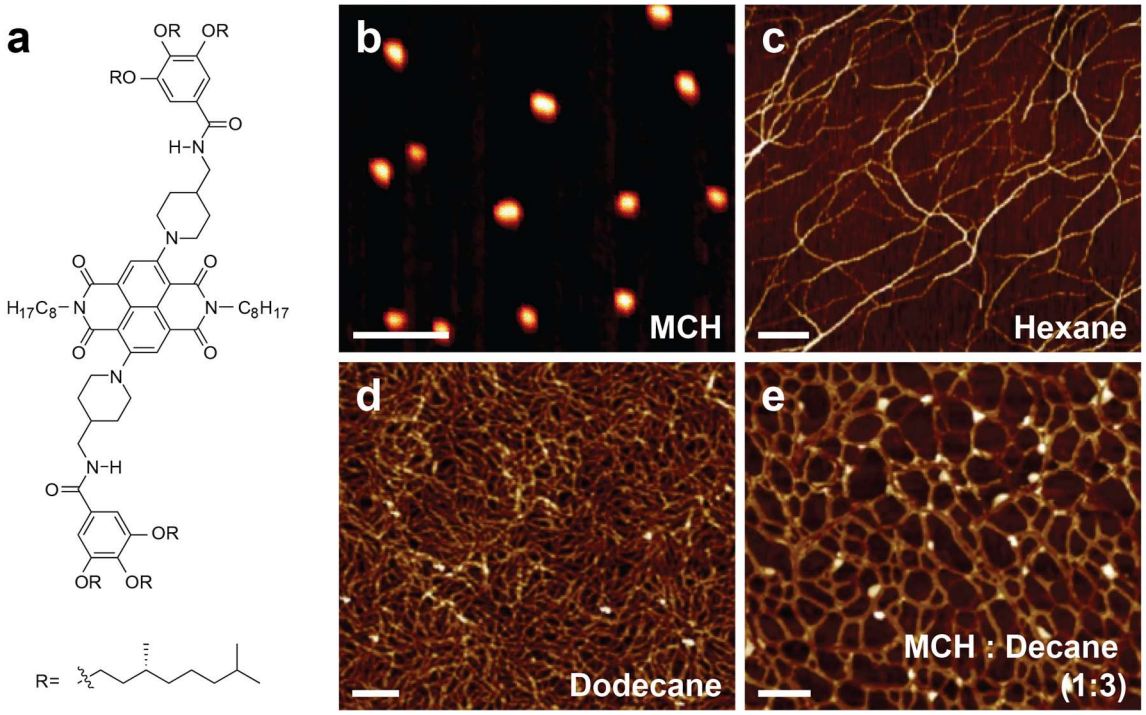

Figure 1.6 | Solvent induced supramolecular gelation. (a) Molecular structure of the NDI-based gelator. (b–e) AFM images of the assemblies in different solvents at a concentration of $2.5 \cdot 10^{-5}$ M: (a) methylcyclohexane, (b) *n*-hexane, (c) *n*-dodecane, and (e) a methylcyclohexane/*n*-decane mixture at a ratio of 1:3. Scale bars represent 1 µm. Figure adapted from reference [35] with permission from the Royal Society of Chemistry.

Besides guiding assembly and disassembly, interactions between specific building blocks and solvent molecules can be used to switch the supramolecular chirality of helical assemblies.[36,37]

Ionic strength. Changing the ionic strength of a system often reflects on supramolecular polymerization, either through electrostatic interactions, coordination, or overall solubility of the building blocks in the solvent. A very illustrative example has been reported by the group of Meijer.[38] A C_3-symmetrical benzene-tricarboxamide (BTA), decorated with Gd-DTPA units (*cf.* section 1.2.3.3) at its three extremities, is six-fold negatively charged. In citrate buffer (100 mM, pH 6), it aggregates weakly to globular assemblies in an anti-cooperative mechanism. A more favorable assembly to larger, fiber-like structures, as it is found for a charge neutral analog, is inhibited by the electrostatic repulsion of the charged moieties. When sodium chloride is added to the solution of the Gd-containing BTA to balance out the electrostatic repulsive interactions, the latter assembles to fibers in a cooperative mechanism.

Lee and coworkers have shown reversible switching between sheet-like and tubular structures of aromatic amphiphiles through reversible coordination to Ag^+.[39] Bent amphiphiles based on *m*-pyridine units assemble through π-π stacking to flat sheets in a zig-zag motif. When Ag^+ is added as a triflate salt, the pyridines reversibly coordinate to the cation disturbing the initial, π-π stacked arrangement. Instead, discrete dimeric rings are formed, which assemble to helical tubules if the concentration is increased from 0.01 to 0.03 wt%. Adding tetrabutylammonium fluoride leads to an instant decomplexation, whereby the initial sheet structures can be recovered from either the assembled or dimeric species.

pH. In a similar way, pH changes can direct supramolecular assembly. This trigger is well suitable and often used in peptide building blocks containing pH sensitive amino acids. Besenius and coworkers, for example, have shown that it is possible to switch between homo- and copolymers in a two-component system of BTA derivatives.[40] Both monomers contain a heptapeptide with a sequence of alternating phenylalanine (F) and Lysine (K, positively charged at neutral pH) in Monomer 1, or Glutamate (E, negatively charged at neutral pH) in monomer 2. A tetraethylene glycol dendron unit was coupled to the BTA-pentapeptide to improve solubility. By spectroscopy and microscopy, a copolymer of the monomers 1 and 2 is found, as attractive electrostatic interactions between the opposite charges dominate. Upon a pH switch to acidic pH, E moieties are protonated. The now charge-neutral monomer 2 forms a homopolymer, while monomer 1 remains monomeric in solution. In the opposite case, at basic pH, the K moiety is deprotonated, and the then charge neutral monomer 1 forms homopolymers.

Moreover, a pH trigger is often used to induce supramolecular gelation.[34] Tirrell and coworkers have developed a pH-responsive hydrogel based on branched peptide amphiphiles. The peptide backbones are end-capped with three histidine (H) and three Serine (S) residues and cross-linked via a fatty acid, which is conjugated through a lysine (K). The histidine units are used as the pH switch, which gets deprotonated above pH 6. In mildly acidic pH, it is protonated, and the amphiphile forms a viscoelastic liquid, which transitions to a self-supporting hydrogel upon a pH increase, as electrostatic repulsions are reduced through deprotonation. Depending on the concentration, stiffnesses of up to 10 kPa can be reached at a gelator concentration of 10 $mg \cdot mL^{-1}$.[41]

Redox potential. Redox chemistry is another powerful way to manipulate supramolecular assembly. Oxidizing or reducing agents can be used in variable ways, as physical compounds like sodium dithionite or dithiothreitol, as gases like oxygen in air, by light irradiation (photoreduction / photooxidation), or electrochemically. Aida and collaborators have shown redox-response of an *o*-phenylene oligomer end-capped with nitro groups, which assembles into a single handed 3_1 helical conformation due to the straining angles between the phenyl groups along the chain.[42] In solution, the helices undergo spontaneous and fast chiral inversion, which the authors found out could be blocked by a one-electron oxidation. The half-life of helical inversion could be extended drastically from around 6 minutes to 44 hours at –10 °C in acetonitrile. X-ray scattering elucidated that the 3_1 helical conformation is maintained after oxidation, however the interplanar distances are significantly reduced, indicating that the generated electron hole is widely delocalized over the π-system of the helix.

Two examples of redox-driven systems are subject to previous work of our group. Reversible, chemical reduction of a perylene diimide (PDI) derivative mediated by dithionite and oxygen has allowed Leira-Iglesias *et al.* to develop a dynamic reaction cycle, in which assemblies of neutral PDI disassemble upon reduction to the PDI dianion.[43] The neutral PDI assembles by a nucleation-elongation mechanism, and the redox cycle adds two more kinetic contributions (reduction and oxidation) to the system. If the rate constants of all the participating steps are well adjusted, the system can be driven away from the thermodynamic equilibrium, showing non-linear dynamic processes like oscillations, travelling fronts, and patterns.[44] Similarly, Singh *et al.* have developed a sol-gel reaction cycle based on an aldehyde saccharide hydrogelator, which disassembles upon the addition of dithionite under the formation of the corresponding α-hydroxy sulfonate.[45]

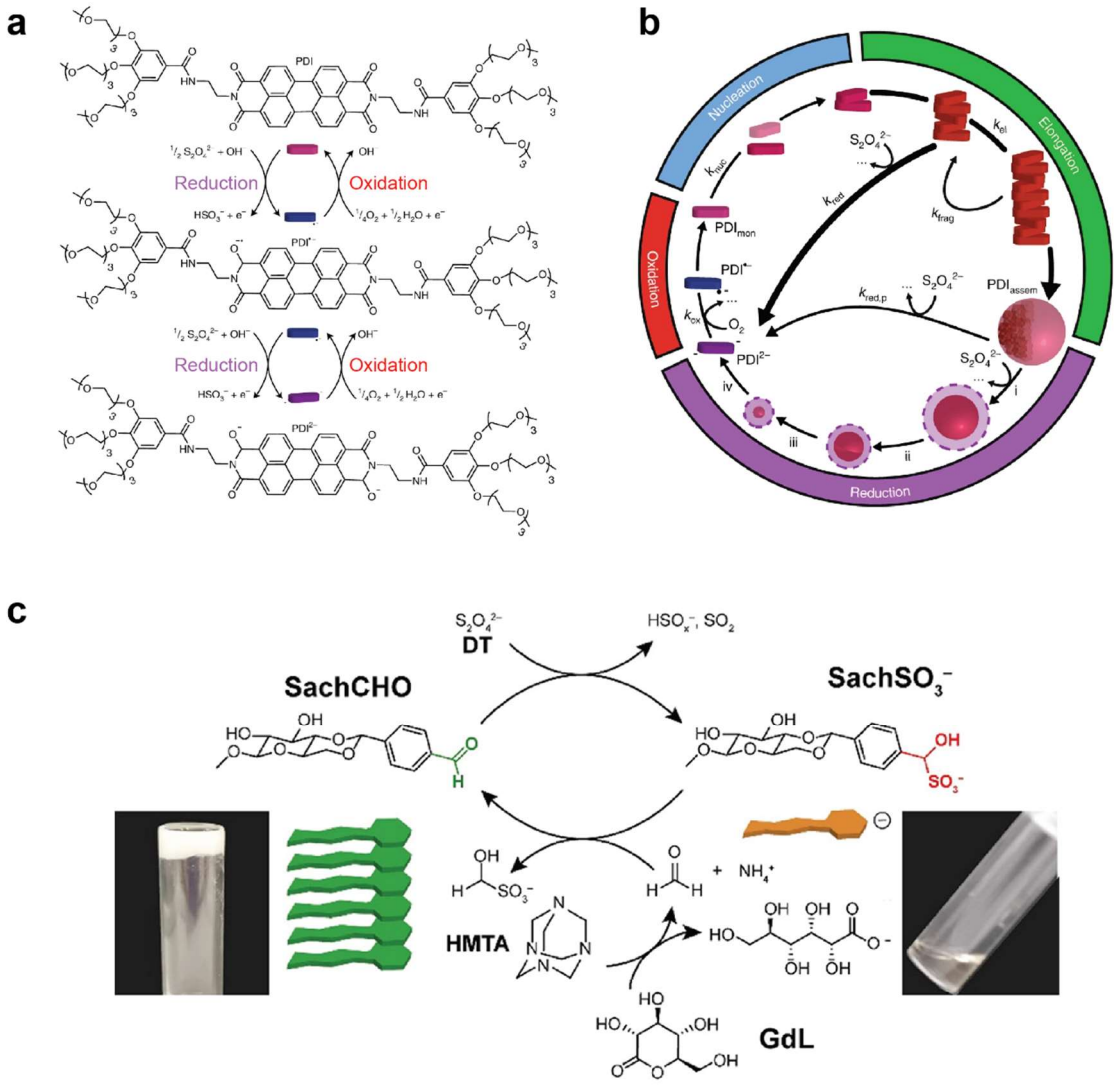

Figure 1.7 | Redox-driven reaction cycles. (a) Reaction scheme of the reversible reduction of the neutral perylenediimide (PDI) to the radical anion ($PDI^{\bullet-}$) and the dianion (PDI^{2-}). (b) Reaction cycle of the PDI system, including nucleation, elongation, reduction, and oxidation.[44] (c) Sol-gel reaction cycle of the aldehyde saccharide hydrogelator **SachCHO**, which is reduced to the soluble α-hydroxy sulfonate **$SachSO_3^-$**.[45] Reproduced from references [44,45] with permission from Springer Nature and the American Chemical Society.

Enzymes. Such non equilibrium reaction cycles have equally been developed on the basis of enzymatic reactions, as reported by Sorrenti *et al.*[46] In this case, a PDI is functionalized with a LRRASL peptide sequence, which is recognized by a protein kinase. Said kinase catalyzes the phosphorylation of the serine residue in the presence of adenosine triphosphate (ATP), which is thereby transformed to adenosine diphosphate (ADP). The phosphorylation introduces four negative charges in the molecule, which compensate four positive charges of the arginine residues, causing further assembly. Interestingly, the handedness of the helical assemblies inverts upon phosphorylation. The backward reaction is catalyzed by another enzyme, a λ-protein phosphatase, which can dephosphorylate the serine residue, releasing inorganic phosphate.

The phosphorylation/dephosphorylation reaction mechanism is analogous to previous work presented by the group of Stupp, who have shown the reversible assembly of peptide amphiphiles through enzymatic catalysis, switching from the monomeric (sol) to the polymeric

(gel) state.[47] Ulijn and coworkers have reported a similar sol-gel system based on a Fmoc-dipeptide methyl ester. The enzyme subtilisin hydrolyzes the methyl ester, inducing self-assembly of the "deprotected" Fmoc dipeptide to a hydrogel.[48]

Light is a well-studied and non-invasive stimulus of supramolecular polymerization.[49] By including molecular photoswitches like azobenzenes or diarylethenes in the monomers, their conformation can be switched by light irradiation with a specific wavelength, which will depend on the selected photo-sensitive moiety. Stupp and collaborators have shown that the pitch of helical nanostructures based on azobenzene end-capped peptide-amphiphiles can be adapted by UV-light irradiation.[50] The amphiphiles assemble to self-supporting gels in cyclohexyl-chloride exhibiting a helical fiber nanostructure. When irradiated with 360 nm UV-light, triggering *trans*-to-*cis* isomerization of the azobenzene moiety, the average pitch of the helix was reduced from 78 nm to 40–70 nm, as determined from AFM imaging. The *cis*-isomer exhibits a more planar structure, which is expected to induce a stronger torque, thus reducing the pitch of the helix.

Yagai and coworkers have shown the light-induced formation of a unique internal order of a one-dimensional supramolecular polymer, leading to spontaneous curvature of the system.[51] An azobenzene photoswitch was incorporated in a known foldamer, based on a barbiturated naphthalene. In methylcyclohexane these monomers assemble into star-like hexamers when in *trans*-conformation, which further assemble to spirally folded fibers upon slow cooling. If the solution is cooled abruptly, long linear fibers are formed. If the spirals are irradiated with UV light for 20 minutes, they undergo a transition to linear fibers. If further exposed to Vis light, they transition to randomly folded fibers. The latter process is reversible by applying, once again, UV light for 20 minutes. The randomly folded fibers relax back to the spiral confirmation over 24 h. This example shows nicely, how different triggers can be used to interconvert various nano-conformations.

Mechanical force has been used by Feringa and coworkers to induce supramolecular gelation of a carbazole-derived organogelator.[52] At relatively large concentrations (10–40 $mg \cdot mL^{-1}$) in DMSO, gels are formed upon ultrasonication, shaking or spontaneously. Upon heating to > 75 °C, all gels solubilize and remain dissolved in supersaturation. If a vertical oscillation (0.8 cm amplitude, 9.6 Hz) is applied to these supersaturated solutions for 1 to 10 s, a gel is formed almost immediately. Clear morphological differences between thermally annealed and mechanically induced gels can be visualized by TEM imaging, showing shorter, fragmented fibers for the mechanically triggered gels. Upon mechanical induction, the chain growth is accelerated, so consequently the nanostructure of the gel occurs more spontaneously, inhibiting the formation of higher ordered fibers over time.

Shaking and stirring of a self-assembling system has shown to influence the self-replication of peptide-macrocycles, as reported by Otto and coworkers.[53] In a system of two competing self-replicators, mechanical force is decisive to select which one of the oligomers will be the main species. Surprisingly, the formation of a hexamer is predominant under mechanical stirring, while shaking promotes the formation of heptamers. Without agitation, a mixture of trimers and tetramers is obtained. The selectivity remains unchanged over three months without agitation, showing no signs of relaxation to a possibly thermodynamically more favored state. In an approach to explain these selectivities, it comes down to the elongation and fragmentation rates of the respective species. The mechanically induced breaking of fibers frees more active, growing ends for fiber elongation. The heptamer exhibits faster elongation and will thus

dominate if all fiber species are destroyed at a similar extent (under stirring). Instead, shaking is more favorable for the fragmentation of hexamer fibers, leading to an increased propagation of this species.

More exotic stimuli to control supramolecular polymerization include strong centrifugal gravity, shear-flow, and strong electric or magnetic fields.[54] The latter is the central interest of this work and will be introduced more thoroughly in the following.

1.2. Magnetism

1.2.1 History and global impact

From early stages of human civilization, marked by the first use of a navigational compass in the early 11th century by Chinese scientist Shen Kuo (沈括) during the Song dynasty[55], magnetism has not ceased to play a central role in the development and technological progress of human life. In today's advanced technology, we exploit magnetic effects for modern medical imaging[56], robotics[57], data storage[58], spintronics[59], engineering[60], and catalysis[61], to name only few of many more fields of applications.[62,63]

With an increasing knowledge and understanding of magnetism, it has become more and more apparent how fundamental it is for life on Earth. The Earth's magnetic field is, for instance, protecting the planet from solar winds[64,65], making it habitable in the first place, and providing several animal species (such as migratory species of birds, pigeons, fish, insects, sea turtles, lobsters, and bats) with orientation to navigate.[66,67]

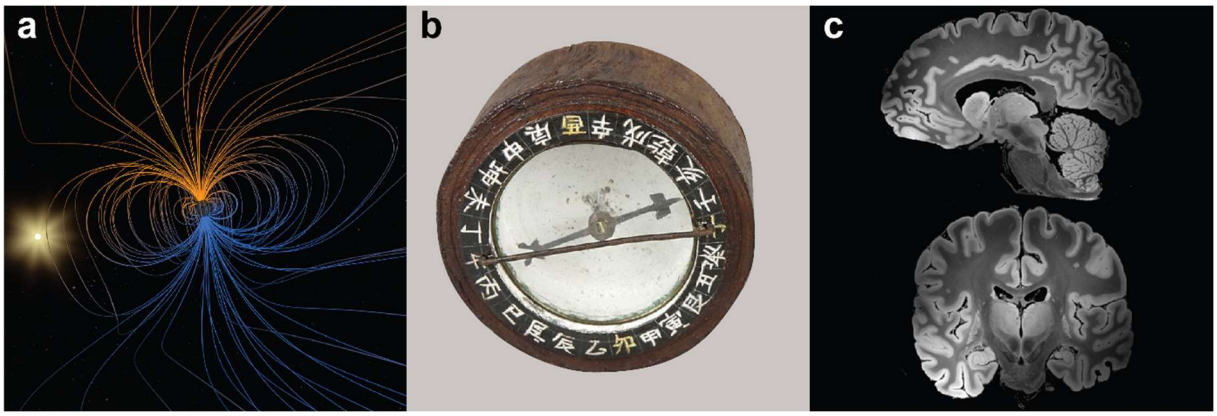

Figure 1.8 | The impact of magnetism from the formation of the earth to ancient and modern life. (a) Illustration of the Earth's magnetic field, showing the field lines from one pole to the other (orange and blue, respectively).[68] The Earth's magnetic field started developing in the Hadean eon (around 4 billion years ago). By deflecting solar winds, it makes Earth habitable. (b) A Chinese mariner's compass from the mid-1800s, exposed in the Museum of Applied Arts and Sciences, Sydney, Australia.[69] (c) Magnetic Resonance Image (MRI) of the human brain in sagittal (top) and coronal (bottom) planes reaching a resolution of 100 µm.[70]

1.2.2 Magnetic fields

When discussing magnetic field effects, different types of magnetic fields have to be distinguished.[71] First, we can define an applied field by its variation in time, where we discriminate between dynamic fields, which can be rotating or oscillatory, with a time-dependent field strength or direction. On the other hand, there are static fields, for which — at any given point in space — the field strength and direction are constant over time. In analogy, magnetic fields can be dynamic or static in space, differentiating homogeneous fields, where the magnetic field strength and direction are constant over a certain space unit, and inhomogeneous fields, where the magnetic field strength varies in space.[62,71]

A single permanent cube magnet generates an inhomogeneous, gradient field exhibiting higher intensities and gradients at its edges (Figure 1.9a–c). Homogeneous magnetic fields over significant space units, in contrast, are obtained from electromagnets (Figure 1.9p–r) or in specific magnetic arrays (Figure 1.9j–l). Custom fields can be achieved by a targeted arrangement of several permanent magnets (Figure 1.9d–I and m–o). In routine and widely available laboratory conditions, magnetic flux densities of up to 2 T can be reached. For stronger fields, advanced experimental setups including elaborate resistive or superconducting magnets with adapted cooling systems are needed. The machinery becomes larger, more expensive, rarer, and therefore less accessible (Figure 1.10). Fields of around 12 T can be achieved by superconducting magnets of 500 MHz NMR spectrometers, which are commonly found in research institutions. For fields exceeding this range, highly specialized research facilities are required, as for example the Nijmegen High Field Magnet Laboratory (Netherlands), where a field of 38 T can be generated in a resistive Bitter magnet.[72] The strongest non-destructive field that is known up to date is of 100 T (=1 MGs). This record value can only be reached in pulses of few milliseconds by a multi-shot magnet located in the Los Alamos National Laboratory (USA).[73]

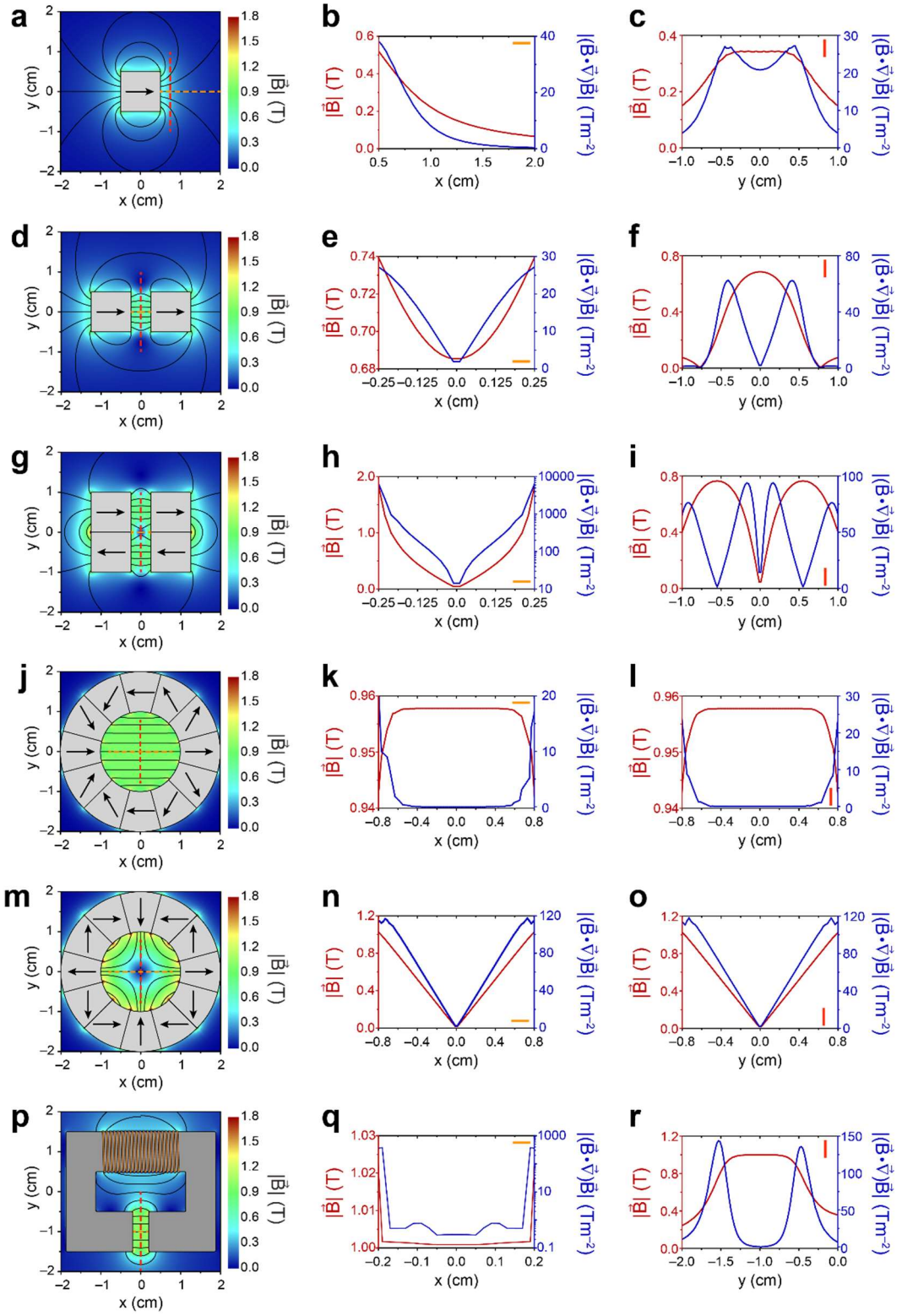

Figure 1.9 | 2D simulations of the magnetic flux density generated by different arrays of magnets.[24,62] Left: heat map of the norm of the magnetic flux density. Black lines represent the magnetic field lines. Black arrows show the north-south orientation of the magnet. Grey areas are the magnets. Center and right: Norm of the magnetic flux density $|\vec{B}|$ (left axis) and the product of the norm and gradient of field $|(\vec{B}\cdot\nabla)\vec{B}|$ (right axis) along the horizontal (yellow) and vertical (red) dashed line, respectively. (a–c) Single 1 cm x 1 cm N52 NdFeB magnet. (d–f) Two 1 cm x 1 cm N52 NdFeB magnets arranged in line, separated by 0.5 cm. (g–i) Four 1 cm x 1 cm N52 NdFeB magnets arranged in a quadrupole array. (j–l) Magnets arranged in a Halbach array creating a strong, homogeneous field. (m–o) Magnets arranged in a Halbach array creating strong field gradients. (p–r) An electromagnet creating a homogeneous field.

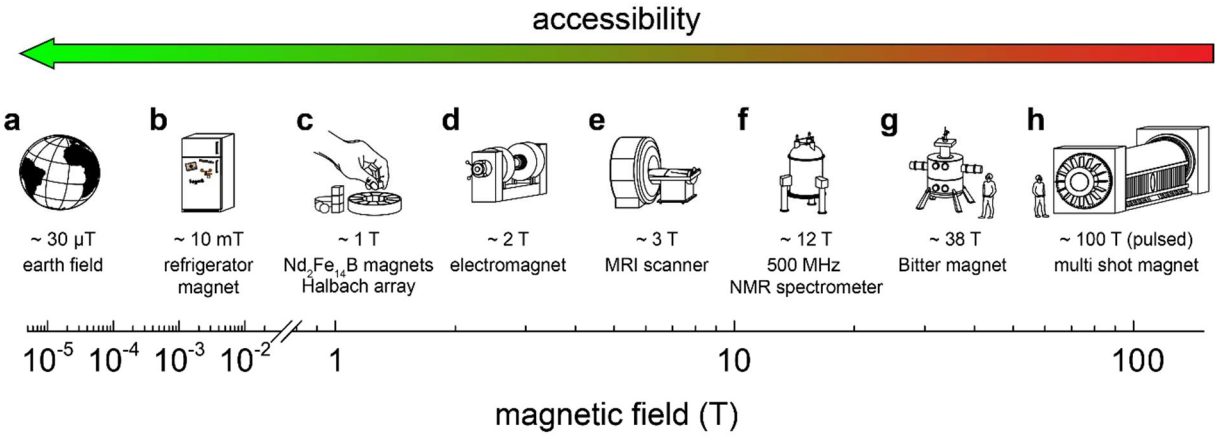

Figure 1.10 | Generation of magnetic fields. Illustrations of magnets and experimental setups generating magnetic fields of different strengths. From left to right: (a) The earth magnetic field, which is of around 30 µT at the equator. (b) Common refrigerator magnets, with field strength of around 10 mT. (c) $Nd_2Fe_{14}B$ permanent magnets, which are commercialized as cubes, cylinders or spheres and generate fields up to 1 T. Arranged into Halbach arrays[74,75], the field geometry and strength can be tuned with high precision. (d) Electromagnet, commonly available on a laboratory scale. (e) MRI scanner, routinely generating fields of around 3 T.[76] High performance scanners can produce fields of up to 8 T. (f) NMR spectrometer, generating around 9 T at 400 MHz and around 12 T at 500 MHz.[77] (g) A 38 T Bitter magnet, located in Nijmegen, the Netherlands.[72,78] (h) A multi shot magnet, creating a 100 T field in pulses of few ms. It is the strongest known non-destructive field, located in Los Alamos, NM, USA.[79–81] Weaker magnetic fields are generally simpler to generate, thus more easily and cheaply accessible.

1.2.3 Magnetic materials

1.2.3.1 Characterization[62,82]

The magnetic properties of materials are described by few key parameters, which will be used in the following to classify and quantify their magneto-response. For isotropic materials (without domains, see below in section 1.2.3.2), the magnetic susceptibility χ relates the magnetization M of a material to the H field. In other words, it expresses the density of the magnetic moment per unit volume at a given field strength. It can be expressed per mass (χ_m), volume (χ_V), or number of moles (χ_n). The magnetic permeability μ (in $H \cdot m^{-1}$ or $N \cdot A^{-2}$), on the other hand, relates the magnetic field strength H (in $A \cdot m^{-1}$) with the magnetic flux density B (in T). Hereby the H and B field are not to be confused. In simple terms, the H field is the magnetic field strength, which is the amount of magnetizing force of a field. The B field, instead, describes the induced magnetization in a certain material by the magnetizing force H. μ_0, the vacuum permeability, is so to say the magnetic counterpart to the more widely known dielectric constant ε_0.

The magnetic parameters describing the response of a material to a magnetic field are commonly determined by SQUID magnetometry, which is an acronym for Superconducting Quantum Interference Device. This technique relies on measuring the phases of an oscillating voltage between two so-called Josephson junctions connecting two superconductors. The phase changes can be correlated to flux changes. SQUID magnetometers can detect very small magnetizations as of 10^{-11} $A \cdot m^2 = 10^{-8}$ emu, which are measured as a function of temperature (zero field cooling – field cooling, ZFC-FC) of magnetic field strength in conventional experiments.

1.2.3.2 Classification

Magnetic materials are classified according to the orientation and arrangement of their electron spins, which lead to a characteristic response of the material to a magnetic field.[62,82] In general, five categories of magnetic materials are distinguished (Figure 1.12).

Diamagnetism arises from orbitals containing lone or bound electron pairs, where the opposite spins of the electron pair compensate each other to an overall apolarity. By this definition, all materials are diamagnetic, but they will only show observable diamagnetic properties if there are no other types of magnetism outpowering it. When a magnetic field is aligned, the electrons will orbit around the field axis, in a so-called Larmor precession. According to Lenz' law, a current induced by a magnetic field gives rives to a magnetic field opposed to the initial field. The electrons "flowing" in an atom due to Larmor precession can be regarded as a current in the sense of Lenz' law, creating said opposite field. Thus, diamagnetic species weaken the initial field, and are therefore repelled by the field and will move to low-intensity regions in gradient fields. The magnetic susceptibility of diamagnetic materials is negative ($\chi < 0$). Aromatic molecules exhibit an anisotropic diamagnetic susceptibility, which refers to the difference of the diamagnetic susceptibility in the planes that are parallel and perpendicular to the planar molecule. The diamagnetic anisotropy increases with a larger aromatic system due to an increased conjugation of the π-system, as of 5.6 to $22.2 \cdot 10^{-5}$ for benzene and pyrene. Bismuth (see Figure 1.11, $\chi_V = -2 \cdot 10^{-4}$) and pyrolytic graphite ($\chi_V \geq -4 \cdot 10^{-4}$) are examples for strongly diamagnetic materials.

Paramagnetism, on the other hand, presents itself in materials with permanent magnetic dipole moments, as in non-compensated, localized single electrons, which will align with an external magnetic field. They stabilize the field and will therefore move to high-field regions in a gradient field. They exhibit positive magnetic susceptibilities ($\chi > 0$). The magnetization of paramagnetic materials follows the Curie-law, with the material-specific Curie constant C and the absolute temperature T.

$$\chi = CT \tag{1.i}$$

Paramagnetism is typically found in elemental Aluminum, Sodium, and Oxygen, many transition-metal complexes such as myoglobin, and radicals.

Isolated, single atoms or ions are either diamagnetic (all paired electrons) or paramagnetic (unpaired electrons). The magnetic susceptibilities of the elements are shown in Figure 1.11.

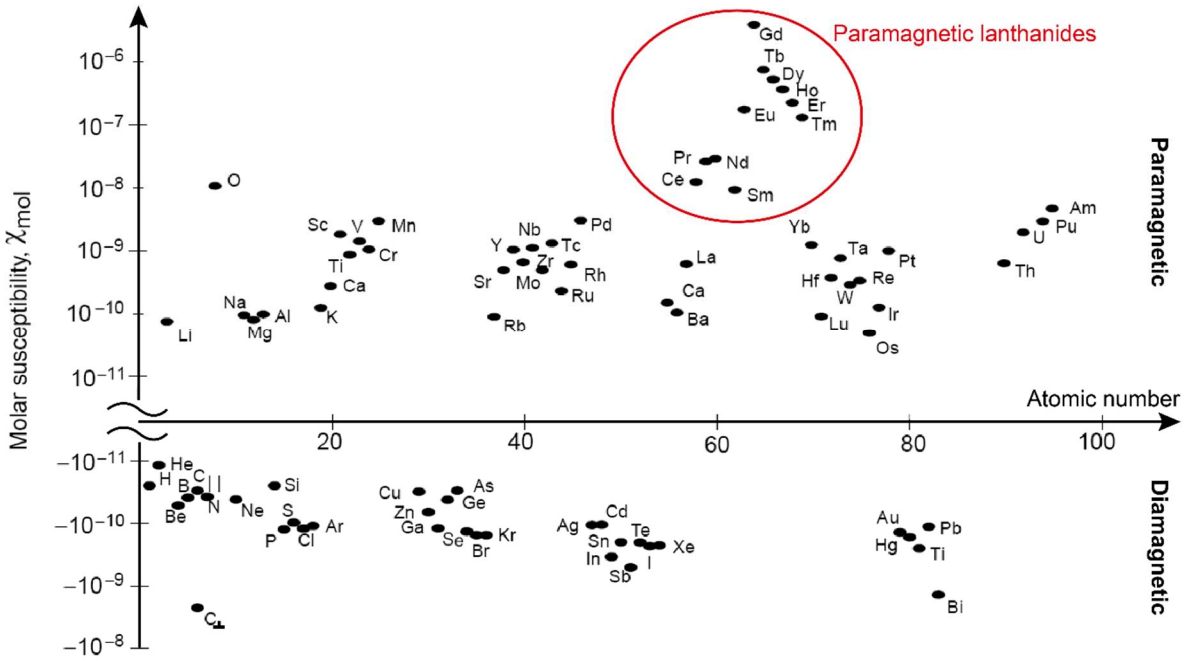

Figure 1.11 | Molar magnetic susceptibility of the elements. Elements with a positive susceptibility are paramagnetic, elements with negative susceptibility are diamagnetic. The red circle highlights paramagnetic lanthanides, which exhibit the largest magnetic susceptibility among the elements. Figure adapted from reference [62].

Further types of magnetism derive from a collective spin constellation of co-operating magnetic moments of a group of atoms or ions.

Ferromagnetism appears in materials exhibiting Weiss domains, which are 10 µm to 1 mm large crystal regions of equal magnetization. The changeover region between Weiss domains, where the magnetization is transitioning, are called Bloch walls. Alignment of such domains leads to ferromagnetism. Ferromagnetic materials typically exhibit a strong response to a magnetic field. Thereby, their magnetization curve is non-linear, as Bloch walls are displaced either reversibly or irreversibly with a progressing magnetization. The magnetization energy required to align Weiss domains corresponds to the area enclosed by the hysteresis curve of magnetization. If the hysteresis curve is wide, a material is referred to as magnetically 'hard'. Vice versa, the magnetization of a magnetically 'soft' ferromagnet is more reversible and shows a narrow hysteresis curve.

Once saturation induction is reached, meaning that all magnetic moments are aligned with the magnetic field, the flux density B varies linearly with the field strength H if the field strength is further increased (paramagnetic behavior). For ferromagnetic materials, the temperature dependence of the susceptibility χ follows the Curie-Weiss law, with the material specific constant C, the temperature T, and the Curie-temperature T_C. Above the Curie temperature, the spins of the material become disordered, and the ferromagnet transitions to a paramagnet.

$$\chi = \frac{C}{T - T_C} \tag{1.ii}$$

Typical ferromagnetic materials are Fe, Co, and Ni in their elemental state or as alloys.

Superparamagnetism refers to single-domain ferromagnetic particles in the nanoparticle size range. Their volume is so small that the related anisotropy energy can be compensated by

thermal energy. Consequently, the overall magnetic moment fluctuates, and the particle behaves like a large paramagnet, or macrospin. Its susceptibility χ follows the Curie law (paramagnetic behavior).[83]

Antiferromagnetism and Ferrimagnetism appear in materials with two or more sublattices of different magnetization. In antiferromagnetic materials, the magnetic moments of the structure components are of equal magnitude and aligned in anti-parallel, compensating each other. The overall magnetization is zero, and the material shows macroscopically diamagnetic behavior. The susceptibility of antiferromagnetic materials depends on the material specific constant C, the absolute temperature T, and the Néel temperature T_N.

$$\chi = \frac{C}{T + T_N} \tag{1.iii}$$

If the magnetic moments of the structure components are not equal, *i.e.,* they are only partly compensating, the material is ferrimagnetic, and behaves like a weak ferromagnet on the macroscopic level. Most oxides with net ordered magnetic moments are ferrimagnetic, such as Fe_3O_4 (magnetite), or $Y_3Fe_5O_{12}$ (yttrium-iron garnet, IOG).

Helimagnetism occurs if ferromagnetic and antiferromagnetic couplings are in conflict. This can occur in a layer structure, for instance, and a helical spin structure emerges. The material is therefore called helimagnetic.

As magnets are defined solely by their spin configuration, the physical appearance of magnetic materials is diverse: from (mechanically) hard cm-sized permanent magnets, to gels and ionic liquids, to nanoparticles and single molecule nm-sized magnets.

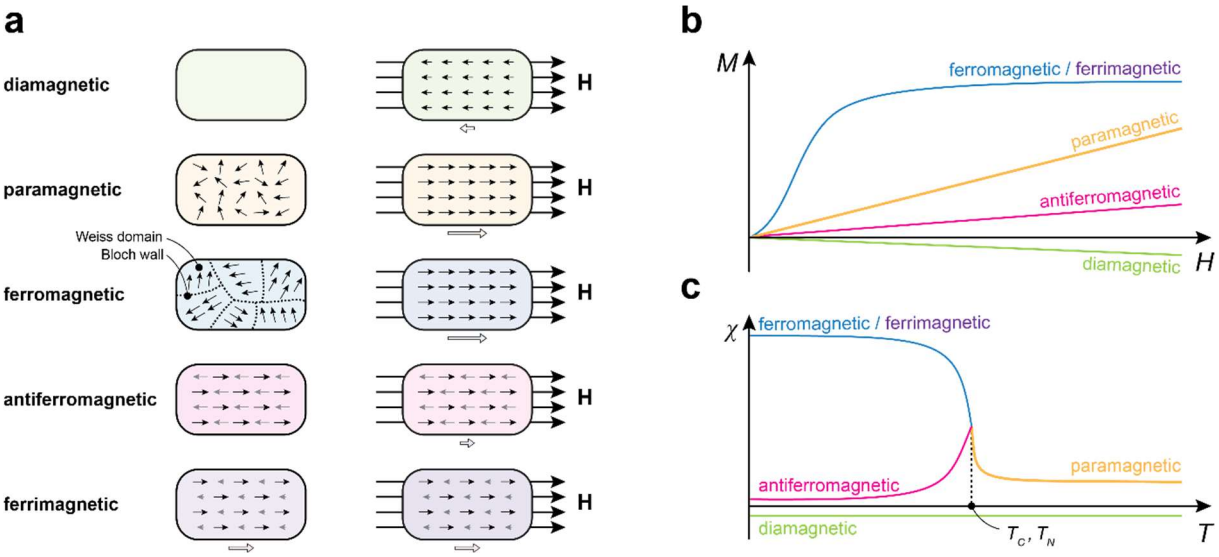

Figure 1.12 | Classification of magnetic materials. (a) Magnetic dipole arrangement of diamagnetic, paramagnetic, ferromagnetic, antiferromagnetic and ferrimagnetic materials in the absence (left) and presence (right) of an applied field. Hollow arrows represent the net magnetization. (b) Schematic illustrations of the field-dependent magnetization M. (c) Schematic illustration of the temperature-dependent magnetic susceptibility χ in a constant field. The dotted line refers to the Curie- and Néel temperatures T_C and T_N, respectively.[84,85,82,83]

1.2.3.3 Lanthanides

As highlighted in Figure 1.11, lanthanides are the elements with the highest molecular susceptibility in the elemental state. According to IUPAC, the correct terminology for the 15 elements from $_{57}$La to $_{71}$Lu, commonly referred to as "lanthanides", is "lanthanoids" (lanthanum-like elements). Along with Sc and Y, these elements are collectively known as rare earths. Not only because of their large magnetic moments, but also their magnetic anisotropy, they are indispensable in the global technological sector and deserve a closer look.

Up to the 1970s, lanthanides have not received much attention from the scientific community, as their redox- and molecular chemistry is very limited.[86] Notably, Pimentel and Spratley[87] assessed that "Lanthanum has only one important oxidation state in aqueous solution, the +3 state. With few exceptions, this tells the whole boring story about the other 14 lanthanides." Although their chemistry is indeed very limited, lanthanides are nowadays used in a vast range of fields, due to their magnetic, physical, electro-, and photochemical properties. Their applications range from performance enhancement of alloys, ceramics, and coatings, over lasing and fiber optics, the production of permanent magnets, to diagnostic and therapeutic medicine, where lanthanides are essential in radionucleotide therapy and as contrast agents for magnetic resonance imaging (see Figure 1.8c).[88]

The latter is probably the most prominent example of commercial use of lanthanide complexes. As of today, eight Gadolinium-based contrast agents are FDA-approved. All of them are derivatives of Gd(DTPA) or Gd(DOTA), commercialized under tradenames such as Magnevist®, Ablavar®, or Eovist® (Figure 1.13).[89,90] Unlike other imaging techniques such as radio imaging, in MRI the contrast agent is not detected directly. It is the magnetism of the unpaired electrons of the lanthanide that affects the longitudinal relaxation of the bound water molecules, creating a contrast between the water molecules that are bound to the contrast agent and those that are not.[88]

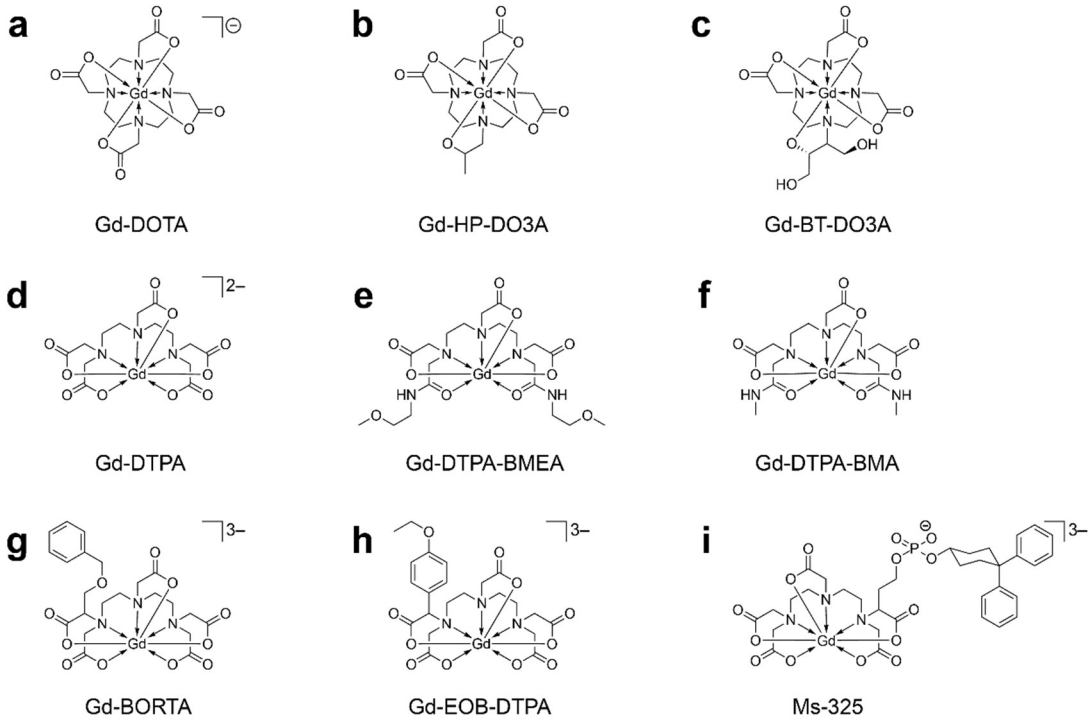

Figure 1.13 | Clinically used MRI contrast agents based on Gd. (a-c) Gd-DOTA and derivatives. (d-i) Gd-DTPA and derivatives.[89]

The particularity of lanthanides arises from their unpaired 4*f* electrons, which are well-shielded from their direct environment by the surrounding, full 5*s* and 5*p* orbitals. Due to this steric limitation, the formation of dative covalent bonds with donor atoms of ligands is rendered impossible, which is in sharp contrast with transition-metal based complexation. The nature of the ion-ligand interaction in lanthanide complexes is thus predominantly electrostatic, and the coordination numbers and geometries depend to a large extent on steric, and not electronic factors, often imposed by the ligand. Complexes of a same ligand are thus often isostructural over the lanthanide series.

If deviations from isostructural geometries appear, they are most likely to originate from lanthanide contraction, a trend that describes a decreasing ionic radius with an increasing nuclear charge. The changes are greater than expected with respect to other periods of the elements. Owing to the geometry of the 4*f* shell, the *f*-electrons do not shield the nuclear charge well from the outer 5*s* and 5*p* shells, resulting in enhanced contraction and charge density of the ions with an increasing atomic number.[91]

The average coordination geometry of lanthanides switches from tricapped trigonal prismatic (CN = 9) to square antiprismatic (CN = 8) over the series.[92] Due to their high coordination numbers, they form stable chelate complexes with octadentate ligands, such as DOTA, diethylenetriamine-pentaacetic acid (DTPA), or other functionalized tetra- or pentaacetic acids with stability constants log*K* of over 20.[88,93]

The poor interaction of the 4*f* electrons with their environment allows for the preservation of their magnetism.[86] As orbital momenta and the corresponding spin-orbit coupling remain largely unquenched, many elements exhibit a well-pronounced anisotropy in crystal fields. For this reason, they qualify for the production of (mononuclear) single-molecule magnets.[94] Depending on their magnetic anisotropy $\Delta\chi$, the paramagnetic lanthanides can be classified in

prolate ($\Delta\chi < 0$; Pm, Sm, Er, Tm, Yb), oblate ($\Delta\chi > 0$; Ce, Pr, Nd, Sm, Tb, Dy, Ho), and isotropic ($\Delta\chi = 0$; Eu, Gd, Lu).[95] Simulated electron density distributions for the elements of the lanthanide series are shown in Figure 1.14.

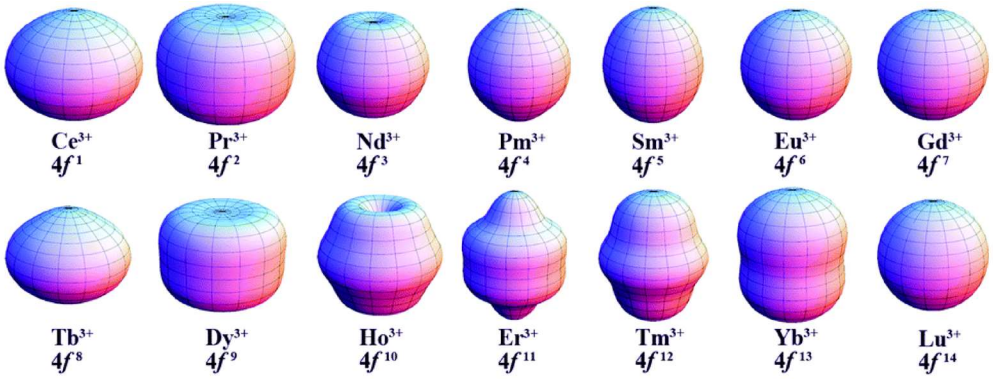

Figure 1.14 | Predicted (an)isotropic electron-density distribution of the lanthanide series. Analytical simulations of the 4*f* electron density, which is perturbed by the crystal field effect. Ce^{3+}, Pr^{3+}, Nd^{3+}, Tb^{3+}, Dy^{3+} and Ho^{3+} are oblate ions (axially pressed); Pm^{3+}, Sm^{3+}, Er^{3+}, Tm^{3+} and Yb^{3+} are prolate ions (axially elongated); Eu^{3+}, Gd^{3+} and Lu^{3+} are isotropic ion (spherical). Figure reproduced from reference [96] with permission from the Royal Society of Chemistry.

The ensemble of the relatively recently discovered applications led to a drastic increase in the demand of rare earths over the last years, whereas the amount of extractable raw material from the earth crust is limited. As a result, the prices of many rare earth elements have experienced a dramatic increase, with fluctuations of up to a factor 10.[97] Considering the increasing scarcity and their key role in wind- and solar energy, the European Commission declared Dysprosium and Neodymium so-called critical metals, mentioning risks on a political level by international competition. According to Global Market Insights[98], the global rare earth market was of 9.4 billion US-dollars in 2016 and is predicted to rise to over 20 billion by the year 2024. Up to date, recycling of rare earths is restricted to few elements (La, Ce, Ne, Pr) and products containing large amounts of these.[88]

Unraveling and understanding how magnetic properties of lanthanide-containing materials are influencing their environment can be a crucial step in developing new technologies for recycling, separation, and purification of these precious and “critical” elements.

1.3. Magnetic control over soft matter

1.3.1 Magnetic energies and forces

Effects of a magnetic field on a particle will depend on the magnetic field (uniform or gradient) and the magnetism of the particle.[71] The nature of the latter can range from a single ion to nano- or microparticles. Here, we will estimate magnetic contributions for three cases: magnetic energies in static fields, magnetic forces in gradient fields, and dipolar coupling between two magnetic moments in the absence of an external field.

1.3.1.1 Magnetic energy in constant fields

In uniform fields, magnetic effects can be quantified by the magnetic energy E_{mag} acting on a particle, which depends on the magnetic dipole moment m and the magnetic flux density B.[71]

$$E_{mag} = -\frac{1}{2}mB \tag{1.iv}$$

The magnetic moment m is the magnetization M of the particle multiplied by its volume V. In other words, the magnetization expresses the magnetic moment per volume unit.

$$m = M \cdot V \tag{1.v}$$

In ferromagnets, the magnetization is constant within one domain. Ferromagnetic materials are characterized by their so-called saturation magnetization M_S.

In dia- and paramagnetic materials, the magnetization is induced by a magnetic field, and their linear dependence is described by the volumetric magnetic susceptibility χ.

$$M = \chi H \tag{1.vi}$$

H represents the magnetic field strength, or magnetizing force. The magnetic field strength (**H**-field) and the magnetic flux density (**B**-field) are related by equation (1.vii), including the vacuum permeability $\mu_0 = 4\pi \cdot 10^{-7}$ H·m^{-1} = $1.256 \cdot 10^{-6}$ N·A^{-2}.

$$B = \mu_0 (M + H) = \mu_0 H (1 + \chi) \tag{1.vii}$$

If the magnetic susceptibility $|\chi|$ is much smaller than 1, as it is the case for dia- and paramagnetic materials, this term can be simplified to equation (1.viii).

$$B = \mu_0 H \tag{1.viii}$$

All equations (1.iv–viii) can be combined to an expression for the magnetic energy of paramagnetic and diamagnetic materials.

$$E_{mag} = -\frac{1}{2\mu_0}\chi V B^2 \tag{1.ix}$$

The magnetic energy is proportional to the squared magnetic field, making the latter an important parameter for the manipulation of particles in the field. In common laboratory conditions, fields of up to 2 T are typically accessible, limiting particles which are suitable for magnetic manipulation to large nano- or micrometer range. For smaller particles, more advanced and expensive magnets and setups are required (see section 1.2.2).

1.3.1.2 Magnetic forces in gradient fields

In gradient fields, the field inhomogeneity gives rise to the magnetic force F_{mag}.[71]

$$\overrightarrow{F_{mag}} = -\vec{\nabla}E_{mag} = \frac{1}{2}m\vec{\nabla}B = \frac{1}{2}MV\vec{\nabla}B \tag{1.x}$$

Considering equations (1.iv) and (1.viii) for dia- and paramagnetic materials, we obtain equation (1.xi).

$$\overrightarrow{F_{mag}} = \frac{1}{2\mu_0}\chi V\left(B \cdot \vec{\nabla}\right)B \tag{1.xi}$$

Unlike the magnetic energy, discussed in section 0, the magnetic force scales linearly with both the magnetic field and its gradient. In common laboratory conditions, field gradients of up to 1 $kT \cdot m^{-1}$ can be achieved in spatially small fields.[99,100] Little, sub-micrometer particles are thus more suitable to be controlled by gradient fields than by homogeneous fields.

In biphasic systems, as for example dispersions of nanoparticles, the susceptibility term is split into the respective contributions of the particle (χ_p) and the liquid medium (χ_m).[99]

$$\overrightarrow{F_{mag}} = \frac{1}{2\mu_0} \cdot \left(\chi_p - \chi_m\right) \cdot V\left(B \cdot \vec{\nabla}\right)B \tag{1.xii}$$

1.3.1.3 Dipolar coupling

Even in the absence of external magnetic fields, soft matter can be dominated magnetically, by the so-called dipolar coupling. It is the energy arising from the interaction between two magnetic dipoles *i* and *j*, following equation (1.xiii) including the magnetic moments m_i and m_j of *i* and *j*, the inter-dipolar distance r_{ij}, and their respective unit space vectors.[101]

$$E_{mag,dipolar} = -\frac{\mu_0 \cdot m_i m_j}{4\pi r_{ij}^3}\left(3\left(\overrightarrow{m_i} \cdot \overrightarrow{r_{ij}}\right)\left(\overrightarrow{m_j} \cdot \overrightarrow{r_{ij}}\right) - \overrightarrow{m_i} \cdot \overrightarrow{m_j}\right) \tag{1.xiii}$$

The energy is inversely proportional to the cubic inter-dipolar distance r_{ij} and is thus most significant when the two dipoles *i* and *j* are in close proximity. Equation (1.xiii) represents a simple way to calculate the dipolar coupling for two specific dipoles in a specific spatial arrangement with respect to each other, which is considered by the two unit space vectors m_i and m_j. In an isotropic solution, however, the overall magnetic energy will be averaged to zero due to rotational diffusion.[102]

1.3.1.4 Energetic significance

The energies and forces described in sections 0 – 1.3.1.3 are well pronounced in "extreme" conditions using concentrated, strongly magnetic materials[103], strong fields[104], or immobilization by cooling to temperatures below 70 K[105]. In contrast, if we want to apply magnetic control on a (supra-) molecular level and in "soft" conditions —meaning in solution, dispersion, or gel state, at room temperature and atmospheric pressure — we expect these contributions to be rather small, and thus to be in competition with thermal fluctuations (Brownian motion). The proportion of thermal and magnetic contributions, may it be energy (E_{mag}/E_{therm}) or force (F_{mag}/F_{therm}), will be represented by the merit number β. Its magnitude gives an indication as to whether magnetic effects can be expected to be significant in a respective scenario.

The counterparts to E_{mag} and F_{mag} will be thermal energy E_{therm} and the thermal force and F_{therm}

$$E_{therm} = -\frac{3}{2}k_B T \tag{1.xiv}$$

$$\overrightarrow{F_{therm}} = \sqrt{2k_B T(6\pi\eta R)} \cdot \overrightarrow{\omega(t)} \tag{1.xv}$$

with Boltzmann's constant k_B, the temperature T, the dynamic viscosity η of the surrounding fluid, the particle radius R, and a Gaussian white noise operator $0 < \omega(t) < 1$.[106] For simplification, the latter will be maxed to 1 in the following calculations.

To illustrate these estimations, let us look at three different scenarios, and compare the magnetic and thermal contributions for a 36 nm iron oxide nanoparticle (IO-NP, with a saturation magnetization M = 396 emu·cm^{-3} = 3.96·10^5 A·m^{-1}) with a single Ho^{3+} ion (χ_n = 5.702·10^{-7} m^3·mol^{-1}, R = 0.901 Å). Using the respective equations to determine the magnetic energies and forces and their thermal equivalents, we can estimate the β values for all three scenarios. The numerical results are given in the following tables. Detailed calculations for all values are given in the appendix (section 1.5).

Scenario I: 1 T uniform magnetic field, at room temperature (298 K).

species	E_{mag} (J)	E_{therm} (J)	β (-)
IO-NP	3.9·10^{-17}	6.2·10^{-21}	6.3·10^3
Ho^{3+} ion	3.8·10^{-25}	6.2·10^{-21}	6.2·10^{-5}

Scenario II: gradient magnetic field with B = 1 T and ∇B = 2000 T·m^{-1} at 298 K in water.

species	F_{mag} (N)	F_{therm} (N)	β (-)
IO-NP	7.7·10^{-14}	2.2·10^{-15}	35
Ho^{3+} ion	7.5·10^{-22}	1.1·10^{-16}	6.8·10^{-6}

Scenario III: two individuals of each species at π-π stacking distance (≈ 4 Å) at 298 K, forming an equilateral triangle with the coordinate origin (all angles 60°).

species	$E_{mag,dipolar}$ (J)	E_{therm} (J)	β (-)
IO-NP	4.8·10^{-11}	6.2·10^{-21}	7.7·10^8
Ho^{3+} ion	7.5·10^{-23}	6.2·10^{-21}	1.2·10^{-3}

In all three examples, $\beta > 1$ for the IO-NP, meaning that the magnetic contributions can dominate the thermal ones, whereas they are expected to be insignificant for the Ho^{3+} ion ($\beta < 1$). Estimations of β will be used as a reference in the later chapters of this thesis.

1.3.2 Effects in constant fields

1.3.2.1 Diamagnetic alignment

Exploiting diamagnetic anisotropy, even nm-scale assemblies of diamagnetic, organic molecules can be aligned in strong fields of 10 T or more.[107] Maan and coworkers reported the deformation of spherical nanocapsules, composed of self-assembled sexithiophene, in a 20 T constant field (Figure 1.15). The sexithiophene is a bolaamphiphile, consisting of a rigid, apolar sexithiophene backbone and polar ethylene oxide chains at both ends. In 2-propanol, it forms spherical capsules with an average radius of 55 nm at 20 °C. Due to the large diamagnetic susceptibility anisotropy ($\Delta\chi = 8.0 \cdot 10^{-6}$) of the thiophene chains, exposure to a strong magnetic field leads to an alignment of the axis of lowest susceptibility (along the long axis of the sexithiophene) with the field to minimize the magnetic energy (see equation 1.ix). As a result, the nanocapsules are axially pressed along the field direction. Unlike the sexithiophene molecules, the capsule is overall isotropic in its susceptibility, so there is no alignment of the capsule itself.

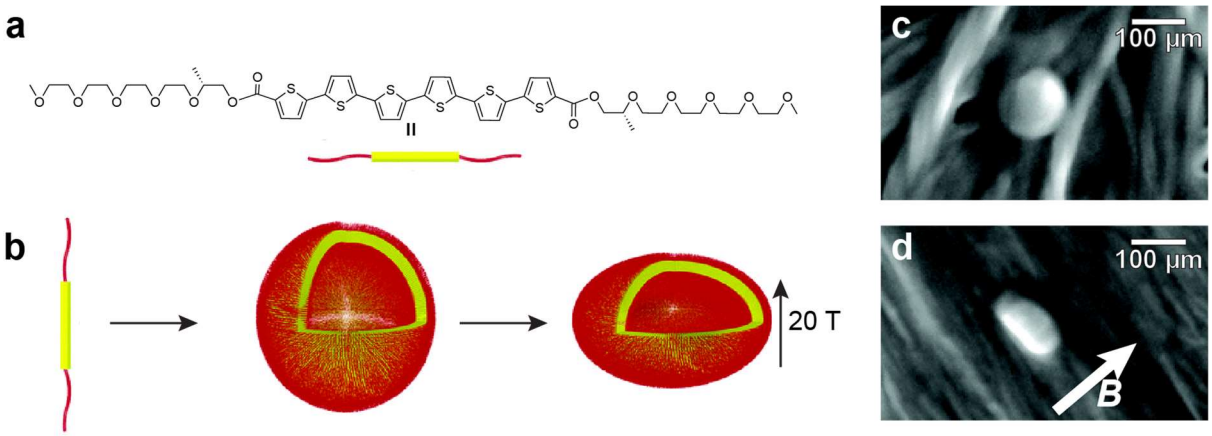

Figure 1.15 | Magnetic deformation of diamagnetic sexithiophene-based nanocapsules. (a) Molecular structure of the sexithiophene monomer. (b) Illustration of the deformation upon the application of a 20 T field. (c,d) Scanning electron micrographs of spherical (c: 0 T) and deformed (d: 20 T) nanocapsules. The field direction is indicated by the arrow. Figure adapted from reference [104] with permission from the American Chemical Society.

The diamagnetic anisotropy of conjugated π-systems is utilized in several other examples, as for instance the diamagnetic alignment of diphenylalanine(FF)-based nanotubes reported by Tendler and coworkers (see Figure 1.16).[108] In fields of 3 to 12 T, they exhibit an increasing alignment along the magnetic field direction. The observed alignment raises the question about the molecular packing of the nanotubes: If the phenyl rings were to π-π stack along the tube length, we would expect an alignment perpendicular to the field direction. In this case, however, the alignment along the field direction suggests that phenylalanine stacks perpendicular to the long axis of the nanotube.

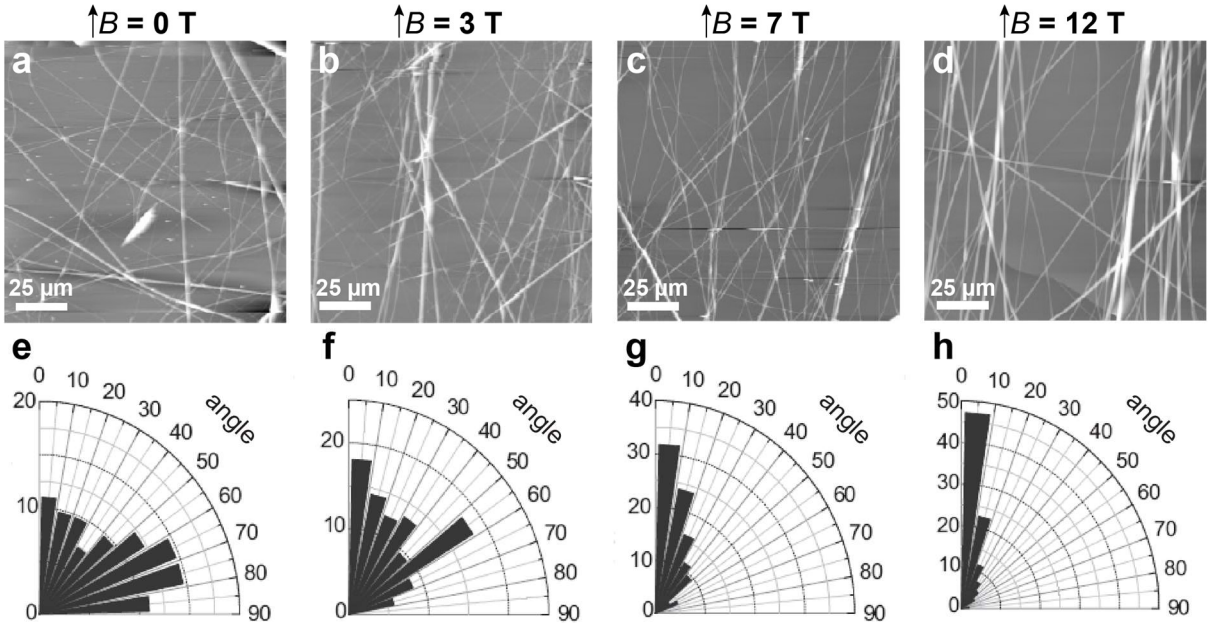

Figure 1.16 | Diamagnetic alignment of diphenylalanine nanotubes. (a-d) AFM topography images of diphenylalanine nanotubes in (a) 0 T, (b) 3 T, (c) 7 T, and (d) 12 T fields. Droplets of the dipeptides in aqueous HFIP were allowed to dry at room temperature in the magnetic field. (e-h) Polar histograms of the respective samples showing the distribution of a representative sets of FF tubes as a function of the angle relative to the field direction. The field direction is indicated by the arrow. Figure adapted from reference [108] with permission from Wiley.

Similarly, Adams and coworkers were able to align the fibers of a naphthalene-FF dipeptide based supramolecular hydrogel when gelled in a 9.4 T field.[109] Moreover, a magnetic orientation perpendicular to the magnetic field has been shown for phospholipid bilayers in solution. Due to the parallel arrangement of the molecules, their molecular diamagnetic anisotropies combine, and this amplification enables the observed magneto-response.[95,110,111]

Chan, Ishida and coworkers have reported field alignment for metallo-supramolecular polymers.[112] The supramolecular block-copolymer in question is based on a polythiophene (anisotropic diamagnetic susceptibility), and an ethylene oxide chain, both functionalized with terpyridine moieties which allow reversible cross-linking via coordination to Zn^{2+} ($\mu = 0$) ions. Field-aligned films were obtained when a Zn-containing solution of the copolymer was dried in a 9 T field. Their alignment has been shown to be highly dependent on the ratio of the components, and thus their assembly prior to drying.

If the molecular structures are selected carefully, diamagnetic alignment can be achieved at weaker fields, namely when the monomers assemble to structures with large domains of anisotropic diamagnetic susceptibility. Osuji and coworkers showed that fields of less than 1 T are sufficient to reach highly aligned states for an organic, liquid crystalline block copolymer system (Figure 1.17).[113] Specifically, a block-copolymer of ethylene oxide and liquid crystalline methacrylate (**PEO-b-PMA/LC**) is used. At room temperature, hexagonally packed PEO microdomains are formed in a Smectic A mesophase (molecules are oriented liquid-like in layers, parallel to each other along the so-called LC director) of the PMA mesogen. Like the thiophene chain in the sexithiophene, the mesogens have a positive diamagnetic susceptibility anisotropy. Therefore, the application of a magnetic field leads to an alignment of the PEO cylinders and the LC director (axis of the lowest diamagnetic susceptibility) along the magnetic field. For neat **PEO-b-PMA/LC**, a field of 5 T or more is required for alignment (Figure 1.17b and d), and there is no response of the system at fields of 1.5 T or less. If a commercial mesogen,

a phenylene ester diacrylate species (**RM257**) is added to the system at a molar ratio of 0.18, the grain sizes of the neat diblocks are increased (Figure 1.17c and e), and so is their magnetostatic energy. As a result, subjection to a 1 T field leads to pronounced alignment.

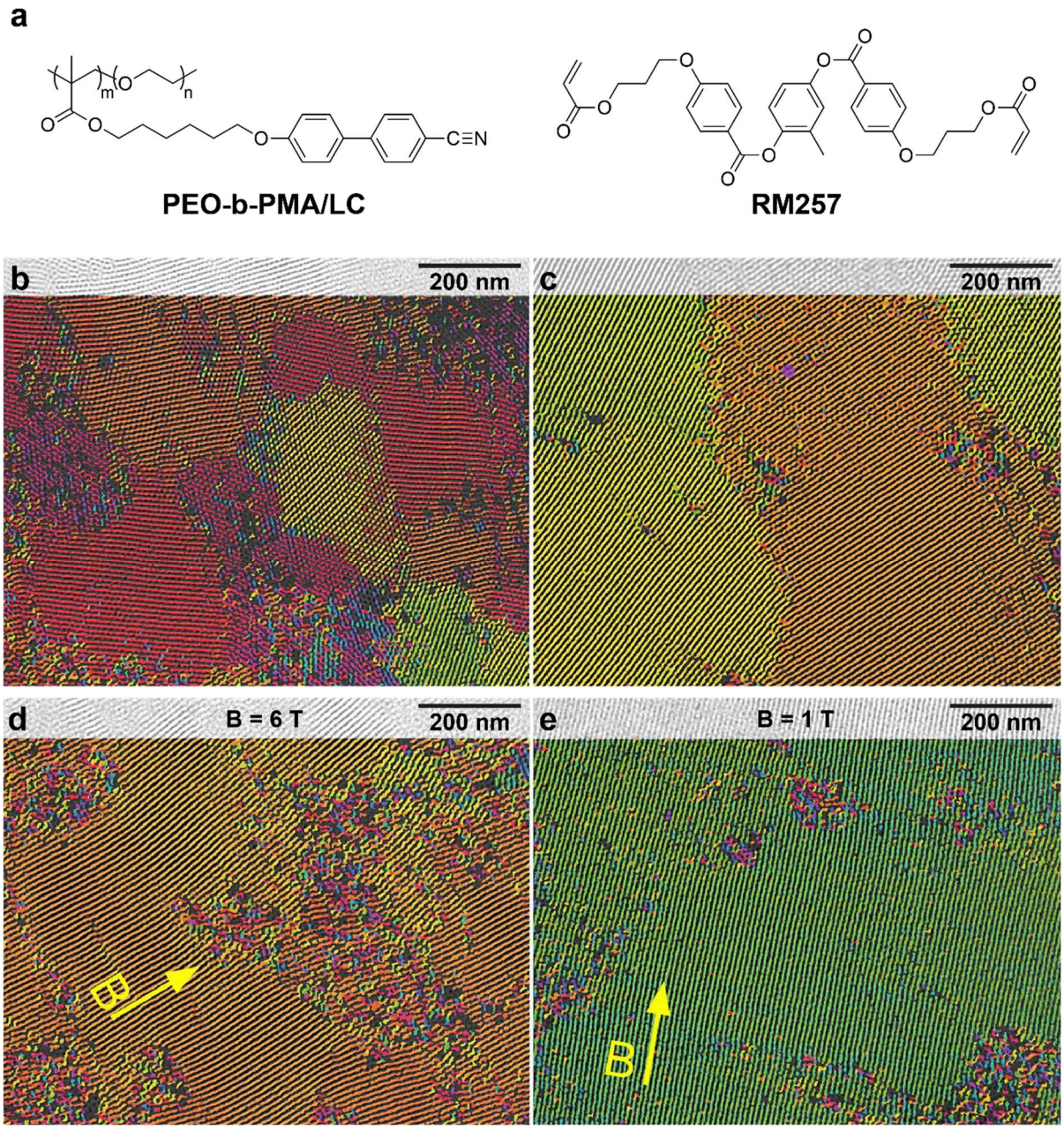

Figure 1.17 | Diamagnetic alignment of a liquid crystalline block-copolymer. (a) Molecular structures of the block copolymer **PEO-b-PMA/LC** (left) and the commercial mesogen **RM257** (right). The latter is used as an additive to increase the size of the diblock domains. (b) TEM image of nonaligned neat **PEO-b-PMA/LC**. (c) TEM image of nonaligned **PEO-b-PMA/LC** with 18 mol% of **RM257**. (d) TEM image of field aligned (6 T) neat **PEO-b-PMA/LC**. (e) TEM image of field-aligned (1 T) **PEO-b-PMA/LC** with 18 mol% of **RM257**. The direction of the magnetic field is indicated by the yellow arrows. All TEM images (b-e) are overlaid with false color mapping for visual guidance. Figure adapted from reference [113].

In a similar manner, self-assembly of aromatic, cationic peptides with hyaluronic acid shows nanofiber alignment within 24 h in a magnetic field of 1 T, as reported by Azevedo and coworkers.[114] The peptide sequences were specifically designed to drive their self-assembly to the formation of domains by positioning four hydrophobic phenylalanines at the C-terminus of the oligopeptides. Through various linkers composed of 3 to 5 amino acids, the F_4 moiety is

connected to two charged lysines at the N-terminus. The latter allow the peptide to electrostatically interact with hyaluronic acid, leading to co-assembly into hydrogels or flat membranes. The diamagnetic anisotropy of the aromatic domain enables diamagnetic alignment in a 1 T field. The incorporation of hyaluronic acid allows for stem cell cultivation on the co-assemblies along the magnetically aligned fibers.

Jung and coworkers investigated the alignment of perfluorinated supramolecular dendrimers.[115] By Small Angle Neutron Scattering (SANS), the changes in their geometric orientation could be followed. The obtained patterns show that the dendrimers are isotropic above 245 °C and develop a highly ordered cylindrical phase upon cooling. The authors analyzed the degree of orientation of the ordered structures when cooled in different field strengths of up to 2 T. The threshold for alignment turned out to be 0.7 T. Upon further increase of the field strength to 2 T, no significant additional alignment was found. Long-range alignment on the µm-scale was confirmed by TEM.

In 2018, Adams and coworkers reported the alignment of self-assembled, worm-like micelles of perylenediimides(PDI)-derivatives in a magnetic field of 9.4 T.[116] Upon exposure to the field, the assemblies of the sodium salt of PDI-alanine align perpendicular to the field. This process can be followed by ^{23}Na-NMR, which shows quadrupolar splitting of the $^{23}Na^{+}$ ion. The splitting does not stem from the anisotropy of the sodium ions themselves, but from the associated, anisotropic PDIs. The spectroscopic measurements are confirmed by the corresponding SANS patterns. The alignment happens spontaneously and is proportional to the field strength. Isotropy is restored when the magnetic field is removed. The process is reversible and was repeated three times without any signs of fatigue.

1.3.2.2 Paramagnetic alignment

As compared to diamagnetic materials, magnetic alignment is significantly facilitated for paramagnetic and ferrimagnetic materials. Owing to a strong positive magnetic susceptibility (see section 1.2.3.2), the material is attracted by a magnetic field, and the lone or parallel spins align along the field direction.

For instance, macro-sized, Dy-containing supramolecular assemblies in the shape of dumbbells can be oriented along the field direction at less than 1 T field strength, which can be easily obtained using commercial permanent magnets (Figure 1.18).[117] The structure and formation of the assemblies will be discussed in further detail in section 1.3.6.

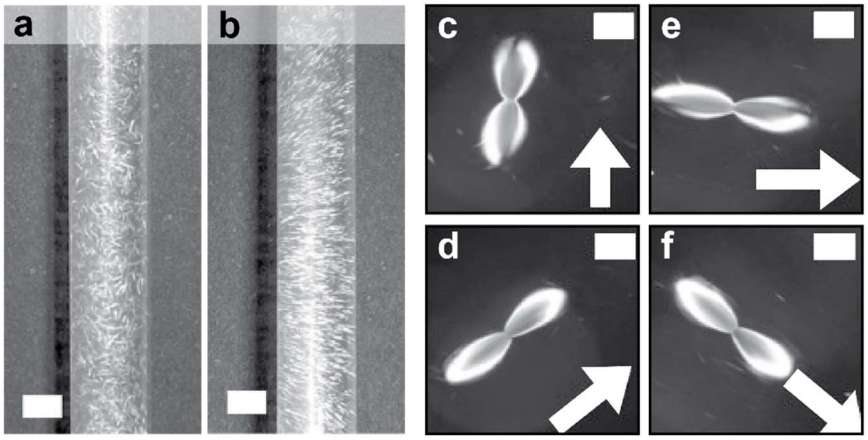

Figure 1.18 | Field alignment of Dy-containing, dumbbell-shaped supramolecular assemblies. (a,b) Photographic images of randomly oriented dumbbells in the absence of a magnetic field (a) and field-aligned assemblies (b). Scale bars are 2.5 mm. (c-f) Polarization micrographs of one assembly and its alignment to a field at different field directions. The magnetic field direction is indicated by the white arrows. Arrow lengths are not quantitative. Scale bars are 100 µm. Figure adapted from reference [117] with permission from Wiley.

Yue and coworkers reported the magnetically directed self-assembly of block copolymers (BCP), in which paramagnetic ions are electrostatically coupled to the polymer side chains.[118] Using a commercial magnet of less than 0.35 T, they reach control with high precision (see Figure **1.19**). Upon application of the field, the polymer forms microphase-segregated nanostructures in alignment with the field direction. As by rinsing with water the magnetic ions can be easily removed from the BCP under preservation of its nano-pattern, the BCP can serve as a template for further functionalization.

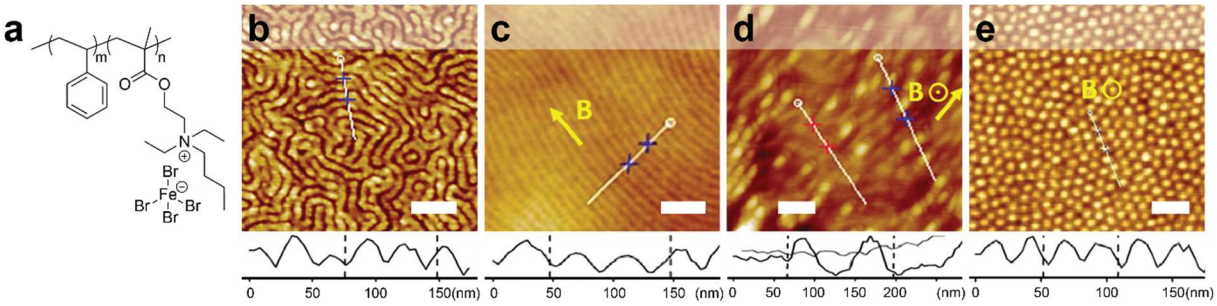

Figure 1.19 | Magnetically directed self-assembly of an Fe(III)-containing block copolymer. (a) Molecular structure of the block copolymer. Paramagnetic iron ions are attached to the organic backbone via electrostatic interactions. (b) AFM image of randomly aligned polymer chains. (c) AFM images of parallelly packed cylindrical nanostructures along the field direction. (d) AFM image of parallelly and perpendicularly mixed nanostructures when the field is tilted by 45°. (e) Perpendicularly packed cylindrical nanostructures perpendicular to the magnetic field direction. The field direction is indicated by yellow arrows. The graphs on the bottom of each image represent the relative height profile along the white lines. Scale bars are 200 nm. Figure adapted from reference [118] with permission from Wiley.

Mao and coworkers have achieved to form highly structured patterns over several layers in the assembly of biomolecules decorated with 5–8 nm sized Fe_3O_4 nanoparticles.[119] Bacterial flagella (Figure **1.20**a–c) and bacterial pili (Figure 1.20d–f) are naturally occurring supramolecular nanofibers exhibiting wave-like or straight morphologies, respectively. Decorated with 5–8 nm sized iron oxide nanoparticles, they could be field-aligned when air-dried in a 1 T field (Figure 1.20a,d). Through layer-by-layer deposition, the alignment could be twisted from one layer to another (Figure 1.20b,c,e,f).

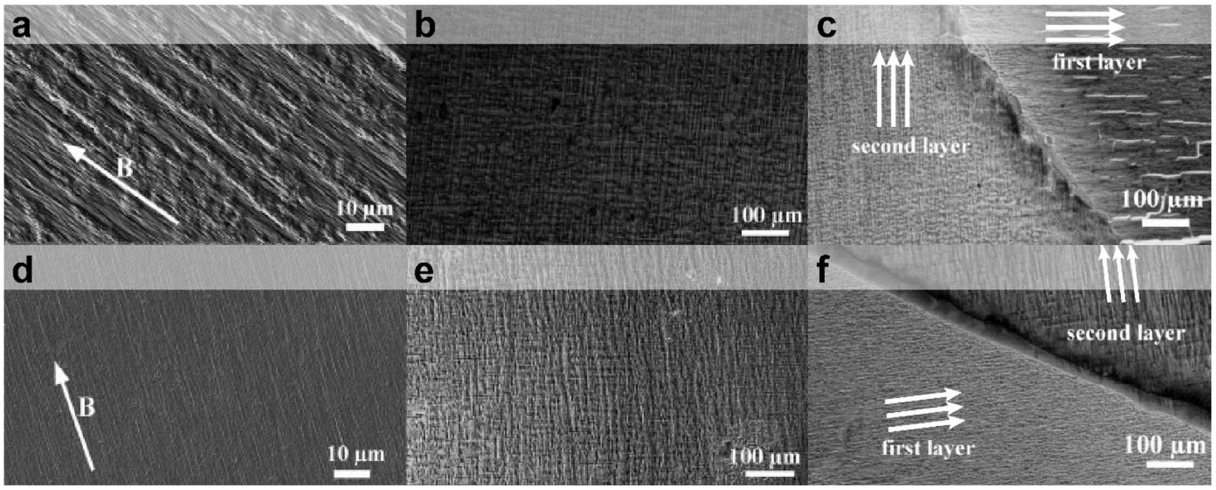

Figure 1.20 | Multi-layer field alignment of biomolecules decorated with Fe_3O_4 nanoparticles. (a,d) SEM image of field-aligned single-layer NP-flagellum (a) and NP-pilus (d) complexes. (b,e) Optical images of double-orientation layered complexes in top view. (c,f) Tilt-view of intentionally broken double layers. Figure adapted from reference [119] with permission from Wiley.

The field alignment of paramagnetic species is routinely exploited for protein structure determination in NMR spectroscopy. The orientation-dependent parameters can be extracted from residual dipolar couplings.[120–122]

1.3.2.3 Magneto-crystalline anisotropy in paramagnetic alignment

As discussed in section 1.2.3.3, paramagnetic lanthanide ions can exhibit an anisotropic electron density distribution, which is stable as the unpaired electrons of the *f*-shell are well shielded from the environment by the surrounding, full 5*s* and 5*p* shells. In the crystal state, this property is decisive for the overall magnetic properties of isostructural DOTA-complexes of Gd^{3+} and Dy^{3+}.[86,123] While the crystal incorporating anisotropic, oblate Dy^{3+} acts as a single molecule magnet (crystal structure shown in Figure 1.21), the isotropic Gd^{3+} containing crystal does not.[123] Single molecule magnets are defined by their characteristic of maintaining their magnetization, induced by an external field, below a certain so-called blocking temperature.[124] Advanced angle-dependent SQUID measurements allowed for the determination of the anisotropy axis (green line in Figure 1.21), which is surprisingly neither along a Dy–N or Dy–O coordination bond, nor linked to the symmetry axis of the tetragonal coordination geometry around the Dy ion. These measurements accentuate that anisotropy axes and their effects are complex and not simply dependent on the coordination geometry.

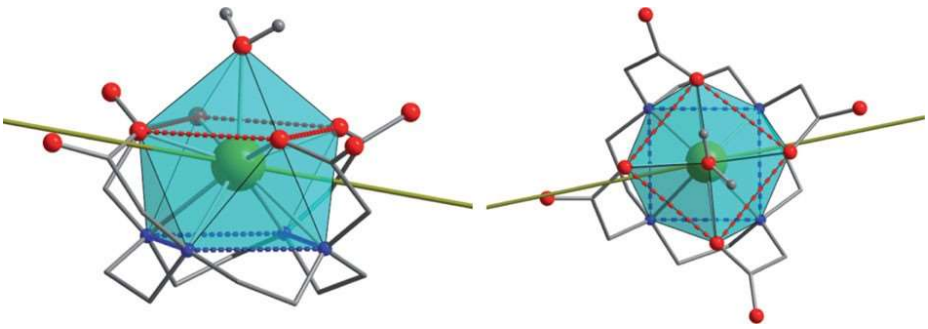

Figure 1.21 | Crystal structure of a Dy-DOTA crystal acting as a single molecule magnet. A square antiprism (light blue) comprises two planes, one that is formed by four nitrogen atoms (dark blue) and the other four oxygen atoms (red). The antiprism is capped by a water molecule and has a dysprosium ion (green) located in the center. The green rod represents the orientation of the magnetic anisotropy axis. Figure reprinted from reference [86] with permission from Springer Nature.

In a system of phospholipid-based vesicles, reported by Liebi and coworkers, the direction of magnetic alignment switches upon the incorporation of prolate Tm^{3+} ions, and oblate Dy^{3+} ions in a system based on the phospholipid POPC (1-palmitoyl-2-oleyl-sn-glycero-3-phosphocholine) and the chelator lipid DMPE-DTPA (1,2-dimyristoyl-sn-glycero-3-phosphoethanolamine-diethylenetriaminepenaacetate, Figure 1.22).[95] The around 100 nm sized vesicles containing paramagnetic ions (Tm^{3+} and Dy^{3+}) showed a temperature-dependent response to magnetic fields of up to 8 T. A decrease of temperature leads to an increasing formation of lipid domains, which become alignable upon reaching a certain critical size at 2.5 °C. The orientation of the alignment, however, depends on the lanthanide, and its magnetic anisotropy. The lipid domains orient in parallel to the magnetic field for prolate Tm^{3+} (Figure **1.22**b), but perpendicularly with oblate Dy^{3+} (Figure 1.22d). Upon an increase of the lanthanide proportion in the vesicle, the deformation was more pronounced (Figure 1.22c). Lanthanide-free vesicles remained unaffected by the exposure to an 8 T field. A similar system has previously been described by Prosser and coworkers.[125,126]

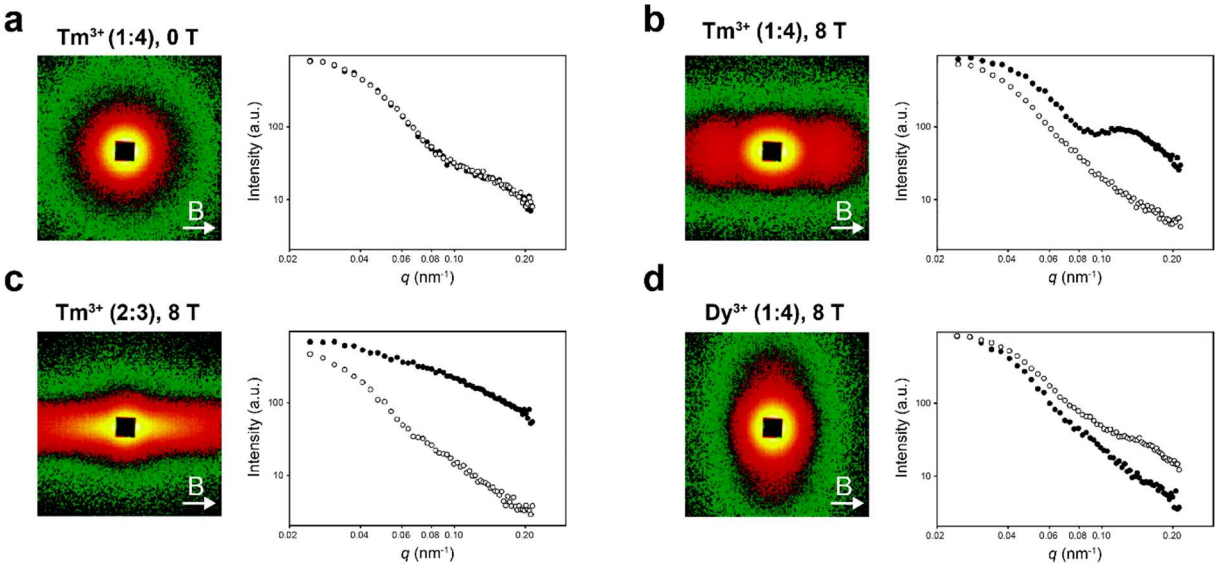

Figure 1.22 | Paramagnetic alignment depending on the magnetic anisotropy of lanthanide ions. 2D SANS patterns (left in each panel) and sectoral intensity (right in each panel) of lanthanide-containing DMPE-DTPA vesicles at 2.5 °C. (a) DMPE-DTPA-Tm^{3+} (molar ratio 4:1:1) at 0 T. (b) DMPE-DTPA-Tm^{3+} (molar ratio 4:1:1) at 8 T. (c) DMPE-DTPA-Tm^{3+} (molar ratio 3:2:2) at 8 T. (d) DMPE-DTPA-Dy^{3+} (molar ratio 4:1:1) at 8 T. Hollow and full circles represent the vertical and horizontal average at 15°, respectively. Incorporation of prolate Tm^{3+} leads to alignment parallel to the field direction, oblate Dy^{3+} to alignment perpendicular to the field direction. Arrows indicate the magnetic field direction. Figure adapted from reference [95] with permission from the American Chemical Society.

1.3.3 Effects in gradient fields

1.3.3.1 Deformation of fluids

In gradient fields, a typical reported phenomenon is the attraction of (super)paramagnetic matter by the field gradient, which can occur in one or multiple phases, in liquid or in solid state. Well established liquid systems are paramagnetic ionic liquids (ILs). ILs are commonly defined as salts with a melting point below an arbitrarily chosen temperature of 100 °C.[127] More accurately, they can be called molten salts with organic moieties.[128] A range of magnetic ILs have been developed over the last years, such as 1-butyl-3-methyl-imidazolium tetrachloroferrate ([bmim][$FeCl_4$]) by Hamaguchi and coworkers[129], and libraries of ILs based on methyl-imidazolium ($bmim^+$)- and tetraalkylphosphonium (PR_4^+) by Del Sesto and coworkers[130], dodecyltriammonium (DTA^+) by Eastoe and coworkers[131], or pyrrolidinium by Castner and coworkers[132], with Fe^{3+}, Co^{2+}, Ho^{3+}, Gd^{3+}, or Ce^{3+} containing counterions.

Drops of magnetic ILs respond to NdFeB cube magnet of 0.4 T or 0.55 T by a deformation directed toward the high field region of the gradient field (Figure 1.23a).[129,133] Similarly, micro-emulsions can be deformed.[134] This phenomenon is typically accompanied by a decrease in the surface tension of the IL, which can be by up to –12 % for a 0.1 M [C_{14}mim][$HoCl_4$]. In biphasic systems, the magneto-attraction can be used for phase inversion in liquid-liquid emulsions (Figure 1.23b)[133,135], or emulsion droplets (Figure 1.23c)[135].

The magneto-response of ionic liquids can be exploited for magnetic direction of biomacromolecules like DNA and proteins[131], and reversible recovery of graphene oxide.[136]

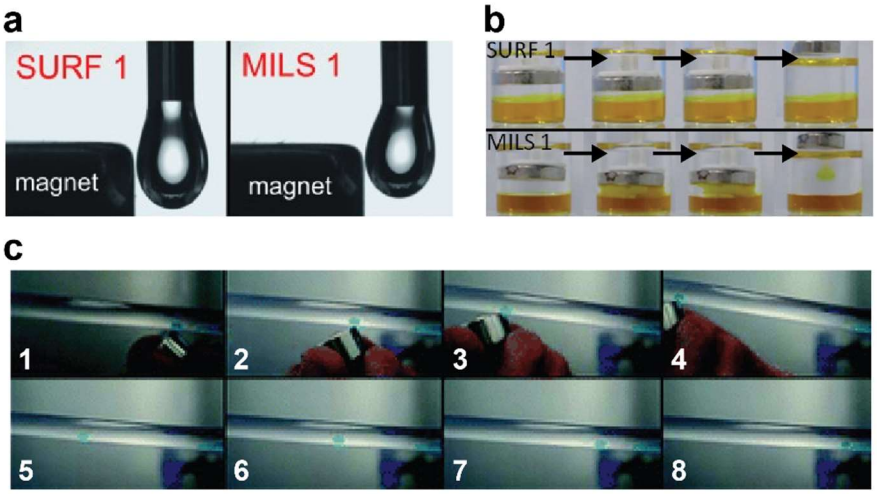

Figure 1.23 | Magneto-responsive ionic liquids. (a) Droplets of $[C_{10}mim]Cl$ (SURF 1, left, diamagnetic anion) and $[C_{10}mim][FeCl_4]$ (MILS 1, paramagnetic anion) next to a 0.4 T NdFeB magnet. The paramagnetic Fe^{3+} containing IL MILS 1 droplet shows deformation towards the magnet.[133] (b) Effect of a moving magnet on 20 wt% aqueous surfactant solutions of $[C_{10}mim]Cl$ (SURF 1, left, diamagnetic anion) and $[C_{10}mim][FeCl_4]$ (MILS 1, paramagnetic anion). In the case of the paramagnetic Fe^{3+} containing IL MILS 1, phase inversion is achieved upon slow movement of a cylindrical NdFeB magnet. The diamagnetic control SURF 1 shows no signs of phase inversion. The sequence from left to right describes a movement during around 30 s.[133] (c) Magnetically guided movement of a dyed droplet of $[DTA][GdCl_3Br]$, in a 50 wt% emulsion in dodecane. The droplet is pulled against gravity (1–4) by a 0.37 T cylindrical magnet, and drops back upon removal of the magnet (5–8).[135] Figure adapted from references [*133,135*] with permission from the Royal Society of Chemistry and Wiley.

Ferrofluids are stable colloidal liquids of single-domain magnetite (Fe_3O_4) in a carrier liquid with typically large magnetic susceptibilities.[137] Not to be confused by their name, ferrofluids show paramagnetic behavior. They contain superparamagnetic nanoparticles, which are stabilized with surfactants to avoid agglomeration through van der Waals interactions. When an external field is applied, the fluid reversibly aligns with the field direction, forming spikes following the shape of the respective field (Figure 1.24). As they are easily manipulated into a variety of geometries, they are attractive components in advanced technical applications such as acoustics, lubrification and sealing, micro-fluidics, and pumping. Their applications in biomedicine include magnetic resonance imaging, magnetically targeted or triggered drug delivery, and hypothermia treatment of cancer.[138] Various types of ferrofluids are commercialized. Recently, ferromagnetic ferrofluids have been developed in shape of iron-based liquid crystals.[139,140]

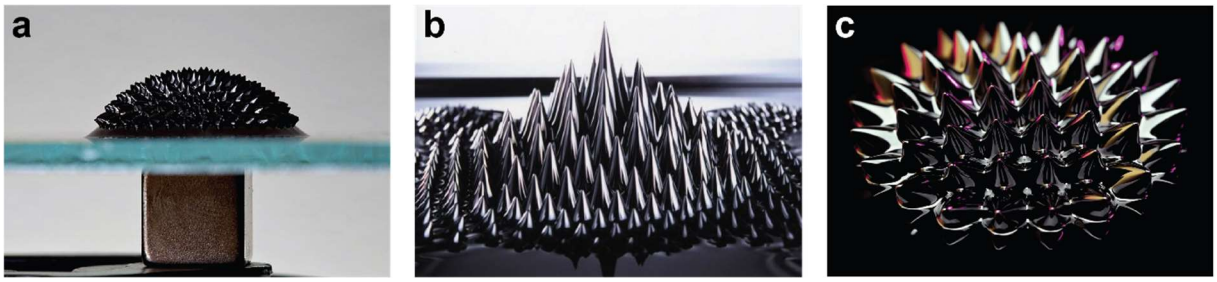

Figure 1.24 | Ferrofluids. Photographic images of field-aligned ferrofluids. (a) Ferrofluid on top of a glass slide, following the field lines of the cube magnet below.[141] (b,c) Field-aligned commercial ferrofluids from HSMAG® and Applied Magnets®, respectively.

1.3.3.2 Magnetophoresis

In biphasic solid-liquid dispersions of micro- or nanoparticles, the field-directed movement of magnetic particles through viscous medium is called magnetophoresis. Thereby, magnetic particles migrate in an advection stream through the solvent towards a high field region, where they accumulate. This technique of magnetic separation is rather old, and is employed to enrich minerals in iron, and to separate heavy metal ions from liquid waste in chemical plants or laboratories. So-called high gradient magnetic field separation (HGMS) uses columns packed with iron fibers under high field as of 10 T, and finds application in a wide range of fields from atomic power industry to tap-water treatment.[142] Practically, magnetic separation is commonly performed by field-flow fractionation, split-flow thin fractionation, continuous flow particle sorting, or in micro-channels.[143]

In moderate, and easily accessible fields and gradients, micro-sized magnetic particles can be well manipulated and guided. The simply implementable trigger has been used to direct matter of different types. For instance, magnetic microspheres, which can be functionalized chemically, biologically, or immunologically, can be used to separate and purify antibodies, which has become an essential technique in biology.[143] Dreyfus *et al.* successfully manipulated functionalized particles mimicking flagellum (hair-like structure of a cell, locomotes a cell), and their oscillatory or cork-screw-like motion.[144] In 2019, Cui and coworkers have shown magneto-attractive movement in the field of magnetogenetics.[145] A genetically encoded ferritin-based protein crystal, growing inside mammalian cells, was engineered. Each crystal containing more than 10^{10} ferritin subunits, they are attracted by an applied magnetic field ($B\nabla B \approx 210\ T^2 \cdot m^{-1}$) even when internalized into cells. Feringa and coworkers reported the magnetically guided movement of molecular motors decorated with magnetite nanoparticles, which allows cargo transport on the micro-scale.[26] This study will be discussed in more detail in section 1.3.5.

As the magnetic force F_{mag} scales linearly with the particle volume (*i.e.*, the cubic particle radius), magnetic separation and magnetophoresis become more challenging for particles on the nm-scale. The competing forces, in contrast, being the viscous drag force and the Brownian (thermal) force, change less drastically. They are proportional to the particle radius and its square root, respectively. Majetich and coworkers have analyzed magnetophoretic effects on polymer- and gold-coated, superparamagnetic iron-oxide nanoparticles in aqueous dispersion.[99] The nanoparticle cores are 35 nm in size, and exhibit a saturation magnetization of 76 $emu \cdot g^{-1}$. The hydrodynamic radius of the coated nanoparticles is about 85 nm. A triangular piece of mu metal (magnetically soft Ni Fe alloy) was used to generate the magnetic field gradient of 3000 $T \cdot m^{-1}$. The sharp end of the tip was placed in the nanoparticle dispersion with the blunt end connected to a solenoid (coil), magnetizing the tip when electric current is applied. A single magnetic tip was used to collect the particles and release them in a controlled way when the current was turned off. The authors find that particles within a radius of around 140 µm from the tip migrate towards it, whereas particles at a larger distance showed no obvious drift. The trajectory of individual particles was tracked in real-time by optical microscopy, and the forces were deconvoluted into the different contributing forces with a scrupulous effort. At this scale, the quantitative analysis is tricky, because the magnetic drag force, the viscous drag force, and the Brownian force interplay.

1.3.4 Dipolar coupling

Dipolar coupling (see section 1.3.1.3) is a major driving force in the self-assembly of magnetic nanoparticles. The self-assembly of nanoparticles is generally interesting from a magnetic point of view, because their magnetic moments are large enough to experience both mutual magnetic interactions (dipolar coupling) as also interactions with an external field. Particles in the two digit nanometer range provoke a special interest, as they are applied in high-density magnetic storage devices, hypothermal cancer therapy, and magnetic resonance imaging[146].[147] As the magnetic moment of nanoparticles is volume dependent, sub-10 nm particles are too small to be considered for these applications, and thus more rarely studied.

Luis *et al*. have studied the dipolar interactions in nanometer-sized Co-clusters and reported a slower spin relaxation with an increasing number of neighboring particles.[148] To be able to draw valid conclusions without changing several other factors, the measurements are performed on clusters growing in quasi-ordered layer structures, where the relevant parameters can be fine-tuned and measured separately. The clusters are obtained in a layer-by-layer deposition of Al_2O_3 and Co. In this multilayer system, varying the number of Co-Al_2O_3 bilayers or the layer thickness of the alumina layers allows to tailor the number of neighbors to a given cluster and the distance between Co-layers (0.7–10 nm). The found results show that the dipole-dipole interactions between superparamagnetic Co-nanoparticles slow down their reversal of magnetic moments, increasing their blocking temperatures by almost 40 % going from 1 to 15 bilayers at an Al_2O_3 layer thickness of 3 nm. At an Al_2O_3 layer thickness of 10 nm, the blocking temperature is only 2 % higher for 20 Co layers than for a single Co layer, confirming that the effect is caused by interparticle distance-dependent dipole-dipole interactions. Similar observations were made by Park and coworkers for monodisperse Fe_3O_4 particles.[149]

Klajn and coworkers have shown the self-assembly of 13 nm sized cubic magnetite nanoparticles to single, double, and triple helical superstructures (Figure 1.25).[150] What usually requires templating, can be achieved in a single step with a yield of > 99 %. The formation of these assemblies is a result of the interplay of van der Waals and magnetic dipole-dipole interactions, Zeeman coupling, and entropic forces.

In cubic nanoparticles, the axes of preferential magnetization (easy axes, in this case the second diagonal of the cube) are incompatible with any configuration that allow close packing. Therefore, a competition arises between shape anisotropy, favoring face-to-face assembly, and magnetocrystalline anisotropy, favoring corner-to-corner assembly. The helical assemblies were obtained at the diethylene glycol-air interface, when a solution of the superparamagnetic nanocubes in hexane was placed there under a field of 0–0.07 T, and the solvent was allowed to evaporate. First, dipole-dipole coupling between the cubes leads to belt formation, which further aggregate to higher-ordered superstructures as the solvent evaporates.

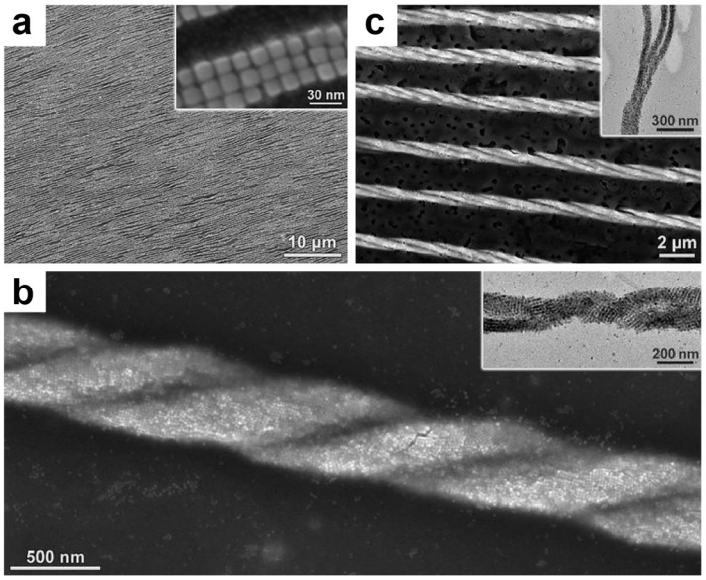

Figure 1.25 | Helical superstructures assembled from cubic magnetite nanoparticles. (a) SEM images of belts at two different magnifications. (b) SEM image of a well-defined double-helix. Inset: TEM image of two belt wrapped around one another. (c) SEM image if an array of triple helices. Inset: End of a triple helix showing the three strains. Figure adapted from reference [150].

Förster and coworkers have studied the self-assembly of sub-15 nm sized iron oxide nanoparticles, which spontaneously assemble to into chains (1D assembly), sheets (2D assembly), and cuboids (3D assembly) under exposure to a magnetic field.[147] More specifically, the assemblies were observed by SEM and cryo-TEM, where 0.2–3 wt% solutions of 8.2 nm sized nanoparticles, which are sterically stabilized by oleic acid, in toluene were drop-casted at room temperature and 253 K (–20 °C), respectively, under a constant field of 0.13 T (Figure **1.26**). To analyze the assembly in solution, the aggregate sizes were obtained by dynamic light scattering at different temperatures and in the presence or absence of a magnetic field. At room temperature (25 °C), the nanocubes remain singly dispersed over several days, regardless of the magnetic field. At 253 K (-20 °C) at 0.13 T, large aggregates were obtained, and a second population with hydrodynamic diameters in the range of a few hundreds of nanometers are found. In the absence of a magnetic field, only slight changes are observed upon decreasing the temperature to 253 K. At room temperature, larger assemblies are only obtained at higher concentrations (11 or 18 wt%). The cubic shape of the nanoparticles seems to be decisive, as spherical analogs of roughly the same size do not show this kind of highly ordered structures.

According to a proposed theoretical model, the first step of the assembly from cubes to chains in a head-to-tail arrangement is energetically favored and becomes more favorable with an increasing chain length. Single chains will then attract each other or single cubes, arranging in a brick wall constellation, with their spins aligned in parallel. The face-to-face assembly of the cubes (as opposed to corner-to-corner assembly following their magnetic easy axis) is believed to be caused by van der Waals interactions. In this size range of particles, the magnetic energy is in the same order of magnitude as thermal energy and van der Waals forces. For spherical particles, no such assembly was found, which can be because the contact area is significantly reduced as compared to cubic nanoparticles, reducing the short-range attractive interactions. Cubes below a particle size of 7.5 nm do not show any magnetic-field induced assembly either, even though the surface to volume ratio is increased as compared to the larger cubes.

Presumably, the magnetic moments are too small to achieve significant forces or energies. Even though the directing dipolar interactions and the stabilizing van der Waals forces seem to be the most important contributions in this case, the external field is indispensable for the assembly. It causes alignment of the nanoparticles in the first place, paving the path for short range interactions, which stabilize the arrangement to assemblies even after removal of the magnetic field.

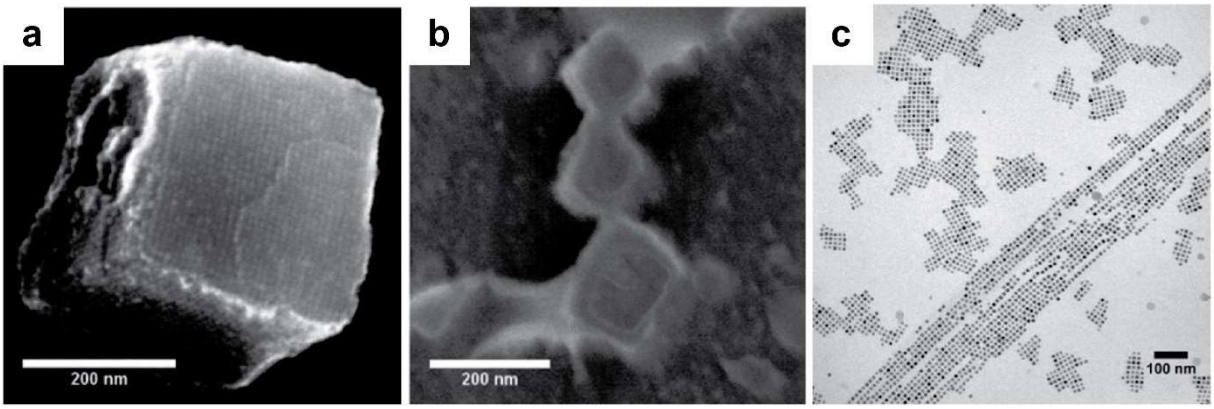

Figure 1.26 | Self-assembly of smallest nanocubes. (a) SEM image of a 3D cuboid containing around 10^4 nanocubes. (b) Cryo-TEM image of the nanoparticle solution in toluene. (c) SEM image showing chains, ribbons, and sheets. Figure adapted from reference [147].

Recently, Macfarlane and coworkers have shown that supramolecular bonding between polymer-brushes can be reinforced by dipolar coupling of iron oxide nanoparticles, if the polymer is coated on the latter.[151] The polymer chains are end-capped with complementary, triple hydrogen bonding diamino pyridine- and thymine groups. The strengthening of triple hydrogen bonding upon simultaneous dipolar coupling can be identified by an increased melting- and blocking temperature of the polymers. Notably, the melting temperature of the polymer is increased by 10 K. The authors are able to control the dipole–dipole coupling between the nanoparticles, as well as the strength of the ligand–ligand interaction by varying the polymer spacer between the hydrogen bonding groups and the surface of the nanoparticle. A unique superlattice structure can be stabilized, which only occurs if the nanoparticles couple magnetically.

1.3.5 Dually controlled systems

Evidently, the magnetic stimulus can be combined—synergistically or orthogonally—with other stimuli (section 1.1.3), allowing for unique structures formed with impressive precision, directionality, and symmetry. Among sheerly endless possibilities, two examples will be discussed to sketch the scope.

Maan and coworkers have combined magnetic with rotational forces, and are able to select supramolecular chirality in helical assemblies of an achiral monomer, tris-(4-sulfonatophenyl)phenylporphyrin ($TPPS_3$, see Figure 1.27a).[152] Driven by electrostatic and π-π interactions, $TPPS_3$ assembles to J-aggregates over a time span of three days following a nucleation-elongation mechanism, forming nano-sized aggregates ($R_H \leq 0.8$ mm). Their small

size prevents the aggregates from sedimentation. Therefore, they do not align under normal gravity.

Inside a magnet of 18 or 25 T with the field direction along z, samples were rotated clockwise (CW) or counterclockwise (CCW) in cylindrical vessels at 15 Hz, 23 °C, and over time periods from 30 to 120 minutes, at different z positions. Afterwards, the solutions were removed from the magnet and allowed to sit for three days at 23 °C, and then analyzed by UV-Vis and CD spectroscopy (Figure 1.27b,c).

In this system, two magnetic phenomena play a role, being the alignment force, which originates from the anisotropy of the diamagnetic susceptibility of the porphyrin (see section 1.2.3.2), and which is proportional to the field strength $B(z)$, and a magnetic levitation force. The latter is proportional to the product of the magnetic susceptibility and the field gradient $\chi B(z)B'(z)$. Moreover, the field gradient contributes to a z-dependent effective gravity $G_{eff} = G_n(1+ B(z)B'(z)\ |\chi|\cdot(\mu_0\rho)^{-1})$, with the normal gravitation G_n, the density of the material ρ, and the vacuum permeability μ_0. Depending on their z position, the solutions experience different field strengths $B(z)$ and field gradients $B(z)'B(z)$, so the forces act in different proportions.

The CD measurements show that for $G_{eff} > 0$ and clockwise rotation in a magnetic field, the signal increased significantly. The observed handedness is determined by how spinning and effective gravity are oriented with respect to each other. So is the dissymmetry factor Δg negative for clockwise rotation with $G_{eff} > 0$ and counterclockwise rotation with $G_{eff} < 0$. By inverting either the rotation direction or the G_{eff}, Δg becomes positive. Without exposure to a magnetic field, CD spectra exhibit low-intensity signals for either direction of rotation.

The authors hypothesize that the generated hydrodynamic flow gives a chiral twist to the nanoaggregates, which are formed in the nucleation step of the polymerization. The magnetic field then orients the nuclei along the rotation axis, damping the influence of Brownian motion. During the elongation phase, the nanoaggregates act as chiral seeds promoting the amplification of their own handedness.

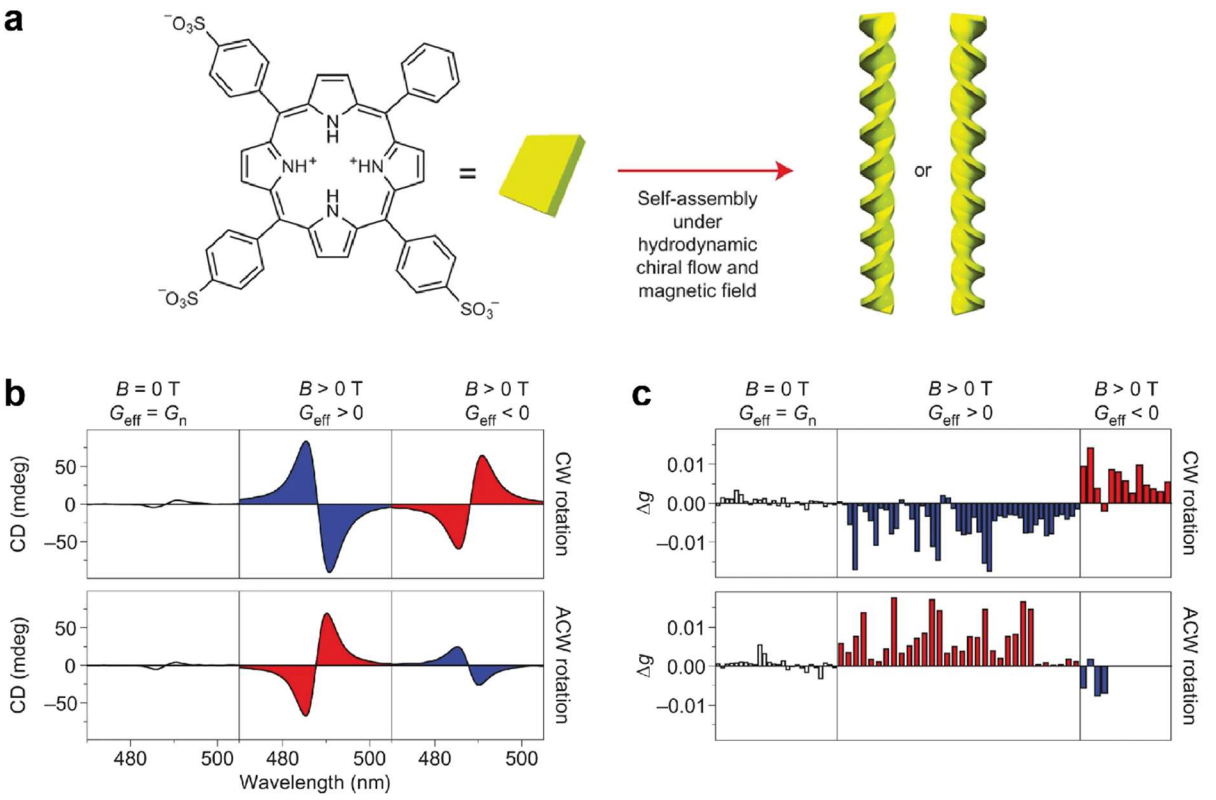

Figure 1.27 | Symmetry selection by rotation in a magnetic field. (a) Molecular structure of the porphyrin-based monomer $TPPS_3$ and a schematic illustration of its self-assembly to helices. (b) Typical CD spectra showing the correlation between the handedness of the final aggregates, the spinning directions, and effective gravity G_{eff}, with and without magnetic field. (c) The dissymmetry factor Δg measured for clockwise (CW) and anti-clockwise (ACW) spinning, with and without field, and different effective gravities G_{eff}. Figure adapted from reference [152] with permission from Springer Nature.

Feringa and coworkers, for their part, have shown an orthogonal dual-control of molecular motors by light and magnetism in a hybrid assembly of molecular motor amphiphiles decorated with iron nanoparticles (NP).[26] The system provides fast photo-triggered movements and magnetically induced movements, which allow precisely controlled cargo transport (Figure **1.28**).

Magnetite nanoparticles were attached to macroscopic length-scale supramolecular nanofibers of motor amphiphiles (MA) through electrostatic interactions between the nanoparticles and the histidine groups of the MA. Upon photoirradiation at 365 nm, the MA/NP fibers bend towards the light source, increasing the bending angle from 0° to 90° within 25 s. When a magnet was placed close to a MA/NP fiber, it moved towards the magnet within 2 s. The two responses were combined in a dual-controlled process in a cargo transport experiment.

In an aqueous $CaCl_2$ solution, a MA/NP string was placed in position A, and a piece of paper in position B. Using a magnet, the MA/NP string was moved from position A to B, where it was photo-irradiated for 60 s, transitioning from a linear to a curved shape. Upon the conformation change, curved MA/NP can grab the paper clip, and transport it to a new position C guided by the magnet. In position C, the convex side of the of the MA/NP string was irradiated to reverse the conformation to a linear shape, unloading the paper cargo. The linear MA/NP was finally guided to position D, leaving behind the cargo in position C. This

experiment shows how dual stimuli responsive supramolecular materials can imitate muscle-like functions and can be used to generate soft robotic materials.

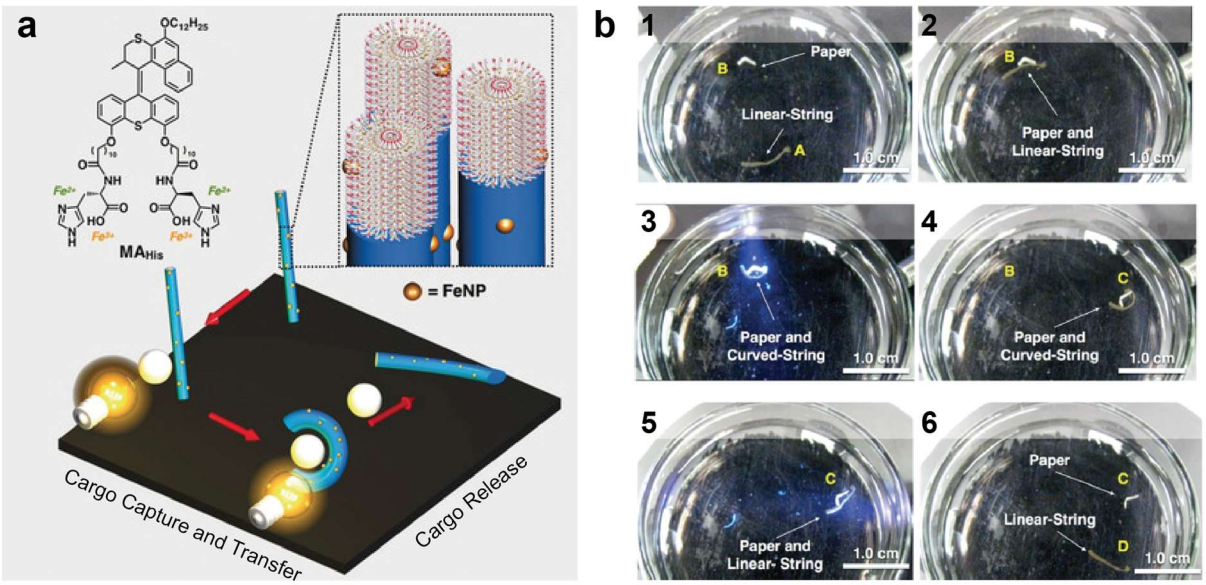

Figure 1.28 | Cargo transport by a combined magnetic and light stimulus. (a) Molecular structure of the motor amphiphile and a schematic illustration of the cargo-transport experiment. (b) Snapshots of the MA/NP string and the paper cargo. The initially separated paper and string (position A and B, 1) are reunited through magnetic direction of the string to position B (2). In position B, the paper cargo is captured by the MA/NP string as the latter is phot-irradiated (3). The cargo is transported to position C (4), where it is released upon photoirradiation (5). The MA/NP string is moved to position D (6). Figure adapted from reference [26] with permission from Wiley.

1.3.6 Non-trivial observations

Recently, some so-far not well understood phenomena including magnetic species have been reported in different contexts. They are non-trivial in a sense that current theoretical models fail to explain the observed effects. First, Polarz and coworkers have shown a remarkable multi-step self-assembly of Dy^{3+} containing surfactant to anisotropic macro-sized dumbbells, after a solution of the surfactant was heated to 80 °C and cooled down to room temperature (Figure **1.29**, *cf.* Figure 1.18).[117] From the nanometer to the micrometer scale, an extraordinary hierarchy of self-assembled structures has been elucidated using various microscopic, spectroscopic and scattering techniques. When an analogous surfactant containing diamagnetic Lu^{3+} instead of Dy^{3+} was subjected to the same procedure, no similar structures were formed. This leads to the assumption that interactions between the paramagnetic head groups (intermetallic crystal field interactions) cause the highly complex self-assembly. SQUID measurements of the species show ordinary paramagnetic behavior of the Dy^{3+} species, leaving behind a number of unanswered questions.

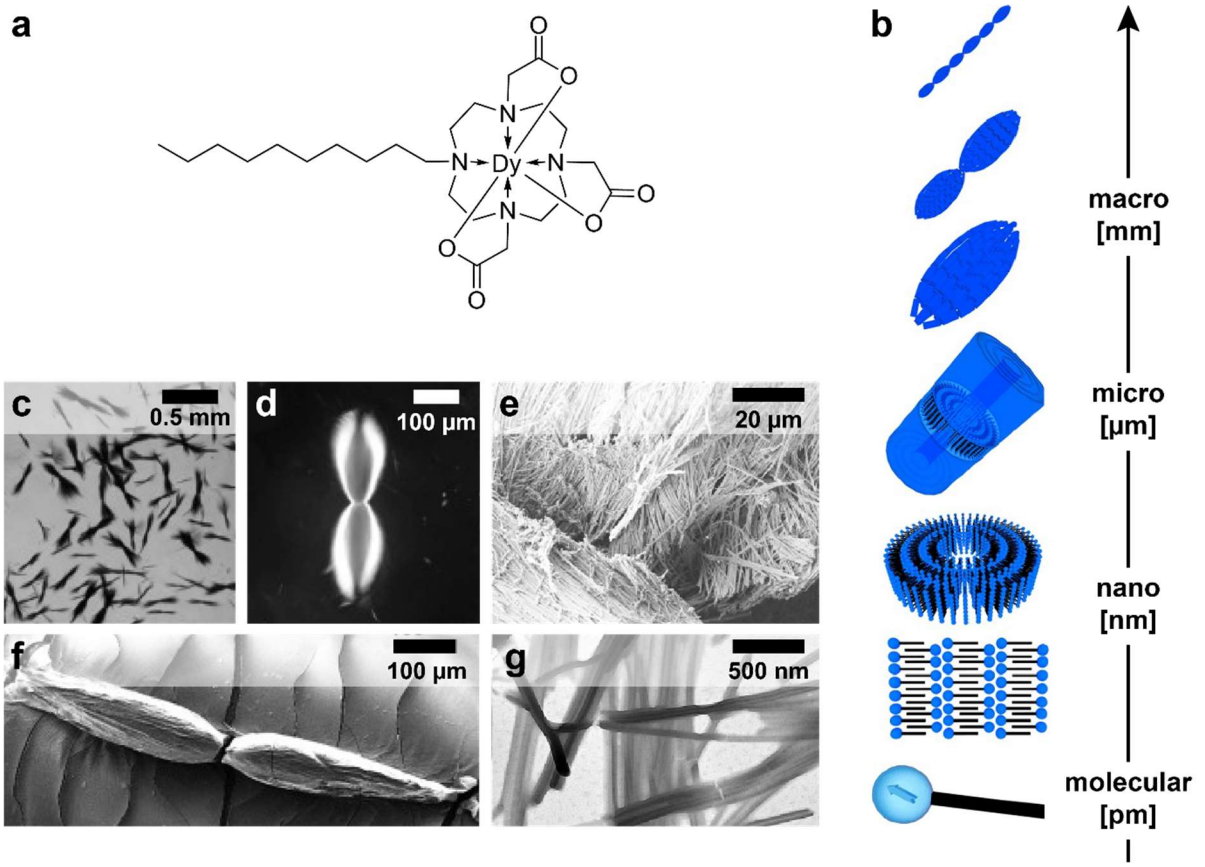

Figure 1.29 | Panoscopic self-assembly of a Dy-containing surfactant. (a) Molecular structure of the Dy-containing amphiphile. (b) Schematic illustration depicting the panoscopic multi-step assembly. (c,d) Optical (c) and polarization (d) microscopy images of the dumbshell aggregates. (e,f) SEM images at two different magnifications. (g) TEM image of fiber-like structures. Figure adapted from reference [117] with permission from Wiley.

A similar conclusion was drawn by Meijer and coworkers, who have investigated Gd^{3+}-containing dendrimers of different generations as MRI contrast agents.[16] Surprisingly, they found that the largest dendrimer of their library (5th generation) exhibits unproportionally large ionic relaxivities as compared to lower generations. Without going into further detail, they hypothesize magnetic interactions between the paramagnetic Gd^{3+} ions, which are forced into a high density and short ion-ion distances by the molecular structure of the dendrimer.

As discussed in section 1.3.1.4, the dipolar coupling energy between two paramagnetic ions at room temperature is around three orders of magnitude weaker than the thermal fluctuations, even at 4 Å, which is roughly π-π stacking distance. In this context, these observations are very surprising. The energy of Brownian motion might be reduced due to supramolecular assembly, forcing the ions in a certain configuration, and thereby reducing their degrees of freedom.

Another astounding example was reported by Fujiwara and coworkers in 2004.[153] In a gradient field of $(B\cdot\nabla)B = 410\ \mathrm{kOe^2cm^{-1}} = 410\ \mathrm{T^2m^{-1}}$, different magnetic transition metal salts, placed on silica gel as 2–3 M solutions at 100 mm from the field center, migrate towards the field center within 14 h. As a function of their magnetic susceptibility, their concentration, and the grain size of the silica gel, they cover distances of up to the full 100 mm to the field center (Figure 1.30, Mn^{2+}). Since the ion movement is enhanced for larger concentrations, the authors assume that the ions do not move as single ions, but that groups of ions and water molecules travel collectively as one unit. If a diamagnetic Ag^{+} is co-spotted with paramagnetic Cu^{2+}, the two species can be separated, since only Cu^{2+} migrates towards the field center, as shown in precedent work.[154]

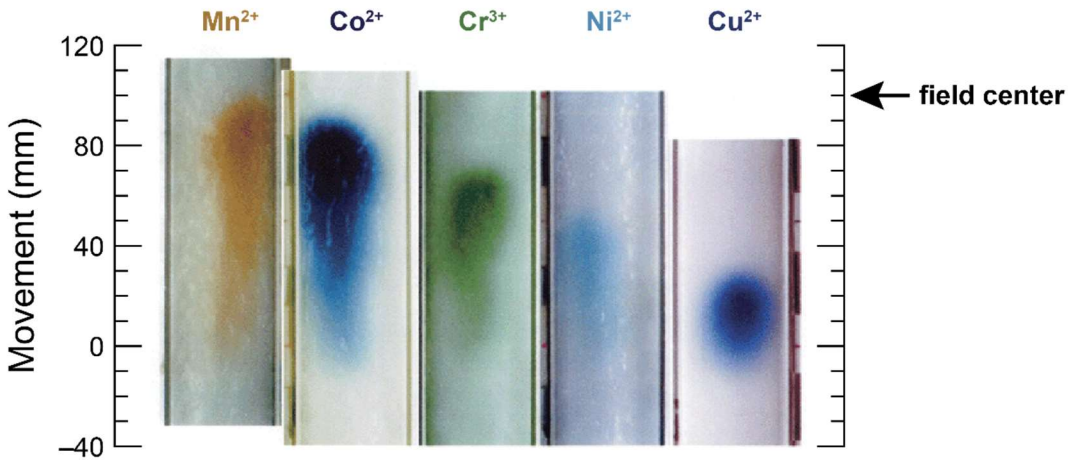

Figure 1.30 | Migration of paramagnetic transition metal ions deposited on silica gel. The ions were spotted at the 0 mm position 100 mm from the field center. Figure adapted from reference [153] with permission from the American Chemical Society.

Eckert and coworkers showed a concentration gradient of initially homogeneous 1 M solutions of the paramagnetic ions Mn^{2+}, Gd^{3+}, and Dy^{3+} after the solutions had been exposed to a cylindrical NdFeB permanent magnet.[155,156] After around 100 s, the ion concentration starts to increase in proximity of the magnet and a simultaneously decrease slightly at larger distance. The ion concentration was enriched by up to 2 %, in a convex layer reproducing the gradient field force, as they determined by interferometry. Upon removal of the magnet, the enriched layer drops down to the bottom as a convection flow.

The group of Fransaer reported a similar study in a gel matrix.[157] 3 mM solutions of Y^{3+}, Gd^{3+}, and Y^{3+} were incorporated in gelatin gels, and exposed to a gradient either on top of an NdFeB magnet, or a 5 T superconducting magnet. When the gel was sliced in 2 mm thick layers perpendicular to the field direction, so that all sliced experienced different field strength, and the concentrations were determined by atom emission spectroscopy. For Dy^{3+}, the authors report a concentration increase of about 0.8 % using the commercial magnet, and up to 10 % using the superconducting magnet for the slice in the strongest field after 24 hours. Moreover, porous glass disks were immersed in solutions of Dy^{3+} (4 mM) and Y^{3+} (10 mM). Again, samples of 3 mm thickness were analyzed for their ion concentration, showing a 6% increase for paramagnetic Dy^{3+} and a 7 % decrease for diamagnetic Y^{3+}, which is repelled by the field, after 6 hours.

According to our estimations, the thermal forces defeat the magnetic forces on single ions by a factor of 10^8 in these conditions. On this account, Gorobets and coworkers have hypothesized that the magnetic field force does not act on single ions, but on clusters, composed of several ions acting as a unit, which they named "magnions".[158] These magnions would then have an effective susceptibility, combining the individual magnetic moments in one. This assumption is congruent with the claim of Fujiwara[153], could however not be evidenced up until now. Coey and coworkers have looked into whether or not there is a concentration gradient force[159]—a force arising from a uniform magnetic field on an already existing concentration gradient of single ions. In conclusion, they state that there is no such force in a uniform field, neither acting on diamagnetic nor on paramagnetic species. There seems to be a small effect due to the inhomogeneity of the demagnetizing field, which gives rise to a concentration gradient force perpendicular to the electrode surface. It remains, however, negligible being 10^8 times inferior to diffusion for a 1 M solution in a 1 T field. The concentration gradient field force is, in contrast, confirmed for gradient fields.[160] It is thus imaginable that in some of the reported

studies a concentration inhomogeneity was unknowingly induced by solvent evaporation or other unexpected side phenomena. The gradient could then be subjected to the concentration gradient force from an inhomogeneous magnetic field. A final explanation remains to be presented.

Mezzenga and coworkers reported a conformation change of single Fe containing polysaccharide chains in a constant field of 1.1 T.[161] Polymer solutions of an Fe(II) and Fe(III)-enriched anionic carrageenan polysaccharide were deposited on a functionalized silica wafer in a Halbach array. The chains typically appear as coexisting random coils and single helices. When comparing AFM images, an overall 1.5-fold stiffening and a 1.1-fold stretching is observed for the sample prepared in the field as compared to the control experiment in the absence of a magnetic field. In both cases, the bimodal distribution in random coils and single helices is preserved. If we consider the magnetic energy in this case of a 1.1 T field and single iron ions, the approximated merit number $\beta = E_{mag} \cdot E_{therm}^{-1}$ is below 0.03, so we do not expect significant magnetic effects. The authors suggest that the distribution of the iron ions along the chains may not be homogeneous, inducing a sort of anisotropy in the system.

1.4. Aim and contents of this thesis

Controlling supramolecular assembly offers vast possibilities for the development of new smart materials, and still leaves room for improvement and new approaches. A magnetic stimulus can offer many benefits compared to the more conventional alternatives, as it is non-invasive, non-destructive, easily tunable in intensity, direction, space, and time. Moreover, it tolerates a wide range of materials, conditions, and atmospheres. In awareness of these advantages, magnetic control is well established in the field of micro- and nanoparticles. On the (supra-) molecular level, however, the possibilities are so far limited, as the magnetic energies and forces decrease with the size of the magnetic species. Consequently, the magnetic forces and energies tend to be small as compared to the competing thermal contributions in standard conditions. Few examples have been reported in the field of magnetic control over supramolecular polymers, and many of these reports describe non-trivial observations, which lack a clear explanation and understanding.

In the context of this poorly explored field of research, this thesis aims to obtain a general overview over the possibilities a magnetic stimulus can offer to control supramolecular systems. The final goal is to understand how magnetic stimuli and impulses can complete the toolbox of non-covalent interactions in supramolecular self-assembly.

Chapter 2 is focused on the thermodynamics of supramolecular self-assembly of a family of lanthanide-containing, symmetric naphthalenediimide (NDI) derivatives in water. When comparing dia- and paramagnetic species, we find that the incorporation of paramagnetic lanthanide ions leads to a decrease of the enthalpy of supramolecular polymerization as compared to diamagnetic ions. The overall Gibbs free energy, however, is identical for all species, indicating a reverse action of the entropy.

The self-assembly of the same monomers in a water/THF system leads to the formation of micro-sized colloids, which are described in **Chapter 3**. When a commercial, permanent cube magnet is placed in a dispersion to the colloidal assemblies, the formation of an organic layer is observed on the surface of the magnet. The reversible assembly to colloids allows for pre-programming of this magnetophoretic effect.

Chapter 4 presents the self-assembly of a benzenetricarboxamide (BTA) derivative decorated with paramagnetic Gd^{3+} ions into rod networks in solution. A fast change of the rod network to more randomly branched structures, and a reversible densification of the rod network over 10 to 12 h indicate that the equilibrium is shifted by the magnetic field.

Finally, **Chapter 5** is oriented towards the development of magneto-responsive materials. An NDI-based supramolecular hydrogel containing paramagnetic Dy^{3+} ions and its response to uniform fields of up to 0.8 T is presented. By magneto-rheology we find a significant acceleration of the gelation kinetics upon application of a magnetic field.

Chapter 6 finally concludes this work with a summary of the main findings and integrates these in the larger picture.

1.5. Appendix

Parameters

IO-NP[99]: M_S = 396 emu·cm^{-3} = 3.96·10^5 A·m^{-1}

R = 36 nm

Ho^{3+} ion[62,162,163]: χ_n = 5.702·10^{-7} m^3·mol^{-1}

R = 0.901 Å

m = 10.6 μ_B = 9.83·10^{-23} J·T^{-1}

water[164]: η = 8.91·10^{-4} Pa·s

Scenario I: 1 T uniform magnetic field, at room temperature (298 K).

$$E_{mag}(\mathrm{IO-NP}) = -\frac{1}{2}M_S V B^2 = -\frac{1}{2}\cdot 3.96\cdot 10^5\,\frac{\mathrm{A}}{\mathrm{m}}\cdot\frac{4}{3}\pi\cdot(36\cdot 10^{-9}\mathrm{m})^3\cdot(1\mathrm{T})^2$$

$$= -3.9\cdot 10^{-17}\ \mathrm{J}$$

$$E_{mag}(\mathrm{Ho^{3+}}) = -\frac{1}{2\mu_0}\chi V B^2 = -\frac{1}{2\mu_0}\chi_{mol} n B^2$$

$$= -\frac{1}{2\cdot 4\pi\cdot 10^{-7}\,\frac{\mathrm{N}}{\mathrm{A^2}}}\cdot 5.702\cdot 10^{-7}\,\frac{\mathrm{m^3}}{\mathrm{mol}}\cdot\frac{1}{6.022\cdot 10^{-2}\ \mathrm{mol^{-1}}}\cdot(1\mathrm{T})^2$$

$$= -3.8\cdot 10^{-25}\ \mathrm{J}$$

$$E_{therm} = -\frac{3}{2}\mathrm{k_B}T = -\frac{3}{2}\cdot 1.38\cdot 10^{-23}\,\frac{\mathrm{J}}{\mathrm{K}}\cdot 298\ \mathrm{K}$$

$$= -6.2\cdot 10^{-21}\ \mathrm{J}$$

species	E_{mag} (J)	E_{therm} (J)	β (-)
IO-NP	3.9·10^{-17}	6.2·10^{-21}	6.3·10^3
Ho^{3+} ion	3.8·10^{-25}	6.2·10^{-21}	6.2·10^{-5}

Scenario II: gradient magnetic field with B = 1 T and ∇B = 2000 T·m^{-1} at 298 K in water.

$$F_{mag}(\mathrm{IO-NP}) = \frac{1}{2} M_S V \cdot B\nabla B = \frac{1}{2} \cdot 3.96 \cdot 10^5 \frac{\mathrm{A}}{\mathrm{m}} \cdot \frac{4}{3}\pi \cdot (36 \cdot 10^{-9}\mathrm{m})^3 \cdot 2000 \frac{\mathrm{T}}{\mathrm{m}} \cdot 1\ \mathrm{T}$$
$$= 7.7 \cdot 10^{-14}\ \mathrm{N}$$

$$F_{therm}(\mathrm{IO-NP}) = \sqrt{2k_B T(6\pi\eta R)}\omega(t)$$
$$= \sqrt{2 \cdot 1.38 \cdot 10^{-23} \frac{\mathrm{J}}{\mathrm{K}} \cdot 298\ \mathrm{K} \cdot 6\pi \cdot 8.91 \cdot 10^{-4}\mathrm{Pa \cdot s} \cdot 36 \cdot 10^{-9}\mathrm{m} \cdot 1}$$
$$= 2.2 \cdot 10^{-15}\ \mathrm{N}$$

$$F_{mag}(\mathrm{Ho^{3+}}) = \frac{1}{2\mu_0}\chi V(\vec{B}\cdot\vec{\nabla})\vec{B} = \frac{1}{2\mu_0}\chi_{mol} n(\vec{B}\cdot\vec{\nabla})\vec{B}$$
$$= \frac{1}{2 \cdot 4\pi \cdot 10^{-7}\frac{\mathrm{N}}{\mathrm{A^2}}} \cdot 5.702 \cdot 10^{-7} \frac{\mathrm{m^3}}{\mathrm{mol}} \cdot \frac{1}{6.022 \cdot 10^{20}\ \mathrm{mol^{-1}}} \cdot 2000 \frac{\mathrm{T}}{\mathrm{m}} \cdot 1\ \mathrm{T}$$
$$= 7.5 \cdot 10^{-22}\ \mathrm{N}$$

$$F_{therm}(\mathrm{IO-NP}) = \sqrt{2k_B T(6\pi\eta R)}\omega(t)$$
$$= \sqrt{2 \cdot 1.38 \cdot 10^{-23} \frac{\mathrm{J}}{\mathrm{K}} \cdot 298\ \mathrm{K} \cdot 6\pi \cdot 8.91 \cdot 10^{-4}\mathrm{Pa \cdot s} \cdot 0.901 \cdot 10^{-10}\mathrm{m} \cdot 1}$$
$$= 1.2 \cdot 10^{-1}\ \mathrm{N}$$

species	F_{mag} (N)	F_{therm} (N)	β (-)
IO-NP	$7.7 \cdot 10^{-14}$	$2.2 \cdot 10^{-15}$	35
Ho^{3+} ion	$7.5 \cdot 10^{-22}$	$1.1 \cdot 10^{-16}$	$6.8 \cdot 10^{-6}$

Scenario III: two individuals of each species at ππ-stacking distance (~ 4 Å) at 298 K, forming an equilateral triangle with the coordinate origin (all angles 60°).

$$E_{mag,dipolar} = -\frac{\mu_0 \cdot m_i m_j}{4\pi r_{ij}^3}\left(3\left(\overrightarrow{m_i} \cdot \overrightarrow{r_{ij}}\right)\left(\overrightarrow{m_j} \cdot \overrightarrow{r_{ij}}\right) - \overrightarrow{m_i} \cdot \overrightarrow{m_j}\right)$$

$$E_{mag,dipolar}(\mathrm{IO-NP}) = -\frac{\mu_0}{4\pi r_{ij}^3} \cdot m_i m_j \left(3\left(\overrightarrow{m_i} \cdot \overrightarrow{r_{ij}}\right)\left(\overrightarrow{m_j} \cdot \overrightarrow{r_{ij}}\right) - \overrightarrow{m_i} \cdot \overrightarrow{m_j}\right)$$

$$= -\frac{4\pi \cdot 10^{-7}\,\frac{\mathrm{N}}{\mathrm{A}^2}}{4\pi \cdot (4 \cdot 10^{-10}\mathrm{m})^3} \cdot \left(3.96 \cdot 10^5\,\frac{\mathrm{A}}{\mathrm{m}} \cdot \frac{4}{3}\pi \cdot (36 \cdot 10^{-9}\mathrm{m})^3\right)^2 \cdot (3\cos^2(60°) - \cos(60°))$$

$$= -4{,}8 \cdot 10^{-12}\ \mathrm{J}$$

$$E_{mag,dipolar}(\mathrm{Ho^{3+}}) = -\frac{\mu_0}{4\pi r_{ij}^3} \cdot m_i m_j \left(3\left(\overrightarrow{m_i} \cdot \overrightarrow{r_{ij}}\right)\left(\overrightarrow{m_j} \cdot \overrightarrow{r_{ij}}\right) - \overrightarrow{m_i} \cdot \overrightarrow{m_j}\right)$$

$$= -\frac{4\pi \cdot 10^{-7}\,\frac{\mathrm{N}}{\mathrm{A}^2}}{4\pi \cdot (4 \cdot 10^{-10}\mathrm{m})^3} \cdot \left(10.6 \cdot 9.27 \cdot 10^{-24}\,\frac{\mathrm{J}}{\mathrm{T}}\right)^2 \cdot (3\cos^2(60°) - \cos(60°))$$

$$= -7.5 \cdot 10^{-24}\ \mathrm{J}$$

species	$E_{mag,dipolar}$ (J)	E_{therm} (J)	β (-)
IO-NP	$4.8 \cdot 10^{-12}$	$6.2 \cdot 10^{-21}$	$7.7 \cdot 10^{8}$
Ho^{3+} ion	$7.5 \cdot 10^{-24}$	$6.2 \cdot 10^{-21}$	$1.2 \cdot 10^{-3}$

1.6. References

1. Aida, T., Meijer, E. W. & Stupp, S. I. Functional Supramolecular Polymers. *Science* **335**, 813–817 (2012).
2. Aida, T. & Meijer, E. W. Supramolecular Polymers – We've Come Full Circle. *Isr. J. Chem.* **60**, 33–47 (2020).
3. Lehn, J.-M. Toward Self-Organization and Complex Matter. *Science* **295**, 2400–2403 (2002).
4. Insua, I. & Montenegro, J. Synthetic Supramolecular Systems in Life-like Materials and Protocell Models. *Chem* **6**, 1652–1682 (2020).
5. Lehn, J.-M., Truter, M. R., Simon, W., Morf, W. E., Meier, P. C., Izatt, R. M., Eatough, D. J. & Christensen, J. J. *Alkali Metal Complexes with Organic Ligands*. (Springer, 1973).
6. Cram, D. J., Kaneda, T., Lein, G. M. & Helgeson, R. C. A Spherand Containing an Enforced Cavity that Selectively Binds Lithium and Sodium Ions. *J. Chem. Soc. Chem. Commun.* 948–950 (1979).
7. MacNicol, D. D., McKendrick, J. J. & Wilson, D. R. Clathrates and Molecular Inclusion Phenomena. *Chem. Soc. Rev.* **7**, 65 (1978).
8. Dietrich, B. & Lehn, J. M. Complexes Macrobicycliques, Formation, Structure, Propriétés. *Tetrahedron* **29**, 1647–1658 (1973). French.
9. Pedersen, C. J. Cyclic Polyethers and their Complexes with Metal Salts. *J. Am. Chem. Soc.* **89**, 2495–2497 (1967).
10. Cram, D. J. & Cram, J. M. Host-Guest Chemistry. *Science* **183**, 803–809 (1974).
11. Stupp, S. I. Supramolecular Materials: Self-Organized Nanostructures. *Science* **276**, 384–389 (1997).
12. Gardner, G. B., Venkataraman, D., Moore, J. S. & Lee, S. Spontaneous Assembly of a Hinged Coordination Network. *Nature* **374**, 792–795 (1995).
13. Ulman, A. Formation and Structure of Self-Assembled Monolayers. *Chem. Rev.* **96**, 1533–1554 (1996).
14. De Greef, T. F. A. & Meijer, E. W. Supramolecular Polymers. *Nature* **453**, (2008).
15. Hartgerink, J. D., Beniash, E. & Stupp, S. I. Self-Assembly and Mineralization of Peptide-Amphiphile Nanofibers. *Science* **294**, 1684–1688 (2001).
16. Hardin, J., Bertoni, G. P. & Kleinsmith, L. J. *Becker's World of the Cell*. (Pearson, 2017).
17. Betts, J. G., Young, K. A., Wise, J. A., Johnson, E., Poe, B., Kruse, D. H., Korol, O., Johnson, J. E., Womble, M. & DeSaix, P. *Anatomy and Physiology*. (OpenStax, 2013).
18. Görl, D., Zhang, X. & Würthner, F. Molecular Assemblies of Perylene Bisimide Dyes in Water. *Angew. Chem. Int. Ed.* **51**, 6328–6348 (2012).
19. Jelley, E. E. Spectral Absorption and Fluorescence of Dyes in the Molecular State. *Nature* **138**, 1009–1010 (1936).
20. Würthner, F., Kaiser, T. E. & Saha-Möller, C. R. J-Aggregates: From Serendipitous Discovery to Supramolecular Engineering of Functional Dye Materials. *Angew. Chem. Int. Ed.* **50**, 3376–3410 (2011).
21. Zhai, D., Xu, W., Zhang, L. & Chang, Y.-T. The Role of "Disaggregation" in Optical Probe Development. *Chem. Soc. Rev.* **43**, 2402 (2014).
22. Cai, K., Xie, J., Zhang, D., Shi, W., Yan, Q. & Zhao, D. Concurrent Cooperative J-Aggregates and Anticooperative H-Aggregates. *J. Am. Chem. Soc.* **140**, 5764–5773 (2018).
23. Sorrenti, A., Leira-Iglesias, J., Markvoort, A. J., de Greef, T. F. A. & Hermans, T. M. Non-Equilibrium Supramolecular Polymerization. *Chem. Soc. Rev.* **46**, 5476–5490 (2017).
24. Formon, G. J. M. Towards better Control over Supramolecular Polymerization. (Université de Strasbourg, 2020).
25. De Greef, T. F. A., Smulders, M. M. J., Wolffs, M., Schenning, A. P. H. J., Sijbesma, R. P. & Meijer, E. W. Supramolecular Polymerization. *Chem. Rev.* **109**, 5687–5754 (2009).
26. Leung, F. K., Kajitani, T., Stuart, M. C. A., Fukushima, T. & Feringa, B. L. Dual-Controlled Macroscopic Motions in a Supramolecular Hierarchical Assembly of Motor Amphiphiles. *Angew. Chem. Int. Ed.* **58**, 10985–10989 (2019).
27. van Herrikhuyzen, J., Syamakumari, A., Schenning, A. P. H. J. & Meijer, E. W. Synthesis of n-Type Perylene Bisimide Derivatives and Their Orthogonal Self-Assembly with p-Type Oligo(*p*-phenylene vinylene)s. *J. Am. Chem. Soc.* **126**, 10021–10027 (2004).
28. Syamala, P. P. N., Soberats, B., Görl, D., Gekle, S. & Würthner, F. Thermodynamic Insights into the Entropically Driven Self-Assembly of Amphiphilic Dyes in Water. *Chem. Sci.* **10**, 9358–9366 (2019).
29. Venkata Rao, K., Miyajima, D., Nihonyanagi, A. & Aida, T. Thermally Bisignate Supramolecular Polymerization. *Nat. Chem.* **9**, 1133–1139 (2017).
30. Huang, Z., Lee, H., Lee, E., Kang, S.-K., Nam, J.-M. & Lee, M. Responsive Nematic Gels from the Self-Assembly of Aqueous Nanofibres. *Nat. Commun.* **2**, 459 (2011).

31. Zhang, H., Nguyen, K. T., Ma, X., Yan, H., Guo, J., Zhu, L. & Zhao, Y. Host–Guest Complexation Driven Dynamic Supramolecular Self-Assembly. *Org. Biomol. Chem.* **11**, 2070 (2013).
32. Su, H., Wang, F., Ran, W., Zhang, W., Dai, W., Wang, H., Anderson, C. F., Wang, Z., Zheng, C., Zhang, P., Li, Y. & Cui, H. The Role of Critical Micellization Concentration in Efficacy and Toxicity of Supramolecular Polymers. *Proc. Natl. Acad. Sci.* **117**, 4518–4526 (2020).
33. Korevaar, P. A., Schaefer, C., de Greef, T. F. A. & Meijer, E. W. Controlling Chemical Self-Assembly by Solvent-Dependent Dynamics. *J. Am. Chem. Soc.* **134**, 13482–13491 (2012).
34. Chivers, P. R. A. & Smith, D. K. Shaping and Structuring Supramolecular Gels. *Nat. Rev. Mater.* **4**, 463–478 (2019).
35. Ghosh, G. & Ghosh, S. Solvent Dependent Pathway Complexity and Seeded Supramolecular Polymerization. *Chem. Commun.* **54**, 5720–5723 (2018).
36. Kulkarni, C., Korevaar, P. A., Bejagam, K. K., Palmans, A. R. A., Meijer, E. W. & George, S. J. Solvent Clathrate Driven Dynamic Stereomutation of a Supramolecular Polymer with Molecular Pockets. *J. Am. Chem. Soc.* **139**, 13867–13875 (2017).
37. Nagata, Y., Nishikawa, T. & Suginome, M. Poly(quinoxaline-2,3-diyl)s Bearing (*S*)-3-Octyloxymethyl Side Chains as an Efficient Amplifier of Alkane Solvent Effect Leading to Switch of Main-Chain Helical Chirality. *J. Am. Chem. Soc.* **136**, 15901–15904 (2014).
38. Besenius, P., Portale, G., Bomans, P. H. H., Janssen, H. M., Palmans, A. R. A. & Meijer, E. W. Controlling the Growth and Shape of Chiral Supramolecular Polymers in Water. *Proc. Natl. Acad. Sci.* **107**, 17888–17893 (2010).
39. Shin, S., Lim, S., Kim, Y., Kim, T., Choi, T.-L. & Lee, M. Supramolecular Switching between Flat Sheets and Helical Tubules Triggered by Coordination Interaction. *J. Am. Chem. Soc.* **135**, 2156–2159 (2013).
40. Frisch, H., Nie, Y., Raunser, S. & Besenius, P. pH-Regulated Selectivity in Supramolecular Polymerizations: Switching between Co- and Homopolymers. *Chem. – Eur. J.* **21**, 3304–3309 (2015).
41. Lin, B. F., Megley, K. A., Viswanathan, N., Krogstad, D. V., Drews, L. B., Kade, M. J., Qian, Y. & Tirrell, M. V. pH-Responsive Branched Peptide Amphiphile Hydrogel Designed for Applications in Regenerative Medicine with Potential as Injectable Tissue Scaffolds. *J. Mater. Chem.* **22**, 19447 (2012).
42. Ohta, E., Sato, H., Ando, S., Kosaka, A., Fukushima, T., Hashizume, D., Yamasaki, M., Hasegawa, K., Muraoka, A., Ushiyama, H., Yamashita, K. & Aida, T. Redox-Responsive Molecular Helices with Highly Condensed π-Clouds. *Nat. Chem.* **68–73**, 6 (2011).
43. Leira-Iglesias, J., Sorrenti, A., Sato, A., Dunne, P. A. & Hermans, T. M. Supramolecular Pathway Selection of Perylenediimides Mediated by Chemical Fuels. *Chem. Commun.* **52**, 9009–9012 (2016).
44. Leira-Iglesias, J., Tassoni, A., Adachi, T., Stich, M. & Hermans, T. M. Oscillations, Travelling Fronts and Patterns in a Supramolecular System. *Nat. Nanotechnol.* **13**, 1021–1027 (2018).
45. Singh, N., Lainer, B., Formon, G. J. M., De Piccoli, S. & Hermans, T. M. Re-Programming Hydrogel Properties Using a Fuel-Driven Reaction Cycle. *J. Am. Chem. Soc.* **142**, 4083–4087 (2020).
46. Sorrenti, A., Leira-Iglesias, J., Sato, A. & Hermans, T. M. Non-Equilibrium Steady States in Supramolecular Polymerization. *Nat. Commun.* **8**, 15899–15907 (2017).
47. Webber, M. J., Newcomb, C. J., Bitton, R. & Stupp, S. I. Switching of Self-Assembly in a Peptide Nanostructure with a Specific Enzyme. *Soft Matter* **7**, 9665–9672 (2011).
48. Hirst, A. R., Roy, S., Arora, M., Das, A. K., Hodson, N., Murray, P., Marshall, S., Javid, N., Sefcik, J., Boekhoven, J., van Esch, J., Santabarbara, S., Hunt, N. T. & Ulijn, R. V. Biocatalytic Induction of Supramolecular Order. *Nat. Chem.* **2**, 1089–1094 (2010).
49. Yagai, S. & Kitamura, A. Recent Advances in Photoresponsive Supramolecular Self-Assemblies. *Chem. Soc. Rev.* **37**, 1520 (2008).
50. Li, L., Jiang, H., Messmore, B. W., Bull, S. R. & Stupp, S. I. A Torsional Strain Mechanism To Tune Pitch in Supramolecular Helices. *Angew. Chem. Int. Ed.* **119**, 5977–5980 (2007).
51. Adhikari, B., Yamada, Y., Yamauchi, M., Wakita, K., Lin, X., Aratsu, K., Ohba, T., Karatsu, T., Hollamby, M. J., Shimizu, N., Takagi, H., Haruki, R., Adachi, S. & Yagai, S. Light-Induced Unfolding and Refolding of Supramolecular Polymer Nanofibres. *Nat. Commun.* **8**, 15254 (2017).
52. van Herpt, J. T., Stuart, M. C. A., Browne, W. R. & Feringa, B. L. Mechanically Induced Gel Formation. *Langmuir* **29**, 8763–8767 (2013).
53. Carnall, J. M. A., Waudby, C. A., Belenguer, A. M. & Stuart, M. C. A. Mechanosensitive Self-Replication Driven by Self-Organization. *Science* **327**, 1502–1506 (2010).
54. Ciferri, A. *Supramolecular Polymers*. (Taylor & Francis, 2005).
55. Guarnieri, M. Once Upon a Time... The Compass [Historical]. *IEEE Ind. Electron. Mag.* **8**, 60–63 (2014).

56. Maniam, S. Magnetic Resonance Imaging: Review of Imaging Techniques and Overview of Liver Imaging. *World J. Radiol.* **2**, 309 (2010).
57. Bira, N., Dhagat, P. & Davidson, J. R. A Review of Magnetic Elastomers and Their Role in Soft Robotics. *Front. Robot. AI* **7**, 588391 (2020).
58. Coufal, H., Dhar, L. & Mee, C. D. Materials for Magnetic Data Storage: The Ongoing Quest for Superior Magnetic Materials. *MRS Bull.* **31**, 374–378 (2006).
59. Yakout, S. M. Spintronics: Future Technology for New Data Storage and Communication Devices. *J. Supercond. Nov. Magn.* **33**, 2557–2580 (2020).
60. Sethulakshmi, N., Mishra, A., Ajayan, P. M., Kawazoe, Y., Roy, A. K., Singh, A. K. & Tiwary, C. S. Magnetism in Two-Dimensional Materials Beyond Graphene. *Mater. Today* **27**, 107–122 (2019).
61. Kharzeev, D., Landsteiner, K., Schmitt, A. & Yee, H.-U. *Strongly Interacting Matter in Magnetic Fields*. (Springer Berlin Heidelberg, 2013).
62. Coey, J. M. D. *Magnetism and Magnetic Materials*. (Cambridge University Press, 2010).
63. Gutfleisch, O., Willard, M. A., Brück, E., Chen, C. H., Sankar, S. G. & Liu, J. P. Magnetic Materials and Devices for the 21st Century: Stronger, Lighter, and More Energy Efficient. *Adv. Mater.* **23**, 821–842 (2011).
64. Coey, J. M. D. Magnetism in Future. *J. Magn. Magn. Mater.* **226–230**, 2107–2112 (2001).
65. Nisticò, R. Magnetic Materials and Water Treatments for a Sustainable Future. *Res. Chem. Intermed.* **43**, 6911–6949 (2017).
66. Johnsen, S. & Lohmann, K. J. The Physics and Neurobiology of Magnetoreception. *Nat. Rev. Neurosci.* **6**, 703–712 (2005).
67. Tian, L.-X., Pan, Y.-X., Metzner, W., Zhang, J.-S. & Zhang, B.-F. Bats Respond to Very Weak Magnetic Fields. *PLoS One* **10**, e0123205 (2015).
68. Merzdorf, J. NASA Researchers Treck Slowly Splitting 'Dent' in Earth's Magnetic Field. (2020).
69. *Chinese mariner's compass*. (mid 1800s).
70. Edlow, B. L., Mareyam, A., Horn, A., Polimeni, J. R., Witzel, T., Tisdall, M. D., Augustinack, J. C., Stockmann, J. P., Diamond, B. R., Stevens, A., Tirrell, L. S., Folkerth, R. D., Wald, L. L., Fischl, B. & van der Kouwe, A. 7 Tesla MRI of the Ex Vivo Human Brain at 100 Micron Resolution. *Sci. Data* **6**, 244 (2019).
71. Rikken, R. S. M., Nolte, R. J. M., Maan, J. C., van Hest, J. C. M., Wilson, D. A. & Christianen, P. C. M. Manipulation of Micro- and Nanostructure Motion with Magnetic Fields. *Soft Matter* **10**, 1295–1308 (2014).
72. Wiegers, S. A. J., Rook, J., den Ouden, A., Perenboom, J. A. A. J. & Maan, J. C. Design and Construction of a 38 T Resistive Magnet at the Nijmegen High Field Magnet Laboratory. *IEEE Trans. Appl. Supercond.* **22**, 4301504–4301504 (2012).
73. Sims, J., Baca, A., Boebinger, G., Boenig, H., Coe, H., Kihara, K., Manzo, M., Mielke, C., Schillig, J., Eyssa, Y., Lesch, B., Li, L. & Scneider-Muntau, H. First 100 T Non-Destructive Magnet. *IEEE Trans. Appiled Supercond.* **10**, 510–513 (2000).
74. Halbach, K. Design of Permanent Multipole Magnets with Oriented Rare Earth Cobalt Material. *Nucl. Instrum. Methods* **169**, 1–10 (1980).
75. Mallinson, J. One-Sided Fluxes - A Magnetic Curiosity? *IEEE Trans. Magn.* **9**, 678–682 (1973).
76. Nowogrodzki, A. The Strongest Scanners. *Nature* **563**, 24–26 (2018).
77. Bruker. NMR Frequency Tables. (2012).
78. High Field Magnet Laboratory (HFML), Radboud University Nijmegen. https://www.ru.nl/hfml/ (2021).
79. Service, R. F. Los Alamos Magnet Leads the Field. *Science* **5381**, 1262–1264 (1998).
80. Sims, J. R., Rickel, D. G., Swenson, C. A., Schillig, J. B., Ellis, G. W. & Ammerman, C. N. Assembly, Commissioning and Operation of the NHMFL 100 Tesla Multi-Pulse Magnet System. *IEEE Trans. Appl. Supercond.* **18**, 587–591 (2008).
81. Los Alamos National Laboratory. https://lanl.gov/ (2021).
82. Benenson, W., Harris, J. W., Stöcker, H. & Lutz, H. *Handbook of Physics*. (Springer, 2006).
83. Jeong, U., Teng, X., Wang, Y., Yang, H. & Xia, Y. Superparamagnetic Colloids: Controlled Synthesis and Niche Applications. *Adv. Mater.* **19**, 33–60 (2007).
84. Tarling, D. & Hrouda, F. *Magnetic Anisotropy of Rocks*. (Springer Science & Business Media, 1993).
85. O'Handley, R. C. *Modern Magnetic Materials Principles and Applications*. (Wiley, 1999).
86. Murugesu, M. The Orientation is in the Details. *Nat. Chem.* **4**, 347–348 (2012).
87. Pimentel, Georges C, S., Richard D. *Understanding Chemistry*. (Holden-Day, 1971).
88. Sastri, V. S., Bünzli, J.-C., Ramachandra Rao, V., Rayudu, G. V. S. & Perumareddi, J. R. *Modern Aspects of Rare Earths and their Complexes*. (Elsevier B.V., 2003).
89. Xiao, Y.-D., Paudel, R., Liu, J., Ma, C., Zhang, Z.-S. & Zhou, S.-K. MRI Contrast Agents: Classification and Application (Review). *Int J Mol Med* **38**, 1319–1326 (2016).

90. Information on Gadolinium-Based Contrast Agents. https://www.fda.gov/drugs/postmarket-drug-safety-information-patients-and-providers/information-gadolinium-based-contrast-agents (2020).
91. Peters, J. A., Djanashvili, K., Geraldes, C. F. G. C. & Platas-Iglesias, C. The Chemical Consequences of the Gradual Decrease of the Ionic Radius along the Ln-Series. *Coord. Chem. Rev.* **406**, 213146 (2020).
92. King, R. B., Crabtree, R. H., Lukehart, C. M., Atwood, D. A. & Scott, R. A. *Encyclopedia of Inorganic Chemistry*. (John Wiley & Sons, Ltd, 2006).
93. Byegård, J., Skarnemark, G. & Skålberg, M. The Stability of Some Metal EDTA, DTPA and DOTA Complexes: Application as Tracers in Groundwater Studies. *J. Radioanal. Nucl. Chem.* **241**, 281–290 (1999).
94. Woodru, D. N. Lanthanide Single-Molecule Magnets. *Chem Rev* 39 (2013).
95. Beck, P., Liebi, M., Kohlbrecher, J., Ishikawa, T., Rüegger, H., Zepik, H., Fischer, P., Walde, P. & Windhab, E. Magnetic Field Alignable Domains in Phospholipid Vesicle Membranes Containing Lanthanides. *J. Phys. Chem. B* **114**, 174–186 (2010).
96. Jiang, S.-D. & Qin, S.-X. Prediction of the Quantized Axis of Rare-Earth Ions: The Electrostatic Model with Displaced Point Charges. *Inorg. Chem. Front.* **2**, 613–619 (2015).
97. de Boer, M. A. & Lammertsma, K. Scarcity of Rare Earth Elements. *ChemSusChem* **6**, 2045–2055 (2013).
98. Pulidindi, K. & Pandey, H. *Rare Earth Metals Market Size By Metal (Cerium, Dysprosium, Erbium, Europium, Gadolinium, Holmium, Lanthanum, Lutetium, Neodymium, Praseodymium, Promethium, Samarium, Scandium, Terbium, Thulium, Ytterbium, Yttrium), By Applications (Magnets, Colorants, Alloys, Optical Instruments, Catalysts), Industry Analysis Report, Regional Outlook, Growth Potential, Price Trends, Competitive Market Share & Forecast, 2017 – 2024*. https://www.gminsights.com/industry-analysis/rare-earth-metals-market (2017).
99. Lim, J., Lanni, C., Evarts, E. R., Lanni, F., Tilton, R. D. & Majetich, S. A. Magnetophoresis of Nanoparticles. *ACS Nano* **5**, 217–226 (2011).
100. Tschulik, K., Cierpka, C., Gebert, A., Schultz, L., Kähler, C. J. & Uhlemann, M. In Situ Analysis of Three-Dimensional Electrolyte Convection Evolving during the Electrodeposition of Copper in Magnetic Gradient Fields. *Anal. Chem.* **83**, 3275–3281 (2011).
101. Elfimova, E. A., Ivanov, A. O. & Camp, P. J. Static Magnetization of Immobilized, Weakly Interacting, Superparamagnetic Nanoparticles. *Nanoscale* **11**, 21834–21846 (2019).
102. Tjandra, N. Direct Measurement of Distances and Angles in Biomolecules by NMR in a Dilute Liquid Crystalline Medium. *Science* **278**, 1111–1114 (1997).
103. Odenbach, S. *Ferrofluids: Magnetically Controllable Fluids and Their Applications*. (Springer, 2002).
104. Shklyarevskiy, I. O., Jonkheijm, P., Christianen, P. C. M., Schenning, A. P. H. J., Meijer, E. W., Henze, O., Kilbinger, A. F. M., Feast, W. J., Del Guerzo, A., Desvergne, J.-P. & Maan, J. C. Magnetic Deformation of Self-Assembled Sexithiophene Spherical Nanocapsules. *J. Am. Chem. Soc.* **127**, 1112–1113 (2005).
105. Layfield, R. A. & Murugesu, M. *Lanthanides and Actinides in Molecular Magnetism*. (Wiley, 2015).
106. Berg-Sørensen, K. & Flyvbjerg, H. The Colour of Thermal Noise in Classical Brownian Motion: A Feasibility Study of Direct Experimental Observation. *New J. Phys.* **7**, 1–10 (2005).
107. Yamato, M. & Kimura, T. Magnetic Processing of Diamagnetic Materials. *Polymers* **12**, 1491 (2020).
108. A. Hill, R. J., Sedman, V. L., Allen, S., Williams, P., Paoli, M., Adler-Abramovich, L., Gazit, E., Eaves, L. & Tendler, S. J. B. Alignment of Aromatic Peptide Tubes in Strong Magnetic Fields. *Adv. Mater.* **19**, 4474–4479 (2007).
109. Wallace, M., Cardoso, A. Z., Frith, W. J., Iggo, J. A. & Adams, D. J. Magnetically Aligned Supramolecular Hydrogels. *Chem. - Eur. J.* **20**, 16484–16487 (2014).
110. Speyer, J. B., Sripada, P. K., Das Gupta, S. K., Shipley, G. G. & Griffin, R. G. Magnetic Orientation of Sphingomyelin-Lecithin Bilayers. *Biophys. J.* **51**, 687–691 (1987).
111. Qiu, X., Mirau, P. A. & Pidgeon, C. Magnetically Induced Orientation of Phosphatidylcholine Membranes. *Biochim. Biophys. Acta BBA - Biomembr.* **1147**, 59–72 (1993).
112. Tu, T., Sakurai, T., Seki, S., Ishida, Y. & Chan, Y. Towards Macroscopically Anisotropic Functionality: Oriented Metallo-supramolecular Polymeric Materials Induced by Magnetic Fields. *Angew. Chem. Int. Ed.* **133**, 1951–1956 (2021).
113. Gopinadhan, M., Choo, Y., Kawabata, K., Kaufman, G., Feng, X., Di, X., Rokhlenko, Y., Mahajan, L. H., Ndaya, D., Kasi, R. M. & Osuji, C. O. Controlling Orientational Order in Block Copolymers Using Low-Intensity Magnetic Fields. *Proc. Natl. Acad. Sci.* **114**, E9437–E9444 (2017).
114. Radvar, E., Shi, Y., Grasso, S., Edwards-Gayle, C. J. C., Liu, X., Mauter, M. S., Castelletto, V., Hamley, I. W., Reece, M. J. & S. Azevedo, H. Magnetic Field-Induced Alignment of Nanofibrous Supramolecular Membranes: A Molecular Design Approach to Create Tissue-like Biomaterials. *ACS Appl. Mater. Interfaces* **12**, 22661–22672 (2020).

115. Yoon, D. K., Lee, S. R., Kim, Y. H., Choi, S.-M. & Jung, H.-T. Large-Area, Highly Aligned Cylindrical Perfluorinated Supramolecular Dendrimers Using Magnetic Fields. *Adv. Mater.* **18**, 509–513 (2006).
116. Draper, E. R., Wallace, M., Honecker, D. & Adams, D. J. Aligning Self-Assembled Perylene Bisimides in a Magnetic Field. *Chem. Commun.* **54**, 10977–10980 (2018).
117. Polarz, S., Bährle, C., Landsmann, S. & Klaiber, A. Panoscopic Structures by Hierarchical Cascade Self-Assembly of Inorganic Surfactants with Magnetic Heads Containing Dysprosium Ions. *Angew. Chem. Int. Ed.* **52**, 13665–13670 (2013).
118. Yue, B., Jin, X., Zhao, P., Zhu, M. & Zhu, L. Directed Self-Assembly of Templatable Block Copolymers by Easily Accessible Magnetic Control. *Small* **15**, 1804572 (2019).
119. Cao, B., Zhu, Y., Wang, L. & Mao, C. Controlled Alignment of Filamentous Supramolecular Assemblies of Biomolecules into Centimeter-Scale Highly Ordered Patterns by Using Nature-Inspired Magnetic Guidance. *Angew. Chem. Int. Ed.* **52**, 11750–11754 (2013).
120. Tolman, J. R., Flanagan, J. M., Kennedy, M. A. & Prestegard, J. H. Nuclear Magnetic Dipole Interactions in Field-Oriented Proteins: Information for Structure Determination in Solution. *Proc. Natl. Acad. Sci.* **92**, 9279–9283 (1995).
121. Rodriguez-Castañeda, F., Haberz, P., Leonov, A. & Griesinger, C. Paramagnetic Tagging of Diamagnetic Proteins for Solution NMR. *Magn. Reson. Chem.* **44**, S10–S16 (2006).
122. Zhuang, T., Lee, H.-S., Imperiali, B. & Prestegard, J. H. Structure Determination of a Galectin-3-Carbohydrate Complex Using Paramagnetism-Based NMR Constraints. *Protein Sci.* **17**, 1220–1231 (2008).
123. Car, P.-E., Perfetti, M., Mannini, M., Favre, A., Caneschi, A. & Sessoli, R. Giant Field Dependence of the Low Temperature Relaxation of the Magnetization in a Dysprosium(iii)–DOTA Complex. *Chem. Commun.* **47**, 3751 (2011).
124. Christou, G., Gatteschi, D., Hendrickson, D. N. & Sessoli, R. Single-Molecule Magnets. *MRS Bull.* **25**, 66–71 (2000).
125. Prosser, R. S., Hunt, S. A., DiNatale, J. A. & Vold, R. R. Magnetically Aligned Membrane Model Systems with Positive Order Parameter: Switching the Sign of S_{zz} with Paramagnetic Ions. *J. Am. Chem. Soc.* **118**, 269–270 (1996).
126. Prosser, R. S., Hwang, J. S. & Vold, R. R. Magnetically Aligned Phospholipid Bilayers with Positive Ordering: A New Model Membrane System. *Biophys. J.* **74**, 2405–2418 (1998).
127. Welton, T. Room-Temperature Ionic Liquids. Solvents for Synthesis and Catalysis. *Chem. Rev.* **99**, 2071–2084 (1999).
128. Brown, P., Alan Hatton, T. & Eastoe, J. Magnetic Surfactants. *Curr. Opin. Colloid Interface Sci.* **20**, 140–150 (2015).
129. Hayashi, S. & Hamaguchi, H. Discovery of a Magnetic Ionic Liquid [bmim]FeCl4-. *Chem. Lett.* **33**, 1590–1591 (2004).
130. Del Sesto, R. E., McCleskey, T. M., Burrell, A. K., Baker, G. A., Thompson, J. D., Scott, B. L., Wilkes, J. S. & Williams, P. Structure and Magnetic Behavior of Transition Metal Based Ionic Liquids. *Chem. Commun.* 447–449 (2008).
131. Brown, P., Khan, A. M., Armstrong, J. P. K., Perriman, A. W., Butts, C. P. & Eastoe, J. Magnetizing DNA and Proteins Using Responsive Surfactants. *Adv. Mater.* **24**, 6244–6247 (2012).
132. Krieger, B. M., Lee, H. Y., Emge, T. J., Wishart, J. F. & Castner, Jr., E. W. Ionic Liquids and Solids with Paramagnetic Anions. *Phys. Chem. Chem. Phys.* **12**, 8919 (2010).
133. Brown, P., Bushmelev, A., Butts, C. P., Cheng, J., Eastoe, J., Grillo, I., Heenan, R. K. & Schmidt, A. M. Magnetic Control over Liquid Surface Properties with Responsive Surfactants. *Angew. Chem. Int. Ed.* **51**, 2414–2416 (2012).
134. Klee, A., Prevost, S., Kunz, W., Schweins, R., Kiefer, K. & Gradzielski, M. Magnetic Microemulsions Based on Magnetic Ionic Liquids. *Phys. Chem. Chem. Phys.* **14**, 15355 (2012).
135. Brown, P., Butts, C. P., Cheng, J., Eastoe, J., Russell, C. A. & Smith, G. N. Magnetic Emulsions with Responsive Surfactants. *Soft Matter* **8**, 7545 (2012).
136. McCoy, T. M., Brown, P., Eastoe, J. & Tabor, R. F. Noncovalent Magnetic Control and Reversible Recovery of Graphene Oxide Using Iron Oxide and Magnetic Surfactants. *ACS Appl. Mater. Interfaces* **7**, 2124–2133 (2015).
137. Sim, W., Oh, J. & Choi, B. Fabrication, Experiment of a Microactuator Using Magnetic Fluid for Micropump Application. *Microsyst. Technol.* **12**, 1085–1091 (2006).
138. Torres-Díaz, I. & Rinaldi, C. Recent Progress in Ferrofluids Research: Novel Applications of Magnetically Controllable and Tunable Fluids. *Soft Matter* **10**, 8584–8602 (2014).

139. Mertelj, A., Lisjak, D., Drofenik, M. & Čopič, M. Ferromagnetism in Suspensions of Magnetic Platelets in Liquid Crystal. *Nature* **504**, 237–241 (2013).
140. Clark, N. A. Ferromagnetic ferrofluids. *Nature* **504**, 229–230 (2013).
141. Maxwell, G. F. *Ferrofluid Magnet under glass*. (2006).
142. Yavuz, C. T., Prakash, A., Mayo, J. T. & Colvin, V. L. Magnetic Separations: From Steel Plants to Biotechnology. *Chem. Eng. Sci.* **64**, 2510–2521 (2009).
143. Suwa, M. Magnetoanalysis of Micro/Nanoparticles: A review. *Anal. Chim. Acta* **690**, 137–147 (2011).
144. Dreyfus, R., Baudry, J., Roper, M. L., Fermigier, M., Stone, H. A. & Bibette, J. Microscopic Artificial Swimmers. *Nature* **437**, 862–865 (2005).
145. Li, T. L., Wang, Z., You, H., Ong, Q., Varanasi, V. J., Dong, M., Lu, B., Paşca, S. P. & Cui, B. Engineering a Genetically Encoded Magnetic Protein Crystal. *Nano Lett.* **19**, 6955–6963 (2019).
146. Gleich, B. & Weizenecker, J. Tomographic Imaging Using the Nonlinear Response of Magnetic Particles. *Nature* **435**, 1214–1217 (2005).
147. Mehdizadeh Taheri, S., Michaelis, M., Friedrich, T., Förster, B., Drechsler, M., Römer, F. M., Bösecke, P., Narayanan, T., Weber, B., Rehberg, I., Rosenfeldt, S. & Förster, S. Self-Assembly of Smallest Magnetic Particles. *Proc. Natl. Acad. Sci.* **112**, 14484–14489 (2015).
148. Luis, F., Petroff, F., Torres, J. M., García, L. M., Bartolomé, J., Carrey, J. & Vaurès, A. Magnetic Relaxation of Interacting Co Clusters: Crossover from Two- to Three-Dimensional Lattices. *Phys. Rev. Lett.* **88**, 217205 (2002).
149. Bae, C. J., Angappane, S., Park, J.-G., Lee, Y., Lee, J., An, K. & Hyeon, T. Experimental Studies of Strong Dipolar Interparticle Interaction in Monodisperse Fe3O4 Nanoparticles. *Appl. Phys. Lett.* **91**, 102502 (2007).
150. Singh, G., Chan, H., Baskin, A., Gelman, E., Repnin, N., Kral, P. & Klajn, R. Self-Assembly of Magnetite Nanocubes into Helical Superstructures. *Science* **345**, 1149–1153 (2014).
151. Santos, P. J. & Macfarlane, R. J. Reinforcing Supramolecular Bonding with Magnetic Dipole Interactions to Assemble Dynamic Nanoparticle Superlattices. *J. Am. Chem. Soc.* **142**, 1170–1174 (2020).
152. Micali, N., Engelkamp, H., van Rhee, P. G., Christianen, P. C. M., Scolaro, L. M. & Maan, J. C. Selection of Supramolecular Chirality by Application of Rotational and Magnetic Forces. *Nat. Chem.* **4**, 201–207 (2012).
153. Fujiwara, M., Chie, K., Sawai, J., Shimizu, D. & Tanimoto, Y. On the Movement of Paramagnetic Ions in an Inhomogeneous Magnetic Field. *J. Phys. Chem. B* **108**, 3531–3534 (2004).
154. Fujiwara, M., Kodoi, D., Duan, W. & Tanimoto, Y. Separation of Transition Metal Ions in an Inhomogeneous Magnetic Field. *J. Phys. Chem. B* **105**, 3343–3345 (2001).
155. Yang, X., Tschulik, K., Uhlemann, M., Odenbach, S. & Eckert, K. Enrichment of Paramagnetic Ions from Homogeneous Solutions in Inhomogeneous Magnetic Fields. *J. Phys. Chem. Lett.* **3**, 3559–3564 (2012).
156. Pulko, B., Yang, X., Lei, Z., Odenbach, S. & Eckert, K. Magnetic Separation of Dy(III) Ions from Homogeneous Aqueous Solutions. *Appl. Phys. Lett.* **105**, 232407 (2014).
157. Franczak, A., Binnemans, K. & Jan Fransaer, J. F. Magnetomigration of Rare-Earth Ions in Inhomogeneous Magnetic Fields. *Phys. Chem. Chem. Phys.* **18**, 27342–27350 (2016).
158. Yu. Gorobets, O., Yu. I. Gorobets, Rospotniuk, V. P., Kyba, A. A., & Yu. A. Legenkiy. Liquid-Liquid Phase Separation Occurring under the Influence of Inhomogeneous Magnetic Field in the Process of the Metal Deposition and Etching of the Magnetized Ferromagnetic Ball. *J. Solid State Electrochem.* **19**, 3001–3012 (2015).
159. Coey, J. M. D., Rhen, F. M. F., Dunne, P. & McMurry, S. The Magnetic Concentration Gradient Force—Is It Real? *J. Solid State Electrochem.* **11**, 711–717 (2007).
160. Butcher, T. A., Formon, G. J. M., Dunne, P., Hermans, T. M., Ott, F., Noirez, L. & Coey, J. M. D. Neutron Imaging of Liquid-Liquid Systems Containing Paramagnetic Salt Solutions. *Appl. Phys. Lett.* **116**, 022405 (2020).
161. Schefer, L., Bulant, A., Zeder, C., Saha, A. & Mezzenga, R. Magnetic Control of Macromolecular Conformations in Supramolecular Anionic Polysaccharide–Iron Complexes. *Angew. Chem. Int. Ed.* **127**, 13487–13490 (2015).
162. Kittel, C. *Introduction to Solid State Physics*. (Wiley, 2004).
163. Shannon, R. D. Revised Effective Ionic Radii and Systematic Studies of Interatomic Distances in Halides and Chaleogenides. *Acta Cryst* **A32**, 751–767 (1976).
164. Atkins, P. W. & De Paula, J. *Atkins' Physical Chemistry*. (Oxford University Press, 2014).

THIS PAGE IS INTENTIONALLY LEFT BLANK

Chapter 2. Thermodynamics of the supramolecular assembly of lanthanide containing NDI derivatives

Abstract

In this chapter we show the preparation, characterization, and thermodynamic self-assembly studies of a family of naphthalene diimide derivatives incorporating various paramagnetic and diamagnetic lanthanide ions. The supramolecular polymerization is analyzed quantitatively by UV-Vis spectroscopy and the experimental data is interpreted by fitting isodesmic models. The developed synthetic methodology allows for a reliable preparation and characterization of this new class of magnetic coordination complexes. The Gibbs free energy of supramolecular polymerization in water was determined with high precision using a combination of temperature- and concentration dependent studies. Whereas the Gibbs free energy of all monomers is identical irrespective of the chelated ion, the enthalpy/entropy balance shifts significantly as a function of the magnetic moment of the ion. The enthalpic contribution is up to 60 % greater for the paramagnetic ions as compared to the diamagnetic controls. This surprising finding helps to narrow down the origin of several non-trivial observations in the supramolecular assembly of magnetic monomers.

Parts of this chapter contribute to a manuscript in preparation:

Schicho, Michaela K.; Formon, Georges J.M., Hermans, Thomas M. “Assembly and magnetophoresis of lanthanide-containing naphthalene diimide derivatives” *Manuscript in preparation*

2.1. Introduction

Magnetic materials are essential for a wide range of present and future technologies, such as modern medical imaging[1,2], robotics[3,4], data storage[5], spintronics[6], engineering[7,8], and catalysis[9], to name only a few.[10–12] The vast majority of magnetically ordered materials involve 3*d* of 4*f* elements, where the large magneto-crystalline anisotropy, mainly from lanthanides, is exploited. This anisotropy of the electron density distribution arises from their unpaired 4*f* electrons, which are well screened from their direct environment by the filled 5*s* and 5*p* shell. The shielding leads to a typically weak interaction of the *f* electrons with ligands, while they are contributing significantly to the magnetic properties of the material.[13]

For the crystal state, it has been shown diligently that the anisotropy of the magnetic ions is decisive for the magnetic properties of lanthanide-based complexes. More precisely, Sessoli and coworkers have reported that the isostructural sodium salts of Dy-DOTA and Gd-DOTA vary drastically in their magnetic properties, even though their magnetic moments are in the same order of magnitude (11 and 8 μ_B, respectively[10]). The crystal containing anisotropic Dy^{3+} behaves as a single molecule magnet (SMM), yet the analogous containing isotropic Gd^{3+} does not. SMMs refer to species, which, below a certain blocking temperature, retain their magnetization after they have been magnetized by an external field.[13,14]

In 2013, Polarz and coworkers have shown a remarkable multi-step self-assembly of a Dy^{3+} containing surfactant to mm-sized dumbbells-shaped structures.[15] When using the diamagnetic Lu^{3+} instead of Dy^{3+}, structures of similar size or complexity were not observed. The presumably magnetically driven phenomenon cannot be explained by simple paramagnetism and remains poorly understood. The forced spatial proximity of Dy^{3+} head groups, induced by the self-assembly of the surfactants, may lead to intermetallic crystal field interactions.

Meijer and coworkers have investigated Gd^{3+}-containing dendrimers of different generations as MRI contrast agents.[16] For their largest dendrimer (5^{th} generation), they find unproportionally large ionic relaxivities. Without going into further detail, they hypothesize paramagnetic interactions between the ions in the periphery may lead to this observation.

Inspired by these findings, we aim to get an insight on the influence the incorporation of paramagnetic ions has on supramolecular assemblies in a more general context.

Therefore, we designed a novel, simplified system of symmetric naphthalene diimide (NDI)-based paramagnetic monomers, which aggregate to one-dimensional supramolecular polymers through an isodesmic polymerization mechanism. We quantify the thermodynamics of the self-assembly process over a scope of eight para- and diamagnetic lanthanide ions.

2.2. Molecular design

The molecular design of the monomer **M-NDI** (Figure 2.1b) was selected with the aim to reduce the complexity in the paramagnetic surfactant assembly reported by Polarz and coworkers[15]. To this end, naphthalenediimide (NDI) was chosen as the central and assembly driving unit. NDI derivatives are typically weak assemblers, with enthalpies of supramolecular polymerization ΔH of around –20 kJ/mol[16], as compared to derivatives of other classic, and well-studied molecules such as perylene diimide[17] (PDI, $\Delta H \approx$ –70 kJ/mol[18]), benzene-1,3,5-tricarboxamide[19] (BTA, $\Delta H \approx$ –70 kJ/mol[20]), porphyrin[23] ($\Delta H \approx$ –60 kJ/mol[24]), or hexabenzocoronene[21] (HBC, $\Delta H \approx$ –200 kJ/mol[22], all values roughly approximated).[25] This is to ensure that possible magnetic effects are not outcompeted by an overly dominant self-organization process. In order to enable the incorporation of paramagnetic lanthanide ions into NDIs, and thereby equip them with a permanent magnetic moment, 1,4,7,10-tetraazacyclododecane-1,4,7,10-tetraacetic acid (DOTA) units were introduced at both extremities. The octadentate, macrocyclic DOTA is known to form stable complexes with various lanthanide ions[12,26] in a capped square antiprismatic coordination geometry (coordination number 9). Thereby, a non-innocent water molecule completes the primary coordination sphere in the ninth coordination site.[27,28] The central NDI core and the DOTA chelators are connected via an aliphatic C_4 spacing unit, completing the organic skeleton **NDI**. The ligand **NDI** is then used to complex trivalent paramagnetic ions $\mathbf{M}^{3+}$ (**M** = Gd, Tb, Dy, Ho, Er) to form the desired paramagnetic building block **M-NDI** (Figure 2.1b). The five ions are chosen due to their elevated magnetic moments (8–11 μ_B), and their different electron density distributions (isotropic, oblate or prolate, Figure 2.1c).[10] The latter has been shown to be decisive for the magnetic properties in crystal state.[30]

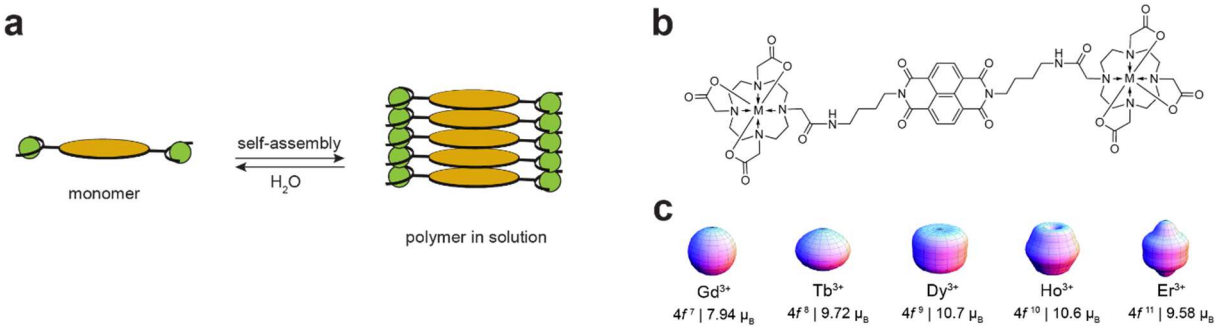

Figure 2.1 | Molecular design of paramagnetic monomers. (a) Scheme depicting self-assembly process of the magnetic building blocks to supramolecular polymers. (b) Molecular structure of the generalized monomeric building block **M-NDI** (M = Y, La, Gd, Tb, Dy, Er, Ho, Lu). (c) Simulated electron density distributions[31], electron configurations, and magnetic moments[10] μ of the magnetic ions $\mathbf{M}^{3+}$ for **M** = Tb, Dy, Gd, Ho and Er. μ is given in $\mu_B = 9.274 \cdot 10^{-24}$ Am². Diamagnetic control ions (not depicted, **M** = Y, La, Lu) exhibit isotropic electron density distribution, noble gas configuration and $\mu = 0$. Panel c partly reproduced from reference [31] with permission from the Royal Society of Chemistry.

2.3. Synthesis and chemical characterization

The organic ligand **NDI** was prepared in four steps, using slightly modified literature procedures[32,33], in a divergent synthetic approach starting from the central NDI core unit (see section 2.9.2 for more details). The commercially available naphthalene tetracarboxylic acid dianhydride **1** was reacted with the singly Boc-protected diamino-*n*-butane in an imidization reaction catalyzed by triethylamine.[32] The thereby obtained **2** was deprotected in acidic conditions, yielding **3**, and then coupled to the three-fold *t*Bu-protected DOTA chelator via a standard amide coupling with HBTU as a coupling reagent, yielding the protected ligand **4**. The ligand **NDI** was obtained through acidic deprotection of the six carboxylic acid groups of **4**.

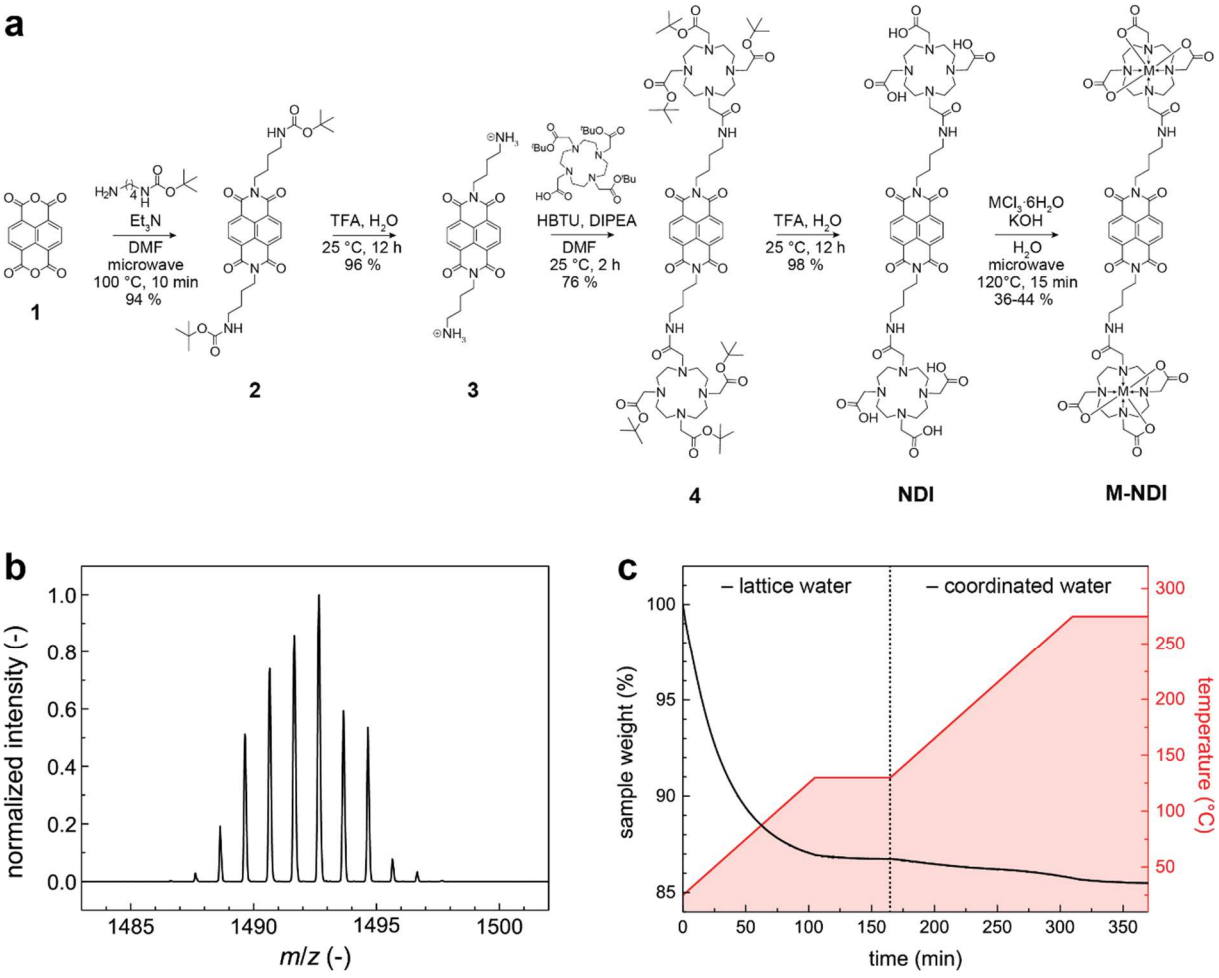

Figure 2.2 | Synthesis and characterization of magnetic monomers. (a) Reaction scheme of the five-step synthetic pathway to **M-NDI**. (b) Extract of the MALDI-TOF mass spectrum of **Gd-NDI**. (c) Normalized TGA curve of **Gd-NDI** and the corresponding temperature profile over time.

Unexpectedly, the coupling agent HBTU was incorporated in **4** after purification by column chromatography. The organic protons of the uronium moiety as well as the PF_6^- counterion are detected in ^{1}H and ^{19}F-NMR, respectively. Diffusion-ordered NMR (DOSY) confirmed that the coupling agent is incorporated in the ligand and not molecularly dissolved. This can be a consequence of co-assembly, electrostatic interactions, or coordination. Upon deprotection, HBTU could be removed. ^{19}F-NMR of the deprotected ligand **NDI** showed a residual trifluoro acetic acid (TFA) signal, which could finally be removed by size exclusion chromatography.

For practical reasons, this was typically done within the final purification of **M-NDI** in a later step.

After purification, the ligand structure of **NDI** was confirmed by HPLC-MS and NMR (see section 2.9.2 and 2.9.3). The DOTA group is known to adopt various conformations of the ethylenic bridges and the acid-holding side arms, which leads to a coexistence of several conformational isomers.[34] Therefore, the ^{1}H-NMR at 298 K shows a broad and indistinctive spectrum in the region of 1–5 ppm. To resolve this inconvenience, the temperature was increased to 343 K, and the concentration was kept at 1 mg·mL^{-1} to avoid assembly-induced signal broadening. Under these conditions, the ligand could be fully characterized (see section 2.9.3).

NDI was then reacted with eight different $\mathbf{M}^{III}Cl_3$ salts (**M** = Y, La, Dy, Tb, Gd, Er, Ho, Lu) under microwave irradiation[3] to obtain a library of five different paramagnetic monomers (**M** = Gd, Tb, Dy, Ho, Er) and three isostructural, diamagnetic analogues (**M** = Y, La, Lu) as control molecules. The characterization of these complexes turned out to be challenging, because their molecular design makes fundamental analytical techniques such as NMR and HPLC inadequate. A concurrence of their paramagnetic nature, their tendency to self-assemble in water—which leads to significant signal broadening as it can be observed for molecular polymers—and their poor solubility in organic solvents, does not allow reliable characterization by NMR spectroscopy. Moreover, the sensitivity of their self-assembly behavior to solvent changes, as well as their instability to TFA, which is present in most common mobile phases of HPLC systems, lead to uncertainty in HPLC analysis. As an alternative methodology, we had to rely on a combination of several other techniques complementing each other.

In an initial step, a successful coordination of the ligand **NDI** to Y^{3+} was indicated by infrared (IR) spectroscopy (see section 2.9.4, Figure 2.13). Upon complexation, the C=O stretch vibration shifted from 1661 cm^{-1} to 1596 cm^{-1}, and the signals of the C–O stretch vibration at 1181 and 1132 cm^{-1} disappeared. These changes refer to a conversion of the free acid moieties of the ligand to the complex[15,16] Further evidence for the formation of the desired compounds was given by mass spectrometry. More specifically, the monomers **M-NDI** were analyzed by MALDI-TOF-MS in positive mode using CHCA as a matrix. The respective signal of the singly protonated species $[M+H]^+$ is predominant in the detection range of *m*/*z* 1000-2500 (Figure **2.2**b). At elevated laser power, typical signal patterns are complemented by a fragmentation of *m*/*z* M-44 corresponding to a loss of CO_2 $[M+H-CO_2]^+$, as well as the adducts $[M+Na]^+$ at *m*/*z* M+23, $[M+K]^+$ at *m*/*z* M+39, and occasionally $[M+H+H_2O]^+$ at *m*/*z* M+17. MALDI-TOF mass spectra of all molecules **M-NDI** are collapsed in section 2.9.5 (Figure 2.14).

To assure that the complexation is complete using the standard method (15 minutes at 120 °C and 4 equivalents of salt), different reaction conditions were screened. For a negative control experiment using 1.5 equivalent of YCl_3 to **NDI**, signals for both the fully complexed **M-NDI** (*m*/*z* 1353) and the mono-complex (*m*/*z* 1267) were detected by MALDI-TOF-MS. Even though mass spectrometry is not quantitative, the detectability of the mono-complex is reassuring and confirms that both the reaction conditions and the detection method are appropriate.

After the completion of the complexation reaction could be confirmed, residual salts were removed by size exclusion chromatography, after several attempts of dialysis had remained unsuccessful. For a final, quantitative characterization, the content of residual water in the obtained **Gd-NDI** powder was determined by thermogravimetric analysis (TGA, Figure 2.2c,

usually 12–15 wt%). A typically observed TGA curve shows a three-step mass loss from 25 to 275 °C. The first, most dominant one is likely to correspond to unbound lattice water, reaching a plateau after around 150 °C. Two more, less pronounced weight loss steps are observed upon further heating, which stabilize at 275 °C and presumably correspond to coordinated water ligands.[36] Upon further heating (> 350 °C), the organic skeleton starts to decompose (not shown). The measured water content and the derived molecular composition was confirmed by CHN elemental analysis and considered accordingly (*i.e.*, to accurately make stock solutions). For other members of the family **M-NDI**, the water content was derived directly from CHN elemental analysis.

The compounds were obtained as yellow-brownish powders after lyophilization. Their density, water content, and morphology varied visibly from one to another, most likely, because the lyophilization conditions can vary from batch to batch. Nevertheless, in most cases their physical appearance showed signs of molecular pre-organization, as in fiber-, or more rarely, crystal-like structures (Figure 2.3). Unfortunately, single crystals of sufficient size for structural resolution by X-ray diffraction could not be obtained.

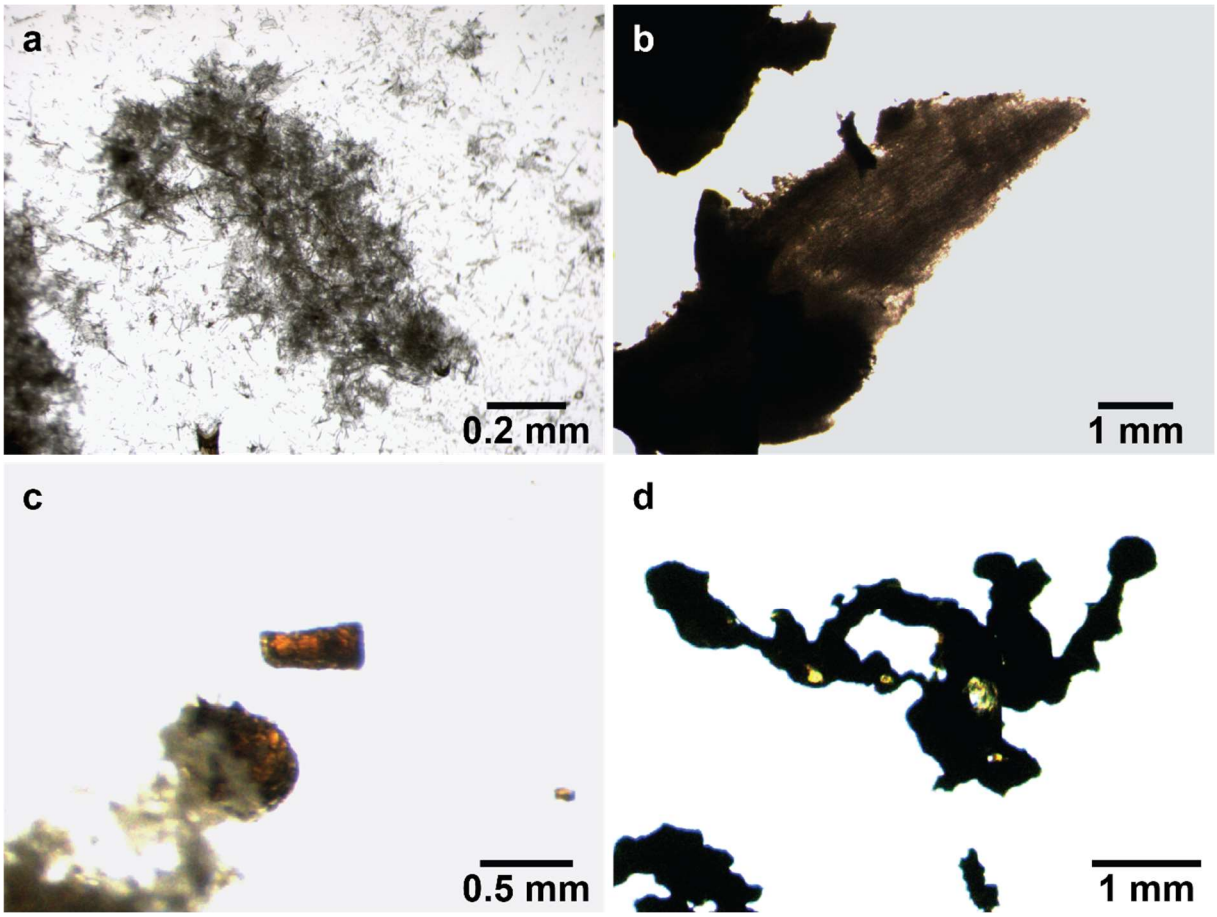

Figure 2.3 | Macroscopic morphologies of M-NDI. (a,b) Stereomicrographs of fiber-like morphologies in **Gd-NDI** and **Tb-NDI**. (c,d) Stereomicrographs of partially crystalline structures, reflecting in shades of yellow or orange, in **Gd-NDI** and **Y-NDI**.

2.4. Magnetic characterization

The magnetic nature of the compounds was characterized by electron paramagnetic resonance (EPR). Figure 2.4a shows electron paramagnetic resonance (EPR) spectra of **Gd-NDI** at concentrations of 50 and 500 µM in aqueous glycerol. The characteristic signal of the electron relaxation of Gd confirms the incorporation of the paramagnetic ion in the material.[37] Additionally, all compounds **M-NDI** were analyzed by SQUID magnetometry in bulk. The field- and temperature dependent measurements confirm paramagnetism in **Gd-NDI** (exemplarily shown in Figure 2.4b,c, see section 1.2.3.2), **Tb-NDI**, **Dy-NDI**, **Ho-NDI** and **Er-NDI**, as well as diamagnetism for **Y-NDI**, **La-NDI**, and **Lu-NDI** (see Figure 2.15 and 2.16, section 2.9.6 in the appendix). From the slope of the *H*-dependent magnetization (Figure 2.4b), the unitless volumetric magnetic susceptibility χ_V of the paramagnetic species could be obtained. The respective sample volumes were estimated using an approximation of the van der Waals volume of **M-NDI** ($1.1 \cdot 10^3$ Å^3).[38]

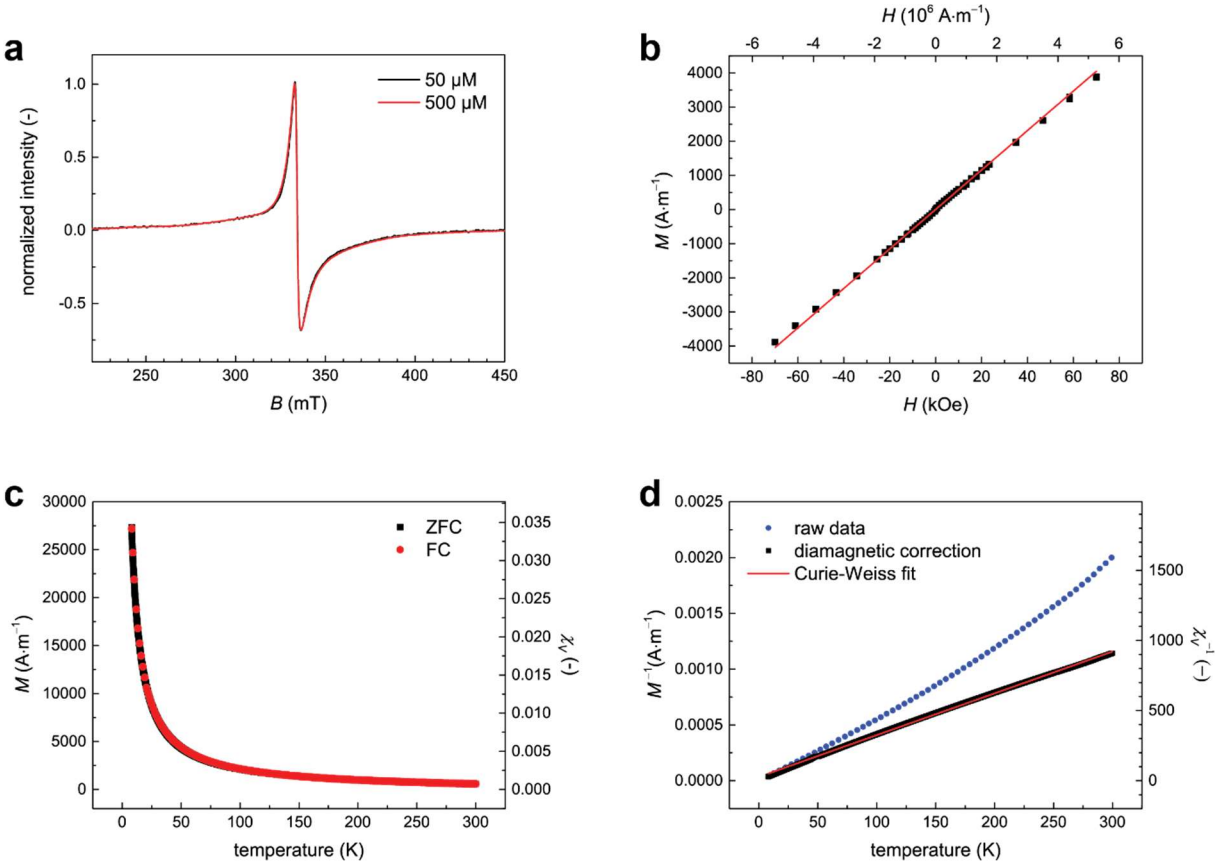

Figure 2.4 | Magnetic characterization. (a) EPR spectra of 50 µM and 500 µM **Gd-NDI** in 10 vol% aqueous glycerol at 100 K. (b) *H*-dependent magnetization *M* of bulk **Gd-NDI** and the linear fit yielding the magnetic susceptibility χ_V. (c) *T*-dependent magnetization *M* and susceptibility χ_V of bulk **Gd-NDI**. Zero field cooling (ZFC, black squares) and field cooling (FC, red circles) curves show no hysteresis. (d) *T*-dependent plot of the reciprocal magnetization M^{-1} and susceptibility $\chi_V{}^{-1}$ of the raw data (blue circles). To identify the magnetic response of the lanthanide ions, the raw signal (blue circles) was corrected for the diamagnetic contribution of the NDI core unit by subtracting the **Y-NDI** signal. The corrected signal (black squares) shows Curie-Weiss behavior (red line).

The obtained susceptibilities are, as expected, positive for all paramagnetic, and negative for all diamagnetic species. Quantitatively, the susceptibilities increase with the magnetic moment from $0.69 \cdot 10^{-3}$ to $1.21 \cdot 10^{-3}$ from **Gd-NDI** (μ = 7.94 μ_B) to **Ho-NDI** (μ = 10.6 μ_B) except for

Dy-NDI (μ = 10.6 μ_B) yielding a slightly lower value of $1.01 \cdot 10^{-3}$. The diamagnetic species exhibit susceptibilities of $-0.3 \cdot 10^{-3}$ to $-0.5 \cdot 10^{-3}$. If we compare these values to the one of unsubstituted naphthalene ($-0.17 \cdot 10^{-3}$ perpendicular to the plane[10]), it seems that in **M-NDI**—in which the naphthalene is functionalized with electron withdrawing imine substituents to promote self-assembly—the conjugation due to π-π stacking reinforces the material's diamagnetism.

Temperature dependent plots show an increase of the magnetic moment upon cooling for paramagnetic **M-NDI**s (Figure 2.4c). A plot of the respective reciprocal temperature dependent magnetization M^{-1} ($\sim\chi_V^{-1}$) is expected to be linear. Yet, in the case of the magnetic **M-NDI**s this is not the case (blue circles in Figure 2.4d). If the signal of the diamagnetic reference species **Y-NDI** is subtracted to correct for the diamagnetism of the NDI core, however, we find a linear trend that follows the Curie-Weiss law (black squares and red line in Figure 2.4d, $R^2 > 0.998$). For the other magnetic ions (**M** = Gd, Tb, Dy, Ho, Er), the corrected Curie-Weiss plot deviates slightly from linearity at temperatures below 100 K, which is most likely due to their magnetocrystalline anisotropy.[39] Therefore, linear regression was limited to a fitting range from 150 to 350 K (Figure 2.17 in the appendix). The slope of the linear fit allows to determine the material specific Curie constant ($\chi^{-1}=C^{-1}T$). The extrapolated Weiss temperature θ, at which the reciprocal susceptibility is 0, is of around –20 K for **Gd-NDI**, and between –30 and –55 K for **Tb-NDI**, **Dy-NDI**, **Ho-NDI**, and **Er-NDI**. A negative θ indicates antiferromagnetic coupling between the magnetic ions.[10] For simple antiferromagnets, the absolute value of the Weiss temperature θ is expected to correspond to the material's Néel temperature T_N. Thus, the observed antiferromagntism should vanish above 20 to 55 K.

For comparison, the Weiss temperature θ of a Gd-DOTA functionalized BTA (discussed in Chapter 4, section 4.3) is –0.7 K, so almost two orders of magnitude smaller than in the **M-NDI** system. It seems possible that the weaker self-assembly between the NDI cores, as well as the less directional supramolecular interactions allow for the magnetic complexes to orient themselves more freely with respect to each other.

The values of χ_V, C, and θ of all molecules **M-NDI** are summarized in Table 2.1.

Table 2.1 | Magnetic characteristics of M-NDI. Found values of the magnetic susceptibility χ_V of all compounds **M-NDI**, as well as Curie's constants C, and the extrapolated temperatures θ of the paramagnetic compounds. Diamagnetic species do not follow Curie-Weiss behavior, therefore there are no values for C and θ. Errors represent the standard errors obtained from linear regression. *preliminary value.

M	μ per ion[10] (μ_B)	χ_V (10^{-3})	C (K)	θ (K)
Y	0	$-0.35 \pm 4.7 \cdot 10^{-4}$	n/a	n/a
La	0	$-0.53 \pm 2.7 \cdot 10^{-3}$	n/a	n/a
Gd	7.94	$+0.69 \pm 2.9 \cdot 10^{-3}$	$0.35 \pm 1.1 \cdot 10^{-4}$	-22.5 ± 0.08
Tb	9.72	$+1.16 \pm 6.6 \cdot 10^{-4}$	$0.52 \pm 4.2 \cdot 10^{-4}$	-37.1 ± 0.22
Dy	10.7	$+1.01 \pm 1.6 \cdot 10^{-3}$	$0.45 \pm 1.2 \cdot 10^{-4}$	-29.9 ± 0.07
Ho*	10.6	$+1.21 \pm 3.3 \cdot 10^{-4}$	$0.58 \pm 5.9 \cdot 10^{-4}$	-54.4 ± 0.29
Er	9.58	$+1.15 \pm 4.3 \cdot 10^{-4}$	$0.54 \pm 2.3 \cdot 10^{-4}$	-44.3 ± 0.12
Lu	0	$-0.29 \pm 5.4 \cdot 10^{-4}$	n/a	n/a

The found χT values of the paramagnetic ions **M** in **M-NDI** at 298 K are in accordance with the theoretical values[40] (see Figure 2.17 and Table 2.4 in the appendix), confirming the purity of the compounds. Minor deviations may stem from the estimated powder densities.

2.5. Spectroscopic characterization

NDI is a well-studied class of assemblers, and it is structurally and spectroscopically analogous to its larger, and more famous kin PDI (perylene diimide). It exhibits three characteristic absorption bands at 340, 362 and 384 nm, which correspond to the 0-2, 0-1 and 0-0 vibrations of the $S_1 \leftarrow S_0$ transition, respectively.[48,49] For both NDI and PDI it has been shown that the spectral properties are strongly correlated with their self-assembly.[41–43] This results in a change of the S_0-S_1(0-1) and S_0-S_1(0-0) absorbance ratio R, which increases with assembly. The R value for the monomeric state R_m is expected to be around 0.82, which is the R we measure for the intermediate **3**, a charged and thus non-assembling NDI, at concentrations up to 1 mM. This evolution is typically accompanied by a decrease of intensity and a slight red shift of the absorption band. As compared to PDI, the spectral changes are considerably less pronounced due to a smaller $S_1 \leftarrow S_0$ transition dipole moment.[44]

Figure 2.5 shows absorbance, excitation and emission spectra of **Gd-NDI** at concentrations of 100 µM (a), and 10 mM (b). The measured UV-Vis absorption spectrum of the more diluted **Gd-NDI** shows a typical S_0-S_1 absorbance pattern, with an absorbance ratio R of 0.92. The excitation spectrum exhibits the same maxima at a ratio R of 0.79. The emission spectrum, recorded at an excitation wavelength of 362 nm, presents itself as a mirror image to the absorbance (R = 0.88), with a slight Stokes shift of around 10 nm.

The same measurements for the 10 mM solution, so 100 times more concentrated, show an inversion of the S_0-S_1 peak intensities in the absorbance, with R = 1.18, as well as in emission, with R = 1.17. The excitation spectrum (R = 0.74) and the Stokes-shift (around 10 nm) remain unchanged. The increase of R implies assembly of the **Gd-NDI** monomers at this concentration. Moreover, a broad, red-shifted signal arises at around 525 nm and suggest excimer emission of ground state aggregates.[39,38]

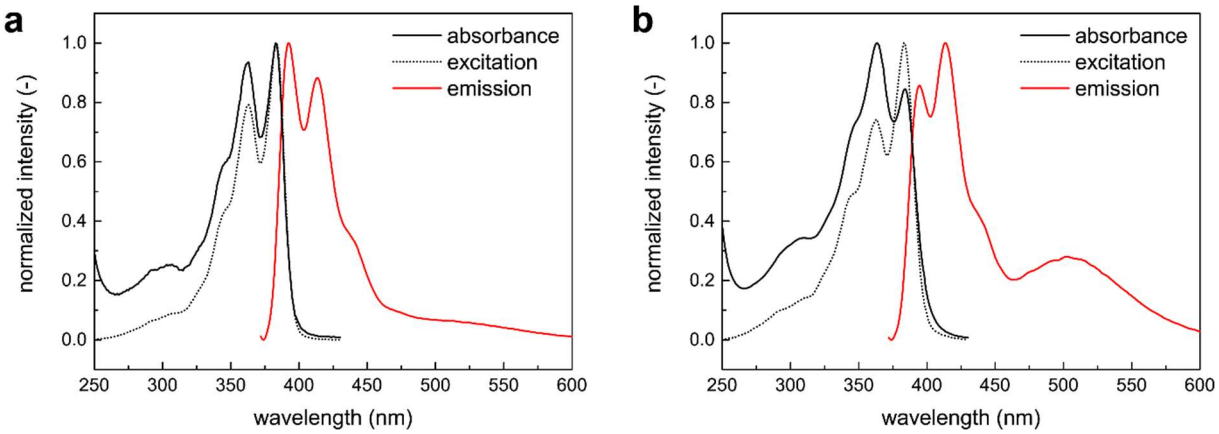

Figure 2.5 | Spectroscopic characterization. Absorbance, excitation, and emission spectra (black full lines, black dotted lines, and red lines, respectively) of (a) 100µM and (b) 10 mM aqueous **Gd-NDI**. Excitation spectra were measured at an emission wavelength of 440 nm, emission spectra were recorded at an excitation wavelength of 362 nm.

Absorbance and excitation spectra of all building blocks **M-NDI** at 100 µM and 10 mM are similar (Figure 2.18 in the appendix). The red-shifted emission band at 525 nm, however, varies in its intensity. For **Y-NDI** and **Lu-NDI** it is the most dominant signal and is the least

pronounced for **Gd-NDI**. Presumably, the different intensities can arise from an overlap with the emission of the different ions.[46]

In the following, *R* will be used as a spectroscopic merit number to quantify the self-assembly of **M-NDI**.

2.6. Thermodynamics of supramolecular polymerization

To investigate the supramolecular polymerization quantitatively, we determined thermodynamic parameters for the self-assembly processes of all eight molecules **M-NDI** in water, using a combination of concentration- and temperature dependent UV-Vis spectroscopy. More specifically, we measured UV-Vis absorbance spectra over a concentration range of 2 µM to 100 mM at 25 °C (Figure 2.6a). For each spectrum, the ratio *R* of the intensities of the S_0-S_1(0-1) (~362 nm) over the S_0-S_1(0-0) (~384 nm) transitions was extracted and plotted as a function of concentration (Figure 2.6b). The data sets could be fitted to sigmoidal curves using a reported isodesmic model[57], allowing for the determination of the equilibrium constant K_{eq} and the Gibbs free energy of supramolecular polymerization ΔG (see section 2.9.9.1). This approach offers a valuable first overview over the self-assembly process, revealing the course of the sigmoidal curve over the entire aggregation process.

The isodesmic model was chosen over a two-constant nucleated assembly model (section 2.9.9.2) for (anti)cooperative mechanisms (see section 1.1.2)[19,47] Both the isodesmic and cooperative models yield a qualitatively well matching fit (see Figure 2.21 in the appendix), which seem identical at first glance. The cooperative model proposes a cooperativity factor σ of 1.3, indicating an anticooperative mechanism. To select the model that is more likely to be correct the Akaike Information Criterion[46] (AIC, section 0) was consulted. It estimates the relative quality of statistical models while penalizing a model for its number of free parameters (3 for isodesmic vs. 4 for anticooperative). From a set of models, the one with the minimum value will be preferred, which is the isodesmic model in our case (AIC 18 vs. 23).

To add more accuracy to our study, it was complemented with temperature dependent measurements. It allows the acquisition of a vast number of measurements to obtain an almost continuous data set.[33] UV-Vis spectra of four solutions between concentrations of 200 µM and 2 mM were recorded temperature dependently from 5 to 95 °C (Figure 2.6d). Thereby, a mild heating rate of 2 $K \cdot min^{-1}$ and three subsequent heating-cooling cycles were applied to ensure thermodynamic control. Indeed, we observe negligible or no hysteresis in our measurements.[58] Due to the required short pathlength of sealable cuvettes, the data acquisition of this otherwise powerful method is restricted to a concentration range of up to 2 mM for **M-NDI**. The enthalpy of supramolecular polymerization ΔH was obtained by fitting a van der Schoot isodesmic model[33] (see section 2.9.9.3) to the measured ratios *R* as a function of temperature (Figure 2.6d).

By combining concentration and temperature dependent measurements, we profit from the globality of the concentration dependent measurements, and the accuracy of temperature dependent measurements. This allows for a reliable analysis of the self-assembly mechanism and determination of the associated thermodynamic parameters.

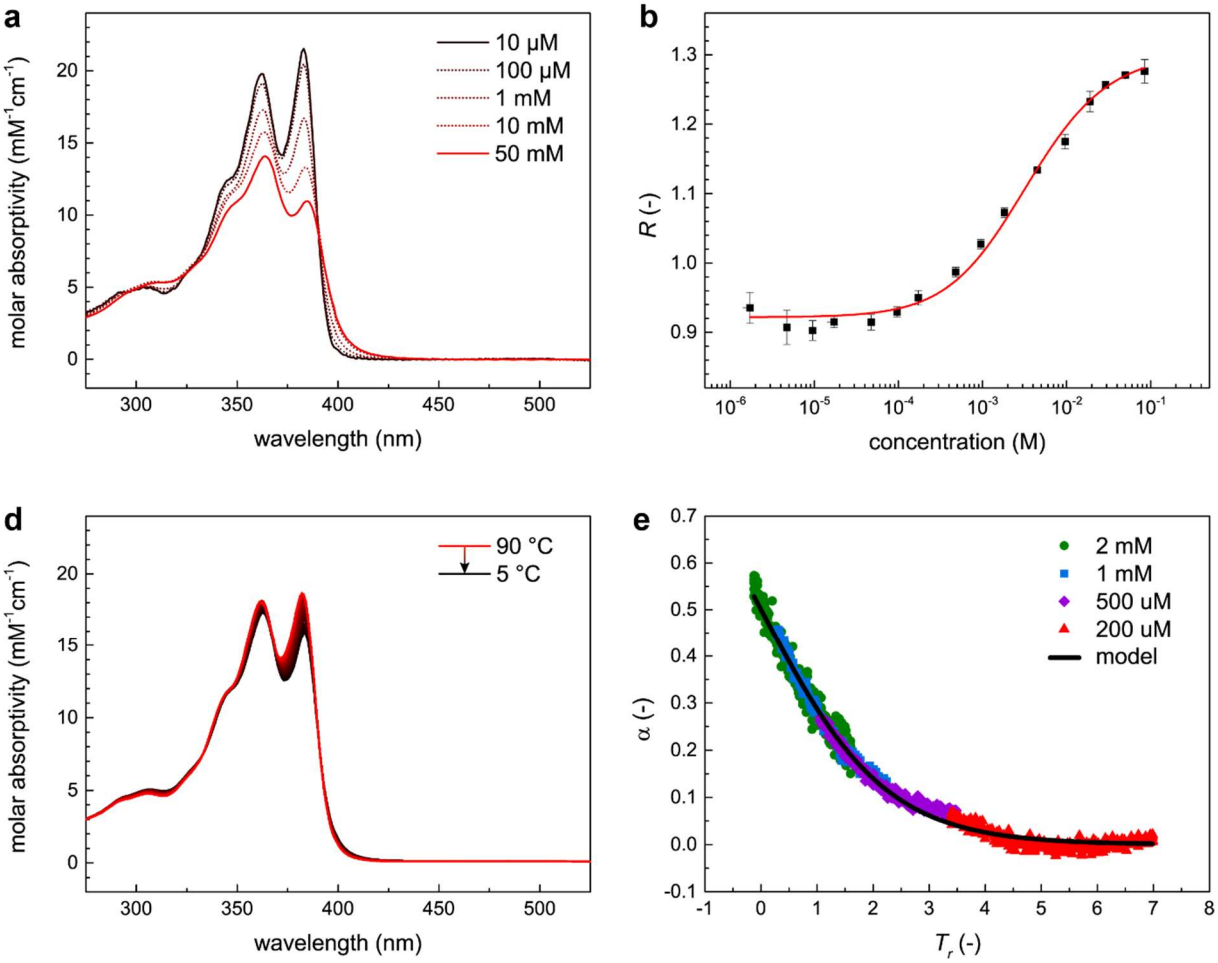

Figure 2.6 | Self-assembly studies in water. (a) UV-Visible absorption spectra of **Gd-NDI** recorded at different concentrations. (b) Plot of the S_0-S_1(0-1) / S_0-S_1(0-0) absorbance ratio R as a function of concentration and the corresponding isodesmic fit (red line). Error bars represent standard deviations over three measurements. (d) UV-Visible absorption spectra of 1 mM **Gd-NDI** at 5–95 °C recorded at a heating rate of 2 K·min^{-1}. (e) Degree of supramolecular polymerization α as a function of the reduced temperature T_r, both obtained from the van der Schoot isodesmic model, and the corresponding best fit for **Gd-NDI**. The plot collapses data sets collected for 2 mM, 1 mM, 500 µM and 200 µM aqueous solutions of **Gd-NDI**.

For both the concentration and temperature dependent data, the isodesmic model gives a well matching fit for all members of the family **M-NDI**, yielding Gibbs free energies ΔG (*i.e.*, equilibrium constants K_{eq} between 200 and 330 M^{-1}) and enthalpies of supramolecular polymerization of –12 to –14 kJ·mol^{-1}. There is no significant difference between the obtained values of ΔG and ΔH greater than the 95% confidence interval ($p \leq 0.05$) for any of the molecules **M-NDI**. These results suggest a negligible entropic contribution ($-T\Delta S \approx 0$), which means that the enthalpy of supramolecular polymerization is directly equated to the Gibbs free energy $\Delta G = \Delta H - T\Delta S \approx \Delta H$ —an assumption which is commonly made in supramolecular assembly.

A visual comparison of the fits and obtained thermodynamic contributions to the self-assembly is given in Figure 2.7. The numerical results for the equilibrium constants K_{eq}, the Gibbs free energies ΔG, and the enthalpies ΔH are given in Table 2.2.

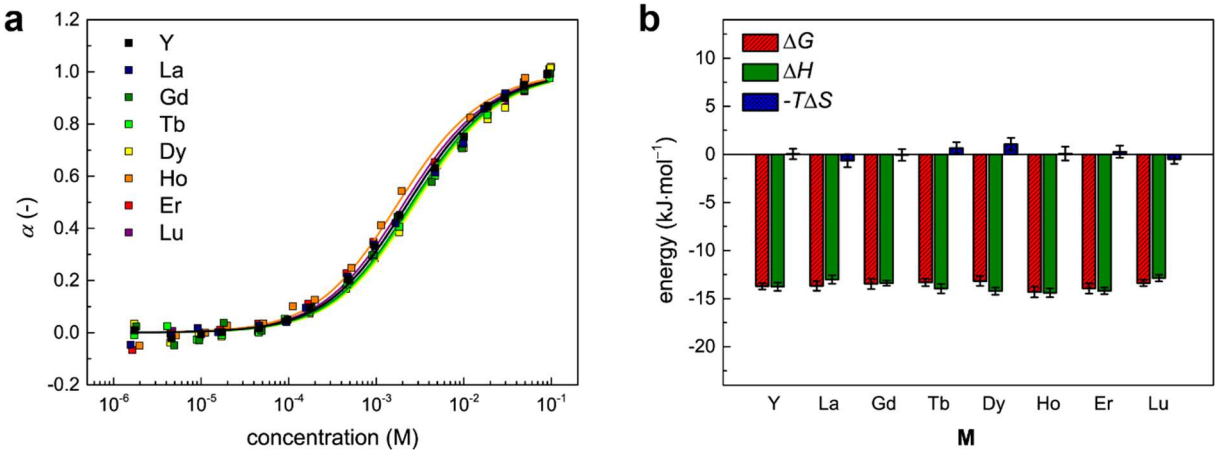

Figure 2.7 | Fitting results for all ions M. (a) Normalized concentration dependent degree of supramolecular polymerization α for all molecules **M-NDI**. (b) Bar diagram of the Gibbs free energies ΔG (obtained from concentration dependent isodesmic fit), enthalpies ΔH (obtained from the van der Schoot isodesmic fit), and entropic contributions $-T\Delta S$ (calculated from ΔG and ΔH) for all molecules **M-NDI**. Error bars represent 95 % confidence intervals ($p \leq 0.05$). The ions **M** are sorted by their atomic numbers.

Table 2.2 | Thermodynamic parameters for constant enthalpy and entropy changes. Equilibrium constants K_{eq}, Gibbs free energies polymerization ΔG, and enthalpies ΔH of supramolecular polymerization of **M-NDI** obtained from concentration- and temperature dependent fits, as well as the derived values for the entropic contributions. The given errors represent 95% confidence intervals ($p \leq 0.05$).

M	K_{eq} (M^{-1}) [*c* fit]	$\Delta G°$ (kJ·mol^{-1}) [*c* fit]	ΔH (kJ·mol^{-1}) [*T* fit]	$-T\Delta S°$ (kJ·mol^{-1}) [calc.]	$\Delta S°$ (J·mol^{-1}·K^{-1}) [calc.]
Y	253 ± 33	-13.71 ± 0.33	-13.76 ± 0.43	0.05 ± 0.46	0.17 ± 1.5
La	249 ± 51	-13.67 ± 0.51	-13.01 ± 0.43	0.66 ± 0.50	2.21 ± 1.7
Gd	228 ± 51	-13.45 ± 0.55	-13.39 ± 0.26	0.06 ± 0.38	0.20 ± 1.3
Tb	215 ± 33	-13.31 ± 0.39	-13.96 ± 0.49	0.65 ± 0.53	2.18 ± 1.8
Dy	203 ± 45	-13.16 ± 0.53	-14.22 ± 0.38	1.06 ± 0.47	3.56 ± 1.6
Ho	324 ± 73	-14.32 ± 0.55	-14.40 ± 0.46	0.08 ± 0.54	0.27 ± 1.8
Er	277 ± 33	-13.93 ± 0.53	-14.20 ± 0.34	0.27 ± 0.43	0.91 ± 1.4
Lu	220 ± 29	-13.37 ± 0.33	-12.87 ± 0.35	0.50 ± 0.39	0.17 ± 1.3

The described fitting procedure including the concentration dependent fit, and the van der Schoot model is well established and commonly applied to quantify the thermodynamics of supramolecular self-assembly.[47] The method is often completed with a so-called van't Hoff plot[19,47], which is a linear fit of the logarithmic equilibrium constant K_{eq} as a function of the reciprocal temperature, yielding a slope of $-\Delta H \cdot R^{-1}$ and an intersect of $\Delta S \cdot R^{-1}$. In this way, the entropy of supramolecular polymerization can be determined directly (*i.e.*, the entropy is not calculated from ΔG and ΔH). These models rely on the assumption that the enthalpy ΔH is temperature-independent, and that the equilibrium constant K_e scales exponentially with temperature.

As recently pointed out by Würthner and coworkers, the mentioned assumptions of constant entropy- and enthalpy changes cannot be held in aqueous systems. Therefore, the van der Schoot and the classic van't Hoff model are insufficient to describe supramolecular self-assembly of (bola)amphiphilic molecules in water accurately. Instead, a Glew-Clark fit[12], otherwise known as the "extended van't Hoff equation", is proposed. This model corrects for changes of enthalpy and entropy with temperature, that are typically observed in water, by including the heat capacity change ΔC_p of the solution.[54]

To apply the Glew-Clarke model (more details in section 2.9.9.4) to our system, the equilibrium constant K_{eq} was determined as a function of temperature. To this end, the R values of four concentrations (200 or 300 µM, 500 µM, 1 mM, and 2 mM), taken from the previously described temperature dependent measurements (Figure 2.6d,e), were reassessed. The concentration dependent isodesmic model (Figure 2.6b and section 2.9.9.1) was fitted to the data for each temperature at a fixed R_p value (see Table 2.5). The resulting values of K_{eq} were plotted as a function of temperature and fitted to the Glew-Clarke model (Figure 2.8a).

When the classic van't Hoff equation and the Glew-Clarke model are compared for our data of **Gd-NDI** using the Akaike Information Criterion (AIC, see section 0 in the appendix), the Glew-Clarke model is preferred by a factor of more than 100 (see section 2.9.9.5 for more details). This shows that the consideration of the heat capacity change as an additional, temperature dependent term does indeed help to describe the thermodynamics of our system more accurately.

The obtained values for the standard Gibbs free energy $\Delta G°$ (=ΔG_{298K}), the enthalpy of supramolecular polymerization ΔH, and the entropic contribution $-T\Delta S°$ (= $-T\Delta S_{298K}$) for all molecules **M-NDI** are given in Table 2.3 and illustrated in Figure 2.8b. The fits of all molecules are given in Figure 2.23 (section 2.9.9.5 in the appendix).

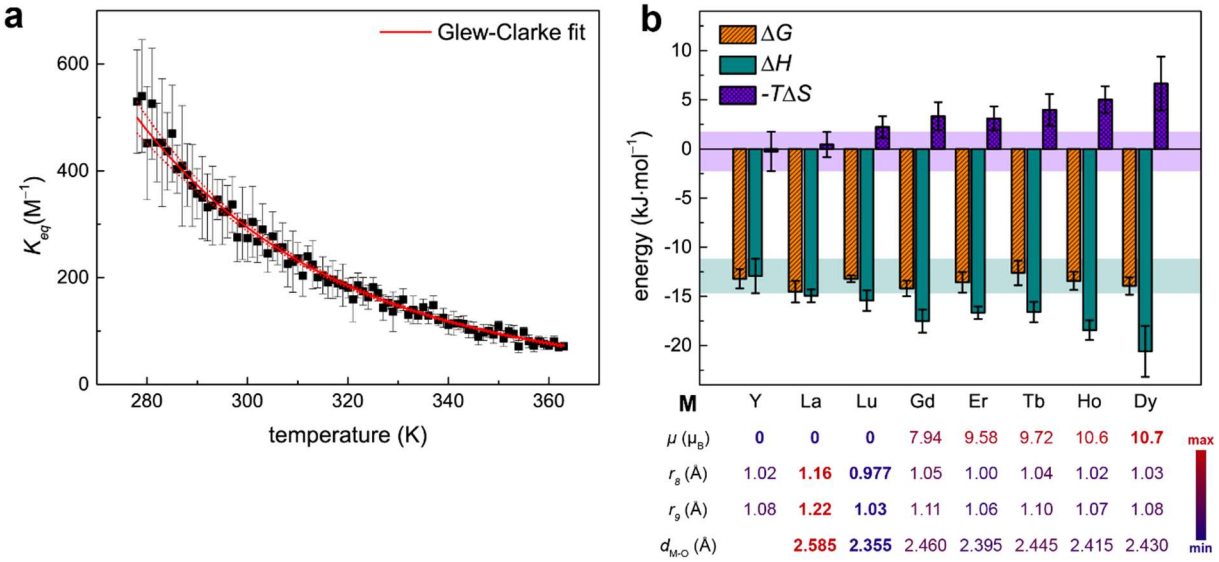

Figure 2.8 | Glew-Clarke model considering thermal fluctuations of enthalpy and entropy. (a) Temperature dependent equilibrium constant K_{eq} and the corresponding Glew-Clark fit for θ = 298 K of **Gd-NDI** (red line), yielding an enthalpy of supramolecular polymerization ΔH = (–17.52 ± 0.52) kJ·mol^{-1}, a Gibbs free energy ΔG = (–14.197 ± 0.029) kJ·mol^{-1}, and a heat capacity change ΔC_p = (–83 ± 24) J·mol^{-1}·K^{-1}. Dotted lines represent the 95% confidence bounds ($p \leq 0.05$). Error bars represent standard errors from the concentration dependent fit. (b) Bar diagram of the Gibbs free energies ΔG, enthalpies ΔH (both obtained from the Glew-Clarke fit), and entropic contributions $-T\Delta S$ (calculated from ΔG and ΔH) for all molecules **M-NDI** at 298 K. The ions **M** are sorted by their magnetic moments μ from 0 μ_B (**M** = Y, La, Lu) to 10.7 μ_B (**M** = Dy). Error bars represent 95% confidence intervals ($p \leq 0.05$). Shaded areas represent the 95% confidence intervals of ΔH and $-T\Delta S$ of **Y-NDI** (turquoise and purple, respectively). The table lists magnetic moments μ[10] in $\mu_B = 9.274 \cdot 10^{-24}$ Am², ionic radii[48] r_8 and r_9 of 8- and 9-coordinate species.

Table 2.3 | Thermodynamic contributions to the Gibbs free energy. Standard Gibbs free energies $\Delta G°$, enthalpies of supramolecular polymerization ΔH, thermodynamic contributions $-T\Delta S°$, and the standard entropy $\Delta S°$ of **M-NDI** obtained from the Glew-Clarke model. All values are given for 298 K. Errors represent 95 % confidence intervals ($p \leq 0.05$). Errors of ΔG were determined from the *c*-dependent isodesmic fit of four concentrations. [a] within the 95 % confidence interval of **Y-NDI**. [b] outside the 95 % confidence interval of **Y-NDI**.

M	$\Delta G°$ (kJ·mol^{-1})	ΔH (kJ·mol^{-1})	$-T\Delta S°$ (kJ·mol^{-1})	$\Delta S°$ (J·mol^{-1}·K^{-1})	ΔC_p (J·mol^{-1}·K^{-1})
Y	–13.20 ± 0.98 [a]	–12.92 ± 1.75 [a]	–0.27 ± 2.00 [a]	+0.9 ± 6.7 [a]	–287 ± 156
La	–14.51 ± 1.10 [a]	–14.95 ± 0.66 [a]	+0.43 ± 1.28 [a]	–1.4 ± 4.3 [a]	–40 ± 61
Gd	–14.20 ± 0.80 [a]	–17.52 ± 1.18 [a]	+3.32 ± 1.43 [a]	–11.1 ± 4.8 [a]	–83 ± 92
Tb	–12.62 ± 1.24 [a]	–16.59 ± 1.03 [b]	+3.97 ± 1.61 [b]	–13.3 ± 5.4 [b]	–250 ± 116
Dy	–13.95 ± 0.88 [a]	–20.59 ± 2.59 [b]	+6.65 ± 2.73 [b]	–22.3 ± 9.2 [b]	–30 ± 188
Ho	–13.42 ± 0.92 [a]	–18.43 ± 1.00 [b]	+5.01 ± 1.35 [b]	–16.8 ± 4.6 [b]	–52 ± 139
Er	–13.58 ± 1.05 [a]	–16.67 ± 0.64 [b]	+3.10 ± 1.23 [b]	–10.4 ± 4.1 [b]	–104 ± 69
Lu	–13.21 ± 0.34 [a]	–15.43 ± 1.05 [b]	+2.22 ± 1.10 [b]	–7.4 ± 3.7 [b]	–16 ± 112

Surprisingly, the enthalpic and entropic contributions ΔH and $-T\Delta S$ obtained from this method (Figure 2.8b) vary for the different ions. They are, however, adding up to the same Gibbs free energy ΔG of –13 to –14 kJ·mol^{-1} for all **M-NDI** within the 95 % confidence interval (Figure **2.8**b, orange bars). As compared to the simpler, concentration-dependent isodesmic model (Figure 2.7b and section 2.9.9.1), there is no significant differences in the values of ΔG (*i.e.*, within the 95 % confidence intervals). Regarding the enthalpies, however, differences of up to 60 % were found among the different **M-NDI**s. The molecules incorporating the two ions with the largest magnetic moments μ of the library, Dy^{3+} and Ho^{3+} (10.7 and 10.6 μ_B, respectively), yield the largest negative enthalpies ΔH of –21 and –18 kJ·mol^{-1}. The diamagnetic Y^{3+} and La^{3+} yield enthalpies of –13 and –15 kJ·mol^{-1}. As the free Gibbs energies ΔG are considered identical within the experimental error, the differences in ΔH translate directly to the entropic contributions $-T\Delta S$. For the paramagnetic **Dy-NDI** and **Ho-NDI** they are 7 and 5 kJ·mol^{-1} at 298 K, whereas they are –0.3 and 0.4 kJ·mol^{-1} for the diamagnetic **Y-NDI** and **La-NDI**. For the ions with intermediate magnetic moments, Gd^{3+}, Tb^{3+} and Er^{3+}, enthalpies ΔH of around -17 kJ·mol^{-1} and entropic contributions $-T\Delta S$ of 3–4 kJ·mol^{-1} were found. The Glew-Clarke fit for **Lu-NDI** yields an enthalpy of –15.4 kJ·mol^{-1} and an entropic contribution $-T\Delta S$ 2.2 kJ·mol^{-1}, which is slightly larger than expected, but nonetheless within the 95 % confidence interval of **Y-NDI**, meaning that the deviation is statistically not significant at a significance level of 5 % ($p \leq 0.05$, turquoise shaded area in Figure 2.8b). All other **M-NDI**s, on the contrary, are considered statistically significant under this criterion.

To rationalize these differences in the enthalpy/entropy balance, we can consider the following: i) different sizes of the chelated ions, and thus different sizes of the DOTA-ion moiety of the molecule (see section 1.2.3.3), or ii) differences in the magnetic moment of the ions.

Add. i: When comparing the ionic radii r_8 and r_9 (for 8- and 9 coordinate species, respectively) of the different lanthanides, one observes a decrease by about 15 % along the series from $_{57}La^{3+}$ to $_{71}Lu^{3+}$, displaying the famous lanthanide contraction (see table in Figure 2.8b). Along with the ionic radii, the reported M–O coordination bond lengths $d_{M–O}$ of free lanthanides in water decrease by around 9 %.[49] The resulting steric effects can impact the coordination geometries of the respective ions in complexes.[44] More specifically, computational studies on the conformations of $Ln(DOTA)^-$ complexes in water indicated —in agreement with experimental data— that for Ln = La, Gd, and Ho there are two minima for 9-coordinate square antiprismatic

and twisted square antiprismatic geometries. For Lu, instead, the 8-coordinate twisted square antiprismatic geometry (*i.e.*, without a water molecule in the first coordination sphere) is preferred.[50] In our system, a smaller coordination sphere, resulting from a shorter ionic radius and a smaller coordination number, suggests a decreased bulkiness of the whole DOTA cage for $_{71}Lu^{3+}$ as compared to earlier lanthanides. If we consider $_{91}La^{3+}$, on the other hand, with an ionic diameter of around 2.4 Å[48], La–N and La–O bond lengths of 2.5 and 2.8 Å[50] in the DOTA complex, and a π-π stacking distance of typically 3–4 Å, the large DOTA cage could limit the π-π stacking distance sterically (see Figure 2.19 in the appendix). Reducing the bulkiness of the DOTA moieties would facilitate the assembly of the central NDI unit, and possibly allow for denser packing. Consequently, the polymeric species would be stabilized. However, our data does not follow the trend of the lanthanide contraction, which would predict the largest negative enthalpy for **Lu-NDI**, and the smallest for **La-NDI**.

Add. ii: Instead, we observe a trend relating the enthalpic and entropic contributions of the self-assembly to the magnetic moment μ of the ions. With an increasing magnetic moment μ, the enthalpy ΔH decreases, which means that the assembly becomes more and more enthalpically favored (Figure 2.8b, turquoise bars). To the same extent, the entropic contribution $-T\Delta S$ (purple bars) seems to counteract, resulting in similar Gibbs free energies for all ions. For better illustration of these results, we can compare the self-assembly of **Dy-NDI** and **Y-NDI** as examples. The self-assembly of **Dy-NDI** is enthalpically more favored as compared to **Y-NDI**. Thus, we would expect larger assemblies for **Dy-NDI**. However, the more repeating units are grouped to an assembly in the polymerization process, the larger will be the entropy loss upon polymerization. The disfavoring entropy is so to say damping the enthalpic driving force in the **Dy-NDI** assembly. This phenomenon is known as enthalpy/entropy compensation.[49]

Regarding the standard Gibbs free energy ΔG, the found results of the concentration dependent and the temperature dependent Glew-Clarke model are in good agreement and internally consistent. The values of $\Delta G°$ for all molecules **M-NDI** could be determined with high precision, and we find no significant difference greater the 95 % confidence interval (*i.e.*, $p > 0.05$) between the different monomers. When considering the entropic and enthalpic contributions to the self-assembly separately, however, there are significant differences between the different ions if enthalpy- and entropy changes with respect to temperature are considered—an observation that a more conventional model fails to identify.

The most apparent factor distinguishing the different **M-NDI**s with respect to the observed enthalpy and entropy changes is the magnetic moment μ of the complexed ions **M**, which our study suggests as the key parameter. The incorporation of paramagnetic ions seems to stabilize the assembled species, which is expressed by a greater enthalpic contribution ΔH increasing by 60 % from around –13 $kJ \cdot mol^{-1}$ to around –21 $kJ \cdot mol^{-1}$. This is very surprising and indicates that magnetic interactions between the ions alter the thermodynamics of self-assembly.

2.7. Conclusions

A family of eight different dia- and paramagnetic monomers **M-NDI** has been synthesized and characterized successfully. In aqueous medium, they self-assemble by an isodesmic polymerization mechanism with Gibbs free energies ΔG of polymerization of about –13 to **–**14 kJ·mol^{-1}. The thermodynamic parameters were obtained from spectroscopic data using three different isodesmic models. A concentration dependent model and the Glew-Clarke model, which is both concentration- and temperature dependent, yielded consistent values of the Gibbs free energies ΔG over the whole scope of eight monomers. Regarding the enthalpic and entropic contributions to the Gibbs free energy, significant changes were found applying the Glew-Clarke model. For aqueous systems, the latter is preferred over the more conventional van der Schoot model, as it takes the temperature-dependence of enthalpy and entropy into account.

We conclude that the magnetic nature of the ions **M** does not influence the Gibbs free energy ΔG of supramolecular self-assembly. In contrast, it does significantly change the proportion of the enthalpic and entropic contributions, showing an increase of the negative enthalpy ΔH by 60 % from around –13 kJ·mol^{-1} to around –21 kJ·mol^{-1} for **M** = Y^{3+} and Dy^{3+} with an increasing magnetic moment of **M**.

The presented work is the first quantitative study of its kind, and the change in the enthalpy of polymerization upon the incorporation of paramagnetic lanthanide ions is very surprising. It suggests magnetic interactions between the lanthanide ions, that are forced in spatial proximity by the π-π-stacking- and hydrophobicity driven supramolecular assembly. SQUID magnetometry of the bulk material exhibits a negative Weiss temperature of the magnetic **M-NDI**s of –20 to –50 K, which points at a weak antiferromagnetic coupling between the magnetic lanthanides.

Beyond this study, these results can help elucidate other poorly understood self-assembly phenomena, like in a Dy^{3+}-containing surfactants system reported by Polarz[15], or Gd^{3+}-containing dendrimers shown by Meijer and coworkers[16], and may be extrapolated to various other supramolecular systems. The possible magnetic interactions may represent a new directional force to precisely control and tune the auto-organization of monomers to supramolecular structures and complete the toolbox of non-covalent interactions in supramolecular assembly.

2.8. Author contributions

Michaela Schicho performed the synthesis, spectroscopic assembly studies, and evaluated all data. Georges Formon assisted in data fitting and authors the MATLAB® code, which was slightly modified to adapt it to this system. Thomas Hermans supervised the research. Elemental analysis was performed by Service d'analyses, de mesures physiques et de spectroscopie optique, Université de Strasbourg. EPR spectoscopy was perfomed by the REseau National de Rpe interDisciplinaire (RENARD, Fédération IR-RPE CNRS # 3443). SQUID magnetometry was performed by Jérôme Robert at Institut de Physique et de Chimie des Matériaux de Strasbourg (IPCMS, UMR7504, CNRS).

2.9. Appendix

2.9.1 Materials and methods

Synthesis. All reagents were obtained from commercial sources (TCI, Sigma Aldrich, VWR) and used without further purification. If no further specifications are given, reactions were performed at 25 °C under atmospheric pressure. DMF was dried over 3 Å molecular sieves. Column chromatography was performed on silica gel 40 Å (40-63 µm). TLC was carried out on 60 Å silica gel TLC plates. Ultrasonication was performed using an ElmaElmasonic E 60 H ultrasonic cleaner. Microwave experiments were conducted on a CEM Discover® monomode microwave reactor at 150 W. Lyophilization was performed on a SP VirTis Benchtop Pro with Omnitronics freeze-dryer.

Elemental analysis (EA). CHN elemental analysis was performed by Service d'analyses, de mesures physiques et de spectroscopie optique, Université de Strasbourg, on a Thermo Fisher Scientific Thermo Scientific™ Flash2000 CHN analyzer with an analytical precision of 0.3 %. Given values represent the mean over two measurements.

Thermogravimetric analysis (TGA). TGA measurements were performed on a Mettler Toledo TGA/DSC 2 using 70 µL alumina crucibles. The samples (around 5 mg) were heated from 25 °C to 350 °C using a specified temperature profile under a nitrogen stream of 100 $mL \cdot min^{-1}$. The recorded data was analyzed using the Mettler Toledo STARe software.

Infrared spectroscopy (IR). Spectra were recorded on a Shimadzu IRAffinity-1 FTIR spectrometer in ATR-FTIR configuration, and 100 scans were cumulated.

Nuclear magnetic resonance (NMR). Spectra were recorded on a Bruker 400 MHz Ultrashield™ NMR spectrometer or a 500 MHz Bruker Ascend™ 500 spectrometer. Unless indicated otherwise, spectra were collected at 25 °C. Chemical shifts (δ) are given in ppm relative to tetramethylsilane (TMS).

Electron paramagnetic resonance (EPR). EPR spectroscopy was perfomed by EPR service of the REseau NAtionalde Rpe interDisciplinaire (RENARD, Fédération IR-RPE CNRS #3443) on a Bruker EMX spectrometer.

Mass spectrometry (MS). MALDI-TOF MS spectra were recorded in positive mode on a Bruker Autoflex Speed spectrometer using cyano-4-hydroxy cinnamic acid (CHCA) as a matrix. Samples were prepared by spotting 2 x 1 µL of a saturated solution of CHCA in ACN containing 0.1 vol% TFA and 2 x 1µL of a 1:1 mixture of a 100 µM solution of the respective complex in MeOH and the saturated solution of CHCA in ACN containing 0.1 vol% TFA alternately on a MALDI plate. After every deposition, the sample spot was allowed to dry at room temperature. The given *m*/*z* values represent the major isotope signal.

LC-MS. Measurements were recorded on a Thermo Fisher Scientific™ Vanquish™ UHPLC system equipped with an Accucore™ Vanquish™ C18+ UHPLC column (1.5 µm particle size 80 Å pore size, 100·2.1 mm), an Accela™ PDA 80 Hz detector and an LCQ Fleet™ ion trap mass spectrometer with an integrated Ion Max™ source.

UV-Vis spectroscopy. Measurements were conducted on an Agilent Cary 300 UV-Vis spectrometer with temperature controller using quartz cuvettes of the path lengths 1.0 mm, 0.1 mm or 0.01 mm. Temperature-dependent measurements were performed under a stream of compressed air to avoid condensation of atmospheric water. Concentration-dependent

measurements were taken at 25.0 °C. Solutions for concentration series were diluted starting from four different stock solutions (100 mM, 50 mM, 30 mM, 10 mM).

Luminescence spectroscopy. Excitation and emission spectra were recorded on a Horiba Fluorolog FL3-22 fluorescence spectrometer using a front-face geometry.

SQUID magnetometry. SQUID measurements were performed by Jérôme Robert at Institut de Physique et de Chimie des Matériaux de Strasbourg (IPCMS, UMR 7504, CNRS) on a MPMS3 magnetometer (Quantum Design). The temperature dependent magnetization was recorded in an AC field of 1 T at a sweeping rate of 5 $K \cdot min^{-1}$. The field dependent magnetization was recorded at 300 K.

2.9.2 Synthesis

Synthesis of Bis(*n*-butylammonium) naphthalene diimide [3]

The Boc procted bis(*N*-(*tert*-butoxycarbonyl)-1,2-diaminobutanyl) naphthalenediimide **2** was prepared following a modified literature procedure.[1] In a pressure-tight 10 mL microwave-vial 1,4,5,8-naphthalene-tetracarboxyldianhydride **1** (0.27 g, 1.0 mmol) and *N*-(*tert*-butoxycarbonyl)-1,2-diaminobutane (0.57 g, 3.0 mmol, 0.57 mL, 3.0 eq.) were suspended in DMF (4mL). Triethylamine (0.30 g, 3.0 mmol, 3.0 eq.) was added and the suspension was sonicated or mechanically stirred until it became homogeneous. The reaction mixture was heated for 10 min at 100°C under microwave irradiation. The solvent was removed under reduced pressure and the residue was taken up into MeCN/MeOH (10 mL 2:1 v/v). The solution was added to 1M HCl (120 mL). The resulting suspension was allowed to coagulate at 4 °C for 12 h. The precipitate was filtered off using a porosity 4 glass sintered funnel and washed with demineralized water. The residue was dissolved in chloroform and dried over $MgSO_4$. The solvent was removed under reduced pressure to yield the compound as a brown powder (0.58 g, 0.94 mmol, 94 %).

To deprotect **2** (0.50 g, 0.82 mmol), TFA (3mL) and demineralized water (0.4 mL) were added to the compound. The reaction was kept stirring at 25 °C for 2 h and followed by LC-MS analysis. Upon completion, diethyl ether (200 mL) was added. The reaction mixture was allowed to coagulate for 12 hours at 4 °C. The precipitate was filtered off using a porosity 4 glass sintered funnel and washed with diethyl ether. The residue was dissolved in demineralized water and lyophilized to yield the TFA salt of **3** as a brown powder (0.50 g, 0.79 mmol, 96 %). ^{1}H-NMR (400 MHz, DMSO-d^6) δ(ppm): 8.69 (s, 4H), 7.74 (br s, 6H), 4.10 (t, 4H), 2.84 (t, 4H), 1.73 (quin, 4H), 1.62 (quin, 4H). MS(ESI+) for $C_{22}H_{26}N_4O_4^{2+}$ (*m*/*z*): $[M]^{2+}$ calc. 205.10, found 205.07; $[M–H]^+$ calc. 409.19, found 409.19; $[2M–3H]^+$ calc. 817.37, found 816.60. Elemental analysis calc. for $C_{26}H_{26}F_6N_4O_4$: %C = 49.06, %H = 4.12, %N = 8.80, found: %C = 49.05, %H = 4.20, %N = 8.93.

Synthesis of the ligand NDI-C_4-DOTA [NDI]

Tri-tert-butyl 1,4,7,10-tetraazacyclododecane-1,4,7,10-tetraacetate (0.91 g, 1.6 mmol, 2.1 eq.) and HBTU (0.74 g, 2.0 mmol, 2.6 eq.) were dissolved in dry DMF (25 mL) under inert atmosphere. To this solution, DIPEA (1.4 mL, 1.0 g, 7.9 mmol, 11 eq.) and a solution of the TFA salt of **3** (0.48 g, 0.75 mmol, 1.0 eq.) in dry DMF (10 mL) were added and the reaction

mixture was kept stirring for 3 h at 25 °C under inert atmosphere in the dark. After completion of the reaction, which was confirmed by LC-MS analysis, chloroform (150 mL) was added to quench the reaction. The reaction mixture was washed with saturated bicarbonate solution (3 x 50 mL) and brine (3 x 50 mL). The organic phase was dried over $MgSO_4$ and the solvents were removed under reduced pressure. The obtained solid was dissolved in the minimal amount of MeOH and precipitated repeatedly in diethyl ether to remove residual DMF. The crude product was purified by column chromatography (SiO_2, 0-2 vol% MeOH in $CHCl_3$, R_f (5 vol% MeOH in $CHCl_3$) = 0.4–0.1; TLC plates were analyzed using 254 nm UV light and $KMnO_4$ stain) yielding 1.0 g (0.66 mmol, 88 %) of the *t*-butyl protected ligand **4**.

For deprotection, TFA (3 mL) and demineralized water (0.3 mL) were added to **4** (0.55 g, 0.36 mmol). The reaction mixture was mechanically stirred at 25 °C for 12 h. After confirmation of complete deprotection by LC-MS analysis, diethyl ether (250 mL) was added and the and the resulting suspension was ultrasonicated before it was allowed to coagulate at −10 °C for 10 hours. The precipitate was collected by filtration over a porosity 4 glass sintered filter, dissolved in demineralized water, and lyophilized to yield **L** as a yellow powder (417 mg, 0,35 mmol, 98%). ^{19}F-NMR spectroscopy revealed residual TFA and HPF_6, which were quantified using hexafluoroisopropanol (HFIP) as an internal standard. The remaining reagents were removed upon desalting in a later step (see purification of **M-NDI**).

^{1}H-NMR (500 MHz, D_2O, 343 K) δ(ppm): 8,94 (s, 4 H), 4.44 (t, 4H), 4.08 (s, 8H), 3.84 (s, 4H), 3.83 (s, 4H), 3.75 (t, 8H), 3.71 (t, 8H), 3.56 (t, 4H), 3.42 (pt, 16H), 2.06 (quin, 4H), 1.96 (quin, 4H). ^{13}C-NMR (500 MHz, D_2O, 343 K) δ(ppm): 25.07, 26.39, 39.47, 41.03, 48.66, 48.90, 50.19, 50.51, 55.05, 55.12, 55.76, 115.74, 118.06, 126.45, 131.39, 163.16, 164.42, 171.70 (m). HRMS(ESI+) for $C_{54}H_{76}N_{12}O_{18}$ (*m/z*): $[M+H]^+$ calc. 1181.5474, found 1181.5476; $[M+2H]^{2+}$ calc. 591.2773, found 591.2785.

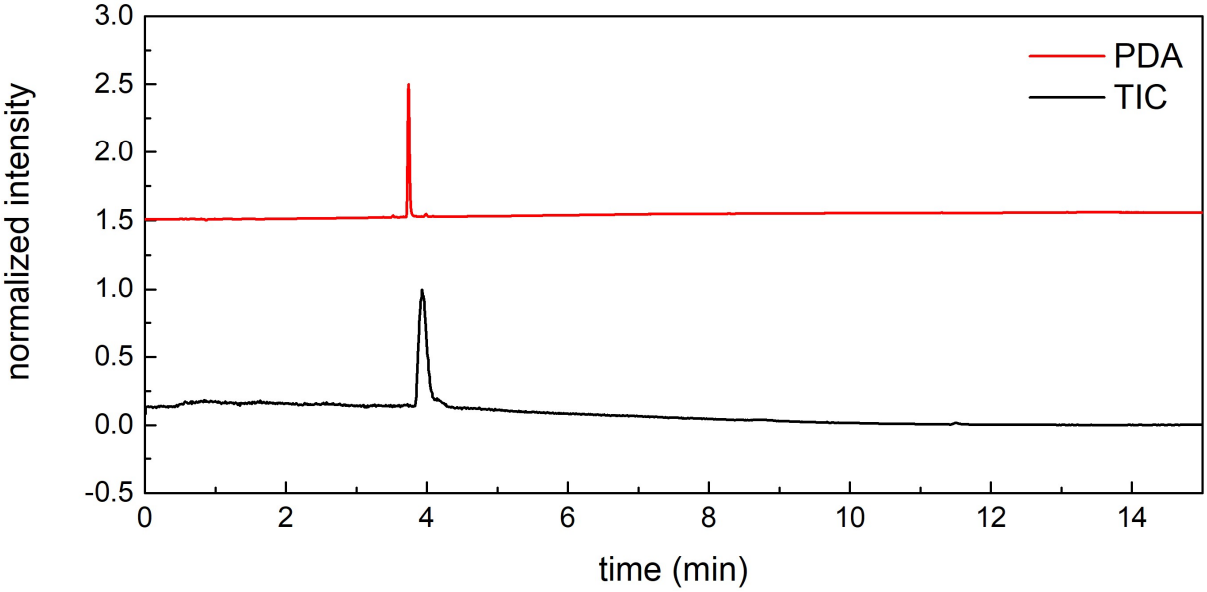

Figure 2.9 | HPLC. Chromatograms (0.5 mL/min, 2-100% ACN in water) of the ligand **NDI** with photo diode array (PDA, red line) total ion current (TIC, black line) detection. Intensities are normalized. The PDA signal is shifted by 1.5 for better visualization.

Synthesis of the target complexes [M-NDI]

In a pressure-tight 10 mL microwave-vial, a solution of **NDI** (0.10 g, 85 mmol, 1.0 eq.) in demineralized water (3 mL), the respective metal(III) trichloride hexahydrate (4 eq.) in demineralized water (2 mL) and aqueous KOH (1M, 0.64 mL, 15 eq.) were added. The reaction mixture was heated for 15 min at 120 °C under microwave irradiation and mechanical stirring. At 25 °C, solid NH_4Cl (50 mg) was added and the mixture was kept stirring for 24 hours. If necessary, the pH was adjusted to 6-8 using aqueous KOH (1 M) before the solvent was removed by lyophilization. The solid residue was taken up in MeOH (10 mL) and centrifuged (3 x 5 min at 6000 G). The obtained solutions were combined, and the solvent was removed under reduced pressure at 25 °C. The crude complexes were desalted by filtration over Sephadex™ G-10 gel in aqueous medium. NDI containing fractions were identified by their fluorescence in response to a 405 nm laser pointer. Salt containing fractions were identified by testing the presence of (1) chloride ions and (2) free lanthanide ions. Therefore, 50 µL of the respective fractions were added to (1) 200 µL of aq. $AgNO_3$ solution (0.1 M), leading to immediate precipitation in the presence of chloride-containing salts and (2) 100 µL of xylenol orange solution[50] (30 mg/mL in acetic acid buffer at pH 5.8), indicating the presence of free lanthanide ions by a color change from yellow to purple. The purified compounds **M-NDI** were lyophilized to yield the compounds as yellow-brownish powders (52-61 mg, 36-44 %). Residual water (typically around 12-17 wt%) was quantified by TGA and considered accordingly by correcting yields and sample masses when preparing solutions. For diamagnetic ions (Y^{3+}, La^{3+}, Lu^{3+}), the absence of TFA and HPF_6 was confirmed by ^{19}F-NMR.

Y-NDI

Yield 29 %. HRMS(ESI+) for $Y_2C_{54}H_{70}N_{12}O_{18}$ (*m*/*z*): $[M+2H]^{2+}$ calc. 677.1597, found 377.1595; $[M+3H]^{3+}$ calc. 451.7756, found 451.7755. MS(MALDI+) for $Y_2C_{54}H_{70}N_{12}O_{18}$ (*m*/*z*): $[M+H]^+$ calc. 1353.31, found 1354.53. Elemental analysis calc. for $Y_2C_{54}H_{70}N_{12}O_{18}$ + 13.5 wt% H_2O: %C = 41.47, %H = 6.02, %N = 10.74, found: %C = 41.10, %H = 6.06, %N = 10.78.

La-NDI

Yield 38 %. HRMS(ESI+) for $La_2C_{54}H_{70}N_{12}O_{18}$ (*m*/*z*): $[M+2H]^{2+}$ calc. 727.1602, found 727.1598; $[M+3H]^{3+}$ calc. 485.1092, found 485.1092. MS(MALDI+) for $La_2C_{54}H_{70}N_{12}O_{18}$ (*m*/*z*): $[M+H]^+$ calc. 1453.31, found 1455.15. Elemental analysis calc. for $La_2C_{54}H_{70}N_{12}O_{18}$ + 12.0 wt% H_2O: %C = 39.28, %H = 5.62, %N = 10.18, found: %C = 39.00, %H = 5.67, %N = 10.49.

Gd-NDI

Yield 41 %. HRMS(ESI+) for $Gd_2C_{54}H_{70}N_{12}O_{18}$ (*m*/*z*): $[M+2H]^{2+}$ calc. 746.1759, found 746.1775; $[M+3H]^{3+}$ calc. 497.7883, found 497.7885. MS(MALDI+) for $Gd_2C_{54}H_{70}N_{12}O_{18}$ (*m*/*z*): $[M+H]^+$ calc. 1493.35, found 1492.66. TGA (25-275 °C): weight loss 14.51 wt%. Elemental analysis calc. for $Gd_2C_{54}H_{70}N_{12}O_{18}$ + 14.51 wt% H_2O: %C = 37.22, %H = 5.68, %N = 9.64, found: %C = 36.92, %H = 5.41, %N = 9.82.

Tb-NDI

Yield 38 %. HRMS(ESI+) for $Tb_2C_{54}H_{70}N_{12}O_{18}$ (*m*/*z*): $[M+2H]^{2+}$ calc. 747.1792, found 747.1794; $[M+3H]^{3+}$ calc. 498.4552, found 498.4553. MS(MALDI+) for $Tb_2C_{54}H_{70}N_{12}O_{18}$ (*m*/*z*): $[M+H]^{+}$ calc. 1493.35, found 1494.31. TGA (25-275 °C): weight loss 14.32 wt%. Elemental analysis calc. for $Tb_2C_{54}H_{70}N_{12}O_{18}$ + 14.32 wt% H_2O: %C = 37.22, %H = 5.66, %N = 9.65, found: %C = 37.51, %H = 5.27, %N = 9.92.

Dy-NDI

Yield 41 %. HRMS(ESI+) for $Dy_2C_{54}H_{70}N_{12}O_{18}$ (*m*/*z*): $[M+2H]^{2+}$ calc. 751.1818, found 751.1830; $[M+3H]^{3+}$ calc. 501.1236, found 501.1239. MS(MALDI+) for $Dy_2C_{54}H_{70}N_{12}O_{18}$ (*m*/*z*): $[M+H]^{+}$ calc. 1501.36, found 1502.68. Elemental analysis calc. for $Dy_2C_{54}H_{70}N_{12}O_{18}$ + 12.5 wt% H_2O: %C = 37.83, %H = 5.51, %N = 9.80, found: %C = 37.49, %H = 5.31, %N = 9.88.

Ho-NDI

Yield 36 %. HRMS(ESI+) for $Ho_2C_{54}H_{70}N_{12}O_{18}$ (*m*/*z*): $[M+2H]^{2+}$ calc. 753.1842, found 753.1838; $[M+3H]^{3+}$ calc. 502.4585, found 502.4587. MS(MALDI+) for $Ho_2C_{54}H_{70}N_{12}O_{18}$ (*m*/*z*): $[M+H]^{+}$ calc. 1505.36; found 1506.62. Elemental analysis calc. for $Ho_2C_{54}H_{70}N_{12}O_{18}$ + 14.2 wt% H_2O: %C = 36.97, %H = 5.61, %N = 9.58, found: %C = 36.66, %H = 5.41, %N = 9.57.

Er-NDI

Yield 36 %. HRMS(ESI+) for $Er_2C_{54}H_{70}N_{12}O_{18}$ (*m*/*z*): $[M+2H]^{2+}$ calc. 755.1852, found 755.1858; $[M+3H]^{3+}$ calc. 503.7925, found 503.7931. MS(MALDI+) for $Er_2C_{54}H_{70}N_{12}O_{18}$ (*m*/*z*): $[M+H]^{+}$ calc. 1509.36, found 1510.66. Elemental analysis calc. for $Er_2C_{54}H_{70}N_{12}O_{18}$ + 14.2 wt% H_2O: %C = 36.86, %H = 5.60, %N = 9.55, found: %C = 37.18, %H = 5.38, %N = 9.66.

Lu-NDI

Yield 39 %. HRMS(ESI+) for $Lu_2C_{54}H_{70}N_{12}O_{18}$ (*m*/*z*): $[M+2H]^{2+}$ calc. 763.1946, found 763.1947; $[M+3H]^{3+}$ calc. 509.1322, found 509.1325. MS (MALDI+) for $Lu_2C_{54}H_{70}N_{12}O_{18}$ (*m*/*z*): $[M+H]^{+}$ calc. 1525.38, found 1526.82. Elemental analysis calc. for $Lu_2C_{54}H_{70}N_{12}O_{18}$ + 14.0 wt% H_2O: %C = 36.58, %H = 5.55, %N = 9.48, found: %C = 36.91, %H = 5.19, %N = 9.78.

2.9.3 NMR spectroscopy

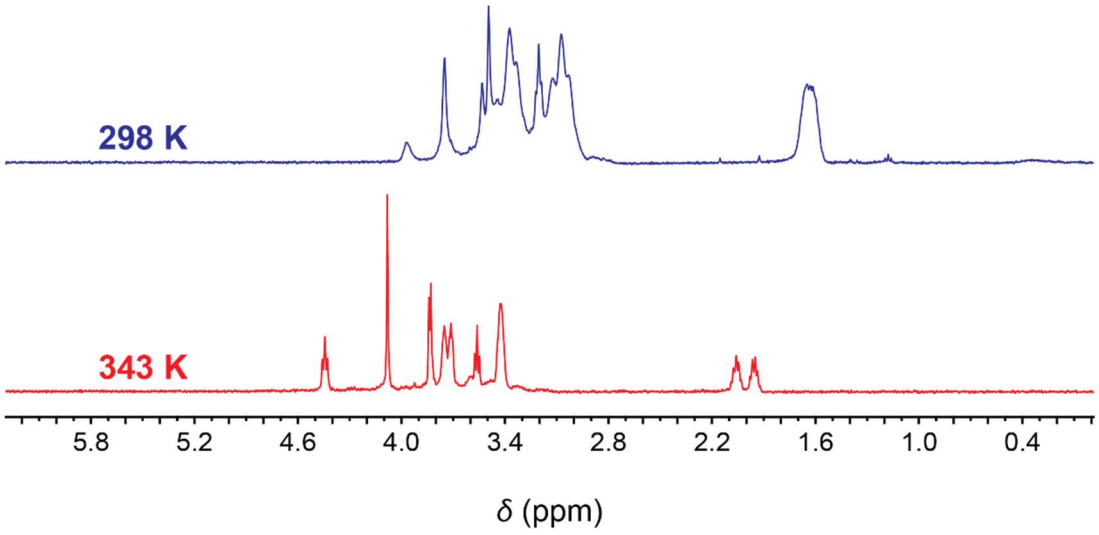

Figure 2.10 | Variable temperature NMR. Extracts of ^{1}H NMR spectra of **NDI** (500 MHz, 1 mg/mL, D_2O) at 298 K (blue, top) and 343 K (red, bottom).

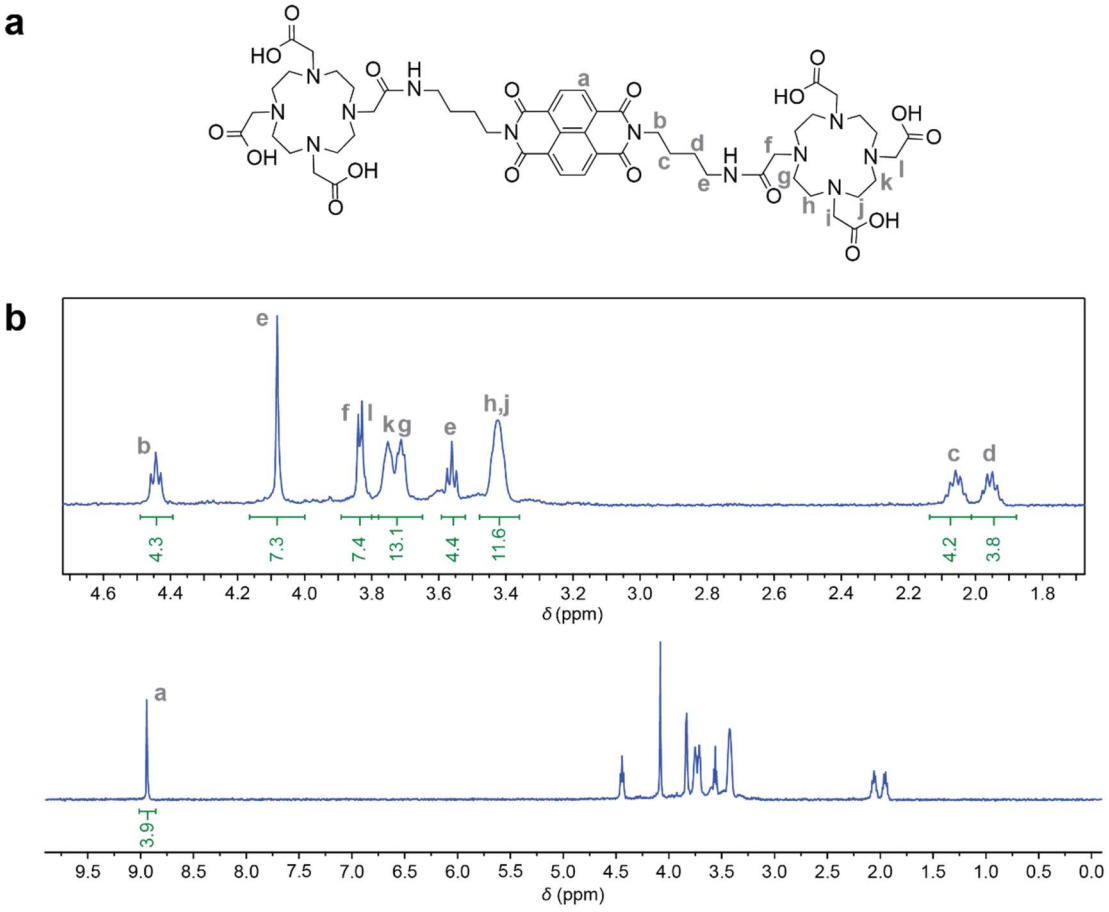

Figure 2.11 | Diffusion ordered ^{1}H-NMR. 1D DOSY of **NDI** (500 MHz, 1 mg/mL, D_2O, 343 K). Grey letters are to attribute the proton signals. For clarity, only protons of one half of the molecule are assigned.

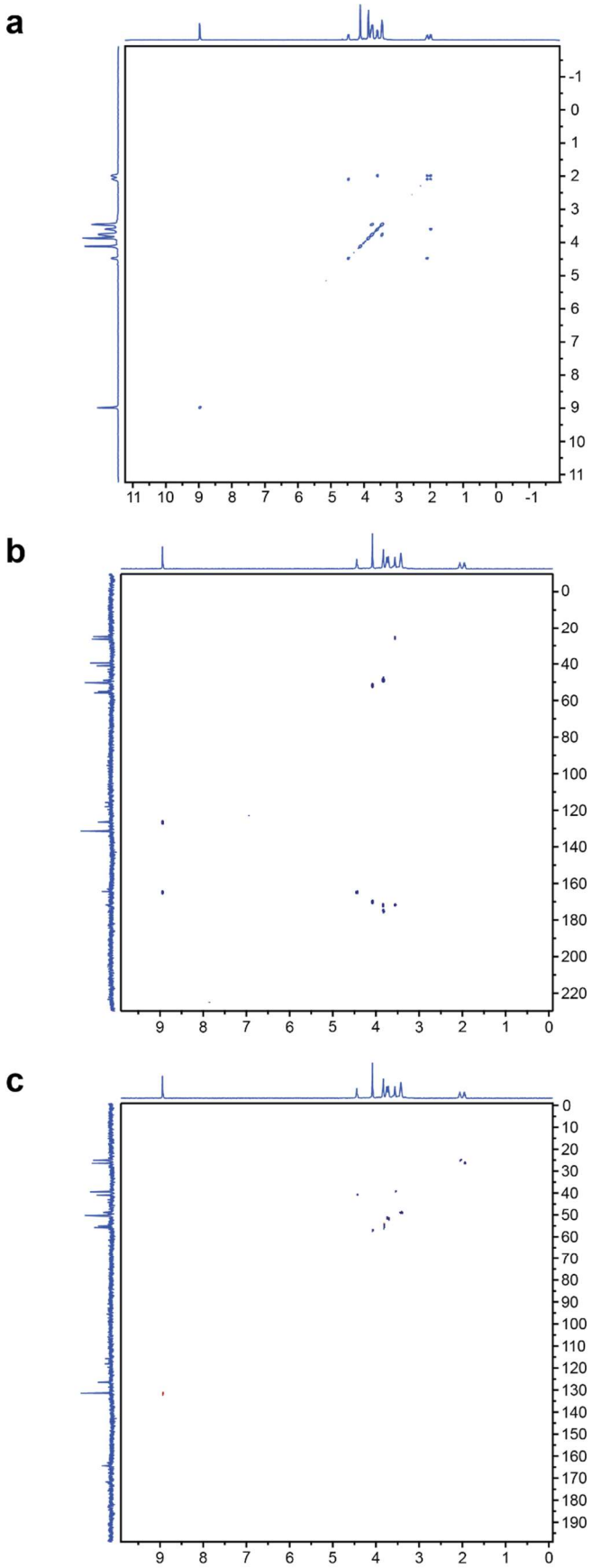

Figure 2.12 | 2D-NMR spectroscopy. (a) COSY, (b) HMBC, and (c) HSQC spectra of **NDI** (500 MHz, 1 mg/mL, D_2O, 343 K).

2.9.4 Infrared spectroscopy

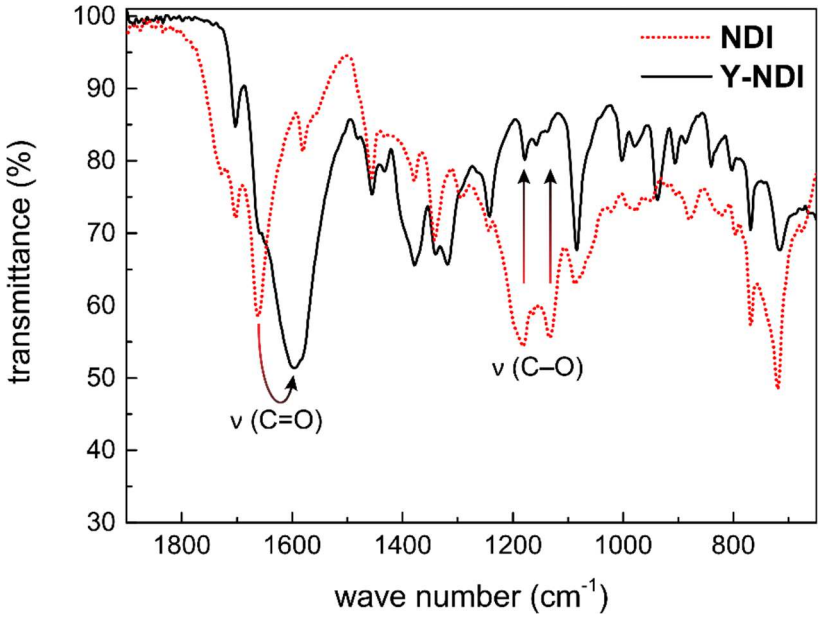

Figure 2.13 | Infrared spectroscopy. FT-IR spectra of **NDI** (red dotted line) and **Y-NDI** (black full line). Raw data was smoothed using a 5 pts Savitzky-Golay filter.

2.9.5 Mass spectrometry

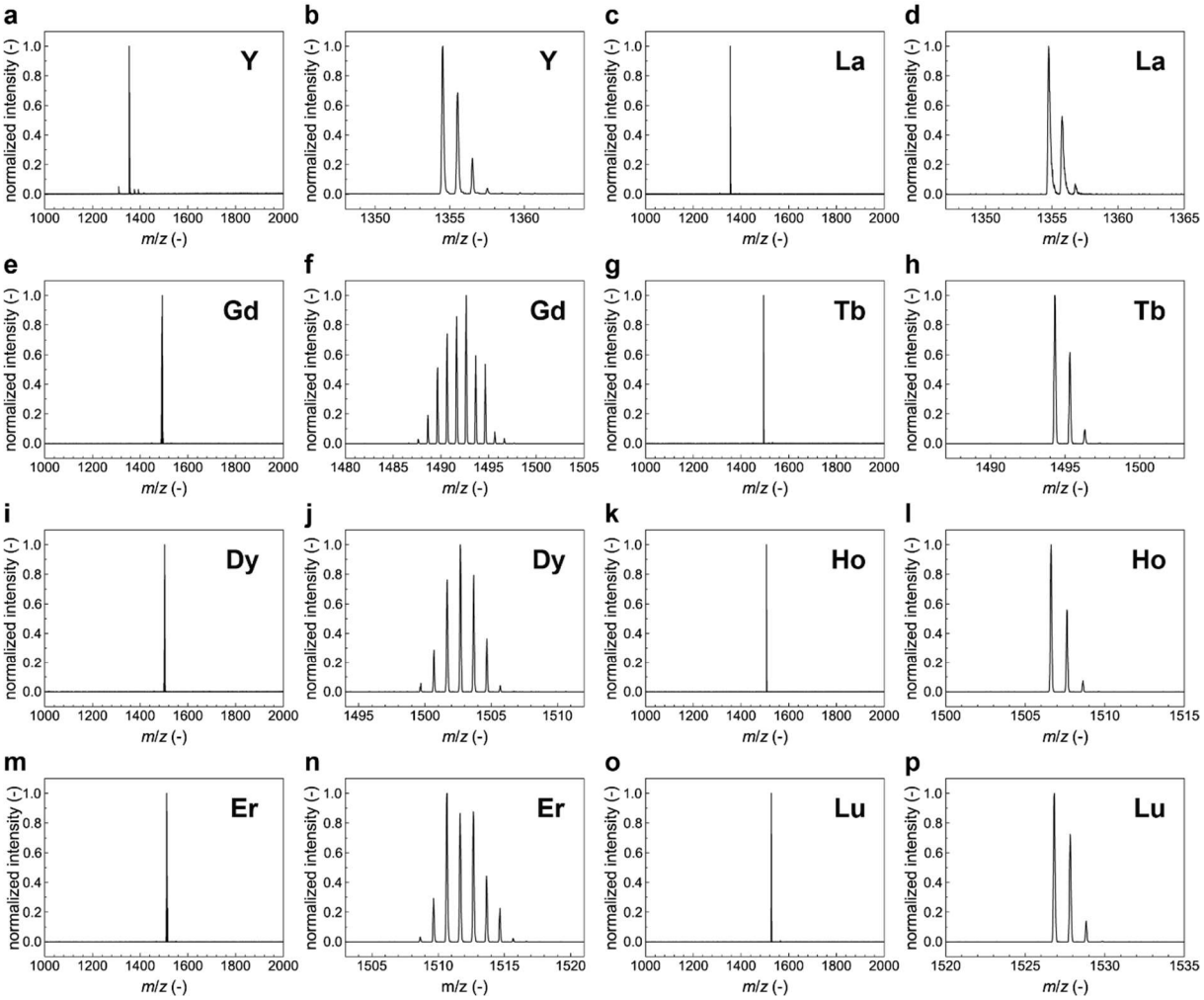

Figure 2.14 | MALDI-TOF mass spectrometry. For each molecule **M-NDI**, one spectrum over the whole recorded range of *m*/*z* 1000 to *m*/*z* 2000, and a zoom to the respective $[M+H]^+$ are shown. Spectra were recorded in positive mode using CHCA as a matrix. (a,b) **Y-NDI**. (c,d) **La-NDI**. (e,f) **Gd-NDI**. (g,h) **Tb-NDI**. (i,j) **Dy-NDI**. (k,l) **Ho-NDI**. (m,n) **Er-NDI**. (o,p) **Lu-NDI**.

2.9.6 SQUID magnetometry

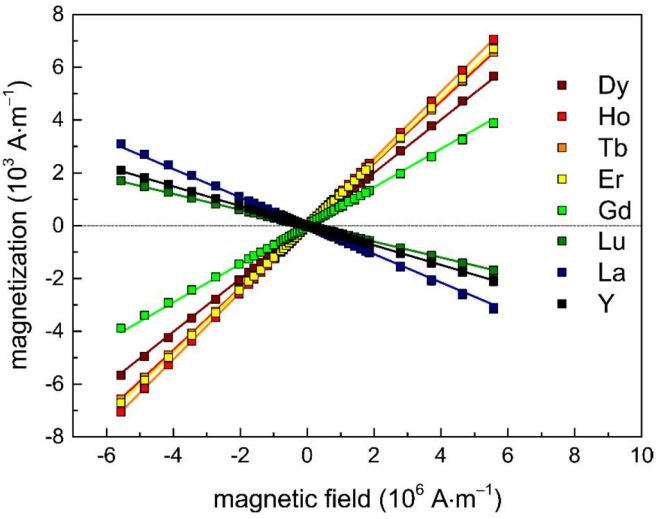

Figure 2.15 | Field dependent magnetometry. *H*-dependent magnetic moment for all ions **M-NDI** and the respective linear fit. The magnetic susceptibility is obtained from the slope.

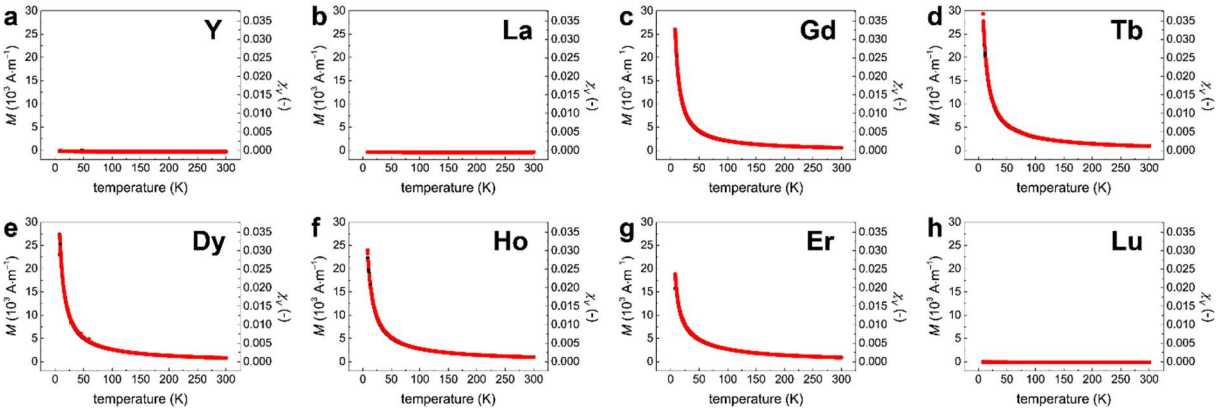

Figure 2.16 | Temperature dependent magnetometry. *T*-dependent magnetic moment for all ions **M-NDI**. Black squares represent zero-field cooling (ZFC), red circles field-cooling (FC) curves.

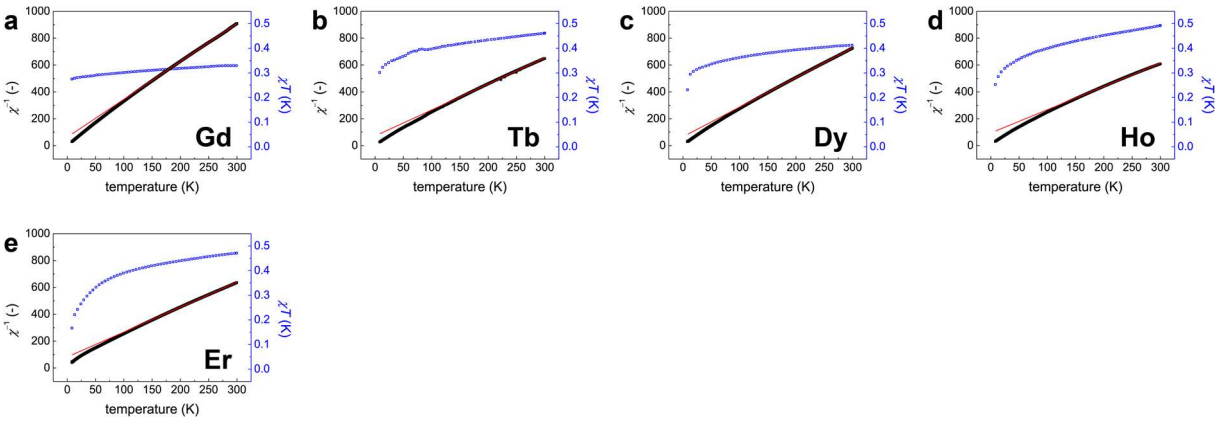

Figure 2.17 | Curie-Weiss fit and χT plots. Linear regression of the reciprocal volumetric susceptibility (red line and black squares, respectively) and temperature dependent χT values (blue squares) of (a) **Gd-NDI**, (b) **Tb-NDI**, (c) **Dy-NDI**, (d) **Ho-NDI**, and (e) **Er-NDI**. The raw data was corrected for the diamagnetic contribution from the NDI core as shown in Figure 2.4d.

Table 2.4 | χT values. Experimental and theoretical χT values per paramagnetic ion **M** in **M-NDI** at 298 K.

M	χT (K) [exp.]	χT (emu·K·mol^{-1}) [exp.]	χT [40] (emu·K·mol^{-1}) [theor.]
Gd	0.33	8.7	7.9
Tb	0.46	12.1	11.8
Dy	0.41	10.8	14.2
Ho	0.49	12.9	14.1
Er	0.47	12.4	11.5

2.9.7 Luminescence spectroscopy

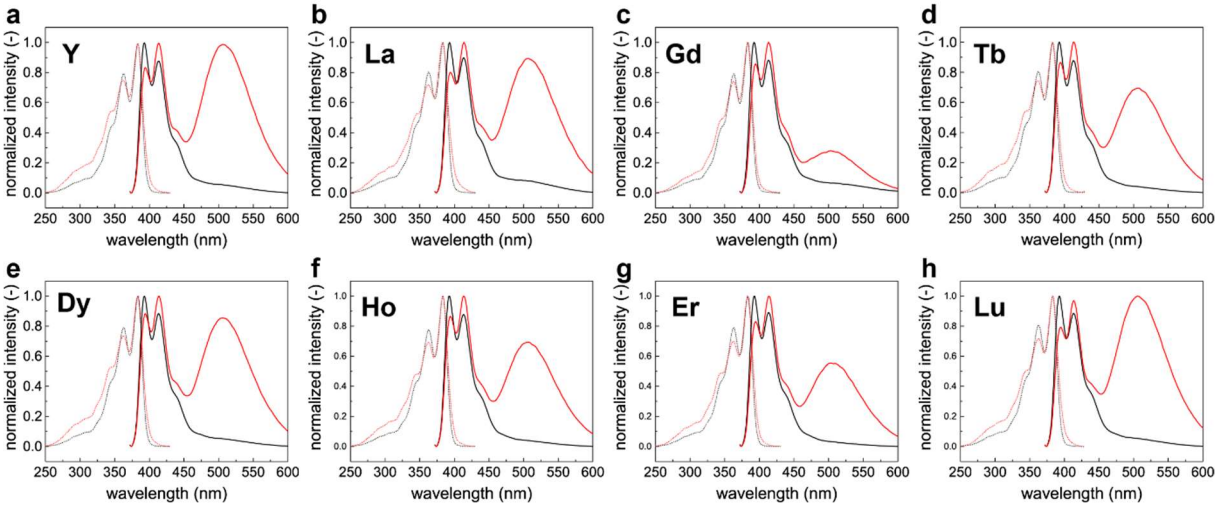

Figure 2.18 | Luminescence. Excitation and emission spectra (dotted and full lines, respectively) of 100µM (black lines) and 10 mM (red lines) aqueous solutions of all molecules **M-NDI**. Excitation spectra were measured at an emission wavelength of 440 nm, emission spectra were recorded at an excitation wavelength of 362 nm.

2.9.8 3D structure simulations

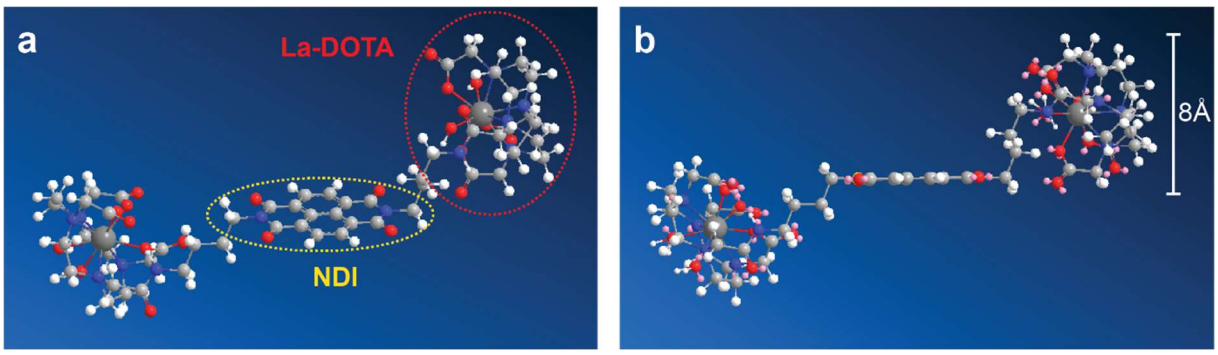

Figure 2.19 | Simulated 3D structure of La-NDI. Three-dimensional molecular structure after an MM2 energy minimization in 10000 iterations, generated in Chemdraw 3D. The NDI core unit (yellow) and the La-DOTA cage (red) are highlighted by dashed circles in panel a. La^{3+} was entered as 9-coordinate, including two bound water molecules per ion. The diameter of the DOTA cage measures approximately 8 Å.

2.9.9 Thermodynamic models

2.9.9.1 Concentration dependent isodesmic model

Concentration dependent *R* plots were fitted non-linearly by applying a described theoretical model[5] following equation (2.i), using a non-linear least squared iteration (Levenberg-Marquardt algorithm).

$$\alpha = 1 - \frac{2\,K_{eq}\cdot c + 1 - \sqrt{4\,K_{eq}\cdot c + 1}}{2\,K_{eq}^2\cdot c^2} \tag{2.i}$$

Where α is the unitless degree of polymerization, K_{eq} the equilibrium constant in M^{-1}, and c the concentration in M. The degree of supramolecular polymerization α is obtained by normalization of the respective variable that is used to quantify the aggregation process. Consequently, α will be 1 if all the molecules are in polymeric state, and 0 if all molecules are in monomeric state. Here, α is derived from the ratio *R* of absorbance intensities of the S_0-S_1(0-1) and S_0-S_1(0-0) transitions, following equation (2.ii),

$$\alpha = \frac{R - R_m}{R_P - R_m} \tag{2.ii}$$

Combining equation (2.i) and (2.ii), we obtain the fitting function (2.iii) with the three parameters K_{eq}, R_m, and R_p.

$$R(c) = \left[1 - \frac{2\,K_{eq}\cdot c + 1 - \sqrt{4\,K_{eq}\cdot c + 1}}{2\,K_{eq}^2\cdot c^2}\right]\cdot\left(R_p - R_m\right) + R_m \tag{2.iii}$$

The equilibrium constant K_{eq} can be related to the free Gibbs energy ΔG, following equation (2.iv), where R = 8.314 $J\cdot mol^{-1}\cdot K^{-1}$ is the gas constant and *T* the temperature in K (here *T* = 298 K).[7]

$$\ln K_{eq} = -\frac{\Delta G}{RT} \tag{2.iv}$$

Figure 2.20 shows concentration dependent *R* values and the respective fitted curves for all molecules **M-NDI**. The results for the fitted parameters are listed in Table 2.5.

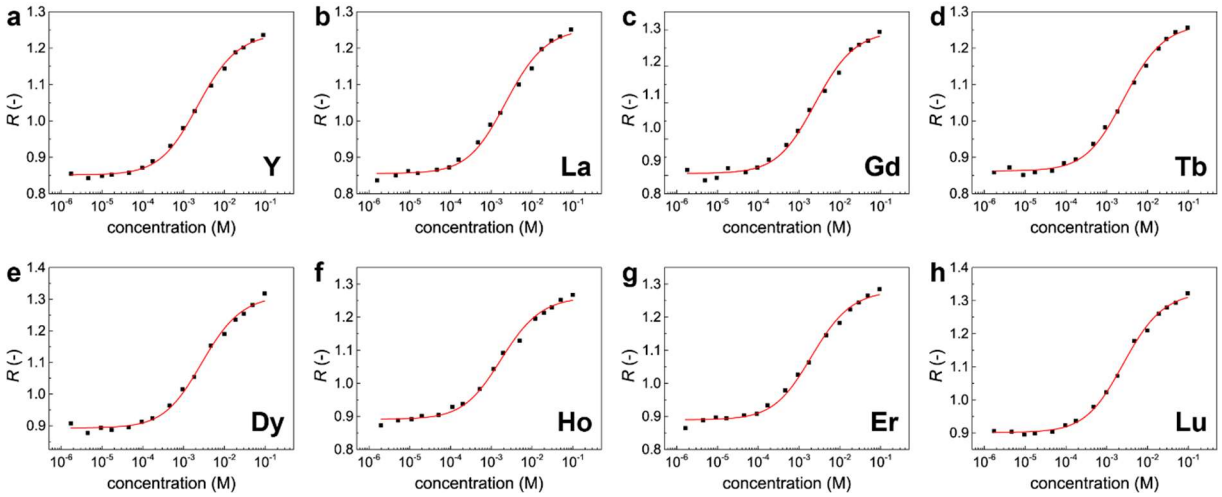

Figure 2.20 | Concentration dependent isodesmic fits. Plot of the S_0-S_1(0-1)/S_0-S_1(0-0) absorbance ratio R as a function of concentration and the corresponding isodesmic fits (red lines) for all molecules **M-NDI**.

Table 2.5 | Concentration dependent fitting results. Fitted parameters of K_{eq}, R_m, and R_p, and the derived parameter ΔH for all ions **M** in **M-NDI** and the corresponding standard errors.

M	K_{eq} (M^{-1})	R_m (-)	R_p (-)	ΔH ($kJ \cdot mol^{-1}$)
Y	253 ± 17	0.8514 ± 0.0030	1.2403 ± 0.0048	-13.71 ± 0.17
La	249 ± 26	0.8553 ± 0.0048	1.2535 ± 0.0078	-13.67 ± 0.26
Gd	228 ± 26	0.8898 ± 0.0050	1.2973 ± 0.0084	-13.45 ± 0.28
Tb	215 ± 17	0.8622 ± 0.0035	1.2659 ± 0.0061	-13.31 ± 0.20
Dy	203 ± 22	0.8929 ± 0.0050	1.3112 ± 0.0086	-13.16 ± 0.27
Ho	324 ± 37	0.8913 ± 0.0051	1.2607 ± 0.0072	-14.32 ± 0.28
Er	277 ± 30	0.8898 ± 0.0050	1.2806 ± 0.0077	-13.93 ± 0.27
Lu	220 ± 15	0.9013 ± 0.0032	1.3256 ± 0.0054	-13.37 ± 0.17

We observe slight variations in R_m and R_p values for the different ions (0.85–0.90 and 1.24–1.33, respectively). At first glance, this is surprising, as we are looking at transitions of the NDI core unit, which is identical for all molecules. R_m values are generally expected to be around 0.82 ± 0.01, which is the R we measure for the intermediate bis(*n*-butylammonium) naphthalene diimide **3**, a charged and thus non-assembling NDI, at concentrations up to 1 mM. Nevertheless, the obtained equilibrium constants K_{eq} and enthalpies ΔH, are in good agreement. The difference between the two values R_m and R_p is around 0.4 for all ions, which means that the spectra are uniformly shifted along the R axis. When normalized to the degree of supramolecular polymerization α, the curves are identical within the experimental error. Therefore, we assume that the discrepancies are not the result of the aggregation process, but of a spectral overlap of the NDI core absorbance and the absorbance of the respective complexed ions. In the examined concentration range, the absorbances of the salt solutions are below the detection limit. However, it has been reported that the absorbance of lanthanide ions can undergo an increase in intensity and a shift in wavelength as compared to free ions, depending on the ligand structure and their hydration.[8,9] Moreover it is possible, that the solutions are slightly photo-reduced, which causes irreversible assembly.[51]

2.9.9.2 Concentration dependent two-constant nucleated assembly model

In this cooperative model, two equilibrium constants for both the nucleation phase K_{nuc}, and the elongation phase K_e are considered. Their ratio is given by the cooperativity constant σ.

$$\sigma = \frac{K_{nuc}}{K_e} \tag{2.v}$$

The degree of polymerization α is given by equation (2.vi). Note that for $\sigma = 1$ ($K_{eq} = K_{nuc} = K_e$, isodesmic), the expression simplifies to the isodesmic analog given in equation (2.iii) in section 2.9.9.1.

$$\alpha = 1 - \frac{2\,K_e \cdot c + \sigma - \sqrt{4\ \cdot \sigma \cdot K_e \cdot c + \sigma^2}}{2\,K_e^2 \cdot c^2} \tag{2.vi}$$

Considering the definition of the degree of supramolecular polymerization α (equation (2.ii) in section 2.9.9.1), we obtain the fitting function (2.x) with the four fitting parameters K_e, σ, R_m, and R_p.

$$R(c) = \left[1 - \frac{2\,K_e \cdot c + \sigma - \sqrt{4 \cdot \sigma \cdot\ K_e \cdot c + \sigma^2}}{2\,K_e^2 \cdot c^2}\right] \cdot \left(R_p - R_m\right) + R_m \tag{2.vii}$$

Figure 2.21 shows the resulting cooperative fit (blue line). The isodesmic fit (red, section 2.9.9.1) is added for comparison. Table 2.2 summarizes all fitted parameters and their standard errors.

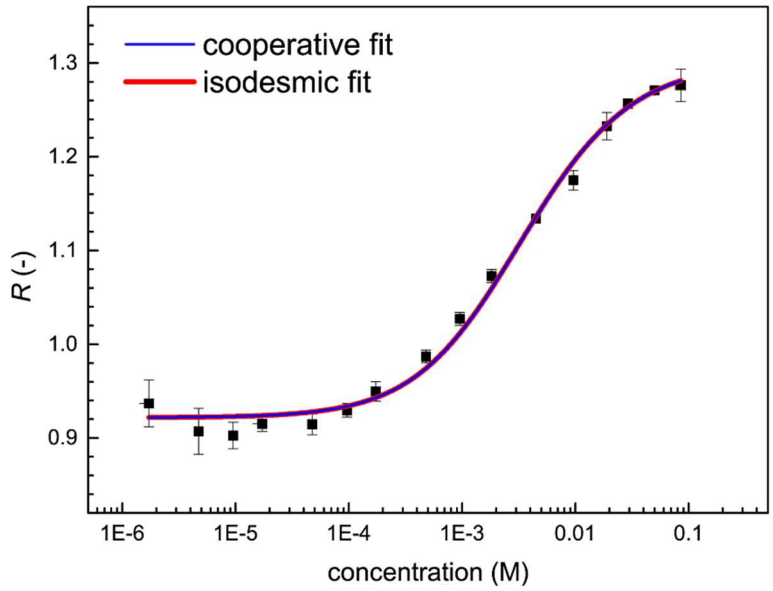

Figure 2.21 | Two-constant nucleated assembly model. Plot of the S_0-S_1(0-1) / S_0-S_1(0-0) absorbance ratio R as a function of concentration and the corresponding cooperative (blue line) and isodesmic fit (red line). Error bars represent standard deviations over three measurements.

Table 2.6 | Two-constant nucleated assembly model. Fitted parameters K_e, σ, R_m, *and* R_p as well as the derived parameter K_{nuc} and their standard errors.

K_e (M^{-1})	σ	K_{nuc} (M^{-1})	R_m (-)	R_p (-)
219 ± 9668	1.25 ± 56	273 ± 24415	0.8232 ± 21	1.301 ± 0.0071

2.9.9.3 Temperature dependent van der Schoot model

Temperature-dependent multi-concentration data was fitted non-linearly by applying a described theoretical model[6] following equation (2.viii), where α is the unitless degree of supramolecular polymerization, ΔH the enthalpy of supramolecular polymerization, T the temperature in K, R = 8.314 $J \cdot mol^{-1} \cdot K^{-1}$ the gas constant, and T_m the concentration dependent melting temperature. The term "melting temperature", the temperature where $\alpha = 0.5$, is used in analogy to physical phase transitions, if we consider the assembly process the transition of monomer to polymer or vice versa.

$$\alpha = \frac{1}{1 + e^{-0.908 \cdot \Delta H \cdot \frac{T - T_m}{R T_m^2}}} \tag{2.viii}$$

α was obtained from R following equation (2.ii). To collapse several data sets obtained for different concentrations in a single multi-fit, the absolute temperature T was transformed to the melting temperature T_m yielding the unitless reduced temperature T_r, as described by equation (2.ix).

$$T_r = \Delta H \, \frac{T - T_m}{R T_m^2} \tag{2.ix}$$

Using a custom MATLAB® algorithm (see section 2.9.10), we obtain ΔH, T_m for each concentration, and R_m as fitted parameters. As we can only trace fractions of the sigmoidal curves (generally $\alpha < 0.6$), R_p was fixed individually for each ion to the respective R_p values obtained from concentration dependent fitting (see Table 2.5).

Figure 2.22 shows the resulting plots of α as a function of T_r, and the respective fitted curves for all molecules **M-NDI**. The results for the fitted parameters are listed in Table 2.7.

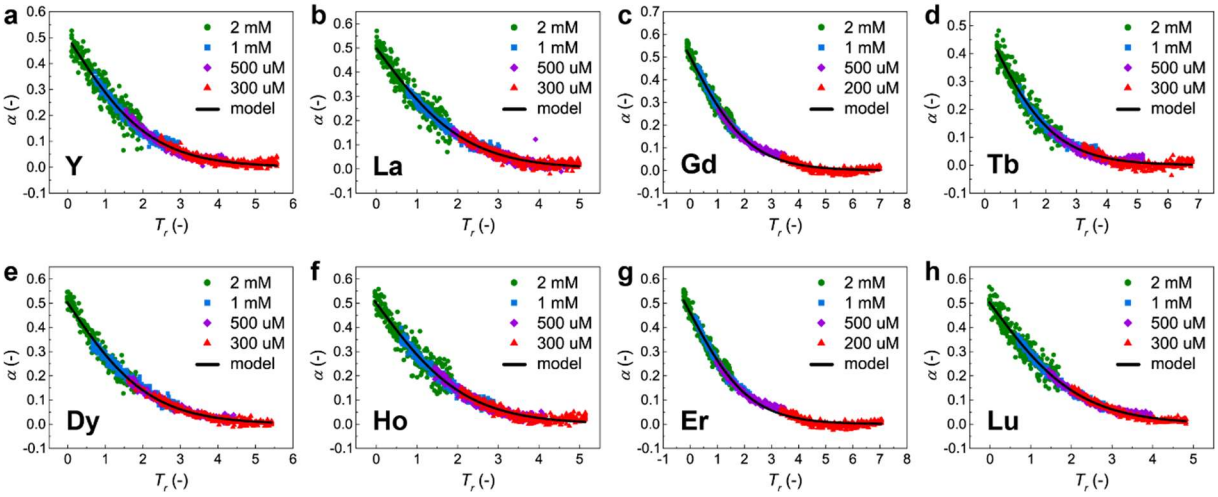

Figure 2.22 | Temperature dependent isodesmic fits. The degree of supramolecular polymerization α as a function of the reduced temperature T_r, obtained from the model, and the corresponding isodesmic fits for all molecules **M-NDI**.

Table 2.7 | Temperature dependent fitting results. Fitted parameters ΔG, R_m, and T_m for all ions **M** in **M-NDI** and the corresponding 95% confidence intervals.

M	ΔG / kJ·mol^{-1}	R_m / -	T_m / K c = 2mM	T_m / K c = 1mM	T_m / K c = 500µM	T_m / K c = 300µM	T_m / K c = 200µM
Y	-13.76 ± 0.43	0.8881 ± 0.0014	274.7 ± 0.9	251.2 ± 1.1	229.2 ± 1.3	211.8 ± 1.6	n/a
La	-13.01 ± 0.43	0.9255 ± 0.0013	274.3 ± 1.0	245.9 ± 1.2	219.0 ± 1.5	215.4 ± 1.5	n/a
Gd	-13.39 ± 0.26	0.9201 ± 0.0010	282.8 ± 0.7	264.8 ± 0.7	239.2 ± 0.9	n/a	196.2 ± 2.1
Tb	-13.96 ± 0.49	0.9372 ± 0.0010	261.5 ± 1.1	239.1 ± 1.4	217.5 ± 1.5	200.5 ± 2.2	n/a
Dy	-14.22 ± 0.38	0.9182 ± 0.0014	278.8 ± 0.8	253.2 ± 1.0	228.4 ± 1.1	215.5 ± 1.4	n/a
Ho	-14.40 ± 0.46	0.9282 ± 0.0015	279.6 ± 0.9	254.9 ± 1.1	233.0 ± 1.8	219.7 ± 1.5	n/a
Er	-14.20 ± 0.34	0.9137 ± 0.0011	281.2 ± 0.8	255.3 ± 0.9	234.9 ± 1.1	n/a	195.2 ± 2.9
Lu	-12.87 ± 0.35	0.9229 ± 0.0016	278.5 ± 0.8	250.0 ± 1.0	229.2 ± 1.1	216.8 ± 1.3	n/a

Typically, R was determined as a function of temperature for the four concentrations 2 mM, 1 mM, 500 µM and 200 µM. In some cases, however, including 200 µM did not yield a satisfactory fit. 300 µM solutions were used instead. Unexpectedly, R_m seems to increase with temperature at low concentrations and elevated temperatures (above ~ 330 K). This can be a consequence of entropic effects or dilution induced aggregation. The latter is a phenomenon, which is commonly observed in protein folding[52], and has been observed in multi-component supramolecular systems[53]. By diluting, a denatured protein will refold, as the concentration of the denaturant decreases. In our case, "renaturation" could be due to the increasing hydrophilicity of the solvent, which would drive the hydrophobic NDI core to assemble. For this reason, we consider R_m values from concentration dependent fitting more reliable, when comparing R_m values from concentration and temperature dependent fitting.

2.9.9.4 Glew-Clarke model

The Glew-Clarke model[44,54] was applied by non-linear fitting following equation (2.x), using a non-linear least squared iteration (Levenberg-Marquardt algorithm).

$$\ln K_{eq}(T) = \ln K_{eq}(\theta) + \frac{\Delta H(\theta)}{\mathrm{R}} \cdot \left(\frac{1}{\theta} - \frac{1}{T}\right) + \frac{\Delta C_p(\theta)}{\mathrm{R}} \cdot \left(\frac{\theta}{T} - 1 + \ln\frac{T}{\theta}\right) \qquad (2.x)$$

It includes an arbitrarily chosen reference temperature θ, here $\theta = 298\ K$, and the gas constant $\mathrm{R} = 8.314\ \mathrm{J \cdot mol^{-1} \cdot K^{-1}}$, yielding the enthalpy of supramolecular polymerization ΔH and the heat capacity change ΔC_p as fitting parameters. The entropic contribution $-T\Delta S$ will be the difference between the Gibbs free energy ΔG, which is directly obtained from the temperature-dependent equilibrium constants K_{eq} according to equation (2.iv), and the enthalpy ΔH obtained from the Glew-Clark fit, equation (2.x). Temperature-dependent equilibrium constants $K_{eq}(T)$ were obtained from concentration dependent fits from 298 to 368 K in intervals of 1 K, for four concentrations (2 mM, 1 mM, 500 µM, and 300 or 200 µM) using equation (2.iii).

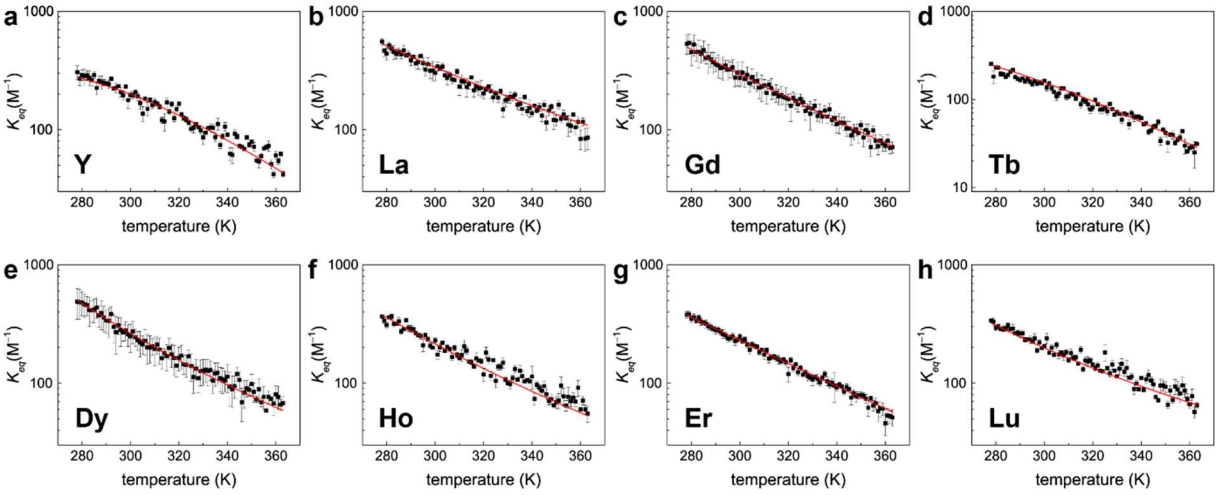

Figure 2.23 | Glew-Clarke fits. Plots of the equilibrium constants K_{eq} as a function of temperature, and the corresponding Glew-Clarke fits for all molecules **M-NDI**. Error bars represent standard errors from the concentration dependent fit.

2.9.9.5 Van't Hoff model

The classic van't Hoff model was fitted following equation (2.xi).[55]

$$\ln K_{eq}(T) = -\frac{\Delta H}{\mathrm{R}T} + \frac{\Delta S}{\mathrm{R}} \qquad (2.xi)$$

Figure 2.24 shows the van't Hoff fit (blue line) for all molecules **M-NDI**, represented in a logarithmic K_{eq} and a reciprocal T scale**.** The Glew-Clarke fit (red line, see section 2.9.9.4) is added for comparison. The preferred model was determined by the Akaike Information Criterion (AIC, see section 0). The quantitative model comparison is summarized in Table 2.8.

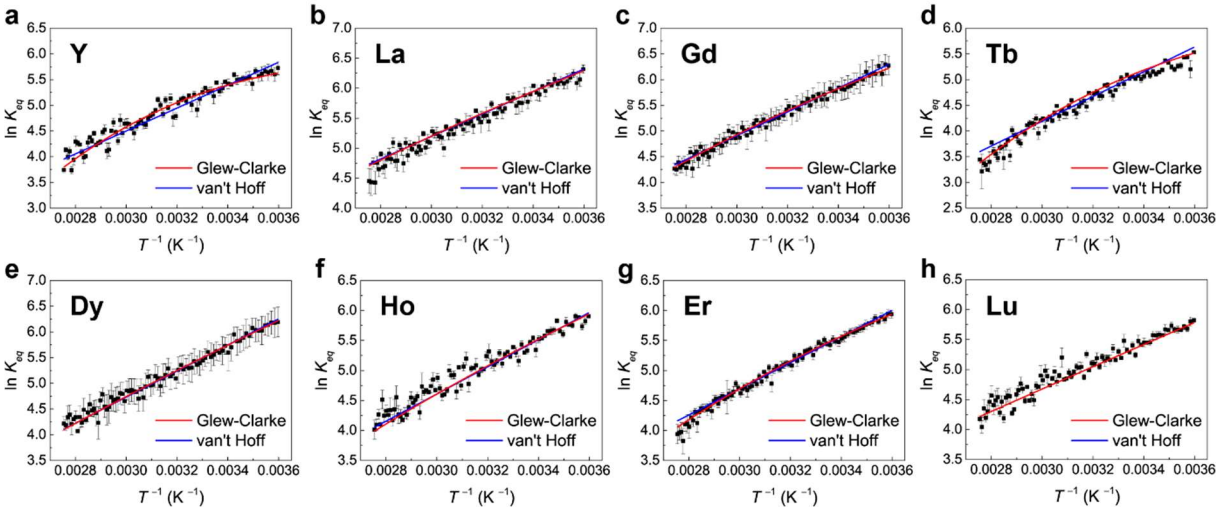

Figure 2.24 | Glew-Clarke and van't Hoff fits. Plots of the logarithmic equilibrium constants K_{eq} as a function of reciprocal temperature, and the corresponding Glew-Clarke (red lines) and Glew-Clarke (blue lines) fits for all molecules **M-NDI**. Error bars represent standard errors from the concentration dependent fit.

The two models yield significantly different values for ΔH for five out of eight molecules (superscript a in Table 2.8). In these cases, the Glew-Clarke model is preferred by a factor of more than 100. For **La-NDI**, **Dy-NDI**, and **Lu-NDI** (superscript b), the respectively obtained values for ΔH are not significantly different from one another and the van't Hoff model is preferred by factors of 1 to 3.

Table 2.8 | Van't Hoff model vs. Glew-Clarke model. Enthalpies of supramolecular polymerization ΔH obtained by van't Hoff and Glew-Clark fits for all molecules **M-NDI**, as well as the respective Akaike weights, preferred models and preference factors obtained from the model comparison using the Akaike Information Criterion. Errors represent 95% confidence intervals ($p \leq 0.05$). [a]within the 95 % confidence interval of the Glew-Clark fitting result. [b]outside the 95 % confidence interval of the Glew-Clarke fitting result.

M	$\Delta H°$ (kJ·mol^{-1})		Akaike weight (-)		preferred	preference
	[van't Hoff]	[Glew-Clarke]	[van't Hoff]	[Glew-Clarke]	model	factor
Y	–18.53 ± 0.62 [a]	–12.92 ± 1.75	$1.3 \cdot 10^{-7}$	1.00	Glew-Clarke	$7.9 \cdot 10^{6}$
La	–15.58 ± 0.62 [b]	–14.95 ± 0.66	0.59	0.41	van't Hoff	1.5
Gd	–19.38 ± 0.59 [a]	–17.52 ± 1.18	0.01	0.99	Glew-Clarke	122
Tb	–20.01 ± 0.74 [a]	–16.59 ± 1.03	$6.1 \cdot 10^{-11}$	1.00	Glew-Clarke	$1.6 \cdot 10^{10}$
Dy	–21.08 ± 0.89 [b]	–20.59 ± 2.59	0.71	0.29	van't Hoff	2.5
Ho	–18.82 ± 0.65 [b]	–18.43 ± 1.00	0.49	0.51	Glew-Clarke	1.02
Er	–18.12 ± 0.45 [a]	–16.67 ± 0.64	$2.9 \cdot 10^{-6}$	1.00	Glew-Clarke	$3.4 \cdot 10^{5}$
Lu	–15.39 ± 0.64 [b]	–15.43 ± 1.05	0.75	0.25	van't Hoff	3.0

2.9.9.6 Akaike's Information Criterion (AIC)

AIC values were obtained from the built-in model comparison option of Origin 9®. The results are given in Table 2.9 and Table 2.10.

Table 2.9 | Model selection for concentration dependent *R* fitting. Residual sum of squares (RSS), numbers of points and parameters, Akaike Information Criterion (AIC), and Akaike weight for the concentration dependent isodesmic and cooperative fits of **Gd-NDI**.

model	RSS	number of points	number of parameters	AIC	Akaike weight
isodesmic	24.27652	16	3	18.31	0.1014
cooperative	24.27652	16	4	22.67	0.8986

Judging from the Akaike weight values, the isodesmic model is 8.9 times more likely to be correct.

Table 2.10 | Model selection for temperature dependent K_{eq} fitting. Residual sum of squares (RSS), numbers of points and parameters, Akaike Information Criterion (AIC), and Akaike weight for the van't Hoff and Glew-Clarke fits of **Gd-NDI**.

model	RSS	number of points	number of parameters	AIC	Akaike weight
van't Hoff	24.85020	86	2	-100.47	0.0081
Glew-Clarke	21.66098	86	3	-110.09	0.9919

Judging from the Akaike weight values, the Glew-Clarke model is 122 times more likely to be correct.

2.9.10 MATLAB® code

The following code is exemplarily for **Gd-NDI**. The bounds for R_p were adapted for every **M** depending on the mean as standard deviation obtained from concentration dependent fitting (values are given in Table 2.5).

2.9.10.1 Function

```
% define function
% isodesmic multifit
% equations taken from E. W. Meijer, et al. Chem. - A Eur. J. 2010, 16,
362-367
% adapted by M. Schicho, original by Georges Formon

    % T = temperature in K
    % alpha = degree of aggregation


function
[Alpha]=isodesmic_multifit_UV(T,Tm2000,Tm1000,Tm500,Tm200,H,Rp,Rm,s_cum)
nT=size(T);
Tu = unique(T);
```

```
nTu=size(Tu);
x_=1;
y=nT(1)/(nTu(1));

%iteration
if nT(1)==nTu(1)
    Alpha(1:nT,1)=1;
else
d2000(:,1)=T(1:s_cum(1,1),1); %suffix 2000 is for 2 mM
d1000(:,1)=T(s_cum(1,1)+1:s_cum(2,1),1); %suffix 1000 is for 1 mM
d500(:,1)=T(s_cum(2,1)+1:s_cum(3,1),1); %suffix 500 is for 500 µM
d200(:,1)=T(s_cum(3,1)+1:s_cum(4,1),1); %suffix 200 is for 200 µM

d2000(:,2)=(Rp-Rm)./(1+exp(-0.908*H*(d2000(:,1)-
Tm2000)/(8.314*Tm2000^2)))+Rm;
d1000(:,2)=(Rp-Rm)./(1+exp(-0.908*H*(d1000(:,1)-
Tm1000)/(8.314*Tm1000^2)))+Rm;
d500(:,2)=(Rp-Rm)./(1+exp(-0.908*H*(d500(:,1)-Tm500)/(8.314*Tm500^2)))+Rm;
d200(:,2)=(Rp-Rm)./(1+exp(-0.908*H*(d200(:,1)-Tm200)/(8.314*Tm200^2)))+Rm;

Alpha(1:s_cum(1,1),1)=d2000(:,2);
Alpha(s_cum(1,1)+1:s_cum(2,1),1)=d1000(:,2);
Alpha(s_cum(2,1)+1:s_cum(3,1),1)=d500(:,2);
Alpha(s_cum(3,1)+1:s_cum(4,1),1)=d200(:,2);
end
end
```

2.9.10.2 Multifit

```
%isodesmic multifit code
%original from Georges Formon
%M. Schicho, 04/08/2020


%define function and variables
function
[Tr_model,Alpha_model]=isodesmic_multifit_UV(d2000,d1000,d500,d200)

%load data
d2000=xlsread('Gd_2mM'); %suffix 2000 is for 2 mM
d1000=xlsread('Gd_1mM'); %suffix 1000 is for 1 mM
d500=xlsread('Gd_500uM'); %suffix 500 is for 500 µM
d200=xlsread('Gd_200uM'); %suffix 200 is for 300 µM

%define matrices
[s(1,1),s(1,2)]=size(d2000);
[s(2,1),s(2,2)]=size(d1000);
[s(3,1),s(3,2)]=size(d500);
[s(4,1),s(4,2)]=size(d200);

s_cum(1,1)=s(1,1);

for i=2:4
s_cum(i,1)=s(i,1)+s_cum(i-1);
end


%content of matrices
```

```
    %T=temperature in K from raw data
T(1:s_cum(1,1),1)=d2000(:,1);
T(s_cum(1,1)+1:s_cum(2,1),1)=d1000(:,1);
T(s_cum(2,1)+1:s_cum(3,1),1)=d500(:,1);
T(s_cum(3,1)+1:s_cum(4,1),1)=d200(:,1);

    %UV=ratio S02/S01 from raw data, unitless
UV(1:s_cum(1,1),1)=d2000(:,2);
UV(s_cum(1,1)+1:s_cum(2,1),1)=d1000(:,2);
UV(s_cum(2,1)+1:s_cum(3,1),1)=d500(:,2);
UV(s_cum(3,1)+1:s_cum(4,1),1)=d200(:,2);


%fit options and fit type
fomm = fitoptions('Method', 'NonLinearLeastSquares', 'StartPoint',
[268,268,250,240,-50e3,1,1], ...
    'Lower', [200,200,200,150,-100e3,1.2889,0], 'Upper', [400,400,400,400,-
10e3,1.3057,2],...
    'TolFun',1e-14,'TolX',1e-
14,'MaxIter',5000,'MaxFunEval',2500,'Display','iter')

ftmm =
fittype('isodesmic_multifit_equations_michi(T,Tm2000,Tm1000,Tm500,Tm200,H,R
p,Rm,s_cum)',...
   'coefficients',{'Tm2000','Tm1000','Tm500','Tm200','H','Rp','Rm'},...
   'independent', {'T'},...
   'problem',{'s_cum'},...
   'options',fomm)


%fit
[f,gof,output]  = fit(T, UV, ftmm,'problem',{s_cum})


%define model
UV_model=isodesmic_multifit_UV_equations_michi(T,f.Tm2000,f.Tm1000,f.Tm500,
f.Tm200,f.H,f.Rp,f.Rm,s_cum);


%equations for the model, taken from E. W. Meijer, et al. Chem. - A Eur. J.
2010, 16, 362-367
    %alpha = degree of aggregation
    %Tr = reduced temperature


%definition of alpha and alpha_model
Alpha=(UV-f.Rm)/(f.Rp-f.Rm);
Alpha_model=(UV_model-f.Rm)/(f.Rp-f.Rm);


%calculation of Tr from T(raw data)
Tr2000=-f.H*(T(1:s_cum(1,1),1)-f.Tm2000)./(8.315*f.Tm2000^2);
Tr1000=-f.H*(T(s_cum(1,1)+1:s_cum(2,1),1)-f.Tm1000)./(8.315*f.Tm1000^2);
Tr500=-f.H*(T(s_cum(2,1)+1:s_cum(3,1),1)-f.Tm500)./(8.315*f.Tm500^2);
Tr200=-f.H*(T(s_cum(3,1)+1:s_cum(4,1),1)-f.Tm200)./(8.315*f.Tm200^2);


%calculation of Tr_model from Tr
Tr_model(1:s_cum(1,1),1)=Tr2000;
```

```
Tr_model(s_cum(1,1)+1:s_cum(2,1),1)=Tr1000;
Tr_model(s_cum(2,1)+1:s_cum(3,1),1)=Tr500;
Tr_model(s_cum(3,1)+1:s_cum(4,1),1)=Tr200;


%sorting data
Tr_model=sort(Tr_model);
Alpha_model=sort(Alpha_model,'descend');


%calculation of alpha
Alpha2000(:,1)=Alpha(1:s_cum(1,1),1);
Alpha1000(:,1)=Alpha(s_cum(1,1)+1:s_cum(2,1),1);
Alpha500(:,1)=Alpha(s_cum(2,1)+1:s_cum(3,1),1);
Alpha200(:,1)=Alpha(s_cum(3,1)+1:s_cum(4,1),1);


%calculation of alpha_model
Alpha_model2000(:,1)=Alpha_model(1:s_cum(1,1),1);
Alpha_model1000(:,1)=Alpha_model(s_cum(1,1)+1:s_cum(2,1),1);
Alpha_model500(:,1)=Alpha_model(s_cum(2,1)+1:s_cum(3,1),1);
Alpha_model200(:,1)=Alpha_model(s_cum(3,1)+1:s_cum(4,1),1);


%plot results
f1=scatter(Tr2000,Alpha2000,'filled','o','MarkerEdgeColor',[1 0 0],
'MarkerFaceColor', [1 0 0]);
hold on
f2=scatter(Tr1000,Alpha1000,'filled','o','MarkerEdgeColor',[0 1
0],'MarkerFaceColor', [0 1 0]);
hold on
f3=scatter(Tr500,Alpha500,'filled','o','MarkerEdgeColor',[0 0 1],
'MarkerFaceColor', [0 0 1]);
hold on
f4=scatter(Tr200,Alpha200,'filled','o','MarkerEdgeColor',[0.5 0.5 0.5],
'MarkerFaceColor', [0.5 0.5 0.5]);
hold on
plot(Tr_model,Alpha_model,'-','LineWidth',3,'Color',[0 0 0])

%format graph
ylabel('\alpha','FontName','arial','FontSize',16);
xlabel('T_r','FontName','arial','FontSize',16);
set(gca,'FontName','arial','FontSize',14,'LineWidth',2,'box','off')
legend({'2 mM' ,'1 mM','500 \muM','200
\muM','Model'},'FontName','arial','FontSize',16,'FontWeight','bold');
legend('boxoff')
title('Gd-NDI','FontName','arial','FontSize',16,'FontWeight','bold')
set(gcf,'color','w');
hold off


%export fitted data to excel file
xlswrite('Gd_fitteddata_bounds',Tr2000,'A2:A300');
xlswrite('Gd_fitteddata_bounds',Tr1000,'C2:C300');
xlswrite('Gd_fitteddata_bounds',Tr500,'E2:E300');
xlswrite('Gd_fitteddata_bounds',Tr200,'G2:G300');
xlswrite('Gd_fitteddata_bounds',Alpha2000,'B2:B300');
xlswrite('Gd_fitteddata_bounds',Alpha1000,'D2:D300');
xlswrite('Gd_fitteddata_bounds',Alpha500,'F2:F300');
xlswrite('Gd_fitteddata_bounds',Alpha200,'H2:H300');
```

```
xlswrite('Gd_fitteddata_bounds',Tr_model,'I2:I1500');
xlswrite('Gd_fitteddata_bounds',Alpha_model,'J2:J1500');
header={'Tr2mM','alpha2mM','Tr1mM','alpha1mM','Tr500uM','alpha500uM','Tr200
uM','alpha200uM','Trmodel','alphamodel'};
xlswrite('Gd_fitteddata_bounds',header,'A1:J1');

end
```

2.9.10.3 Results

```
f =

     General model:
     f(T) =
isodesmic_multifit_equations_michi(T,Tm2000,Tm1000,Tm500,Tm200,H,
                    Rp,Rm,s_cum)
     Coefficients (with 95% confidence bounds):
       Tm2000 =   282.8  (282.2, 283.5)
       Tm1000 =   264.8  (264.1, 265.5)
       Tm500 =    239.2  (238.4, 240.1)
       Tm200 =    196.3  (194.2, 198.4)
       H =        -1.339e+04  (-1.364e+04, -1.313e+04)
       Rp =       1.306  (fixed at bound)
       Rm =       0.9201  (0.919, 0.9211)
     Problem parameters:
       s_cum = 4x1 double

gof =

           sse: 0.0320
       rsquare: 0.9902
           dfe: 962
    adjrsquare: 0.9902
          rmse: 0.0058
```

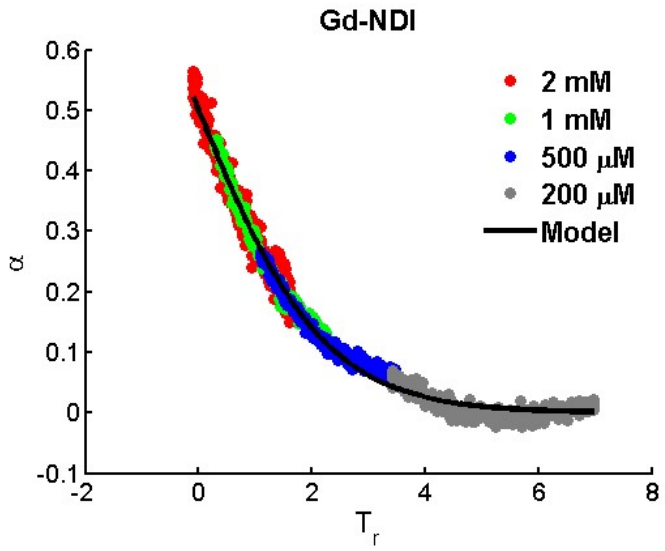

2.10. References

1. Xiao, Y.-D., Paudel, R., Liu, J., Ma, C., Zhang, Z.-S. & Zhou, S.-K. MRI Contrast Agents: Classification and Application (Review). *Int. J. Mol. Med.* **38**, 1319–1326 (2016).
2. Zhou, Z. & Lu, Z.-R. Gadolinium-Based Contrast Agents for Magnetic Resonance Cancer Imaging. *WIREs Nanomed. Nanobiotechnol.* **5**, 1–18 (2013).
3. Bira, N., Dhagat, P. & Davidson, J. R. A Review of Magnetic Elastomers and Their Role in Soft Robotics. *Front. Robot. AI* **7**, 588391 (2020).
4. Lee, H.-S., Jeon, Y.-U., Lee, I.-S., Jeong, J.-Y., Hoang, M. C., Hong, A., Choi, E., Park, J.-O. & Kim, C.-S. Wireless Walking Paper Robot Driven by Magnetic Polymer Actuator. *Actuators* **9**, 109 (2020).
5. Coufal, H., Dhar, L. & Mee, C. D. Materials for Magnetic Data Storage: The Ongoing Quest for Superior Magnetic Materials. *MRS Bull.* **31**, 374–378 (2006).
6. Yakout, S. M. Spintronics: Future Technology for New Data Storage and Communication Devices. *J. Supercond. Nov. Magn.* **33**, 2557–2580 (2020).
7. Dobrzański, L. A., Drak, M. & Ziębowicz, B. Materials with Specific Magnetic Properties. *J. Achiev. Mater. Manuf. Eng.* **17**, 4 (2006).
8. Lewis, L. H. & Jiménez-Villacorta, F. Perspectives on Permanent Magnetic Materials for Energy Conversion and Power Generation. *Metall. Mat. Trans. A* **44**, 2–20 (2013).
9. Kharzeev, D., Landsteiner, K., Schmitt, A. & Yee, H.-U. *Strongly Interacting Matter in Magnetic Fields*. (Springer Berlin Heidelberg, 2013).
10. Coey, J. M. D. *Magnetism and Magnetic Materials*. (Cambridge University Press, 2010).
11. Nisticò, R. Magnetic Materials and Water Treatments for a Sustainable Future. *Res. Chem. Intermed.* **43**, 6911–6949 (2017).
12. Sastri, V. S., Bünzli, J.-C., Ramachandra Rao, V., Rayudu, G. V. S. & Perumareddi, J. R. *Modern Aspects of Rare Earths and their Complexes*. (Elsevier B.V., 2003).
13. Murugesu, M. The Orientation is in the Details. *Nature Chem* **4**, 347–348 (2012).
14. Car, P.-E., Perfetti, M., Mannini, M., Favre, A., Caneschi, A. & Sessoli, R. Giant Field Dependence of the Low Temperature Relaxation of the Magnetization in a Dysprosium(iii)–DOTA Complex. *Chem. Commun.* **47**, 3751 (2011).
15. Polarz, S., Bährle, C., Landsmann, S. & Klaiber, A. Panoscopic Structures by Hierarchical Cascade Self-Assembly of Inorganic Surfactants with Magnetic Heads Containing Dysprosium Ions. *Angew. Chem. Int. Ed.* **52**, 13665–13670 (2013).
16. Sander Langereis, de Lussanet, Q. G., van Genderen, M. H. P., Backes, W. H. & Meijer, E. W. Multivalent Contrast Agents Based on Gadolinium−Diethylenetriaminepentaacetic Acid-Terminated Poly(propylene imine) Dendrimers for Magnetic Resonance Imaging. *Macromolecules* **37**, 3084–3091 (2004).
17. Markiewicz, G., Smulders, M. M. J. & Stefankiewicz, A. R. Steering the Self-Assembly Outcome of a Single NDI Monomer into Three Morphologically Distinct Supramolecular Assemblies, with Concomitant Change in Supramolecular Polymerization Mechanism. *Adv. Sci.* **6**, 1900577–1900586 (2019).
18. Görl, D., Zhang, X. & Würthner, F. Molecular Assemblies of Perylene Bisimide Dyes in Water. *Angew. Chem. Int. Ed.* **51**, 6328–6348 (2012).
19. Smulders, M. M. J., Nieuwenhuizen, M. M. L., de Greef, T. F. A., van der Schoot, P., Schenning, A. P. H. J. & Meijer, E. W. How to Distinguish Isodesmic from Cooperative Supramolecular Polymerisation. *Chem. Eur. J.* **16**, 362–367 (2010).
20. Palmans, A. R. A., Vekemans, J. A. J. M., Havinga, E. E. & Meijer, E. W. Sergeants-and-Soldiers Principle in Chiral Columnar Stacks of Disc-Shaped Molecules withC3 Symmetry. *Angew. Chem. Int. Ed.* **36**, 2648–2651 (1997).
21. Gillissen, M. A. J., Hoeben, T. T., Spiering, A. J. H., Vekemans, J. A. J. M., Palmans, A. R. A. & Meijer, E. W. Supramolecular Chirality Using Both Cooperative and Isodesmic Self-Assembly: Hierarchical Growth Through Competition. *Isr. J. Chem.* **51**, 1118–1127 (2011).
22. Venkata Rao, K., Miyajima, D., Nihonyanagi, A. & Aida, T. Thermally Bisignate Supramolecular Polymerization. *Nat. Chem.* **9**, 1133–1139 (2017).
23. Mabesoone, M. F. J., Markvoort, A. J., Banno, M., Yamaguchi, T., Helmich, F., Naito, Y., Yashima, E., Palmans, A. R. A. & Meijer, E. W. Competing Interactions in Hierarchical Porphyrin Self-Assembly Introduce Robustness in Pathway Complexity. *J. Am. Chem. Soc.* **140**, 7810–7819 (2018).
24. Yamamoto, Y., Fukushima, T., Suna, Y., Ishii, N., Saeki, A., Seki, S., Tagawa, S., Taniguchi, M., Kawai, T. & Aida, T. Photoconductive Coaxial Nanotubes of Molecularly Connected Electron Donor and Acceptor Layers. *Science* **314**, 1761–1764 (2006).
25. Kastler, M., Pisula, W., Wasserfallen, D., Pakula, T. & Müllen, K. Influence of Alkyl Substituents on the Solution- and Surface-Organization of Hexa- *peri* -hexabenzocoronenes. *J. Am. Chem. Soc.* **127**, 4286–4296 (2005).

26. Aida, T. & Meijer, E. W. Supramolecular Polymers – We've Come Full Circle. *Isr. J. Chem.* **60**, 33–47 (2020).
27. Tircsó, G., Tircsóné Benyó, E., Garda, Z., Singh, J., Trokowski, R., Brücher, E., Sherry, A. D., Tóth, É. & Kovács, Z. Comparison of the Equilibrium, Kinetic and Water Exchange Properties of Some Metal Ion-DOTA and DOTA-bis(amide) Complexes. *J. Inorg. Biochem.* **206**, 111042 (2020).
28. Briganti, M., Garcia, G. F., Jung, J., Sessoli, R., Le Guennic, B. & Totti, F. Covalency and Magnetic Anisotropy in Lanthanide Single Molecule Magnets: The DyDOTA Archetype. *Chem. Sci.* **10**, 7233–7245 (2019).
29. King, R. B., Crabtree, R. H., Lukehart, C. M., Atwood, D. A. & Scott, R. A. *Encyclopedia of Inorganic Chemistry*. (John Wiley & Sons, Ltd, 2006).
30. Boulon, M.-E., Cucinotta, G., Luzon, J., Degl'Innocenti, C., Perfetti, M., Bernot, K., Calvez, G., Caneschi, A. & Sessoli, R. Magnetic Anisotropy and Spin-Parity Effect Along the Series of Lanthanide Complexes with DOTA. *Angew. Chem. Int. Ed.* **52**, 350–354 (2013).
31. Jiang, S.-D. & Qin, S.-X. Prediction of the Quantized Axis of Rare-Earth Ions: The Electrostatic Model with Displaced Point Charges. *Inorg. Chem. Front.* **2**, 613–619 (2015).
32. Pengo, P., Pantoş, G. D., Otto, S. & Sanders, J. K. M. Efficient and Mild Microwave-Assisted Stepwise Functionalization of Naphthalenediimide with α-Amino Acids. *J. Org. Chem.* **71**, 7063–7066 (2006).
33. Leira-Iglesias, J., Sorrenti, A., Sato, A., Dunne, P. A. & Hermans, T. M. Supramolecular Pathway Selection of Perylenediimides Mediated by Chemical Fuels. *Chem. Commun.* **52**, 9009–9012 (2016).
34. Liu, S., Pietryka, J., Ellars, C. E. & Edwards, D. S. Comparison of Yttrium and Indium Complexes of DOTA-BA and DOTA-MBA: Models for ^{90} Y- and ^{111} In-Labeled DOTA−Biomolecule Conjugates. *Bioconjug. Chem.* **13**, 902–913 (2002).
35. Velikyan, I., Lendvai, G., Välilä, M., Roivainen, A., Yngve, U., Bergström, M. & Långström, B. Microwave Accelerated 68Ga-Labelling of Oligonucleotides. *J. Labelled Cpd. Radiopharm.* **47**, 79–89 (2004).
36. D'Vries, R. F., Iglesias, M., Snejko, N., Alvarez-Garcia, S., Gutiérrez-Puebla, E. & Monge, M. A. Mixed Lanthanide Succinate–Sulfate 3D MOFs: Catalysts in Nitroaromatic Reduction Reactions and Emitting Materials. *J. Mater. Chem.* **22**, 1191–1198 (2012).
37. Rast, S., Borel, A., Helm, L., Belorizky, E., Fries, P. H. & Merbach, E. EPR Spectroscopy of MRI-Related Gd(III) Complexes: Simultaneous Analysis of Multiple Frequency and Temperature Spectra, Including Static and Transient Crystal Field Effects. *J. Am. Chem. Soc.* 2637–2644 (2001).
38. Zhao, Y. H., Abraham, M. H. & Zissimos, A. M. Fast Calculation of van der Waals Volume as a Sum of Atomic and Bond Contributions and Its Application to Drug Compounds. *J. Org. Chem.* **68**, 7368–7373 (2003).
39. Valenta, J., Honda, F., Vališka, M., Opletal, P., Kaštil, J., Míšek, M., Diviš, M., Sandratskii, L., Prchal, J. & Sechovský, V. Antiferromagnetism and Phase Transitions in Noncentrosymmetric UIrSi3. *Phys. Rev. B* **97**, 144423 (2018).
40. Benelli, C. & Gatteschi, D. Magnetism of Lanthanides in Molecular Materials with Transition-Metal Ions and Organic Radicals. *Chem. Rev.* **102**, 2369–2388 (2002).
41. Seibt, J., Winkler, T., Renziehausen, K., Dehm, V., Würthner, F., Meyer, H.-D. & Engel, V. Vibronic Transitions and Quantum Dynamics in Molecular Oligomers: A Theoretical Analysis with an Application to Aggregates of Perylene Bisimides. *J. Phys. Chem. A* **113**, 13475–13482 (2009).
42. Molla, M. R. & Ghosh, S. Structural Variations on Self-Assembly and Macroscopic Properties of 1,4,5,8-Naphthalene-diimide Chromophores. *Chem. Mater.* **23**, 95–105 (2011).
43. Sikder, A., Ray, D., Aswal, V. K. & Ghosh, S. Stimuli-Responsive Directional Vesicular Assembly with Tunable Surface Functionality and Impact on Enzyme Inhibition. *Langmuir* **34**, 868–875 (2018).
44. Syamala, P. P. N., Soberats, B., Görl, D., Gekle, S. & Würthner, F. Thermodynamic Insights into the Entropically Driven Self-Assembly of Amphiphilic Dyes in Water. *Chem. Sci.* **10**, 9358–9366 (2019).
45. Barros, T. C., Brochsztain, S., Toscano, V. G., Filho, P. B. & Politi, M. J. Photophysical Characterization of a 1,4,5,8-naphthalenediimide Derivative. *J. Photochem. Photobiol. A* **111**, 97–104 (1997).
46. Zhang, F. *Near-infrared Nanomaterials: Preparation, Bioimaging and Therapy Applications*. (Royal Society of Chemistry, 2016).
47. Ciferri, A. *Supramolecular Polymers*. (Taylor & Francis, 2005).
48. D'Angelo, P., Zitolo, A., Migliorati, V., Chillemi, G., Duvail, M., Vitorge, P., Abadie, S. & Spezia, R. Revised Ionic Radii of Lanthanoid(III) Ions in Aqueous Solution. *Inorg. Chem.* **50**, 4572–4579 (2011).
49. Cooper, A. Thermodynamic Analysis of Biomolecular Interactions. *Curr. Opin. Chem. Biol.* **3**, 557–563 (1999).
50. Barge, A., Cravotto, G., Gianolio, E. & Fedeli, F. How to Determine Free Gd and Free Ligand in Solution of Gd Chelates. A Technical Note. *Contrast Media Mol. Imaging* **1**, 184–188 (2006).
51. Guha, S., Goodson, F. S., Corson, L. J. & Saha, S. Boundaries of Anion/Naphthalenediimide Interactions: From Anion−π Interactions to Anion-Induced Charge-Transfer and Electron-Transfer Phenomena. *J. Am. Chem. Soc.* **134**, 13679–13691 (2012).

52. Baskakov, I. V., Legname, G., Prusiner, S. B. & Cohen, F. E. Folding of Prion Protein to Its Native α-Helical Conformation Is under Kinetic Control. *J. Biol. Chem.* **276**, 19687–19690 (2001).
53. Helmich, F., Lee, C. C., Nieuwenhuizen, M. M. L., Gielen, J. C., Christianen, P. C. M., Larsen, A., Fytas, G., Leclère, P. E. L. G., Schenning, A. P. H. J. & Meijer, E. W. Dilution-Induced Self-Assembly of Porphyrin Aggregates: A Consequence of Coupled Equilibria. *Angew. Chem. Int. Ed.* **49**, 3939–3942 (2010).
54. Clarke, E. C. W. & Glew, D. N. Evaluation of Thermodynamic Functions from Equilibrium Constants. *Trans. Faraday Soc.* **62**, 539–347 (1966).

Chapter 3. Magnetophoresis in colloidal assemblies of lanthanide containing NDI derivatives

Abstract

Driven by a decrease of the solvent polarity, lanthanide-containing naphthalene diimide derivatives assemble into micrometer-sized colloids in a binary water / tetrahydrofuran solvent system. The colloid size is thereby controlled by the solvent composition. Colloidal assemblies of 3 µm or larger show magnetophoretic behavior in a simple and cheap experimental setup. When a commercial NdFeB cube magnet is placed in a colloidal dispersion, a ~100 µm thick organic layer is formed along the edges of the magnet face. In a selected region close to the magnet, the trajectory of single colloids could be visualized microscopically and traced using particle tracking velocimetry. In this system, supramolecular polymerization is used as a tool to create a dynamic, solvent dependent on/off switch of the magnetophoretic effect, while the magnetic field can remain applied.

Parts of this chapter contribute to a manuscript in preparation:

Schicho, Michaela K.; Formon, Georges J.M., Hermans, Thomas M. "Assembly and magnetophoresis of lanthanide-containing naphthalene diimide derivatives" *Manuscript in preparation*

3.1. Introduction

Magnetophoresis describes the directed motion of magnetic particles in liquid media under the influence of an external magnetic field.[1] The term is inspired by electrophoresis, which is the analogous movement in an electric field. The phenomenon allows for real-time remote manipulation of nano- and micro-sized particles, which is particularly interesting in cell biology, and in clinical therapy and diagnostics.[2] So-called magnetic tweezers have been developed, in which an electromagnet is used to control the movement of micrometer sized superparamagnetic beads in three dimensional space. This technology can be used for delicate manipulations in biological tissue, as for instance to measure the stiffness of DNA[3], or the viscoelastic properties of cytoplasm.[4] Moreover, with the availability of highly performant magnets, it is relatively easily scalable,[5,6] and can be incorporated in microfluidic systems.[5–9] This makes magnetophoresis attractive for preparative separation and lab-on-a-chip technology. The minimal invasiveness, the level of spatial and rotational control, and the scalability of magnetophoretic techniques make it a convenient alternative to other methods of nanoparticle control[2], such as chemical affinity[7] or optical tweezers.[8,9]

For magnetic colloids and nanoparticles in the hundreds of nanometer size range, the magnetophoretic effects are well understood.[1] However, quantitative analysis of the particle movement is space is often tricky, because of the interplay of magnetic forces, viscous drag, and Brownian motion.[2] All of these scale differently with the particle radius R, leading to a less pronounced magnetic force ($F_{mag} \sim R^3$) for smaller particles, as compared to the viscous drag force ($F_{vis} \sim R$) and the Brownian force ($F_{therm} \sim R^{0.5}$). Majetich and coworkers have shown the magnetic manipulation of gold-coated, superparamagnetic 35 nm iron oxide cores, as an aqueous dispersion in a field gradient of 3000 $T \cdot m^{-1}$.[2] A single magnetic tip is sufficient to collect and release the particles in a controlled manner. The trajectory of individual particles could be tracked in real time by dark field optical microscopy and was successfully deconvoluted into the different force components. For magnetic particles in the size range of 10–30 nm, the small magnetic moments are limiting the magnetic forces and thus the magnetophoretic effect.[2]

In order to elucidate the role of particle size in magnetophoresis, we aim to study whether supramolecular assembly can be a tool to switch dynamically and reversibly between small, non-magneto reactive monomers or oligomers, and large, directable colloids.

3.2. Solvent induced colloid formation

The aggregation of magnetic monomers **M-NDI**, whose self-assembly in water was discussed in Chapter 2, was investigated in less polar solvent systems. To our surprise, a different type of assembly was observed in binary water / tetrahydrofuran (THF) mixtures. Upon the increase of the THF volume fraction φ_{THF}, the UV-Vis spectrum undergoes a hypochromic shift, broadening with a loss of fine structure, and a shoulder appears at 395 nm, as shown in Figure **3.1**a for a 100 µM solution of **Dy-NDI**. These assembly induced changes are similar to reported examples[10,11] of amphiphilic π-systems. Moreover, a gradual rise of the baseline hints at scattering due to the formation of a dispersion. We assume that this type of self-assembly is primarily directed by solvophobic effects, as opposed to the π-π stacking dominated self-assembly in water (Chapter 2).

Monitoring the absorption changes at 395 nm as a function of φ_{THF} results in a sigmoidal rise with a rapid increase of absorbance from around 0.75 (*i.e.*, 75 vol%) onwards to higher THF volume fractions (Figure 3.1b). The experimental data could be fitted to an isodesmic denaturation model[10,12], yielding a Gibbs free energy ΔG of -123.2 ± 2.9 kJ/mol. The applied model is inspired from protein folding, where changes in aggregation typically occur upon the addition of a denaturing agent such as urea, for instance. For supramolecular polymers, the good solvent (here water) can be considered a denaturing agent, which leads to disassembly of the polymer that is assembled in the bad solvent (here THF). The overall Gibbs free energy of polymerization is expressed as the sum of the Gibbs free energy of supramolecular polymerization in the pure bad solvent and the volume fraction φ of the denaturalizing agent with the so-called denaturation potential m as the proportionality constant (see section 3.8.2 in the appendix).

The quantitative result of this fit, however, remains to be interpreted with caution considering the baseline increase due to scattering, and the fact that this model assumes the formation of one-dimensional supramolecular polymers. The observed scattering points at colloid formation, which is visible by the naked eye: an increased turbidity (inset of Figure 3.1b) and precipitation of solid material for φ_{THF} above 0.9 suggest aggregation to increasingly large colloids with an increasing THF volume fraction.

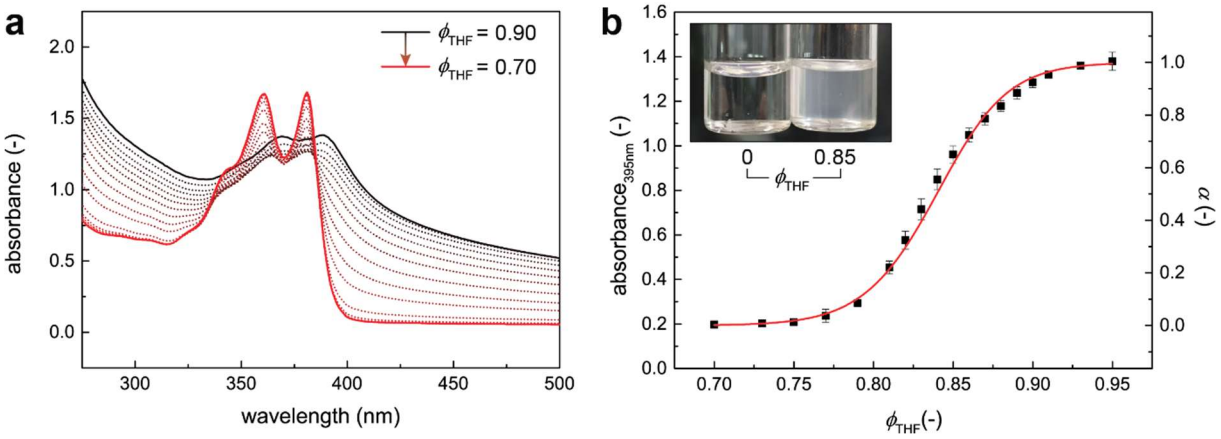

Figure 3.1 | Colloid formation. (a) UV-Visible absorbance spectra of 100 µM **Dy-NDI** in aq. THF at variable volume fractions φ_{THF} recorded at 298 K. (b) Plot of the absorbance intensity at 395 nm (left ordinate: absolute values, right ordinate: normalized to the degree of supramolecular polymerization α) as a function of φ_{THF} and the corresponding isodesmic denaturation fit. Error bars represent standard deviations over three measurements. Inset: Digital photograph of 100 µM **Dy-NDI** in water (φ_{THF} = 0, left) and at φ_{THF} = 0.85 (right).

3.3. Colloid morphology and size

The presence of spherical colloids was confirmed by imaging on a microscopic scale, using confocal (Figure 3.2a) and atomic force microscopy (AFM, Figure 3.2b,c). Using different imaging techniques, a wide size range of colloids from tens of nanometers to tens of micrometers could be observed. Broad polymer size distributions are typically expected for unimodal, non-directional supramolecular polymerization as we find in our system.

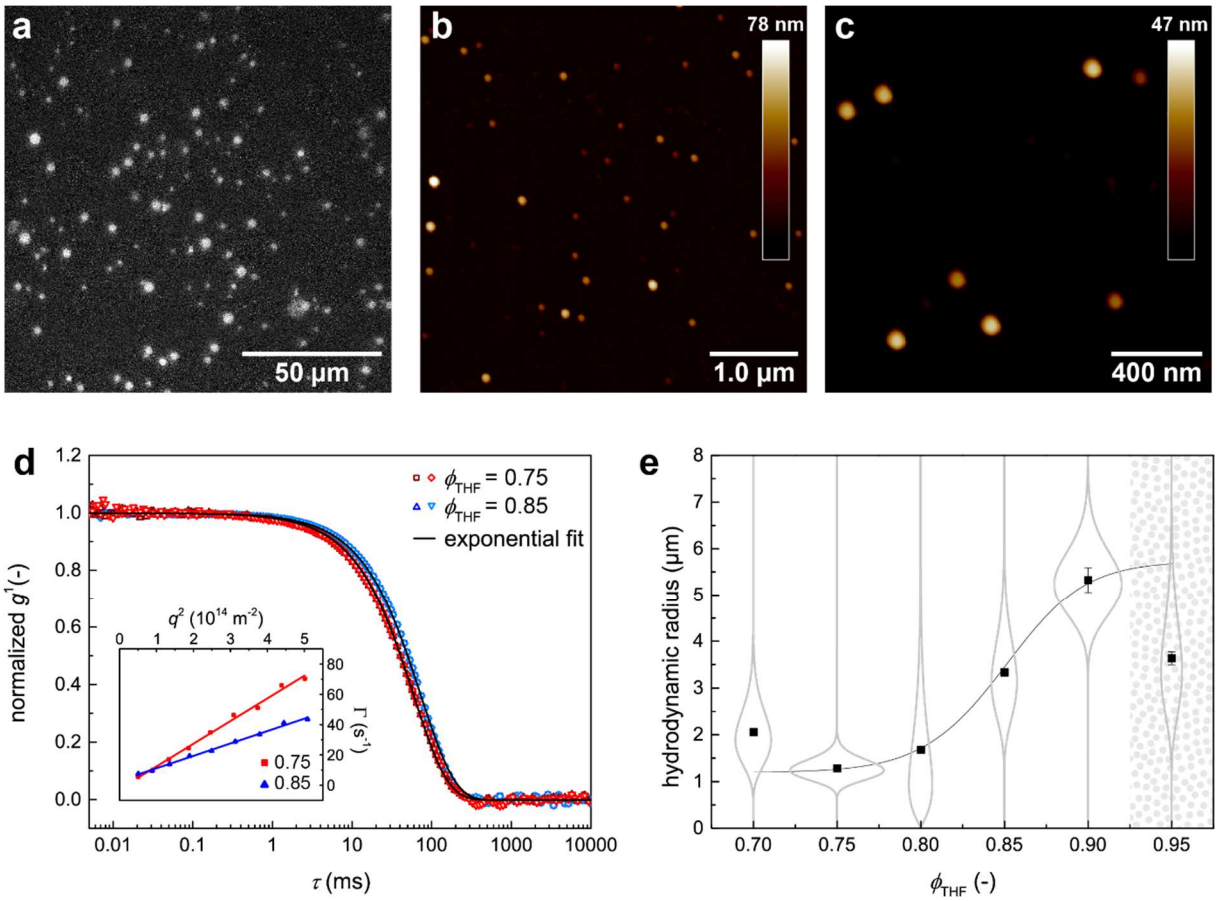

Figure 3.2 | Colloid size and morphology. (a) Confocal micrograph (scale bar = 50 µm) of 100 µM **Dy-NDI** at φ_{THF} = 0.90. (b) Atomic force micrograph (scale bar = 1.0 µm) of 30 µM **Dy-NDI** at φ_{THF} = 0.75, dip-coated for 30 s. (c) Atomic force micrograph (scale bar = 400 nm) of 30 µM **Dy-NDI** at φ_{THF} = 0.95, dip-coated for 30 s. (d) Normalized polarized field correlation function $g^{(1)}$ of 100 µM **Dy-NDI** at φ_{THF} = 0.75 and 0.85 measured at q = 0.0116 nm^{-1}, shown by the hollow symbols, and the respective exponential fits (black lines). Inset: Mean decay rate $\bar{\Gamma}$ as a function of q^2 and the respective linear fits for φ_{THF} = 0.75 and 0.85. (e) Solvent composition dependent hydrodynamic radii R_H of 100 µM **Dy-NDI** (black data points), and their respective Schulz distributions (grey lines). Error bars represent the standard error of the mean. The grey, dotted area represents precipitation. The sigmoidal black line is added to guide the eye.

To quantify the colloid sizes, we performed dynamic light scattering (DLS) on 100 µM **Dy-NDI** at different volume fractions of THF. For each sample, the polarized electric field correlation function $g^{(1)}(q,\tau)$, was recorded at 11 angles (ϑ = 30-130°), which are converted to the respective scattering vectors q (for more details see section 3.8.3), as a function of the relaxation time τ (see Figure 3.2d). Using a single exponential fit, the mean relaxation time $\bar{\tau}$ was determined. The slope of its reciprocal, the decay rate $\bar{\Gamma}$, as a function of q^2 yields the translational diffusion coefficient D_t (inset of Figure 3.2d), which can be related to the hydrodynamic radius R_h using the Stokes-Einstein equation.[13] The size distribution was estimated by a simulated Schultz

distribution[14] including the mean R_H and the normalized standard deviation σ, which could be determined by cumulant analysis.[15] When comparing dispersions at different φ_{THF}, we find a significant increase of the mean particle radius from $\varphi_{THF} = 0.85$ on, which peaks at 5.5 µm in $\varphi_{THF} = 0.90$ as compared to around 2 µm for ≤ 0.80 (see Figure 3.2e). The found size evolution coincides well with the sigmoidal increase of the UV-absorbance at 395 nm (Figure 3.1b). At 0.95, the observed average size is a bit lower than expected, likely due to precipitation of large colloids over the measuring time of around 30 minutes.

The obtained translational diffusion coefficients, and hydrodynamic radii R_H are summarized in Table 3.1.

Table 3.1 | Dynamic light scattering. Translation diffusion coefficients D_t, mean hydrodynamic radii R_H and their standard errors.

φ_{THF} (-)	D_t (10^{-14} m^{-1})	mean R_H (µm)
0.70	9.29 ± 0.32	2.061 ± 0.072
0.75	14.97 ± 0.45	1.279 ± 0.038
0.80	13.56 ± 0.53	1.677 ± 0.066
0.85	8.18 ± 0.20	3.334 ± 0.083
0.90	6.03 ± 0.30	5.324 ± 0.268
0.95	10.53 ± 0.40	3.636 ± 0.139

3.4. Magnetophoresis

When a commercial, permanent cube magnet was placed next to a cuvette containing dispersions of **Dy-NDI** (Figure 3.3a), an accumulation of solid material in its spatial proximity was observed by eye after around 30 minutes to one hour (inset of Figure 3.3b), suggesting a magnetophoretic movement of the dispersed colloids towards the magnet.

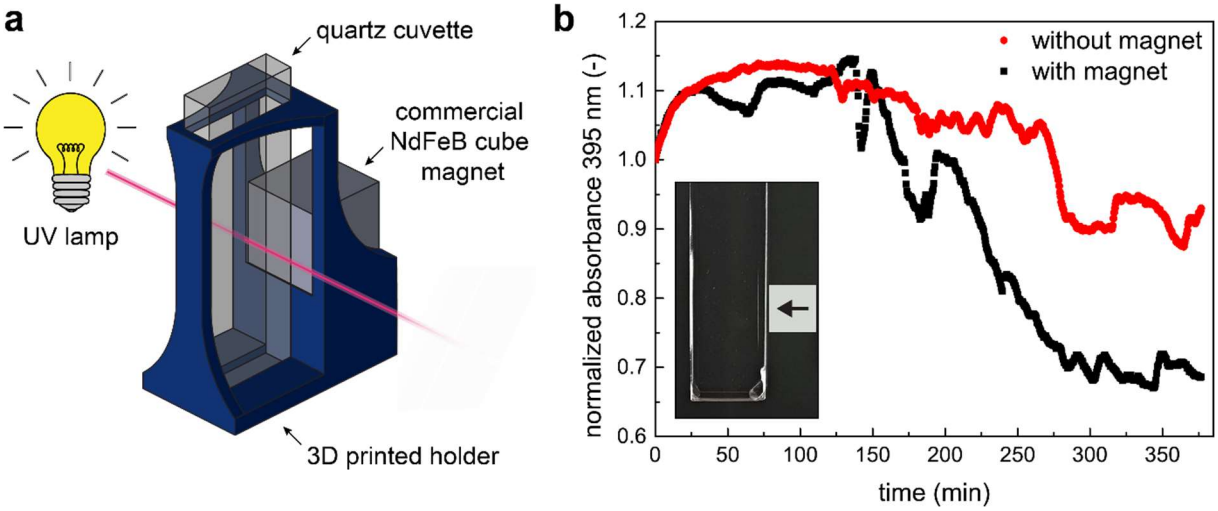

Figure 3.3 | First magnetophoresis experiment. (a) Scheme depicting the first experimental setup, including an **M-NDI** containing quartz cuvette, a custom 3D-printed holder (blue), and a 1 cm NdFeB cube magnet whose North pole points inwards towards the cuvette. The setup can be placed in a UV-Vis spectrometer. (b) 395 nm absorbance of 100 µM **Dy-NDI** in the presence (black squares) and absence (red points) of a magnet over time. The data points represent single experiments. Inset: Digital photograph of 100 µM **Dy-NDI** in $\varphi_{THF} = 0.85$ after 1 h, showing the accumulation of solid material in proximity of the magnet as a thin white layer.

In a first approach to quantify the accumulation of colloids in close to the magnet, the depicted, 3D-printed setup (Figure 3.3a) was placed in a UV-Vis spectrometer and the absorbance in the center of the cuvette was measured over time. A decrease of the intensity at 395 nm was expected, as the colloids are supposedly transported away from the center towards the magnet. In some experiments (Figure 3.3b), the expected decrease was found to be of around 25 %. It remained, however, poorly reproducible.

Instead, the movement of the colloids was visualized by confocal microscopy[16] Therefore, a 0.5 cm commercial NdFeB cube magnet was placed in a sealable quartz cuvette of 1 cm path length and surrounded by a 100 µm **Dy-NDI** dispersion at 85 vol% THF. The magnet was fixed in its position, with the magnetic field direction along the cuvette (*x* direction in Figure 3.4, see also Figure 3.5a), from the outside using a second identical magnet. The speed and direction of the recorded particle movement could be analyzed using the particle tracking software Imaris® (Figure 3.4). Colloids of 10 µm diameter were tracked in a 0.4 per 1.4 mm region centered at 350 µm distance from the magnet corner towards its middle along *y*, over one minute. A complex flow pattern including different currents was observed. Up to about 750 µm from the magnet surface, we find a clearly directional flow towards the magnet (velocity angle X > 90°), that seems to be counteracted by a second stream with opposite flow direction (velocity angle X < 90°). Presumably, this second stream compensates for the concentration and density inhomogeneities caused by the magnetophoretic effect. Moreover, precipitation of colloids over time contributes to the overall motif. At the corner of the magnet, where the strongest field gradient is found[17], the particle speed exceeded traceability.

The complex flow pattern likely causes the poor reproducibility of the UV-Vis measurements (Figure 3.3).

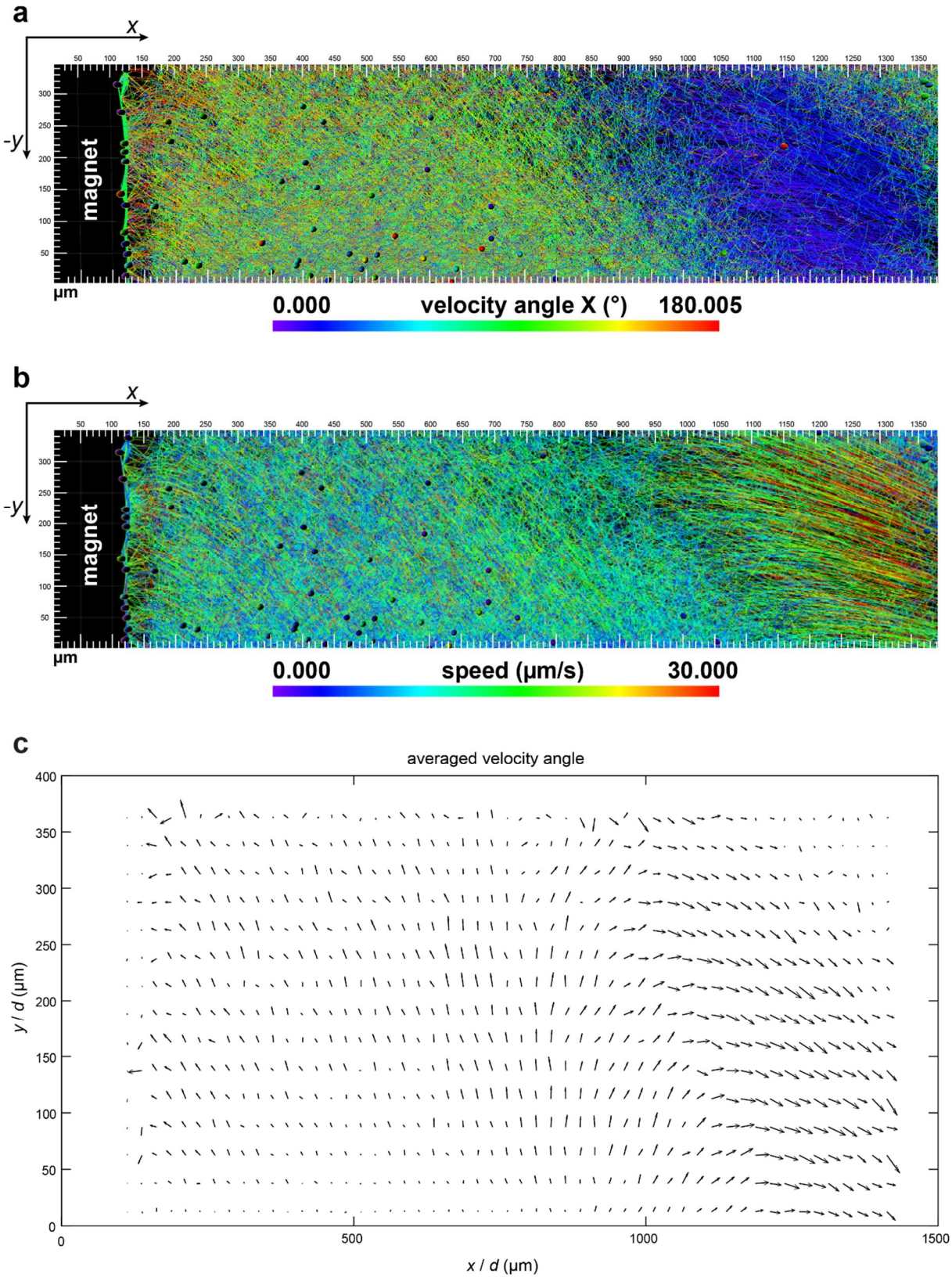

Figure 3.4 | Particle tracking. (a) Space-resolved and color-coded snapshot with a representation of the velocity angle X from 0° (purple, positive *x* direction) to 180° (red, negative *x* direction). (b) Space-resolved and color-coded snapshot with a representation of the particle speed from 0 µm·s^{-1} (purple) to 30 µm·s^{-1} (red). (c) Space-resolved velocity angle X in a vector representation, averaged over 57 seconds. All results are based on 10 µm particles of **Dy-NDI** in φ_{THF} = 0.85.

As a result of the colloid motion towards the magnet, we find the formation of a 100 to 200 µM thick organic layer (Figure 3.5b) along the faces of the magnet, which is fluorescent and exhibits the typical orange NDI color (Figure 3.5c and d). The layer formation was studied systematically for various THF contents of **Dy-NDI**. Similar to the experimental setup described above, a 0.5 cm NdFeB cube magnet was placed in a sealable glass vial containing 5 mL of a solution or dispersion, respectively. The glass vial was then positioned horizontally, and the magnet was fixed on the vertical, short side of the vial by another magnet from the outside, with their magnetic field direction aligned (Figure 3.5a). The residual magnetic field of this setup is around 0.48 T in the center of the *yz* plane of the magnet in contact with the solution. After 4 h, the dispersion was removed with a pipette, and the magnet was placed on a stereomicroscope maintaining the same orientation as in the vial. For **Dy-NDI** samples containing THF volume fractions of 0.80 or more, the formation of an organic layer along the edges of the *yz* plane could be confirmed, whereas for smaller volume fractions of THF or analogous samples of **Y-NDI** no such change was observed (Figure 3.5e).

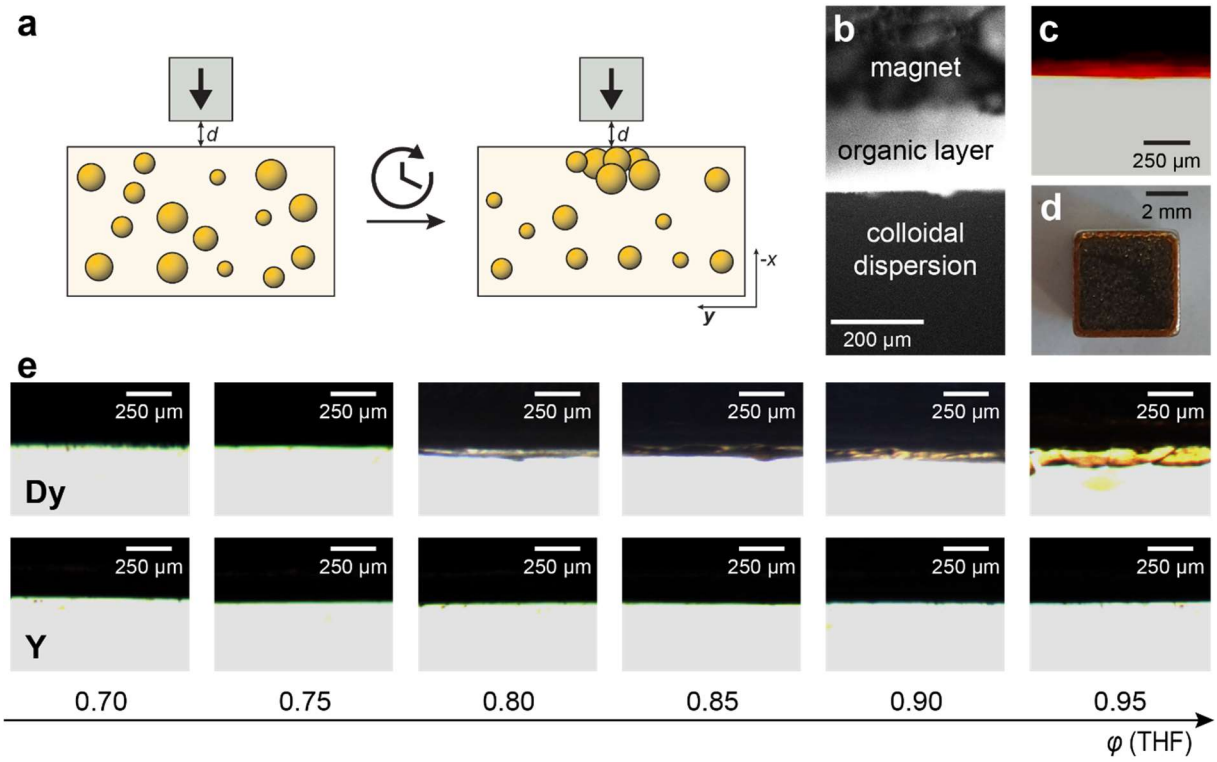

Figure 3.5 | Layer formation. (a) Scheme depicting the cross section of a typical experimental setup, including a commercial NdFeB cube magnet and a colloidal dispersion of **M-NDI** in a quartz cuvette or glass vial. *d* represents the spatial distance between the magnet and the solution and is 0 when the magnet is in direct contact with the dispersion. (b) Confocal micrograph of a 0.5 cm cube magnet in a 100 µM **Dy-NDI** dispersion at φ_{THF} = 0.85 (*d* = 0) after 2 h, showing the formation of a well-distinguishable organic layer at the edge of the 0.5 cm cube magnet. (c) Digital photograph of the same layer through a 10x objective. (d) Digital photograph of the *yz* plane of a 0.5 cm cube magnet showing layer formation along the edges after a typical 4 h experiment at φ_{THF} = 0.95. (e) Stereomicrographs of a 0.5 cm cube magnet in top view, after 4 h in 100 µM **Dy-NDI** (top row) and **Y-NDI** (bottom row) at φ_{THF} = 0.70–0.95 (*d* = 0).

Dispersions of all magnetic ions (**M**= Gd, Dy, Tb, Ho, Er; $\mu > 0$) have shown layer formation at $\varphi_{THF} = 0.95$, whereas diamagnetic control ions (**M** = Y, La, Lu; $\mu = 0$) have not (Figure 3.6).

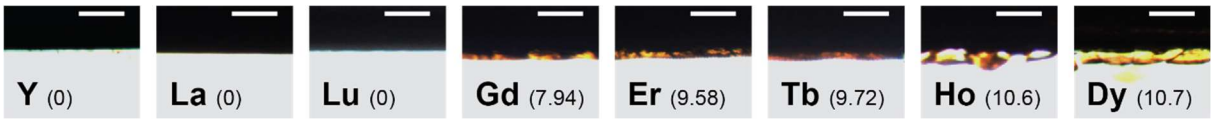

Figure 3.6 | Layer formation for different ions. Stereomicrographs (all scale bars = 250 µm) of a 0.5 cm cube magnet in top view, after 4 h in 100 µM **M-NDI** at 95 vol% THF (x=0) for all ions **M** = Y, La, Gd, Tb, Dy, Ho, Er, Lu. The values in parentheses are the respective magnetic moments of the M^{3+} ions in $\mu_B = 9.274 \cdot 10^{-24}$ Am². The ions are sorted by their magnetic moment.

The formed layers can be removed fast and easily by adding water to decrease φ_{THF} and shaking the sample (Figure 3.8 in the appendix). Experiments over 12 h did not reveal any significant changes as compared to a 4 h experiment.

According to COMSOL® simulations of our experimental setup including two 0.5 cm cube N42 cube magnets, which are oriented with their magnetic field direction in line, and which are separated by 1 mm (*i.e.*, identical to the magnetophoretic experiments), the magnetic field strength on the *xy* plane is distributed as illustrated in Figure 3.7b. If we compare this distribution to the layer we find experimentally (Figure 3.7a), its location mainly along the edges of the plane is coherent. The layer extends in an approximately 0.40 mm wide band from the edge to the center of the plane (Figure 3.7c). This area corresponds to the region with the strongest magnetic field of around 0.8–0.9 T (Figure 3.7d) according to the simulation ($x = 0$). The largest field that was measured with a Teslameter is of around 0.5 T ($0 < x < 2$ mm)

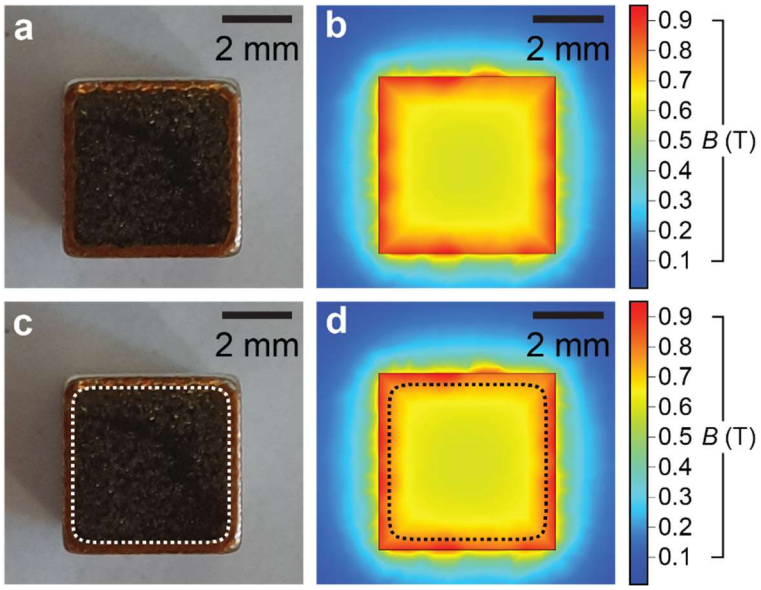

Figure 3.7 | Magnetic field simulation on the *xy* plane. (a) Digital photograph of the *yz* plane of a 0.5 cm cube magnet showing layer formation along the edges after a typical 4 h experiment at $\varphi_{THF} = 0.95$. (b) COMSOL® simulation of the magnetic field strength over the *xy* plane. The limits of the organic layer (around 0.40 mm from the edge) are highlighted by white and black dashed lines in panel (c) and (d), respectively.

3.5. Force considerations

The described observations are supported by the definition of the magnetic field gradient force F_{mag} for a particle dispersion in liquid medium, which is

$$\overrightarrow{F_{mag}} = \frac{1}{2\mu_0} V(\chi_p - \chi_m) B\vec{\nabla}B \tag{3.i}$$

with the vacuum permeability μ_0, the particle volume V, the magnetic susceptibility χ_p of the particle, the magnetic susceptibility χ_m of the medium, the magnetic flux density B, and the field gradient ∇B.[18] At equal magnetic susceptibility, the magnetic force is directly proportional to the particle volume V ($\sim R^3$) as well as the magnetic field gradient ∇B. From the magnetic force, the average magnetophoretic velocity v can be derived.[2]

$$\overrightarrow{v_{mag}} = \frac{\overrightarrow{F_{mag}}}{6\pi\eta R} \tag{3.ii}$$

The competing thermal force, on the other hand, is proportional to the square root of the particle radius R.[19] It can be described as

$$\overrightarrow{F_{therm}} = \sqrt{2k_B T(6\pi\eta R)} \cdot \overrightarrow{\omega(t)} \tag{3.iii}$$

with Boltzmann's constant k_B, the temperature T, the dynamic viscosity η of the surrounding fluid, the particle radius R, and a Gaussian white noise operator $0 < \omega(t) < 1$.[19] The thermal force F_{therm} is proportional to the square root of the particle radius R, and also to the square root of the dynamic viscosity η. As opposed to the magnetic gradient field force F_{mag}, F_{therm} is thus increasing less with a larger average particle radius R ($F_{mag} \sim R^3$, $F_{therm} \sim R^{0.5}$), and is moreover damped by the decrease of the dynamic viscosity η with φ_{THF} (Table 3.4 in the appendix).

Table 3.2 shows calculated values of the magnetic force F_{mag} and the thermal force F_{therm} for 100 µM **Dy-NDI** for THF volume fractions of 0.70–0.95 as well as their ratio β and the magnetophoretic velocity v_{mag}. All values are approximated for a particle at 1 mm distance in all three spatial directions *xyz* from one corner of the *yz* plane (towards the center of the plane for *x* and *y*). Even though the values represent rough estimations, the trends are apparent. With an increasing particle radius from ≤ 2 to about 5 µm, the magnetic force F_{mag} increases more than 10-fold from < 1 to 16 pN. At a similar rate, the particle velocity increases from < 20 to around 240 µm·s^{-1}. The thermal force F_{therm}, on the other hand, changes hardly. The values remain in between 15 and 25 fN over the studied range. Consequently, the values of β indicating the ratio of F_{mag} and F_{therm} rise from < 50 to about 700. The latter means that the magnetic forces exceed the force of the thermal noise by a factor 700 at 298 K. Thus, the layer formation we observe for dispersions with particle radii larger than 3 µm is coherent.

For the cases of φ_{THF} = 0.70–0.80 we only observe layer formation at 0.80, even though we find similar particle sizes (R_H = 1.3–2.1 µm) within this range. The fact that β is indeed far smaller than for φ_{THF} > 0.80, but still significantly larger than 1, implies that these particles can undergo magnetophoresis. Hence, we assume that not only the detected colloid size, but also the degree of polymerization α is decisive for layer formation. α increases from 0.00 to 0.15 for φ_{THF} = 0.70–0.80 (Figure 3.1b), which refers to the proportion of aggregated and monomers in the respective samples. In other words, roughly 15 % of **Dy-NDI** is aggregated in φ_{THF} = 0.80, as compared to less than 2 % in 0.75 and 0.7. This interpretation from UV-Vis spectroscopy

complements our reasoning, as it measures —unlike DLS— the average signal over the entire sample. Moreover, the viscosity dependence of the thermal force ($F_{therm} \sim \eta^{0.5}$) should be noted, which leads to a decrease of F_{therm} with an increasing THF volume fraction at constant colloid size.

Table 3.2 | Magnetic and thermal forces. Values for F_{mag}, v_{mag} and F_{therm} have been calculated using equations (3.i-iii) using the mean hydrodynamic radii obtained from DLS (Table 3.1), $\chi_p = 1.00 \cdot 10^{-3}$, $\chi_m = 0$, $T = 298$ K, $B\nabla B = 65$ T²·m^{-1}, and $\omega(t) = 1$. $B\nabla B$ was estimated from the COMSOL® simulation for a colloid at 1 mm from the xy plane and at 1 mm in each y and z from the corner towards the plane center. Note that F_{mag} given in pN, F_{therm} in fN (*i.e.*, 10^{-3} pN). Indicated errors are propagated from the error of R_H. [a]no layer formation observed. [b]layer formation observed.

φ_{THF} (-)	α (-)	mean R_H (nm)	F_{mag} (pN)	v_{mag} (µm·s^{-1})	F_{therm} (fN)	$\beta = F_{mag}/F_{therm}$ (-)
0.70[a]	0.00	2.061 ± 0.072	0.93 ± 0.01	18.3 ± 2.0	20.5 ± 0.36	45 ± 5
0.75[a]	0.01	1.279 ± 0.038	0.22 ± 0.02	8.2 ± 0.8	15.0 ± 0.22	15 ± 1
0.80[b]	0.15	1.677 ± 0.066	0.51 ± 0.06	16.7 ± 2.1	15.8 ± 0.31	32 ± 4
0.85[b]	0.65	3.334 ± 0.083	4.00 ± 0.30	79.2 ± 6.2	20.4 ± 0.25	198 ± 15
0.90[b]	0.92	5.324 ± 0.268	16.30 ± 2.46	239.1 ± 38.1	23.7 ± 0.59	695 ± 106
0.95[b]	1.00	3.636 ± 0.139	5.21 ± 0.60	132.4 ± 16.0	18.0 ± 0.34	292 ± 34

3.6. Conclusions

We have shown that the magnetic building blocks **M-NDI** are prone to assemble into colloidal particles in water/THF mixtures. Whereas the supramolecular polymers form one-dimensional supramolecular polymers in water (Chapter 2), they from up to 10 micrometer sized spherical colloids in a water/THF system. The colloid size can be adjusted simply and reversibly by changing the solvent composition.

At elevated THF contents of $\varphi_{THF} = 0.8$ or more, we reach magnetophoretic control over the supramolecular system using a single NdFeB magnet with $B\nabla B \leq 500\ T^2 \cdot m^{-1}$ in an experimentally simple and cheap setup at room temperature. When an originally homogeneous dispersion gets in contact with a permanent cube magnet, the aggregates move towards the surface of the magnet. There, they form an around 100 µm thick organic layer along the edges of the face of the magnet over a time span of up to 4 h.

To our knowledge, this is the first report of magnetophoresis in a supramolecular system. It allows for a second, solvent-triggered on/off-switch of the transport phenomenon, which is decoupled from the magnetic field. The simplicity and reversibility of this approach offers a new degree of dynamicity to magnetic spatiotemporal control over soft matter.

Magnetophoresis is commonly described for superparamagnetic or ferromagnetic nanoparticles with large induced magnetic moments. With our example, we extend the scope of magnetoresponsive materials to assemblies of paramagnetic coordination complexes as monomers.

3.7. Author contributions

Michaela Schicho performed spectroscopic and magnetophoretic experiments. Anastasiia Sharko performed atomic force microscopy imaging. Alessandra Tassoni assisted in performing, evaluating, and interpreting dynamic light scattering measurements. Florencia Sacarelli performed particle tracking using Imaris®. Lucas Giacchetti 3D designed and -printed custom-made experimental devices and performed COMSOL® simulations. Thomas Hermans recorded confocal micrographs and supervised the research.

3.8. Appendix

3.8.1 Methods

Synthesis. The monomeric building blocks **M-NDI** were prepared following modified literature procedures as described in Chapter 2.

Sample preparation. Solutions and dispersions of **M-NDI** in a binary water / THF solvent mixture were prepared by dissolving the respective compound in water, before adding THF using a Harvard apparatus PHD 2000 programmable syringe pump at an infusion rate of 4.25 mL·min^{-1} under mechanical stirring at 250 rpm. Typical sample volumes were 3–8 mL.

Atomic force microscopy. AFM imaging was performed by means of a Bruker Dimension Icon set-up operating in air, in tapping mode, by using tip model VESPA-V2 (tip stiffness k = 42 N/m). n-doped silicon substrates were dip-coated for 30 s, then dried under nitrogen and rinsed with isopropanol.

Confocal microscopy. Confocal images were acquired using a ZEISS LSM 710 confocal microscope. No fluorescent markers were used.

Stereomicroscopy. Stereomicroscopy was performed on a Nikon SMZ745T stereomicroscope.

Dynamic light scattering. Electric field correlation functions were measured on a homebuilt light scattering set-up with and ALV7002 digital correlator using a laser diode at λ = 639 nm at 11 scattering angles from 30° to 130° in 10° intervals.

3D-printing. The cuvette holder depicted in Figure 3.3 was 3D-printed in VeroClear using an Objet30 prime printer (both Stratasys).

Particle tracking velocimetry. Particle tracking was performed in 2D using Imaris ®. All shown results are based on a video of **Dy-NDI** at φ_{THF} = 0.85 recorded with confocal microscopy. The tracking traces refer to 10 µm sized particles. The vector representation of the velocity angle is averaged over 57 s.

Magnetic field simulation. The magnetic field simulation for the custom setup was simulated using the commercial modelling software COMSOL Multiphysics®. The magnetic setup was specified by indicating the magnet material, shape, size, field direction, and position.

3.8.2 Solvent denaturation model

Solvent composition-dependent plots of the absorbance at 395 nm were fitted non-linearly to an isodesmic denaturation model using a non-linear least squared iteration (Levenberg-Marquardt algorithm). In analogy to the previously described concentration-dependent measurements, this model is based on the isodesmic equilibrium model[20] (*cf.* equation 2.i), where K_{eq} is the equilibrium constant, and c the concentration.

$$\alpha = 1 - \frac{2\,K_{eq}\cdot c + 1 - \sqrt{4\,K_{eq}\cdot c + 1}}{2\,K_{eq}^2\cdot c^2} \tag{3.iv}$$

If we assume a linear dependence of the Gibbs free energy ΔG on the volume fraction φ of THF, as in protein denaturation models, K_{eq} can be expressed as a function of φ, following equation 3.v. ΔG represents the overall Gibbs free energy of supramolecular polymerization, $\Delta G°$ the Gibbs free energy of supramolecular polymerization in the bad solvent (here THF), and m the denaturation potential.[12]

$$K_{eq}(\varphi) = e^{-\frac{\Delta G}{RT}} = e^{-\frac{\Delta G° + m\varphi}{RT}} \tag{3.v}$$

The degree of supramolecular polymerization α can be expressed as a function of the respective variable that is used to follow the self-assembly process. In this case, the absorbance intensity A at 395 nm, giving equation 3.vi. A_m is the extrapolated absorbance for an exclusively monomeric state ($\alpha = 0$), and A_p is its equivalent for a fully polymeric state ($\alpha = 1$).

$$\alpha = \frac{A - A_m}{A_P - A_m} \tag{3.vi}$$

Combining equations 3.iv–vi, we obtain the fitting function 3.vii, which relates the measured absorbance at 395 nm A to the volume fraction φ of THF, including the four fitting parameters $\Delta G°$, m, A_p, and A_m.

$$A(\varphi) = \left[1 - \frac{2\,e^{-\frac{\Delta G° + m\varphi}{RT}}\cdot c + 1 - \sqrt{4\,e^{-\frac{\Delta G° + m\varphi}{RT}}\cdot c + 1}}{2\,e^{-\frac{2(\Delta G° + m\varphi)}{RT}}\cdot c^2}\right]\cdot\left(A_p - A_m\right) + A_m \tag{3.vii}$$

Table 3.3 summarizes all fitted parameters and their standard errors.

Table 3.3 | Isodesmic denaturation fitting results. Fitted parameters $\Delta G°$, m, A_m, and A_p for 100 µM **Dy-NDI** and their standard errors.

$\Delta G°$ (kJ·mol^{-1})	m (kJ·mol^{-1})	A_m (-)	A_p (-)
-123.2 ± 2.9	121.1 ± 3.4	0.1930 ± 0.0040	1.3745 ± 0.0048

3.8.3 Dynamic light scattering (DLS)

The polarized electric field correlation functions $g^{(1)}(q,\tau)$, were recorded at 11 angles (ϑ = 30-150 °) in dependence of the relaxation time τ. They were fitted using a single exponential function[21] (equation 3.viii), with the amplitude A, the mean relaxation time $\bar{\tau}$, and a baseline correction factor B ($B \approx 0$) as fitting parameters.

$$g^1(q,\tau) = A \cdot e^{-\frac{\tau}{\bar{\tau}}} + B \tag{3.viii}$$

The angles ϑ were converted to the scattering vectors q, following equation 3.ix, with the wavelength of the laser λ = 639 nm) and the refractive index of the solutions n.[22,23]

$$q = \frac{4\pi n \cdot \sin\left(\frac{\vartheta}{2}\right)}{\lambda} \tag{3.ix}$$

The reciprocal relaxation time τ is the decay rate $\Gamma = \tau^{-1}$. In this manner, $\bar{\tau}$ was converted to $\bar{\Gamma}$, plotted as a function of q^2, and fitted linearly. The obtained slope represents the rotational diffusion coefficient D_t in m^{-1}.

$$D_t = \frac{\Gamma}{q^2} \tag{3.x}$$

From the rotational diffusion coefficient, we can deduce the hydrodynamic radius R_h following the Stokes-Einstein equation (3.xi), where η is the dynamic viscosity of the solvent in Pa·s.

$$D_t = \frac{k_B T}{6\pi\eta R_h} \tag{3.xi}$$

To evaluate the size distribution, a cumulant analysis was performed on $g^{(1)}(q,\tau)$, following equation 3.xii.[15]

$$g^1(q,\tau) = e^{-\frac{\bar{\Gamma}}{\tau}\cdot\left[1+\frac{1}{2}\cdot\frac{\mu}{\bar{\Gamma}^2}\cdot(\bar{\Gamma}\tau)^2\right]} \tag{3.xii}$$

The central moment μ can be converted to the normalized standard deviation σ, and to the Schulz distribution parameter z.

$$\sigma = \sqrt{\frac{\mu}{\bar{\Gamma}^2}} = \sqrt{\frac{1}{z+1}} \tag{3.xiii}$$

Using the mean hydrodynamic radius R_H and the normalized standard deviation σ, Schulz distributions (equation 3.xiv) were simulated for all samples.[14]

$$G(R_H) = A \cdot \left(\frac{z+1}{\overline{R_H}}\right)^{z+1} R_H^z \cdot e^{-\frac{z+1}{\overline{R_h}}\cdot R_H} \cdot \frac{1}{\big((z+1)-1\big)!} \tag{3.xiv}$$

with

$$z = \frac{1}{\sigma^2} - 1 \tag{3.xv}$$

The dynamic viscosity η of binary water/THF mixtures does not change linearly with the solvent composition and was calculated for the respective mixtures using a previously described model.[24] Table 3.4. summarizes the used values of the refractive index n, and the dynamic viscosities η for the respective solvent mixtures at 298 K.

Table 3.4 | Parameters for DLS evaluation. Refractive index n and dynamic viscosities η of the different binary THF/water mixtures at 298 K. THF content is given as volume fraction φ_{THF} and mole fraction x_{THF}, both unitless. Values of n are taken from literature[23], η was calculated using a previously described method[24]. All calculations are based on η(THF, 298 K) = 0.46 mPa·s and η(H_2O, 298 K) = 0.89 mPa·s.

φ_{THF} (-)	x_{THF} (-)	n (-)	η (mPa·s)
0.95	0.81	1.40	0.57
0.90	0.67	1.40	0.68
0.85	0.56	1.40	0.80
0.80	0.47	1.39	0.96
0.75	0.40	1.39	1.14
0.70	0.34	1.39	1.31

3.8.4 Reversibility of layer formation

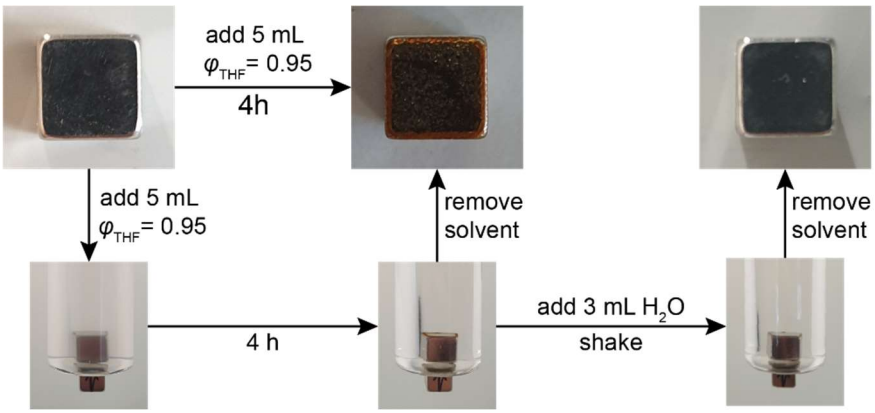

Figure 3.8 | Formation and removal of the organic layer. Scheme depicting the procedures to form and subsequently remove the organic layer. The layer of **Dy-NDI** is formed in φ_{THF} = 0.95 (left). After 4 h, the layer is formed (middle). Upon the addition of water, the layer can be removed instantly by mechanically shaking the sample (right).

3.9. References

1. Zborowski, M. & Chalmers, J. J. Magnetophoresis: Fundamentals and Applications. in *Wiley Encyclopedia of Electrical and Electronics Engineering* (John Wiley and Sons, 2015).
2. Lim, J., Lanni, C., Evarts, E. R., Lanni, F., Tilton, R. D. & Majetich, S. A. Magnetophoresis of Nanoparticles. *ACS Nano* **5**, 217–226 (2011).
3. Gosse, C. & Croquette, V. Magnetic Tweezers: Micromanipulation and Force Measurement at the Molecular Level. *Biophys. J.* **82**, 3314–3329 (2002).
4. Hosu, B. G., Jakab, K., Bánki, P., Tóth, F. I. & Forgacs, G. Magnetic Tweezers for Intracellular Applications. *Rev. Sci. Instrum.* **74**, 4158–4163 (2003).
5. Schwaminger, S. P., Fraga-García, P., Eigenfeld, M., Becker, T. M. & Berensmeier, S. Magnetic Separation in Bioprocessing Beyond the Analytical Scale: From Biotechnology to the Food Industry. *Front. Bioeng. Biotechnol.* **7**, 233 (2019).
6. Hutchins, D. L. & Downey, J. P. Effective Separation of Magnetite Nanoparticles within an Industrial-Scale Pipeline Reactor. *Sep. Sci. Technol.* **55**, 2822–2829 (2020).
7. Koehler, J. M., Visaveliya, N. & Knauer, A. Controlling Formation and Assembling of Nanoparticles by Control of Electrical Charging, Polarization, and Electrochemical Potential. *Nanotechnol. Rev.* **3**, (2014).
8. Grier, D. G. A Revolution in Optical Manipulation. *Nature* **424**, 810–816 (2003).
9. Prikulis, J., Svedberg, F., Käll, M., Enger, J., Ramser, K., Goksör, M. & Hanstorp, D. Optical Spectroscopy of Single Trapped Metal Nanoparticles in Solution. *Nano Lett.* **4**, 115–118 (2004).
10. van Herrikhuyzen, J., Syamakumari, A., Schenning, A. P. H. J. & Meijer, E. W. Synthesis of n-Type Perylene Bisimide Derivatives and Their Orthogonal Self-Assembly with p-Type Oligo(*p*-phenylene vinylene)s. *J. Am. Chem. Soc.* **126**, 10021–10027 (2004).
11. Smulders, M. M. J., Nieuwenhuizen, M. M. L., de Greef, T. F. A., van der Schoot, P., Schenning, A. P. H. J. & Meijer, E. W. How to Distinguish Isodesmic from Cooperative Supramolecular Polymerisation. *Chem. - Eur. J.* **16**, 362–367 (2010).
12. Korevaar, P. A., Schaefer, C., de Greef, T. F. A. & Meijer, E. W. Controlling Chemical Self-Assembly by Solvent-Dependent Dynamics. *J. Am. Chem. Soc.* **134**, 13482–13491 (2012).
13. Pecora, R. *Dynamic Light Scattering*. (Springer US, 1985).
14. Kotlarchyk, M., Stephens, R. B. & Huang, J. S. Study of Schultz Distribution to Model Polydispersity of Microemulsion Droplets. *J. Phys. Chem.* **92**, 1533–1538 (1988).
15. Mailer, A. G., Clegg, P. S. & Pusey, P. N. Particle Sizing by Dynamic Light Scattering: Non-Linear Cumulant Analysis. *J. Phys. Condens. Matter* **27**, 145102 (2015).
16. Video accessible under the following link: https://drive.google.com/file/d/18w6EYRFu7k9K_zdKf1d09lDsMXSwnNPq/view?usp=sharing.
17. Coey, J. M. D. *Magnetism and Magnetic Materials*. (Cambridge University Press, 2010).
18. Suwa, M. Magnetoanalysis of Micro/Nanoparticles: A review. *Anal. Chim. Acta* **690**, 137–147 (2011).
19. Berg-Sørensen, K. & Flyvbjerg, H. The Colour of Thermal Noise in Classical Brownian Motion: A Feasibility Study of Direct Experimental Observation. *New J. Phys.* **7**, 1–10 (2005).
20. Martin, R. B. Comparisons of Indefinite Self-Association Models. *Chem. Rev.* **96**, 3043–3064 (1996).
21. Hassan, P. A., Rana, S. & Verma, G. Making Sense of Brownian Motion: Colloid Characterization by Dynamic Light Scattering. *Langmuir* **31**, 3–12 (2015).
22. Hayduk, W., Laudie, H. & Smith, O. H. Viscosity, Freezing point, Vapor-Liquid Equilibriums, and Other Properties of Aqueous-Tetrahydrofuran solutions. *J. Chem. Eng. Data* **18**, 373–376 (1973).
23. Signer, R., Arm, H. & Daeniker, H. Untersuchungen über das Verhalten organischer Mischphasen. Dampfdrücke, Dichten, thermodynamische Mischungsfunktionen und Brechungsindices der binären Systeme Wasser-Tetrahydrofuran und Wasser-Diäthyläther bei 25°. *Helv. Chim. Acta* **52**, 2347–2351 (1969). German.
24. Das, B., Roy, M. N. & Hazra, D. K. Densities and Viscosities of the Binary Aqueous Mixtures of Tetrahydrofuran and 1,2-dimethoxyethane at 298, 308 and 318 K. *Indian J. Chem. Technol.* **1**, 93.97 (1994).

THIS PAGE IS INTENTIONALLY LEFT BLANK

Chapter 4. Magnetic control over the fractal dimension of supramolecular BTA networks

Abstract

The impact of an external, uniform magnetic field of 1 or 2 T on the thermodynamic equilibrium of supramolecular assemblies based on paramagnetic Gd^{3+}-containing benzene-1,3,5,-tricarboxamide (BTA) derivatives is studied by light scattering and SQUID magnetometry. We find that the monomers assemble in a two-step process, and form rods, which then further assemble to networks of rods. Whereas the rods remain unaffected, the applied magnetic field leads to a reversible densification of the rod network. This conclusion is based on a change of the fractal dimension of the network from 1.7 to 2.6, and an increase of the scattering intensity by 35 % over 10 – 12 h. Simultaneously, the magnetic susceptibility decreases significantly by 2 %. The presented concept can apply to a variety of other supramolecular or polymeric systems that contain magnetic ions and provide better control over dynamic materials.

Parts of this chapter have been published in:

Vincent Marichez, Akihiro Sato, Peter A. Dunne, Jorge Leira-Iglesias, Georges J.M. Formon, Michaela K. Schicho, Isja de Feijter, Pascal Hébraud, Mathieu Bailleul, Pol Besenius, Munuswamy Venkatesan, J.M.D. Coey, E.W. Meijer, and Thomas M. Hermans, "Magnetic Control over the Fractal Dimension of Supramolecular Rod Networks" *J. Am. Chem. Soc.* **2021**, 143, *31*, 11914–11918.

4.1. Introduction

When talking about the control of supramolecular polymers, commonly used external stimuli are temperature[1], enzymes[2–4], mechanical forces[5,6], light[7–9], pH[10–12] or redox potential[13,14] (*cf.* Chapter 1.1.3). More rarely, electric fields, centrifugal gravity, or flow have been shown to affect the growth and orientation of supramolecular polymers due to the arising aligning forces.[15] The application of magnetic fields for this purpose offer many benefits, such as minimal invasiveness, easy modulation of the field strength an direction, and high directionality.

For nm scale assemblies of diamagnetic molecules, large fields of around 10 T or more are needed to achieve alignment.[16] Only at macroscopic scale, as in domain-forming peptide nanofibers[17] or liquid crystalline polymers[18], fields of less than 1 T can be used. In these cases, the diamagnetic anisotropy of the system leads to alignment (see section 1.3.2.1). By introducing ferrimagnetic or paramagnetic species, the magneto-response is majorly facilitated (see section 1.3.2.2). At weak fields (mT to T), alignment of nano- and microstructures can be obtained, as for example of magnetite nanocrystals[19], clay particles[20], bicelles[21], or self-assembled dumbells[22]. From an energetic perspective, the alignment of such self-assembled structures means that the incorporated paramagnetic ions do not act as individual magnetic moments, but collectively. As an illustrative example, let us look at a single paramagnetic Gd^{3+} ion at room temperature in a uniform 1 T field (see section 1.3.1). The magnetic energy E_{mag} is of $-3 \cdot 10^{-25}$ J, which is four orders of magnitude smaller than the energy of Brownian motion E_{therm}, which is $6 \cdot 10^{-21}$ J.

The alignment of self-assembled structures implies a change in their morphology, which can be observed by microscopy. For quantification, the so-called fractal dimension d_F can be used a reference parameter. It is a merit number that relates how detail in a pattern or shape changes with the scale at which it is measured.[23] It can be obtained from different scattering techniques (light, neutron, X-ray)[24] and is commonly used to describe the shapes of aggregated nanoparticles[25] or proteins[26], gels[27], and recently even molecules[28]. The values for d_F are limited by a one-dimensional line, for which d_F will be 1, and a perfect sphere (three-dimensional), with $d_F = 3$.[29] In between the two limits, several fractions are possible (Figure 4.1).

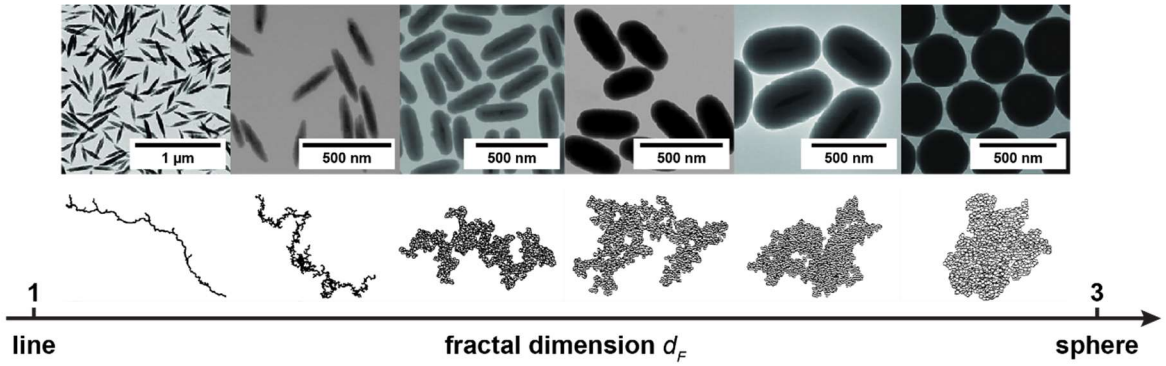

Figure 4.1 | Fractal dimension to quantify morphologies. Illustrative examples of different particle- and aggregate shapes. Top row: Colloidal silica, deviating gradually from prolates to spheres.[30] Different morphologies can be obtained by controlled seeded growth. Bottom row: Two-dimensional, computed projections of self-assembled aggregates of 4096 particles for fractal dimensions d_F of 1.2, 1.6, 2.0, 2.1, 2.3, and 2.5 (from left to right).[31] Figure reproduced from references [30] and [31] with permission from IOP publishing.

Here, we aim to investigate how the application of a uniform magnetic field influences the topology of a supramolecular assembly of a Gadolinium containing benzene-1,3,5-tricarboxamide (BTA) in solution.

4.2. Network characterization

A previously studied, C_3-symmetrical benzene-1,3,5-tricarboxamide (BTA) derivative was used (see Figure 4.2b) in this study. The ligand structure includes a BTA core unit, which is linked to 1,4,7,10-tetraazacyclododecane-1,4,7,10-tetraacetic acid (DOTA) groups via a fluorinated *L*-phenylalanine spacer at each of its three extermities.[32] The octadentate, macrocyclic DOTA is known to form stable, isostructural complexes with various lanthanide ions in a capped square antiprismatic coordination geometry (coordination number 9). Thereby, a non-innocent water molecule completes the primary coordination sphere in the ninth coordination site.[33,34] The BTA ligand was then further functionalized by chelating paramagnetic Gd^{3+}, or diamagnetic Y^{3+} as a negative control, to form the monomer **M-BTA** (**M** = Gd, Y). It has been shown previously that **Gd-BTA** assembles into supramolecular rods in a cooperative nucleation-elongation mechanism (see section 1.1.2), with the nucleation- and elongation constants $K_{nuc} = 10^{-4}$ and K_e $1.4 \cdot 10^{-6}$ M^{-1}.[32] Solutions of 100 µM **Gd-BTA** in 100 mM citrate buffer, which are used in this study, do not show any signs of macroscopic gelation, turbidity, or viscosity change with respect to the buffer.

The previously described system was studied in further detail, revealing that the self-assembled **M-BTA** rods form rod networks (simplistically represented by K_{netw} in Figure 4.2a) in a second assembly step. This can be observed by cryo- transmission electron microscopy (cryo-TEM, Figure 4.2c) and detected by dynamic light scattering (DLS) in solution. Figure 4.2d shows the vertical-vertical (vv) polarized electric field autocorrelation function $g^1(q,\tau)$ versus the relaxation time τ (blue squares and red circles). From this function, the distribution function of relaxation times (blue and red lines) can be extracted using an inverse Laplace transformation.[35] For both molecules **M-BTA**, we find two distinct relaxation processes **P1** (at τ_1) and **P2** (at τ_2), corresponding to rods and rod networks, respectively. They differ by more than one order of magnitude. The respective decay rates $\bar{\Gamma}$, which is the reciprocal relaxation time τ, show q^2 dependence (see Figure 4.5a in the appendix), allowing us to determine their rotational diffusion constants D_t from the slope. The latter can be converted into the corresponding hydrodynamic radii R_H using the Stokes-Einstein equation.[36]

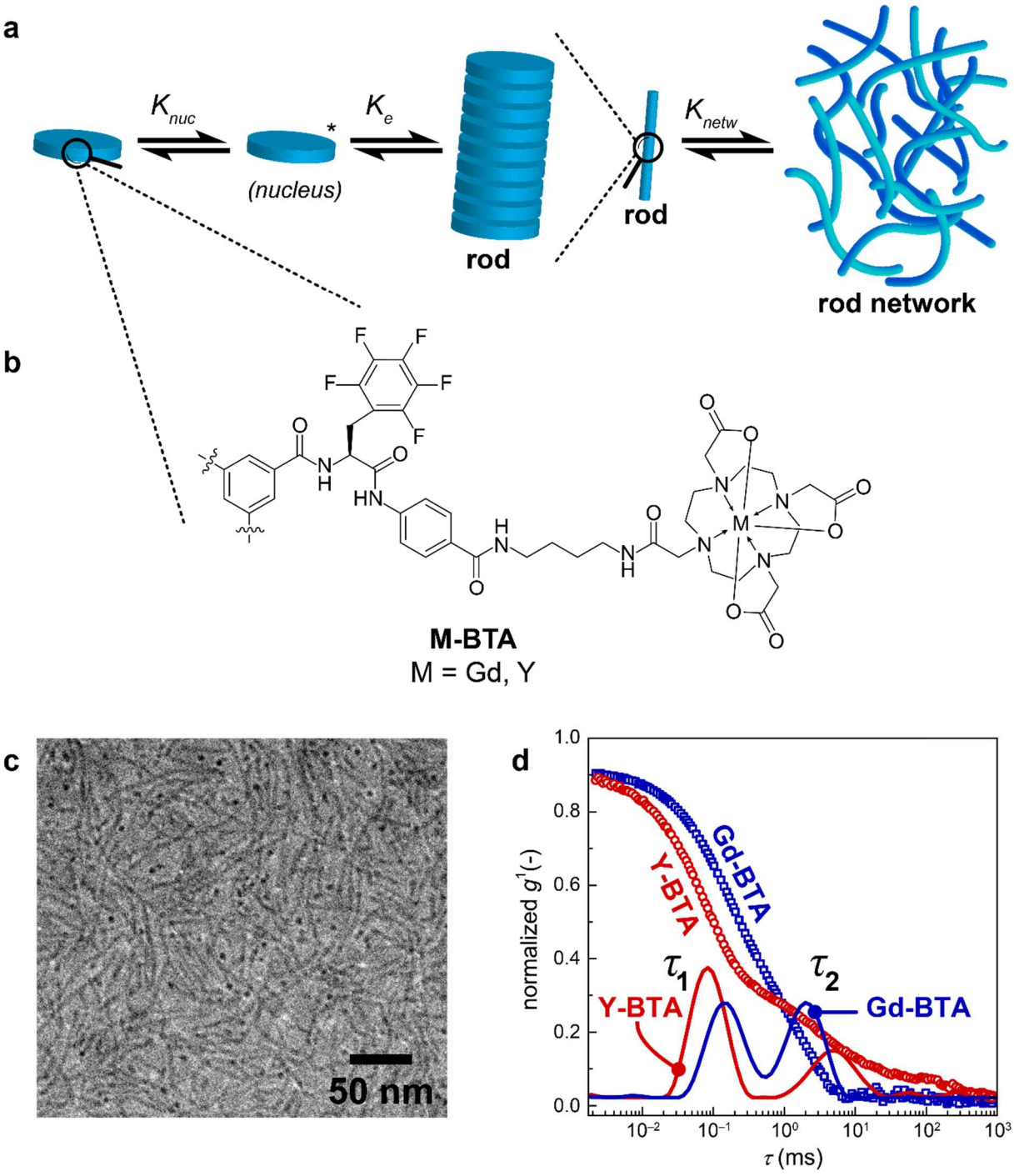

Figure 4.2 | Self-assembly of M-BTA to rods and rod networks. (a) Scheme depicting the two-step assembly of monomeric **M-BTA** to rods in an elongation-nucleation mechanism, and the subsequent network formation with the respective equilibrium constants K_{nuc}, K_e, and K_{netw}. (b) Molecular structure of the monomer **M-BTA** (M=Y, Gd). Only one of three arms is shown for compactness. (c) Cryo-transmission electron microscopy (cryo-TEM) image of the rods and the rod networks formed by 100 µM **Gd-BTA** in 100 mM citrate buffer at pH 6. (d) Normalized polarized field correlation function $g^1(q,\tau)$ of 100 µM **M-BTA** in 100 mM citrate buffer at pH, measured at a scattering vector q = 0.0288 nm^{-1} (hollow symbols), and the respective relaxation time distribution functions, showing a bimodal distribution in both cases (solid lines).

Table 4.1 lists the obtained hydrodynamic radii R_H for both **Gd-BTA** and **Y-BTA**. Using a model described by Tirado *et al.*[37], the rod lengths can be derived from the hydrodynamic radii $R_{H,1}$ of the process **P1**. Thereby, the value of the rod radius was fixed to 3.1 nm, as extracted

from cryo-TEM imaging (Figure 4.2c). The found rod lengths are of around 245 nm for **Gd-BTA** and of ~ 120 nm for **Y-BTA**. Even though a prior study[38] has shown that Y^{3+} was a good control ion for Gd^{3+}, with identical assembly behavior and size, in this case the rods of **Y-BTA** are about half as long as those of **Gd-BTA**. A reason for this discrepancy could be, that Y^{3+} is often 8-coordinate, whereas Gd^{3+} can be 8 or 9-coordinate, leading to the coordination of one or two non-innocent water- or citrate ions. Keeping this in mind, additional control experiments will be included. The difference in the rod size will be disregarded in the following.

Table 4.1 | Dynamic light scattering results. Hydrodynamic radii R_H of rods and the rod networks from dynamic light scattering and the respective rod lengths obtained from the Tirado model.[37]

species	$R_{H,1}$ (nm) **P1**, *rods*	rod length from $R_{H,1}$ (nm) **P1**, *rods*	$R_{H,2}$ (nm) **P2**, *rod network*
Gd-BTA	30.5 ± 4.5	245 (calc.)	348.2 ± 69
Y-BTA	17.9 ± 1.5	120 (calc.)	503.7 ± 169.6

Static light scattering (SLS) provided more detailed information about the structure of the assemblies with respect to their morphology. The Rayleigh ratio $R(q)$, which is obtained from the scattering intensity I_{sam} of the sample solution (for more details see section 4.7.3.1), follows a $R(q) \propto q^{-d_F}$ power law dependency (Figure 4.3a) including the fractal dimension d_F.

For our **Gd-BTA** rod network, we find the fractal dimension d_F to be of 1.7 ± 0.2, which is in agreement with literature.[38,39] The values could be confirmed by box-counting analysis of cryo-TEM images of **Gd-BTA** (see section 4.7.3.2), yielding values of 1.77–1.85. In the following, d_F will be used to describe the network topology, and the Rayleigh ratio $R(q)$ to estimate the mass of **M-BTA** in the network.

4.3. Magnetically controlled network topology

After the topology of the rod network had been elucidated, we aimed to investigate the influence of an applied magnetic field on the system. To this end, the sample solution was analyzed by light scattering after exposure to a magnetic field of 1 or 2 T, in intervals of 2 h. More precisely, the sample was transferred to a light scattering cuvette, which was placed in between the pole pieces of an electromagnet. After 1 h, the cuvette was removed from the field and analyzed by light scattering during a measuring time of around 1 h. The cuvette was then placed back in the magnetic field, and this cycle was repeated 6 to 7 times (12 – 14 h measuring time). While the hydrodynamic radii remained unaffected (see Figure 4.5b in the appendix), the fractal dimension d_F of **Gd-BTA** changes from 1.7 ± 0.2 to 2.2 ± 0.2 in a 1 T field, or to 2.6 ± 0.2 in a 2 T field within one hour. It then remains constant for the residual measuring time (see Figure **4.6** in the appendix). This implies that the network structure undergoes a densification upon exposure to an increased magnetic field, transforming to randomly branched clusters at 2 T.[24,40,41]

The Rayleigh ratio *R(q)* of the **P2** process of **Gd-BTA** keeps increasing over time, until it stagnates after 10 to 12 h (see Figure 4.3b, full blue circles and squares). The final plateau values are 20 % or 35 % higher than the initial value in no field, for 1 T and 2 T respectively. This shows that with time more and more rods get incorporated in rod networks (**P2**), pointing at a magnetically induced increase in K_{netw}, which will be discussed in more detail in section 4.4. After removal of the field, the network relaxes back to the initial *R* value within one day.

The assembly of monomers into rods (**P1**) are not detectably influenced by the field, since their Rayleigh ratio *R* remains constant in time (see Figure 4.3b, hollow symbols). Without exposure to a magnetic field, no changes were observed for the *R* values of **Gd-BTA** rod networks **P2** (gray shaded area in Figure 4.3b). Likewise, the Rayleigh ratios *R* of diamagnetic **Y-BTA** remained unaffected (triangles in Figure 4.3b).

So far, our light scattering data provides evidence for a qualitative interpretation. The magnetic field triggers the network topology to change fast (≤ 1 h), and additional rods to assemble into rod networks on a slower time scale of around 12 h, which is indicated by the observed changes of the fractal dimension d_F, and the Rayleigh ratio *R*, respectively. It is known that aligning fields (including electric-, flow-, or gravitational/centrifugal fields) provoke elongation of isodesmic supramolecular polymers.[42] If the polymer is (partially) aligned in such a field, polymer elongation is entropically favored, in the sense that the entropy loss upon chain growth is reduced. A longer polymer, in turn, will show a stronger response to the field, resulting in an increased degree of alignment. This mutual dependency of alignment and chain growth provides positive feedback. We assume that a magnetic field acts analogously, favoring the assembly of rods into rod networks.

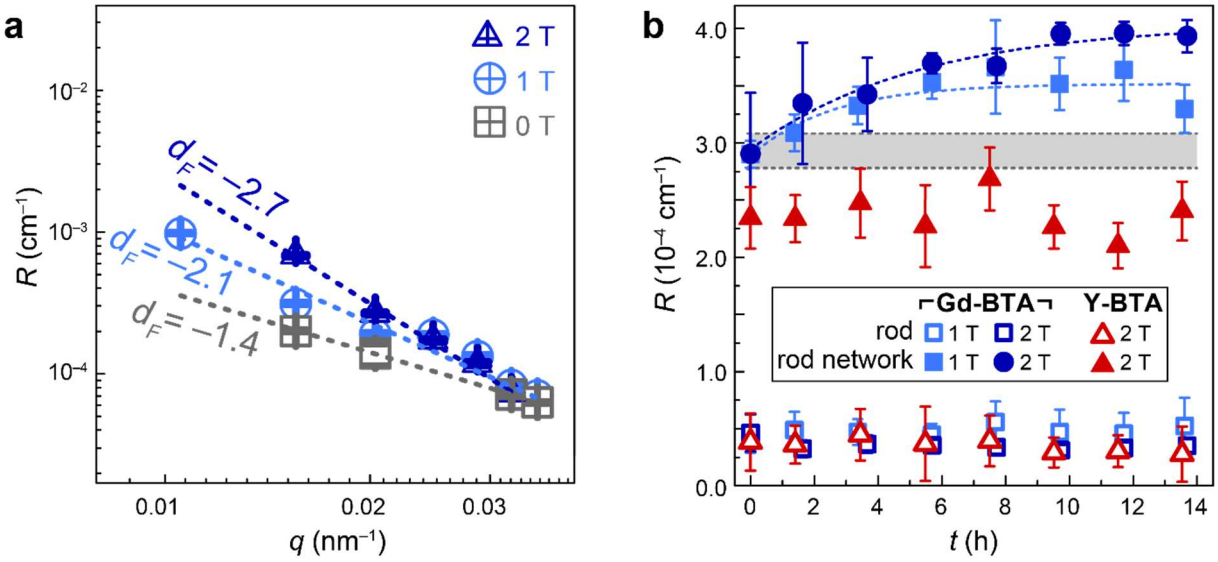

Figure 4.3 | Quantification of rod network topologies under magnetic fields. (a) Rayleigh ratio R of **Gd-BTA** rod networks as a function of the scattering vector q at 0, 1, or 2 T. The slopes of the curves correspond to the fractal dimension d_F. The values are given in the graph. Error bars are standard deviations over 5 measurements. (b) Rayleigh ratio R at q = 0.0288 nm^{-1} over time for rods (hollow symbols), and rod networks (filled symbols). 2 h of measurement include 1 h of exposure to a magnetic field followed by 1 h of light scattering experiments in the absence of a magnetic field. The gray shaded area represents the standard deviation around the mean of **Gd-BTA** at 0 T. Error bars show standard deviations over 50 measurements.

For a more quantitative understanding, the magnetic properties of **Gd-BTA** and **Y-BTA** were compared. Firstly, the temperature dependent magnetic moment of the bulk material was measured using SQUID magnetometry (Figure 4.4a). **Gd-BTA** (blue squares) shows Curie-Weiss behavior ($\chi = C\cdot(T-\theta)$) with a Weiss temperature of θ = –0.7 K, which indicates very weak antiferromagnetic coupling between Gd^{3+} ions in the assembly (*cf.* Chapter 2, section 2.4). At room temperature, such weak coupling is negligible and cannot justify our observation. **Y-BTA** (red squares) shows diamagnetic behavior.

The samples were moreover subjected to a constant field of 5 T for up to 12 h while recording the magnetic susceptibility (Figure 4.4). For **Gd-BTA**, we find a decrease of the susceptibility by around 2 % with respect to the initial value χ_0. Regarding the time scale, this trend coincides well with the decrease of the Rayleigh ratio R we find in light scattering experiments (Figure **4.3**b). These results hint at a correlation of the demagnetization and the evolution of the supramolecular structure, indicating minor alignment of the **Gd-BTA** rods in the magnetic field. However, no changes were observed by optical birefringence at 1 or 2 T. Measurements of **Y-BTA** and buffer showed constant susceptibility over time (green and red data in Figure 4.4b)

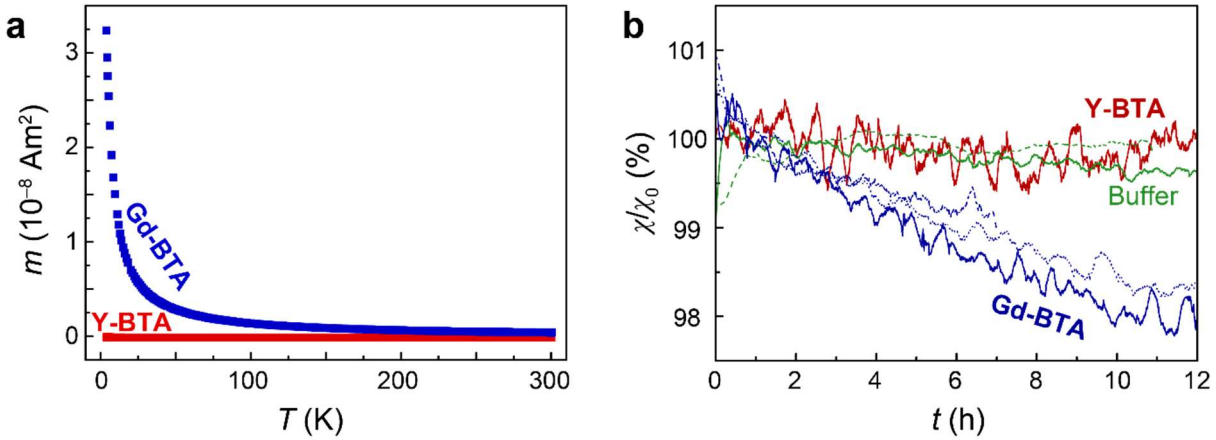

Figure 4.4 | Magnetic characterization of supramolecular rods and rod networks. (a) Temperature dependent magnetic moment *m* of **Gd-BTA** and **Y-BTA** in powder form (blue and red squares). **Gd-BTA** shows weak antiferromagnetic coupling at -0.7 K. **Y-BTA** shows diamagnetic behavior. (b) Time dependent magnetization of **Gd-BTA** and **Y-BTA** solutions (blue and red lines) and buffer (green lines) at room temperature in a 5 T field. Solid and dotted lines represent separate experiments.

4.4. Energetic considerations

In our illustration in Figure 4.2a, the self-assembly of the rods to rod networks is governed by a single equilibrium constant K_{netw}. This representation is simplified, as a single equilibrium constant does not account for distributions of the rod length or size. With this in mind, K_{netw} can be expressed as

$$K_{netw} = e^{-\frac{\Delta G° + \Delta G_m}{RT}} \tag{4.i}$$

with the standard Gibbs free energy $\Delta G°$ at 298 K and 0 T, the gas constant R and the temperature T. The additional term ΔG_m is a magnetic Gibbs free energy, which is induced by the magnetic field. It includes two components:

i) an isotropic term, based on the sum of all individual Gd^{3+} ion contributions

$$U_i = -\frac{1}{2} MB \tag{4.ii}$$

with the magnetization M and the magnetic flux density B, and

ii) an anisotropic free energy[43]

$$U_a = \frac{1}{4} \mu_0 M_s^2 (1 - 3N) \tag{4.iii}$$

including the effective demagnetization factor N ($N = 0$ for an axially magnetized long rod), the induced magnetization M_s, and the vacuum permeability μ_0. In our case (rods with M_s = 600 $A \cdot m^{-1}$, see section 4.7.4 in the appendix), the anisotropy energy is 0.17 $J \cdot m^{-3}$. By equating $U_a V = k_B T$, the volume V of a supramolecular network whose structure can be modified by the applied field can be estimated. We find a volume V of $24 \cdot 10^{-21}$ m^3, corresponding to an around 300 nm sized network.

4.5. Conclusions

We have shown that a 1 or 2 T uniform magnetic field perturbs the equilibrium of the supramolecular assembly of Gd^{3+}-containing BTA derivatives **Gd-BTA**. After identifying the two-step polymerization mechanism including a first assembly from monomers to rods, and a second from rods to rod networks, its response to an applied magnetic field was investigated. Whereas the single rods remain unaffected according to static light scattering, we find pronounced changes in the network topology: when exposed to the field, the fractal dimension of the network increases spontaneously from 1.7 to 2.6, and the light scattering intensity increases by 35 % over 10–12 hours. Simultaneously, the magnetic susceptibility decreases significantly by 2 %. A theoretical model shows that the magnetic shape anisotropy contributes to the overall Gibbs free energy, which can lead to an alignment of the fibers, which then, in turn, serves as positive feedback for fiber growth.

Previously described studies using magnetic fields as an external stimulus focus on irreversible processes such as crystallization[43], drying, pH-change[44], cross-diffusion[17] in layered systems or orientation of pre-formed particles[45]. In our case, the observed topology change is reversible, and the system relaxes back to the initial state after removal of the magnetic field.

We have shown that the magnetic field has a significant influence on the supramolecular assembly of several hundred nanometer large structures. Our approach of magnetically guided structure formation and manipulation could apply to other supramolecular and coordination polymers containing paramagnetic ions.

4.6. Author contributions

Pol Besenius, Isja de Feijter and Jorge Leira-Iglesias synthesized the molecules. Vincent Marichez and Akihiro Sato performed the light scattering experiments with the help of Matthieu Bailleul and Pascal Hébraud. SQUID experiments were performed by Peter Dunne and Munuswamy Venkatesan. Peter Dunne and Michael Coey performed magnetic ground-state calculations. Michaela Schicho calculated the fractal dimensions. Georges Formon, Michaela Schicho, and Thomas Hermans compiled and interpreted the data alongside all authors. Thomas Hermans conceived and supervised the research.

4.7. Appendix

4.7.1 Methods

Synthesis. The monomers **Gd-BTA** and **Y-BTA** were prepared as previously described.[32]

Cryo-TEM The cryoTEM experiments were performed on the TU/e CryoTitan (FEI), using a Gatan cryo-holder operating at ~ –170 °C (www.cryotem.nl). The TU/e CryoTitan is equipped with a field emission gun (FEG) operating at 300 kV. Images were recorded using a 2k x 2k Gatan CCD camera equipped with a post column Gatan Energy Filter (GIF). The sample vitrification procedure was carried out using an automated vitrification robot (FEI Vitrobot™ Mark III). CryoTEM grids, R2/2 Quantifoil Jena grids, were purchased from Quantifoil Micro Tools GmbH. Prior to the vitrification procedure the grids were surface plasma treated using a Cressington 208 carbon coater operating at 5 mA for 40 s.

Dynamic light scattering A Krypton ion laser (Spectra Physics) with a wavelength of 413 nm and a maximum intensity of 1 W was used at a laser power of 200 mW. A DRUSCH electromagnet with a 14 kW power supply with a pole distance of 38 mm was used to generate the magnetic field. Experiments involving the electromagnet were performed by repeating the following experimental cycle: (i) A 100 μM solution of **M-BTA** in 100 mM pH citrate buffer was immersed in a 25 °C thermostatted toluene bath and allowed to thermally equilibrate for 40 mins. (ii) The angle dependent correlation function was recorded at 7 scattering angles from 30° to 120° in 15° intervals at an integration time of 30 s per measurement. (iii) 60 consecutive correlcation functions were measured at an integration time of 60 s per measurement. (iv) The sample was placed in a uniform magnetic field of 1 or 2 T for one hour. The steps (iii) and (iv) were repeated until the recorded scattering intensity reached a plateau.

SQUID magnetometry. SQUID measurements were recorded on a Quantum Design MPMS XL 5 SQUID magnetometer on powders of **M-BTA**. For the relaxation measurements (see Figure 4.4b), 100 μM solutions of **M-BTA** in 100 mM pH 6 citrate buffer were placed in a cuvette in the center of the coil of magnetometer, and a 5 T field was applied. Magnetization and susceptibility were measured *in situ*.

4.7.2 Dynamic light scattering

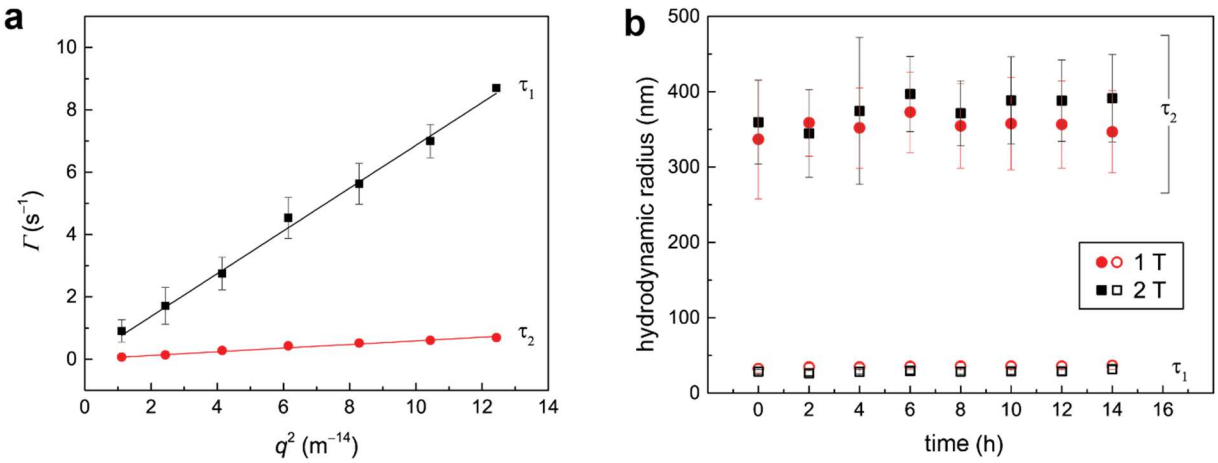

Figure 4.5 | Dynamic light scattering. (a) q^2-dependent decay rate Γ and the respective linear fits for both processes τ_1 (black squares) and τ_2 (red circles), exemplarily shown for 100 µM **Gd-BTA** in 100 mM citrate buffer at 1 T after 12 h. Error bars represent σ from the Schulz distribution fit. (b) Hydrodynamic radii $R_{H,1}$ and $R_{H,2}$ of **Gd-BTA** over time upon exposure to a 1 T (red circles) and 2 T (black squares) field for the same samples shown in Figure 4.3. Hollow and full symbols represent τ_1 and τ_2, respectively. Error bars represent σ from the Schulz distribution fit. 2 h of measurement include 1 h of exposure to a magnetic field followed by 1 h of light scattering experiments in the absence of a magnetic field.

4.7.3 Fractal dimension

4.7.3.1 Static light scattering

Mean scattering intensities I_{sam} were measured for 7 angles ϑ from 30° to 120° in 15° increments. Every measurement was repeated four times. In the measurement in a 1 T field, an ND filter was used for the angles 30° and 45°.

The Rayleigh ratio R is obtained from the measured mean scattering intensity I_{sam} following equation (4.iv)

$$R = \frac{I_{sam} - I_b}{I_{ref}} \cdot R_{ref} \cdot \left(\frac{n_{sam}}{n_{ref}}\right)^2 \tag{4.iv}$$

with the measured intensity of the background I_b, the measured intensity of the reference, which is toluene in this case, the Rayleigh ratio R_{ref} of the reference (R_{ref} = 1.35·10^{-5}·cm^{-1} for toluene[46]), the measured refactive index of the sample solution n_{sam} = 1.338, and the refractive index n_{ref} of the reference toluene (n_{ref} = 1.497).

The angles ϑ were converted to the scattering vectors q, following equation (4.v), with the wavelength of the laser λ = 413 nm and the refractive index of the sample solutions n_{sam}.[47,48]

$$q = \frac{4\pi n_{sam} \cdot \sin\left(\frac{\vartheta}{2}\right)}{\lambda} \tag{4.v}$$

The mean logarithmic Rayleigh Ratio R over all 5 measurements was plotted as a function of the logarithmic scattering vector q under consideration of the respective standard deviations (as shown in Figure 4.3a). The fractal dimension d_F is then obtained as the slope from linear regression. Figure 4.6 shows the obtained d_F values for magnetic fields of 2 T, 1 T and 0 T over time. The values and standard errors are given in Table 4.2.

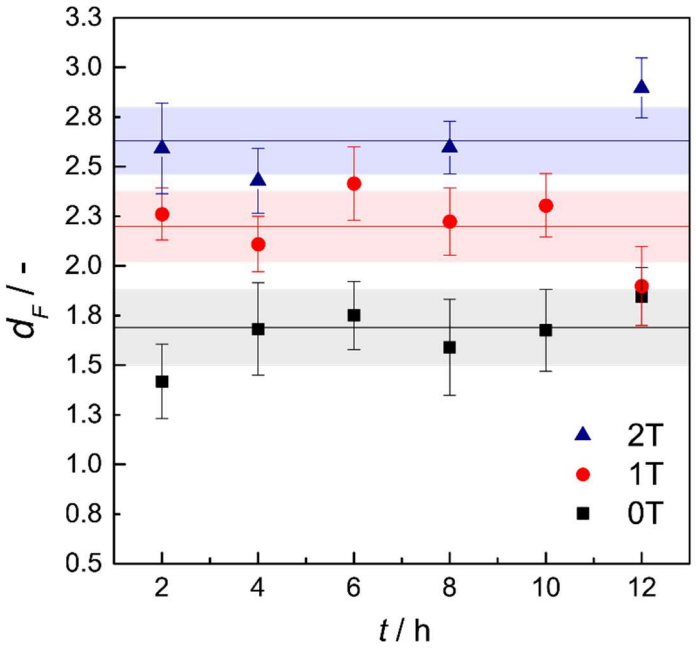

Figure 4.6 | Fractal dimensions from static light scattering. Fractal dimensions d_F over time at 2 T, 1 T and 0 T fields. Error bars represent standard errors from the linear fit. The horizontal lines represent the mean values and the shaded area their standard deviation over 5 or 6 measurements. 2 h of measuring include 1 h of exposure to a magnetic field followed by 1 h of light scattering experiments in the absence of a magnetic field. The mean values and standard deviations are listed in Table 4.2.

Table 4.2 | Fractal dimensions from static light scattering. Mean values and standard errors of d_F obtained from linear regression for 0 T, 1 T, and 2 T. The values are illustrated in Figure 4.6.

B (T)	d_F (-)
0	1.69 ± 0.19
1	2.20 ± 0.18
2	2.63 ± 0.17

4.7.3.2 Cryo-TEM: Box counting

The FracLac application of ImageJ (NIH) was used to calculate the fractal dimension from the obtained cryo-transmission electron images (cryo-TEM). The program works as follows: a series of grids of decreasing caliber ε, referring to the number of pixels per box, is laid over a binary image of the structure to be analyzed. The number of boxes N containing foreground pixels is recorded for every caliber. The fractal dimension d_F is obtained from the slope of the linear regression of logarithmic N versus logarithmic ε.[49]

$$d_F = \lim_{\varepsilon \to 0} \frac{\ln N_\varepsilon}{\ln \varepsilon} \tag{4.vi}$$

For example, the image Figure 4.7a was analyzed using three different methods. In method A (Figure 4.7b), the original image (Figure 4.7b) is automatically converted by the software to produce a binary image, which is then analyzed. In method B (Figure 4.7c), this conversion was done manually. Method C (Figure 4.7d) is a grayscale option, in which the grid caliber is set in relation with the variation in average intensity of the I_ε instead of N_ε. where $\delta I_{j,j,\varepsilon}$ is the difference between the maximum pixel intensity and the minimum pixel intensity.

Three basic types of d_F are reported, that differ in their way of accounting for the number of boxes or the intensity, respectively. For the determination of d_B, the sum of all intensities $I_{j,j,\varepsilon}$ are considered, whereas for d_M it is the mean over all intensities $I_{j,j,\varepsilon}$. For d_X, the average cover over all grids is calculated, and then processed as for d_B. The methods apply analogously for binary images, for which d_B and d_M are inherently equivalent.

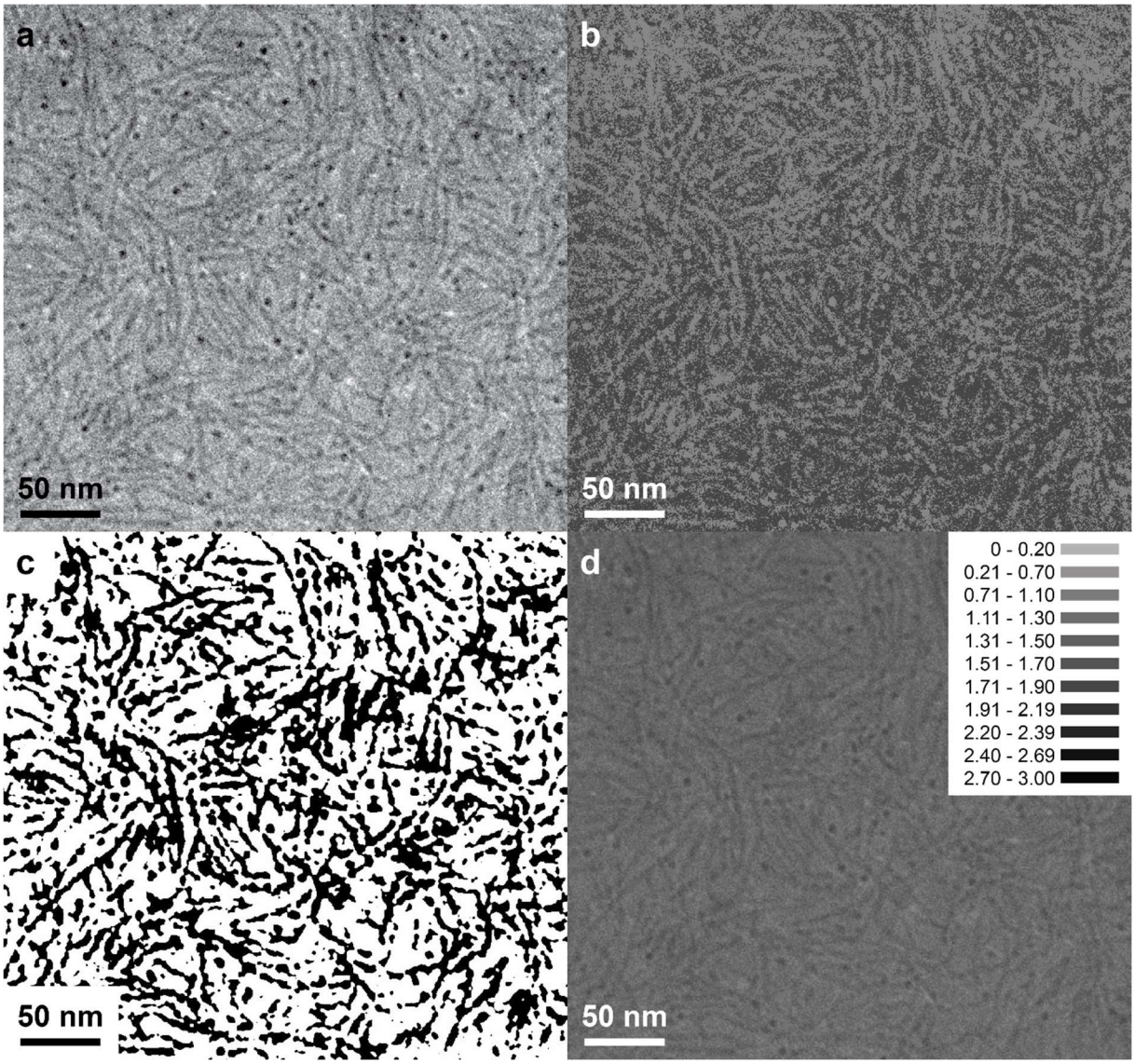

Figure 4.7 | Fractal dimensions from box counting. (a) A typical cryo-TEM image. (b) Image obtained by automatic processing (method A). (c) Image obtained from manual generation of a binary image (method B). (d) Image obtained from the differential grayscale method (method C) and the respective intensity-coded legend. All error bars represent 50 nm. The numerical results are listed in Table 4.3.

Table 4.3 | Fractal dimensions from box counting. Mean values and standard errors of d_B, d_M, and d_X for the three different methods A, B, and C. All values were obtained from image analysis using the FracLac application. Method A refers to the automatic generation of a binary image provided by the application. Method B refers to a manual generation of a binary image using standard ImageJ commands. Method C is the differential gray scaling method divided by FracLac. The respective binary images are depicted in Figure 4.7.

method	$\overline{d_B}$ (a.u.)	$\overline{d_M}$ (a.u.)	$\overline{d_X}$ (a.u.)
A (automatic binary)	1.85 ± 0.113	1.85 ± 0.113	1.85 ± 0.069
B (manual binary)	1.79 ± 0.084	1.79 ± 0.084	1.79 ± 0.059
C (grey differential)	1.77 ± 0.097	0.08 ± 0.065	1.76 ± 0.052

4.7.4 Magnetic ground state calculations

4.7.4.1 Method

To ensure that, at room temperature, the local dipolar fields play no role in the arrangement of the magnetic moments, we calculate the magnetic ground state for a magnetic assembly of length N_m in an external magnetic field using a lattice sum approach:

1. Impose an external field $\mathbf{B} = B_x\,\hat{\mathbf{x}} + B_y\,\hat{\mathbf{y}} + B_z\,\hat{\mathbf{z}}$.
2. Generate the positions of each rare earth atom in the BTA assemblies:

   knowing that in a single monomer those positions are $(x, y, z) = (0, r, 0)$, $\left(\frac{\sqrt{3}r}{2}, \frac{r}{\sqrt{2}}, 0\right)$, and $\left(-\frac{\sqrt{3}r}{2}, \frac{r}{\sqrt{2}}, 0\right)$ where $r = 2.25$ nm, that the stacking distance between monomers is $d = 0.35$ nm, and that there is a helicity of 10° rotation per layer, which for the i^{th} atom of the j^{th} layer is:[50]

$$\begin{bmatrix} x' \\ y' \\ z' \end{bmatrix}_{i,j} = \begin{bmatrix} \cos j\theta & -\sin j\theta & 1 \\ \sin j\theta & \cos j\theta & 1 \\ 0 & 0 & 1 \end{bmatrix} \begin{bmatrix} x \\ y \\ z + jd \end{bmatrix}_{i,j}$$

3. Calculate each local dipole moment using either a Curie-Law or Brillouin function (at $T = 298$ K the difference is negligible) giving and array of

$$\boldsymbol{m} = m_x\,\hat{\mathbf{x}} + m_y\,\hat{\mathbf{y}} + m_z\,\hat{\mathbf{z}}$$

4. At each atomic site, calculate the dipolar field due to all other moments in the assembly using

$$\mathbf{B}(\mathbf{r}) = \frac{\mu_0}{4\pi}\left[\frac{3\mathbf{m}(\mathbf{m}\cdot\hat{\mathbf{r}})}{r^5} - \frac{\mathbf{m}}{r^3}\right]$$

   which is the magnetic field at a point in space due to a magnetic dipole[42], resulting in a matrix

$$\mathbf{B_{dip}} = B_{dip,x}\,\hat{\mathbf{x}} + B_{dip,y}\,\hat{\mathbf{y}} + B_{dip,z}\,\hat{\mathbf{z}}$$

5. At each atomic site sum the external and dipole fields $\mathbf{B_{total}} = \mathbf{B_{ext}} + \mathbf{B_{dip}}$
6. Calculate a new moment $\boldsymbol{m_{new}}$ at each site using the local $\mathbf{B_{total}}$

7. Calculate the mean L_2 norm for the difference between the updated and old moment vectors at each site

$$\overline{||m||_2} = \frac{1}{N_{atoms}} \sum (m_{new} - m_{old})^2$$

8. Repeat 3 – 7 with updated total field and moments until $\overline{||m||_2} < \text{threshold}$

Other minimization approaches are possible, such as by fixing the magnitude of the magnetic moments and minimizing the energy cost function through a free rotation of each moment. A first, simpler cost function, takes a macro-spin approach, assigning one polar (θ) – azimuthal (ϕ) angle pair, with all atomic moments rotating coherently, which is minimized using the L-BFGS-B algorithm. The second allows the free rotation of each moment using basin hopping global optimization, with L-BFGS-B as the local optimizer. However, both approaches are slower than the L_2 norm method presented above, particularly the global optimization method.

4.7.4.2 Results

First, as a reference value, we calculate the ideal magnetization of a rod. The cylindrical volume for N_L = 100 monolayers is $\pi r^2 d N_L$ = 557 nm^3, in which there are 300 Gd atoms, or therefore ~ 0.54 Gd per nm^3. For fully aligned moments, with B = 2 T and T = 298 K, the effective magnetic moment is m_{eff} ~ 0.12 μ_B per Gd atom, and thus the magnetization is M = 0.12 μ_B·0.54 Gd per nm^3 = 600 A·m^{-1}. In other words, the induced M is 0.04 % the external field B_{ext} = 2 T.

We find that for any external field **B**, the local magnetic moments are collinear with **B** in the ground state (Figure 4.8a and b). For a sum over an assembly of 1000 monomers, with **B** parallel to the fiber, (B_z = 2 T) the magnetization is M = 595.1 A·m^{-1}, while with **B** perpendicular to the fiber (B = 2 T) M = 594.8 A·m^{-1}, both marginally smaller than the ideal value of 600 A·m^{-1} arising from the demagnetizing field due to the local dipolar fields. Unlike the atomic moments, the local dipolar fields form complex helical patterns (Figure 4.8c and d). However, we find that their magnitude is ≈ 2 mT, three orders of magnitude smaller than the 2 T external field (Figure 4.9), and lead to the calculated magnetization being marginally smaller than the ideal case as expected for a very weak demagnetizing field.

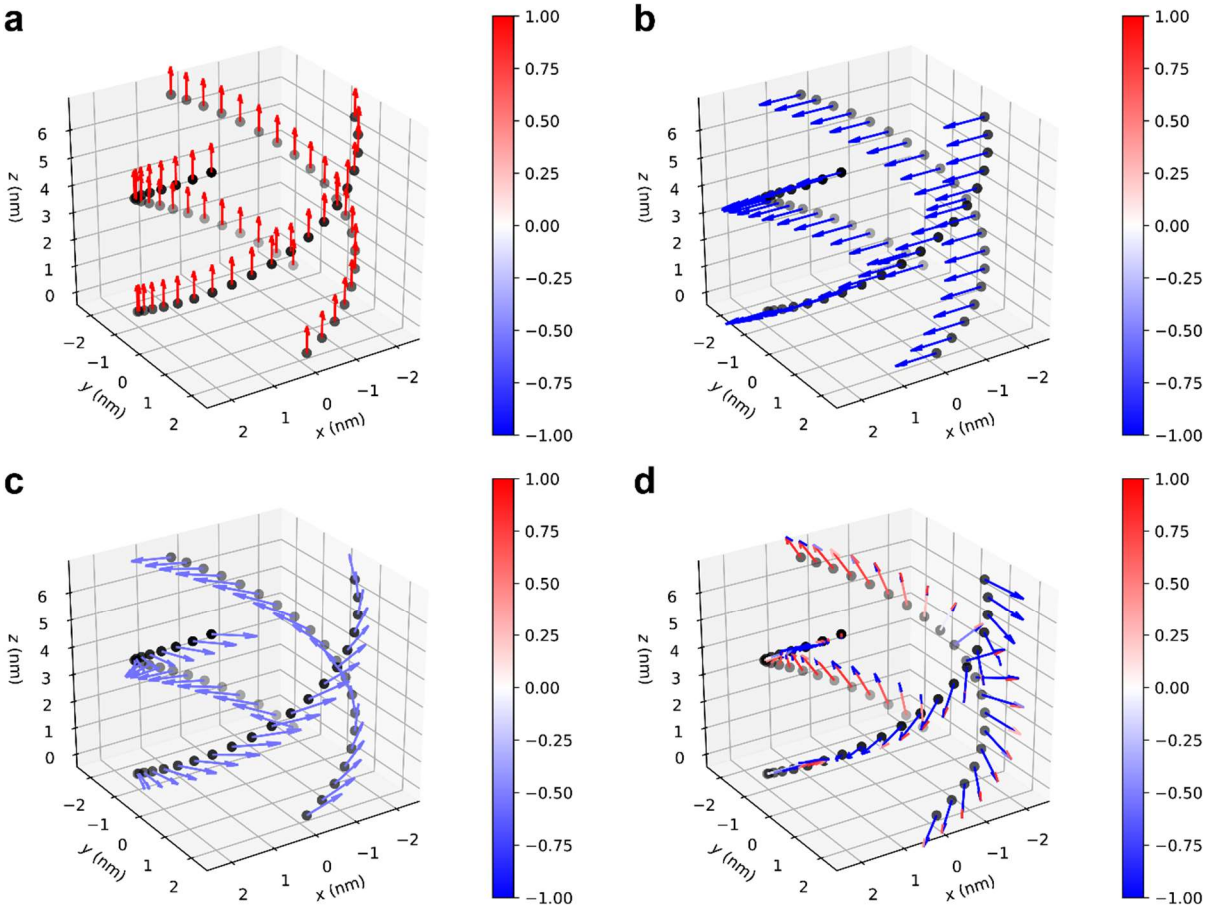

Figure 4.8 | Simulated induced atomic moments. Normalized quiver plot of the induced atomic moments under an external 2 T field (a) along *z*, (b) along *x*, with the corresponding local dipolar fields in (c) and (d) for *B* // *z* and *B* // *x*, respectively. *B* // *y* is not shown but is identical to *B* // *x*.

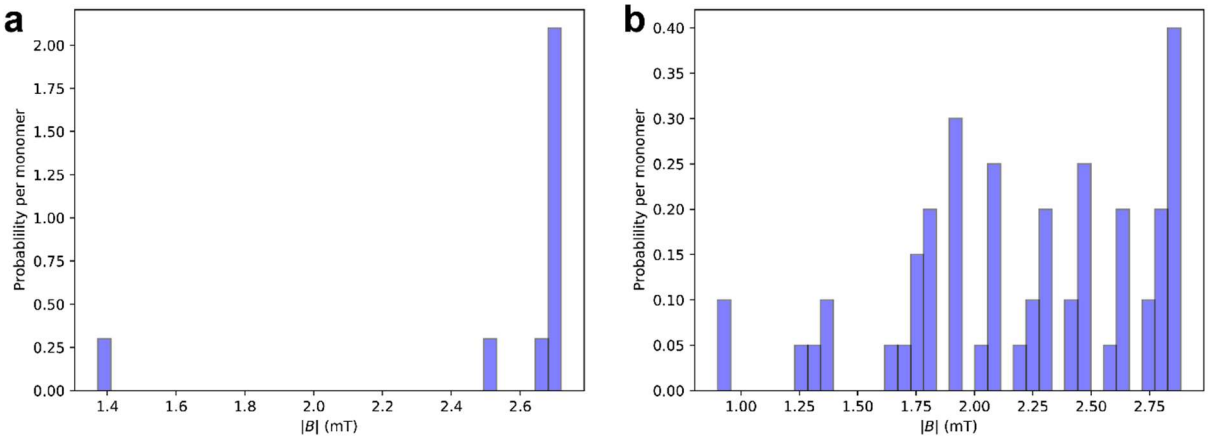

Figure 4.9 | Distribution of the magnitude of the dipolar magnetic fields. Distributions are shown for 100 monomers for **a)** *B* // *z*, and **b)** *B* // *x*. *B* // *y* is not shown but is identical to *B* // *x*.

Table 4.4 | Results of magnetic ground state calculations. The experimental magnetic moment m, magnetic energy per monomer U_m, critical length L_c, and critical monomer number N_c (where the magnetic energy would become relevant as compared to thermal noise) for various transition metal and rare earth ions **M** in a **M-BTA** assembly, with B = 2 T and T = 298 K**.** Beware that these are calculated values and that we assume that the assemblies are all rod-like as those shown in the main text.

M	m (μ_B)	U_m (J·mol^{-1} monomer$^{-1)}$	ΔG (J·mol^{-1} monomer^{-1})	L_c (nm)	N_c (-)
Ti^{3+}, V^{4+}	1.7	-0.07	-0.04	11918	34052
Ti^{2+}, V^{3+}	2.8	-0.20	-0.10	4393	12553
V^{2+}, Cr^{3+}	3.8	-0.36	-0.18	2385	6816
Cr^{2+}, Mn^{3+}	4.9	-0.60	-0.30	1435	4099
Mn^{2+}, Fe^{3+}	5.9	-0.88	-0.44	989	2828
Fe^{2+}, Co^{3+}	5.4	-0.73	-0.37	1181	3375
Co^{2+}, Ni^{3+}	4.8	-0.58	-0.29	1495	4272
Ni^{2+}	3.2	-0.26	-0.13	3364	9611
Cu^{2+}	1.9	-0.09	-0.05	9541	27261
Ce^{3+}	2.5	-0.16	-0.08	5511	15746
Pr^{3+}	3.5	-0.31	-0.15	2812	8034
Nd^{3+}	3.4	-0.29	-0.15	2980	8513
Sm^{3+}	1.7	-0.07	-0.04	11918	34052
Eu^{3+}	3.4	-0.29	-0.15	2980	8513
Gd^{3+}	8.9	-1.99	-1.00	435	1243
Tb^{3+}	9.8	-2.42	-1.21	359	1025
Dy^{3+}	10.6	-2.83	-1.41	307	876
Ho^{3+}	10.4	-2.72	-1.36	318	910
Er^{3+}	9.5	-2.27	-1.14	382	1091
Tm^{3+}	7.6	-1.45	-0.73	596	1704

4.8. References

1. Aida, T. & Meijer, E. W. Supramolecular Polymers – We've Come Full Circle. *Isr. J. Chem.* **60**, 33–47 (2020).
2. Hirst, A. R., Roy, S., Arora, M., Das, A. K., Hodson, N., Murray, P., Marshall, S., Javid, N., Sefcik, J., Boekhoven, J., van Esch, J., Santabarbara, S., Hunt, N. T. & Ulijn, R. V. Biocatalytic Induction of Supramolecular Order. *Nat. Chem.* **2**, 1089–1094 (2010).
3. Webber, M. J., Newcomb, C. J., Bitton, R. & Stupp, S. I. Switching of Self-Assembly in a Peptide Nanostructure with a Specific Enzyme. *Soft Matter* **7**, 9665–9672 (2011).
4. Sorrenti, A., Leira-Iglesias, J., Sato, A. & Hermans, T. M. Non-Equilibrium Steady States in Supramolecular Polymerization. *Nat. Commun.* **8**, 15899–15907 (2017).
5. Carnall, J. M. A., Waudby, C. A., Belenguer, A. M. & Stuart, M. C. A. Mechanosensitive Self-Replication Driven by Self-Organization. *Science* **327**, 1502–1506 (2010).
6. van Herpt, J. T., Stuart, M. C. A., Browne, W. R. & Feringa, B. L. Mechanically Induced Gel Formation. *Langmuir* **29**, 8763–8767 (2013).
7. Adhikari, B., Yamada, Y., Yamauchi, M., Wakita, K., Lin, X., Aratsu, K., Ohba, T., Karatsu, T., Hollamby, M. J., Shimizu, N., Takagi, H., Haruki, R., Adachi, S. & Yagai, S. Light-Induced Unfolding and Refolding of Supramolecular Polymer Nanofibres. *Nat. Commun.* **8**, 15254 (2017).
8. Iwaura, R. & Shimizu, T. Reversible Photochemical Conversion of Helicity in Self-Assembled Nanofibers from a 1,ω- Thymidylic Acid Appended Bolaamphiphile. *Angew. Chem. Int. Ed.* **45**, 4601–4604 (2006).
9. Li, L., Jiang, H., Messmore, B. W., Bull, S. R. & Stupp, S. I. A Torsional Strain Mechanism To Tune Pitch in Supramolecular Helices. *Angew. Chem. Int. Ed.* **119**, 5977–5980 (2007).
10. Zhang, J., Hao, R., Huang, L., Yao, J., Chen, X. & Shao, Z. Self-assembly of a Peptide Amphiphile Based on Hydrolysed Bombyx Mori Silk Fibroin. *Chem Commun* **47**, 10296–10298 (2011).
11. Frisch, H., Unsleber, J. P., Lüdeker, D., Peterlechner, M., Brunklaus, G., Waller, M. & Besenius, P. pH-Switchable Ampholytic Supramolecular Copolymers. *Angew. Chem. Int. Ed.* **52**, 10097–10101 (2013).
12. Moyer, T. J., Finbloom, J. A., Chen, F., Toft, D. J., Cryns, V. L. & Stupp, S. I. pH and Amphiphilic Structure Direct Supramolecular Behavior in Biofunctional Assemblies. *J Am Chem Soc* **136**, 14746–14752 (2014).
13. Ohta, E., Sato, H., Ando, S., Kosaka, A., Fukushima, T., Hashizume, D., Yamasaki, M., Hasegawa, K., Muraoka, A., Ushiyama, H., Yamashita, K. & Aida, T. Redox-Responsive Molecular Helices with Highly Condensed π-Clouds. *Nat. Chem.* **68–73**, 6 (2011).
14. Leira-Iglesias, J., Sorrenti, A., Sato, A., Dunne, P. A. & Hermans, T. M. Supramolecular Pathway Selection of Perylenediimides Mediated by Chemical Fuels. *Chem. Commun.* **52**, 9009–9012 (2016).
15. Ciferri, A. *Supramolecular Polymers*. (Taylor & Francis, 2005).
16. Shklyarevskiy, I. O., Jonkheijm, P., Christianen, P. C. M., Schenning, A. P. H. J., Meijer, E. W., Henze, O., Kilbinger, A. F. M., Feast, W. J., Del Guerzo, A., Desvergne, J.-P. & Maan, J. C. Magnetic Deformation of Self-Assembled Sexithiophene Spherical Nanocapsules. *J. Am. Chem. Soc.* **127**, 1112–1113 (2005).
17. Radvar, E., Shi, Y., Grasso, S., Edwards-Gayle, C. J. C., Liu, X., Mauter, M. S., Castelletto, V., Hamley, I. W., Reece, M. J. & S. Azevedo, H. Magnetic Field-Induced Alignment of Nanofibrous Supramolecular Membranes: A Molecular Design Approach to Create Tissue-like Biomaterials. *ACS Appl. Mater. Interfaces* **12**, 22661–22672 (2020).
18. Gopinadhan, M., Choo, Y., Kawabata, K., Kaufman, G., Feng, X., Di, X., Rokhlenko, Y., Mahajan, L. H., Ndaya, D., Kasi, R. M. & Osuji, C. O. Controlling Orientational Order in Block Copolymers Using Low-Intensity Magnetic Fields. *Proc. Natl. Acad. Sci.* **114**, E9437–E9444 (2017).
19. Singh, G., Chan, H., Baskin, A., Gelman, E., Repnin, N., Kral, P. & Klajn, R. Self-Assembly of Magnetite Nanocubes into Helical Superstructures. *Science* **345**, 1149–1153 (2014).
20. Michot, L. J., Bihannic, I., Maddi, S., Funari, S. S., Baravian, C., Levitz, P. & Davidson, P. Liquid-Crystalline Aqueous Clay Suspensions. *Proc. Natl. Acad. Sci.* **103**, 16101–16104 (2006).
21. Isabettini, S., Massabni, S., Hodzic, A., Durovic, D., Kohlbrecher, J., Ishikawa, T., Fischer, P., Windhab, E. J., Walde, P. & Kuster, S. Molecular Engineering of Lanthanide Ion Chelating Phospholipids Generating Assemblies with a Switched Magnetic Susceptibility. *Phys. Chem. Chem. Phys.* **19**, 20991–21002 (2017).
22. Polarz, S., Bährle, C., Landsmann, S. & Klaiber, A. Panoscopic Structures by Hierarchical Cascade Self-Assembly of Inorganic Surfactants with Magnetic Heads Containing Dysprosium Ions. *Angew. Chem. Int. Ed.* **52**, 13665–13670 (2013).
23. Mandelbrot, B. B. *Fractals and the Geometry of Nature*. (Freeman, 1982).
24. Schaefer, D. W. Polymers, Fractals, and Ceramic Materials. *Science* **243**, 1023–1027 (1989).
25. Cai, J., Hu, X., Xiao, B., Zhou, Y. & Wei, W. Recent Developments on Fractal-Based Approaches to Nanofluids and Nanoparticle Aggregation. *Int. J. Heat Mass Transf.* **105**, 623–637 (2017).
26. Feder, J., Jøssang, T. & Rosenqvist, E. Scaling Behavior and Cluster Fractal Dimension Determined by Light Scattering from Aggregating Proteins. *Phys. Rev. Lett.* **53**, 1403–1406 (1984).

27. Ferri, F., Greco, M., Arcòvito, G., De Spirito, M. & Rocco, M. Structure of Fibrin Gels Studied by Elastic Light Scattering Techniques: Dependence of Fractal Dimension, Gel Crossover Length, Fiber Diameter, and Fiber Density on Monomer Concentration. *Phys. Rev. E* **66**, 011913 (2002).
28. von Korff, M. & Sander, T. Molecular Complexity Calculated by Fractal Dimension. *Sci. Rep.* **9**, 967 (2019).
29. Raper, J. A. & Amal, R. Measurement of Aggregate Fractal Dimensions Using Static Light Scattering. *Part. Part. Syst. Charact.* **10**, 239–245 (1993).
30. Sacanna, S., Rossi, L., Wouterse, A. & Philipse, A. P. Observation of a Shape-Dependent Density Maximum in Random Packings and Glasses of Colloidal Silica Ellipsoids. *J. Phys. Condens. Matter* **19**, 376108 (2007).
31. Thouy, R. & Jullien, R. Structure Factors for Fractal Aggregates Built Off-Lattice with Tunable Fractal Dimension. *J. Phys. I* **6**, 1365–1376 (1996).
32. Besenius, P., Portale, G., Bomans, P. H. H., Janssen, H. M., Palmans, A. R. A. & Meijer, E. W. Controlling the Growth and Shape of Chiral Supramolecular Polymers in Water. *Proc. Natl. Acad. Sci.* **107**, 17888–17893 (2010).
33. Sastri, V. S., Bünzli, J.-C., Ramachandra Rao, V., Rayudu, G. V. S. & Perumareddi, J. R. *Modern Aspects of Rare Earths and their Complexes*. (Elsevier B.V., 2003).
34. Tircsó, G., Tircsóné Benyó, E., Garda, Z., Singh, J., Trokowski, R., Brücher, E., Sherry, A. D., Tóth, É. & Kovács, Z. Comparison of the Equilibrium, Kinetic and Water Exchange Properties of Some Metal Ion-DOTA and DOTA-bis(amide) Complexes. *J. Inorg. Biochem.* **206**, 111042 (2020).
35. Provencher, S. W. A Constrained Regularization Method for Inverting Data Represented by Linear Algebraic or Integral Equations. *Comput. Phys. Commun.* **27**, 213–227 (1982).
36. Pecora, R. *Dynamic Light Scattering*. (Springer US, 1985).
37. Tirado, M. M., Martínez, C. L. & de la Torre, J. G. Comparison of Theories for the Translational and Rotational Diffusion Coefficients of Rod-like Macromolecules. Application to Short DNA Fragments. *J. Chem. Phys.* **81**, 2047–2052 (1984).
38. Mohraz, A., Moler, D. B., Ziff, R. M. & Solomon, M. J. Effect of Monomer Geometry on the Fractal Structure of Colloidal Rod Aggregates. *Phys. Rev. Lett.* **92**, 1555031–1555034 (2004).
39. Hough, L. A., Islam, M. F., Hammouda, B., Yodh, A. G. & Heiney, P. A. Structure of Semidilute Single-Wall Carbon Nanotube Suspensions and Gels. *Nano Lett.* **6**, 313–317 (2006).
40. Schaefer, D. W., Brown, J. M., Anderson, D. P., Zhao, J., Chokalingam, K., Tomlin, D. & Ilavsky, J. Structure and Dispersion of Carbon Nanotubes. *J. Appl. Crystallogr.* **36**, 553–557 (2003).
41. Bauer, B. J., Hobbie, E. K. & Becker, M. L. Small-Angle Neutron Scattering from Labeled Single-Wall Carbon Nanotubes. *Macromolecules* **39**, 2637–2642 (2006).
42. Coey, J. M. D. *Magnetism and Magnetic Materials*. (Cambridge University Press, 2010).
43. Klara, S. S., Saboe, P. O., Sines, I. T., Babaei, M., Chiu, P.-L., DeZorzi, R., Dayal, K., Walz, T., Kumar, M. & Mauter, M. S. Magnetically Directed Two-Dimensional Crystallization of OmpF Membrane Proteins in Block Copolymers. *J. Am. Chem. Soc.* **138**, 28–31 (2016).
44. Wallace, M., Cardoso, A. Z., Frith, W. J., Iggo, J. A. & Adams, D. J. Magnetically Aligned Supramolecular Hydrogels. *Chem. - Eur. J.* **20**, 16484–16487 (2014).
45. Matsumoto, K., Kimura, F., Tsukui, S. & Kimura, T. X-ray Diffraction of a Magnetically Oriented Microcrystal Suspension of L -Alanine. *Cryst. Growth Des.* **11**, 945–948 (2011).
46. Moreels, E., De Ceuninck, W. & Finsy, R. Measurements of the Rayleigh Ratio of Some Pure Liquids at Several Laser Light Wavelengths. *J. Chem. Phys.* **86**, 618–623 (1987).
47. Hayduk, W., Laudie, H. & Smith, O. H. Viscosity, Freezing point, Vapor-Liquid Equilibriums, and Other Properties of Aqueous-Tetrahydrofuran Solutions. *J. Chem. Eng. Data* **18**, 373–376 (1973).
48. Signer, R., Arm, H. & Daeniker, H. Untersuchungen über das Verhalten organischer Mischphasen. Dampfdrücke, Dichten, thermodynamische Mischungsfunktionen und Brechungsindices der binären Systeme Wasser-Tetrahydrofuran und Wasser-Diäthyläther bei 25°. *Helv. Chim. Acta* **52**, 2347–2351 (1969). German.
49. NIH ImageJ. Box Counting. https://imagej.nih.gov/ij/plugins/fraclac/FLHelp/BoxCounting.htm (2020).
50. Kittel, C. *Introduction to Solid State Physics*. (Wiley, 2004).

THIS PAGE IS INTENTIONALLY LEFT BLANK

Chapter 5. Magnetic control over supramolecular gelation kinetics

Abstract

The focus of this chapter is on the development of magneto-responsive materials. We introduce a lanthanide-containing supramolecular hydrogel based on *N*,*N*′-bis (5-aminoisophthalic acid)naphthalene diimide, where gelation is triggered by coordination and a controlled pH decrease. By magnetorheology, we were able to follow the gelation kinetics in uniform magnetic fields. Surprisingly, the gelation time of a Dy^{3+}-containing hydrogel is halved upon exposure to a field of 0.8 T. Even at weak fields of around 0.1 T, the gelation time can be reduced significantly. Unexpectedly, gelation can be inhibited by a magnetic field in a lanthanide-free, diamagnetic system of the same gelator. These surprising results lay a foundation for new approaches to magnetically control supramolecular gelation in both para- and diamagnetic systems.

5.1 Introduction

After having studied lanthanide-containing supramolecular structures both in solution and as colloidal dispersions, the development of magneto-responsive materials is a major step towards future applications. Unidirectionally aligned supramolecular materials are desired in state-of-the-art technologies in regenerative biomedicine[1–3], and (opto-)electronics[4–6].[7] This directionality can be achieved if fibers of a supramolecular material align during spin-coating, or in an electric or magnetic field.[8,9]

Different types of magnetic and magneto-controllable supramolecular gels have been developed. First, it is possible to align diamagnetic gels in strong fields, as reported by Adams and coworkers in 2014.[10] Fibers of a naphthalene-derived FF dipeptide hydrogelator were aligned when gelling in a 9.4 T field. Similarly, an anthracene-based organogel showed fiber alignment in fields of up to 20 T, which was shown by the group of Maan.[11] In both cases, the conformation of the aligned gels is retained after removal of the magnetic field.

As previously discussed, paramagnetic structures are typically much easier to control regarding the required field strength. Paramagnetism in gels can be obtained from a precisely designed monomer, as for example in the TEMPO-radical based organogel presented by Ohkoshi and coworkers.[12] TEMPO, a stable nitroxide-radical, is coupled to an isoleucine-based gelator scaffold. The latter assembles to nanofibers in a β-sheet configuration. The spins of the unpaired ions are aligned one-dimensionally due to the well-defined structural order of the gel, and SQUID measurements have shown that the magnetization of the material is temperature dependent.

In another approach to obtain "supramolecular magneto-gels", as Castanheira and coworkers call it, fibers of supramolecular gels can be conjugated to magnetic nanoparticles.[13] This technique is especially interesting in drug delivery, where nanoparticles are exploited for magnetic hypothermia. Löwik *et al*. showed immobilization of magnetically aligned peptide amphiphile nanoribbons in a two-step approach. In the first step, the nanoribbons are prepared in very strong fields of up to 20 T. The obtained, highly organized structure is then transferred to a polymer backbone, which adapts to the directional structure of the nanoribbons, and allows its conservation.[14]

In line with the previously reported systems, we aim to study the magneto-response of a lanthanide-containing supramolecular hydrogel, with a special interest in the bulk properties of the material. Such lanthanide containing hydrogels have already been reported, where iminodiacetic acid[15], or terpyridine-[16], or nucleoside-based[17] ligands were used to chelate to either Dy^{3+}, Tb^{3+}, Gd^{3+}, or Eu^{3+}. However, these systems were studied exclusively for their exceptional photoluminescence properties. The magnetic properties were not explored, which is unfortunate from our perspective.

We employ a naphthalene diimide (NDI)-based ligand, which forms supramolecular hydrogels through coordination of their carboxylate moieties with lanthanide ions. We use magnetorheology to study the kinetics and the mechanical properties of the obtained gels for three different magnetic lanthanides and two diamagnetic controls.

5.2 Lanthanide-containing supramolecular hydrogels

The lanthanide containing hydrogels are based on *N*,*N*′-bis (5-aminoisphthalic acid)naphthalene diimide (**BINDI**), which is a previously described pH-responsive supramolecular hydrogelator (Figure 5.1a).[18] The four carboxylic acid groups are available for coordination to the lanthanide ions $\mathbf{M}^{3+}$ (**M** = La, Gd, Dy, Er) when deprotonated. Commonly, carboxylates coordinate as monodentate ligands, as in the previously discussed DOTA complexes (Chapter 2–4). More rarely, they chelate as bidentate ligands.[19,20] Self-supporting gels of **M-BINDI** were obtained at a concentration of 5 mg·mL^{-1} (0.5 wt%) and 4 equivalents of lanthanide ions, which were added as trichloride hexahydrate salts (see Figure 5.1b). The gels were prepared by dissolving the gelator in 1 M aqueous NaOH (6 eq.) and adding an aqueous solution of $\mathbf{M}Cl_3$ (4 eq.) and Glucono-δ-lactone (GdL, 6 eq.). GdL is widely used in pH-triggered systems since upon addition of water it hydrolyzes slowly to gluconic acid (see section 5.7.3 in the appendix). Thereby, it enables a slow and controlled pH decrease.[21]

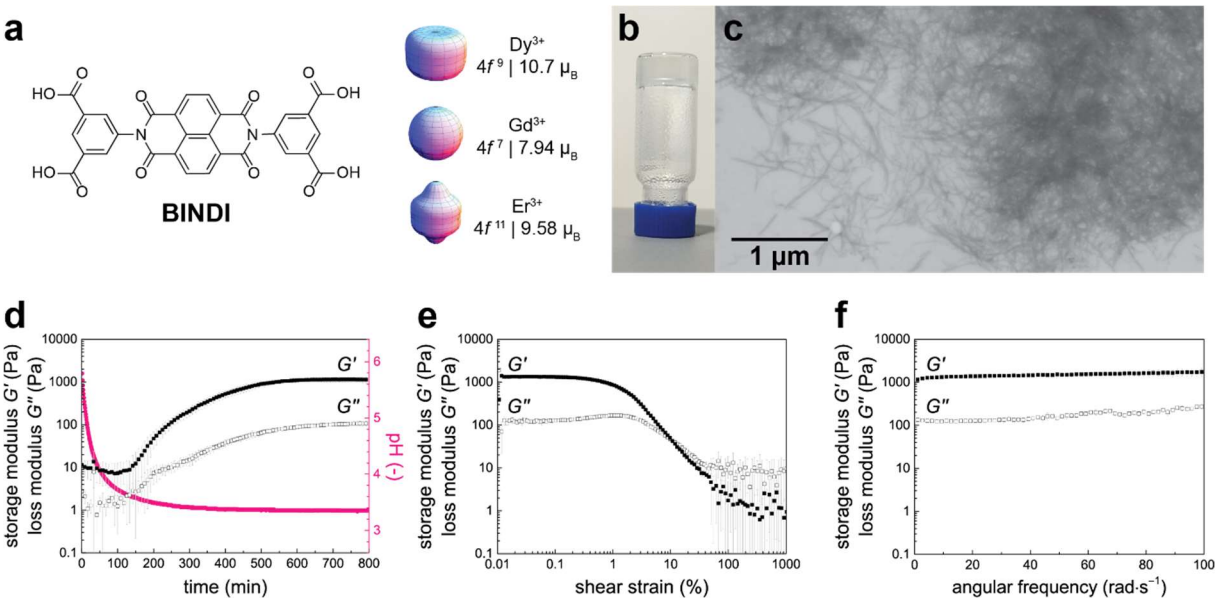

Figure 5.1 | Lanthanide-containing BINDI hydrogel at 6 eq. GdL. (a) Left: Molecular structure of the gelator **BINDI**. Right: Simulated electron density distributions[22] of the ions Dy^{3+}, Gd^{3+}, and Er^{3+}, as well as their electron configurations and magnetic moments μ[23]. μ is given in $\mu_B = 9.274 \cdot 10^{-24}$ Am². The diamagnetic control ion La^{3+} (not depicted) exhibits an isotropic electron density distribution, noble gas configuration and $\mu = 0$. (b) Digital photograph of the inverted vial test of a **Dy-BINDI** gel. (c) STEM image of the fibrous nanostructure of a **Dy-BINDI** gel, drop-cast. (d) Kinetic rheological data (black) and pH evolution (pink) of a **Dy-BINDI** gel at 25 °C, measured in two parallel experiments. (e) Strain sweep, revealing a critical shear strain of 1.4 %. (f) Frequency sweep, showing frequency-independence of the gel (at 0.1% strain). Full squares represent the storage modulus *G′*, hollow squares the loss modulus *G″*. Error bars represent standard deviations over three measurements. Panel a partly reproduced from reference [22] with permission from the Royal Society of Chemistry.

The deprotonation of **BINDI** in aqueous NaOH (1 M, pH 14) is necessary to dissolve **BINDI** in water. At this basic pH, the metal salts precipitate reversibly as hydroxides[24] and can be resolubilized upon a pH decrease. The hydroxides $M(OH)_3$ of the lanthanides that are used in this study resolubilize at pH 6.1 – 6.3 for Dy, Gd, and Er, and at 7.5 for La. The pK_a values of the two carboxylic acids of isophthalic acid are 3.5 and 4.5, respectively.[25] The optimal pH range for coordination is thus between 4.5 and 6 or 7.5. In this regime, the carboxylic acids are

deprotonated, and the salts are in solution. As the sample is prepared, the basic solution of **BINDI** is diluted by a factor 20, reaching a pH within this window (pH 5.5–6.5).

The gel incorporates around 70 % of the solvent, leaving residual solution behind. If the proportion of solvent to **BINDI** is accordingly reduced by 30 %, 30 % of solution nevertheless remains. It is likely that the excess of salt (4 eq. $DyCl_3$ per **BINDI**, 2 eq. of coordination sites per monodentate carboxylic acid) drives the gelation through a "salting out" effect[26]. This would imply that the solubility of **BINDI** decreases in a highly concentrated solution of $DyCl_3$, inducing aggregation of the less hydrophilic **BINDI**. To ensure that the metal ions do not just salt out the gelator, but are incorporated in the gel network, IR spectroscopy was performed (see section 5.7.4 in the appendix). A shift of the C=O carboxyl stretch vibration from 1670 cm^{-1} to 1588 cm^{-1} implies coordination, as previously shown for **Y-NDI** (Chapter 2, Figure 2.13).[27,28] The signals corresponding to the C–O stretch vibration, which disappear upon complexation, cannot be identified in this case, because they overlap with the C–O vibrations of primary and secondary alcohols in GdL. A physical indication of complexation is given by the formation of a suspension upon the addition of **BINDI** (solubilized in 1 M aq. NaOH) to the aqueous salt solution. In the absence of **BINDI** (*i.e.*, addition of 1 M aq. NaOH), the salt remains dissolved. This initial phase separation develops into a homogenous and translucent 3D structure over time[29], following the ongoing network formation with a decreasing pH.

As a first step to characterize the gels, a **Dy-BINDI** gel was prepared following the described method, and its microstructure was imaged by scanning transmission electron microscopy of a drop-cast sample. It reveals a network of fine fibers (Figure 5.1c) with an average fiber thickness of 12 nm ± 5 nm.

The **Dy-BINDI** gel formation can be followed by rheology. To this end, the storage- and loss moduli G' and G'' were recorded as a function of time at a constant shear strain of 0.1 % and an angular frequency of 10 $rad \cdot s^{-1}$ (black squares in Figure 5.1d). The kinetic measurement shows that gelation starts after 140 min, indicated by an increase of both moduli G' and G''. After around 650 min, when the values of G' and G'' stabilize at a plateau, the gel is completely formed. The corresponding measurements changing the shear strain or angular frequency (Figure 5.1e,f) confirm that these conditions (shear strain of 0.1 % and angular frequency of 10 $rad \cdot s^{-1}$) are within the linear viscoelastic region (LVER) of the gel. By using these parameters to follow the kinetics, we ensure that the gel properties are not altered or influenced by the rheological measurement.

After 140 min, which is when the gelation starts, the pH (pink circles in Figure 5.1d) has reached a value of 3.6. Thereafter, the pH keeps decreasing slightly, converging towards a plateau at pH 3.4, which coincides well with the first pK_a of isophthalic acid (3.5).

5.3 Magnetically controlled gelation kinetics

Using a magnetorheological setup, homogenous magnetic fields of up to 0.78 T were applied during the gelation of **Dy-BINDI** gels. The magnetic field is perpendicular to the surface of the plate/plate rheological configuration. Figure 5.2a shows the respective time dependent storage and loss moduli G' and G'' at 0 T (black squares) and 0.78 T (red triangles). At 0.78 T, a plateau of the storage modulus G' and the loss modulus G'' indicate complete gelation after 340 min. This is around half of the time needed for the gel to form in 0 T (650 min). In both cases, the gels reach a final stiffness of around 1.3 kPa.

Intermediate field strengths of 0.13 and 0.52 T were also applied in separate gelation experiments (Figure 5.2b). In terms of half-times (*i.e.*, time at which 50 % of the final stiffness is reached), the gelation was accelerated by 14 and 24 %, respectively. All gels formed in different fields exhibit a similar final strength, with critical shear strains between 1.1 and 1.4 % and crossovers of G' and G'' at 10 to 15 % shear strain (see section 5.7.6, Figure 5.11).

In Figure 5.2b we observe variations of the initial G' plateau during the first 150 min. It should be noted that the data is represented on a logarithmic scale. The discrepancies are of around 20 Pa, which is only around 1 % of the final stiffness, and insignificant (*i.e.*, within two standard deviations).

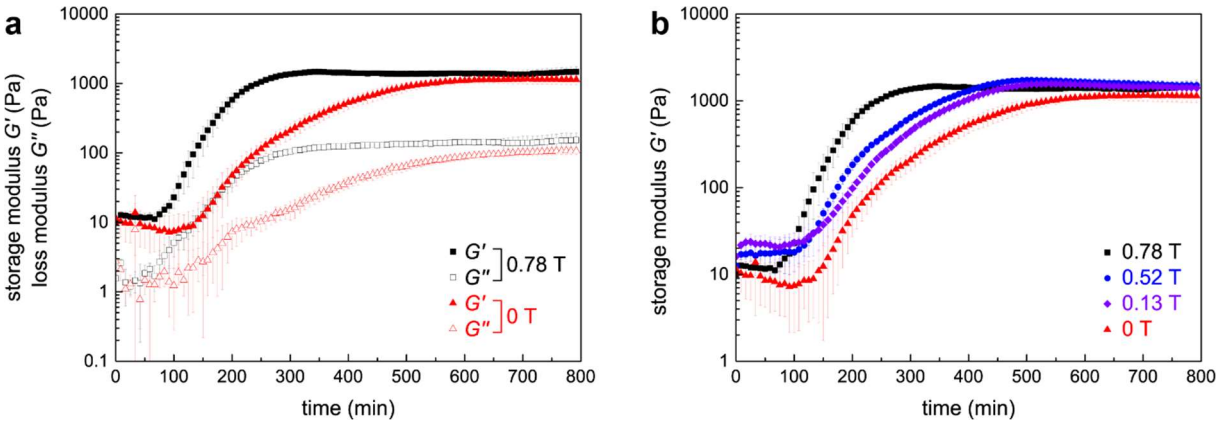

Figure 5.2 | Magnetoresponse of Dy-BINDI. (a) Kinetic rheological data of **Dy-BINDI** gels in the presence (black squares) and absence (red triangles) of a uniform 0.78 T magnetic field. (b) Time-dependent storage moduli G' of **Dy-BINDI** gels at 0.78 T (black squares), 0.52 T (blue circles), 0.13 T (violet diamonds), and 0 T (red triangles). Full symbols represent the storage modulus G', hollow symbols the loss modulus G''. Error bars represent the standard deviations over three measurements.

Table 5.1 lists the starting times of gelation t_s, the half times $t_{1/2}$ at which 50 % of the final stiffness is reached, and the full gelation times t_g of the gels at the different fields B. When these values t_x are compared to their counterparts in absence of a magnetic field ($t°_x$) to find the relative change ($t_x/t°_x$), the observed ratios are in the same range for $t_x = t_s, t_{1/2},$ and t_g. This means that the influence of the magnetic field is affecting the whole gelation process similarly, which is surprising as we expect a stronger magneto-response for larger objects—in this case fibers, which will grow with time.

Table 5.1 | Field-dependent gelation times. Starting times t_s, half times $t_{1/2}$, and full gelation times t_g, as well as their ratios with respect to the values in no field (B = 0 T, see $t°_x$ values). t_s, $t_{1/2}$ and t_g are read off manually and rounded to multiples of 10 minutes.

B (T)	t_s (min)	t_s / $t°_s$	$t_{1/2}$ (min)	$t_{1/2}$ / $t°_{1/2}$	t_g (min)	t_g / $t°_g$
0	140 (= $t°_s$)	1	410 (= $t°_{1/2}$)	1	650 (= $t°_g$)	1
0.13	120	0.86	360	0.88	530	0.82
0.52	110	0.79	330	0.80	500	0.77
0.78	90	0.64	210	0.51	340	0.52

Next, we studied the response of the system if the magnetic field is triggered after a certain time t_{tr} (Figure 5.3). In this respect, the measurement in 0.78 T will correspond to $t_{tr} = t_0$, and the measurement in no field will be $t_{tr} = t_\infty$ (Figure 5.3a). If the field is switched on after 150 min (t_{tr} = 150 min, black squares in Figure 5.3b), once the gelation starts, the gelation rate is immediately accelerated. Full gelation is reached after 410 min, around 60 % earlier as compared to $t_{tr} = t_\infty$. If we switch on the magnetic field after 300 minutes (t_{tr} = 300 min, black squares in Figure 5.3c), which refers to approximately half of the gelation time in no field ($t_{tr} = t_\infty$, red triangles), the gelation is completed after 470 min, 180 min (38 %) before the gelation completes in 0 T. If the field is turned on after t_{tr} = 600 min, when the gel is almost fully developed, no significant changes can be observed (see Figure 5.12 in the appendix).

For all three depicted measurements (t_{tr} = 0, 150, and 300 min), the gelation is accelerated by 86–92 % during the interval in which the magnetic field is turned on (grey shaded areas in Figure 5.3a-c). The corresponding values for gelation times t_g and their ratios with respect to $t_{tr} = t_\infty$ are listed in Table 5.2.

Table 5.2 | Trigger time dependent gelation times. Gelation times from the trigger time t_{tr} on (t_g–t_{tr}), and their ratios with respect to the values measured in no field ($t_{tr} = t_\infty$).

t_{tr} (min)	t_g (min)	$t_g - t_{tr}$ (min)	$(t_g - t_{tr})$ / $(t°_g - t_{tr})$
0	340	340	0.52
150	410	260	0.52
300	470	170	0.49
∞ (no field)	650 (=$t°_g$)	n/a	n/a

The corresponding shear strain- and angular frequency dependent measurements of the fully formed gels do not show any significant differences for the different trigger times (Figure 5.13 in the appendix).

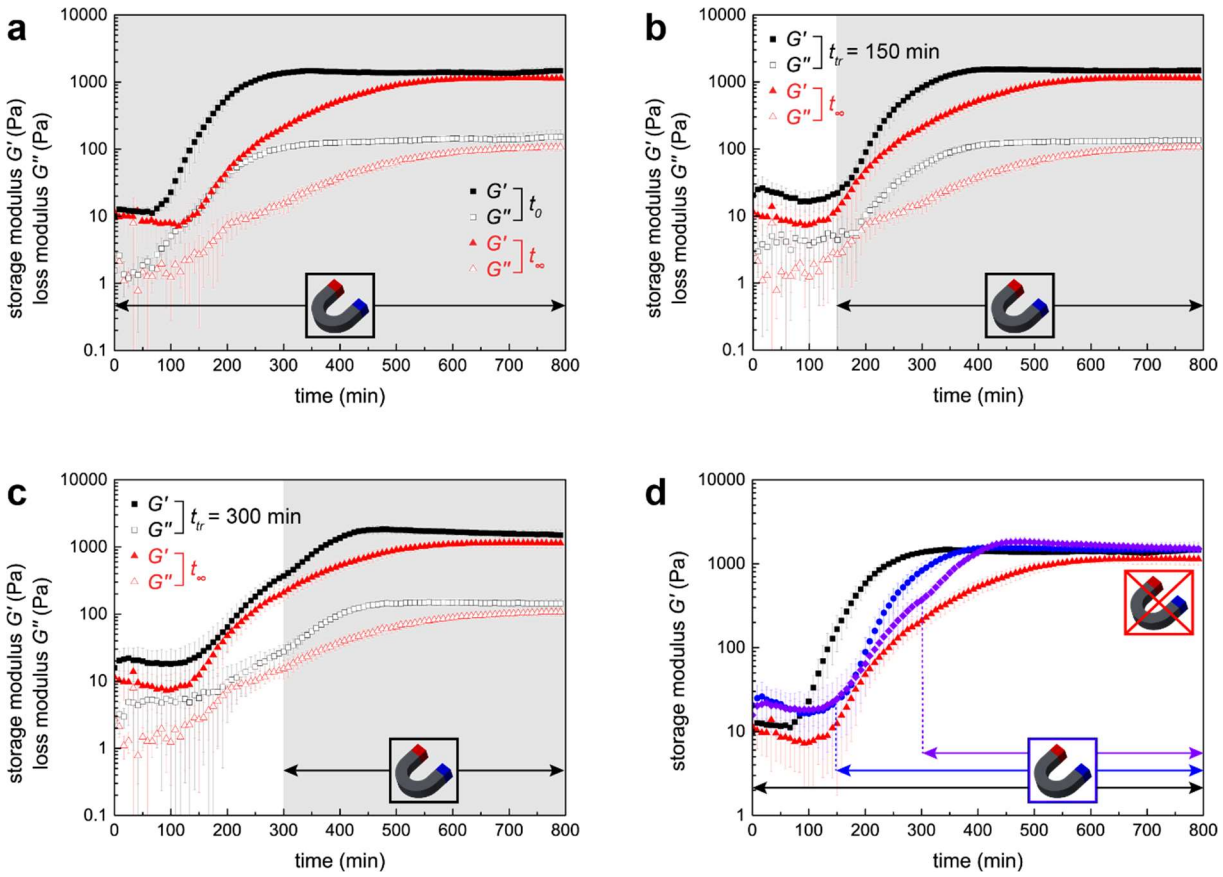

Figure 5.3 | Magnetic trigger profiles. Kinetic rheological data of **Dy-BINDI** gels (black squares), which were magnetically triggered by a 0.78 T magnetic field with different delays t_{tr}: (a) t_{tr} = 0 min, (b) t_{tr} = 150 min, and (c) t_{tr} = 300 min. (d) Time-dependent storage modulus G' of the different magnetic field profiles with t_{tr} = 0 min (black squares), t_{tr} = 150 min (blue circles), t_{tr} = 300 min (purple diamonds), and $t_{tr} = t_\infty$ (red triangles). Red triangles refer to gelation kinetics in no field. Full symbols represent the storage modulus G', hollow symbols the loss modulus G''. Error bars represent the standard deviations over three measurements. The trigger times t_{tr} are accentuated by the horseshoe illustration.

These experiments show that the kinetics of the gelation in a constant magnetic field can be fine-tuned by switching the field on at different times during gelation (Figure 5.3d). The trigger time is thus, along the field strength, a second parameter that allows for targeted magneto-response of the system.

Encouraged by these findings, we aimed to study the gel properties and magneto-response of **M-BINDI** gels incorporating other magnetic lanthanide ions with different electron density distributions. Therefore, **M-BINDI** gels were prepared with Gd^{3+} (isotropic) or Er^{3+} (prolate) in addition to the previously described Dy^{3+} (oblate). La^{3+} serves as a diamagnetic control ion. The gelation kinetics of the different gels were recorded in magnetic fields of 0 and 0.78 T (red triangles and black squares in Figure 5.4). Table 5.3 summarizes the respective half times $t_{1/2}$ at fields of 0 T and 0.78 T and their ratios, as well as the final mechanical stiffnesses of the different gels.

The kinetic measurements reveal that the final mechanical stiffnesses of the **M-BINDI** gels vary depending on the incorporated ion. The final G' is around 1.5 kPa for Dy^{3+} and Er^{3+}, and 1.8 kPa for Gd^{3+}. The stiffest gels are those made of **La-BINDI**, with G' values reaching 4.1 kPa (all values of G' for 0 T). **La-BINDI** is also the gel that forms the fastest, with a half time of 340 min, as compared to 390-410 min for Dy^{3+}, Er^{3+}, and Gd^{3+}. The pH evolution (green in Figure 5.4, see also Figure 5.16a in the appendix) is nearly identical for all four gels. Without

the addition of M^{3+} ions, **BINDI** does not gel in these conditions. It precipitates after around 120 min, when a pH of 4.6 is reached (Figure 5.10a and Figure 5.16b in the appendix). These observations illustrate that coordination is a decisive interaction in the assembly.

The corresponding shear strain- and angular frequency dependent measurements show no significant changes as compared to **Dy-BINDI** (Figure 5.14 in the appendix).

STEM images of drop-cast samples of the different **M-NDI** gels exhibit similar morphologies and fiber thicknesses (see section 5.7.8). This could imply that the changes of the bulk properties result from differences at the molecular level. It is known that the ionic radius decreases (1.2–1.0 Å), and the average coordination number transitions from 9 to 8 along the lanthanide series (with an increasing atomic number).[30] A larger ionic radius can facilitate, and thus accelerate coordination sterically. Moreover, a higher coordination number enables more branching of the network on a molecular level. La^{3+} being the first element in the series, it exhibits the largest ionic radius and average coordination number over this scope (CN ≈ 9), which will decrease in the order $_{57}$La > $_{64}$Gd > $_{66}$Dy > $_{68}$Er. The mechanical stiffnesses of the fully formed gels follow this trend.

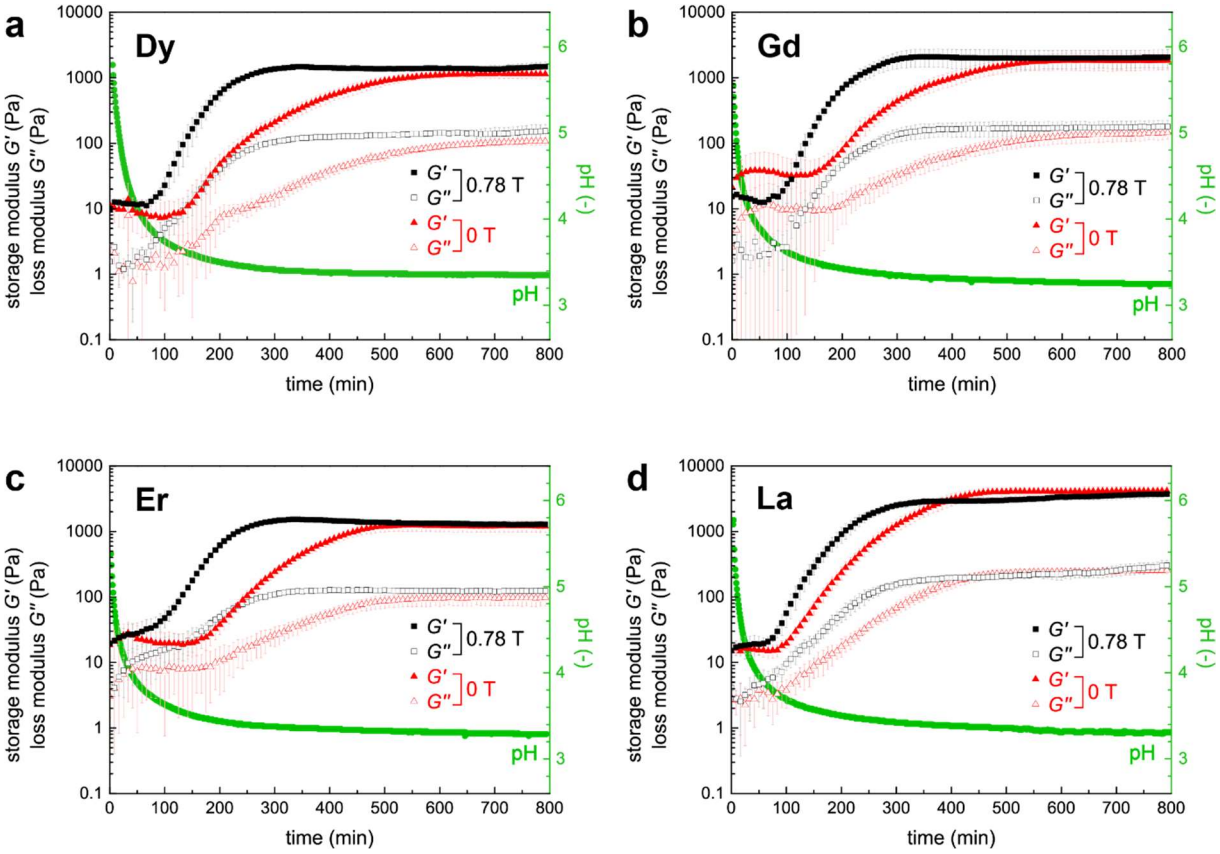

Figure 5.4 | Magnetoresponse of M-BINDI gels incorporating different ions. Time-dependent rheological data of **M-BINDI** gels in the presence (black squares) and absence (red triangles) of a 0.78 T field for (a) **M** = Dy, (b) **M** = Gd, (c) **M** = Er, and (d) **M** = La. Full squares and triangles represent the storage modulus *G′*, hollow squares and triangles the loss modulus *G″*. Error bars represent the standard deviations over three measurements. Green circles refer to the pH evolution, which were measured in separate experiments.

Regarding the magneto-response of the different gels, we find that the gelation times of all four systems can be reduced significantly by the application of the magnetic field. The acceleration is most pronounced for **Dy-BINDI** (95 %), followed by **Er-BINDI** (81 %), **Gd-BINDI** (70 %), and **La-BINDI** (48 %). At first glance, it is surprising that the gelation of the diamagnetic

La-BINDI is affected by the field. This hints at a diamagnetic contribution of the large delocalized π–system of assembled **BINDI** (see Chapter 1, section 1.2.3.2).

Table 5.3 | Ion-dependent half times. Half times of gelation $t_{1/2}$ at fields of 0 T and 0.78 T, as well as their ratios for different ions. Their magnetic moment μ is given in $\mu_B = 9.274 \cdot 10^{-24}$ Am².[23] Values for $t_{1/2}$ are read off manually and rounded to multiples of 10 min.

M	μ^{23} (μ_B)	mean G'_{max} (kPa) 0 T	$t_{1/2}$ (min) 0 T	$t_{1/2}$ (min) 0.78 T	$t_{1/2}^{0.78\ T} / t_{1/2}^{0\ T}$
La	0	4.1	340	230	0.68
Gd	7.9	1.8	390	230	0.59
Er	9.6	1.5	380	210	0.55
Dy	10.7	1.5	410	210	0.51

To rationalize why the gel formation is accelerated, we can draw a parallel to what has been observed in other aligning fields (electric fields or flow fields).[31] From a thermodynamic point of view, (partial) alignment of a supramolecular polymer favors further polymerization entropically. In other words, the entropy loss upon self-assembly is reduced, if the assembling units are field aligned. Consequently, the polymer is driven to elongate. Larger polymers will, in turn, align more. In this way, the co-dependency of alignment and chain growth provides positive feedback.

Quantitatively, the alignment would be considered in the magnetic Gibbs free energy ΔG_m of the system, which includes an isotropic term U_i, which is proportional to the magnetization and the magnetic flux density, and anisotropic term U_a (as discussed for the **Gd-BTA** network in Chapter 4, section 4.4). The latter depends on the geometry-dependent effective demagnetization factor and is minimal for an infinitely long axially magnetized structure.

As discussed in section 1.3.1.4, individual ions would not respond to a magnetic field in these conditions (0.78 T field, 298 K, in solution or hydrogel). Therefore, the magnetic ions are assumed to act as a group, which are joint and immobilized in magnetic fibers through the chelation and assembly of the organic ligand.

Our experiments support these hypotheses, as they show a stronger field-induced acceleration for stronger fields and for ions with a larger magnetic moment μ. The trend appears to correlate the magneto-response with the magnetic moments of the ions, regardless of their (an)isotropic electron density distribution.

In the case of **La-BINDI**, we assume acceleration of the gelation process due to diamagnetic alignment. Through supramolecular assembly of the aromatic **BINDI**, its π-system is extended, and its diamagnetic anisotropy amplified (see Chapter 1, section 1.2.3.2). The axis of largest negative susceptibility, which is along π-π stacking direction, is expected to align perpendicular to the field. Considering the smaller susceptibility of the diamagnetic gelator as compared to the paramagnetic ions, a less pronounced magneto-response is conclusive.

So far, we could not confirm fiber alignment by STEM imaging, polarized optical microscopy, or linear dichroism. Possibly, the field-response translates to a slight deformation, rather than well-pronounced alignment. Scattering experiments (SANS/SAXS) or AFM microscopy[32–34] could give a more detailed insight about the size and morphology of the respective fiber structures.

To confirm the diamagnetic origin of the accelerated gelation process in **La-BINDI**, we aimed to study the gelation of the same **BINDI** gel without adding lanthanides. Unfortunately, no gel is formed in these conditions (see Figure 5.10a in the appendix). For this reason, the gelation conditions were adapted by increasing the GdL concentration, as will be discussed in the following section.

5.4 Magneto-response of an organic supramolecular hydrogel

With the aim to make a lanthanide-free **BINDI** gel, different conditions were tested. An increase of the GdL concentration from 6 to 10 equivalents leads to gelation at a **BINDI** concentration of 5 $mg \cdot mL^{-1}$ (Figure 5.5b). According to the pH evolution of **BINDI** at 10 eq. of GdL, the plateau of the pK_a of around 4.5 is reached significantly earlier, namely after 80 min, as compared to 110 minutes for 6 eq. GdL (see Figure 5.16b in the appendix). In the latter case, the protonation of carboxylates seems to proceed too slowly to form a gel network, and the gelator precipitates. At a larger proportion of GdL, the protonation is accelerated, allowing for gel formation.

Surprisingly, the addition of 0.5 eq. $DyCl_3$ inhibited gelation in these conditions (see Figure **5.10**b in the appendix). The coordination of the gelator to a Dy^{3+} ion might inhibit hydrogen bonding between free and protonated carboxylates. We assume that hydrogen bonding leads to the formation of one-dimensional chains along the long axis of **BINDI**. In parallel arrangement, the chain-like assemblies allow for π-π stacking of the **BINDI** cores. A coordinated ion, on the other hand, has a three-dimensional coordination sphere (CN 8-9). It is so to say a branching point on a molecular level. This branching can limit parallel alignment of the NDI moieties and thus weaken π-π interactions of the NDI moieties (see Figure 5.18 in the appendix for an illustrative representation). Moreover, the relatively large size of the lanthanide with respect to the NDI plane may inhibit further π-π stacking.

These observations suggest that the molecular order in the metal-free **BINDI** gels differs significantly from the **M-BINDI** gels that have been discussed previously. We expect a stronger impact of π-π stacking, which can favor the assembly into larger structures. Indeed, we find experimental evidence for significant differences in the kinetics of gelation (see Figure 5.15 in the appendix), the fiber morphology, and their macroscopic appearance.

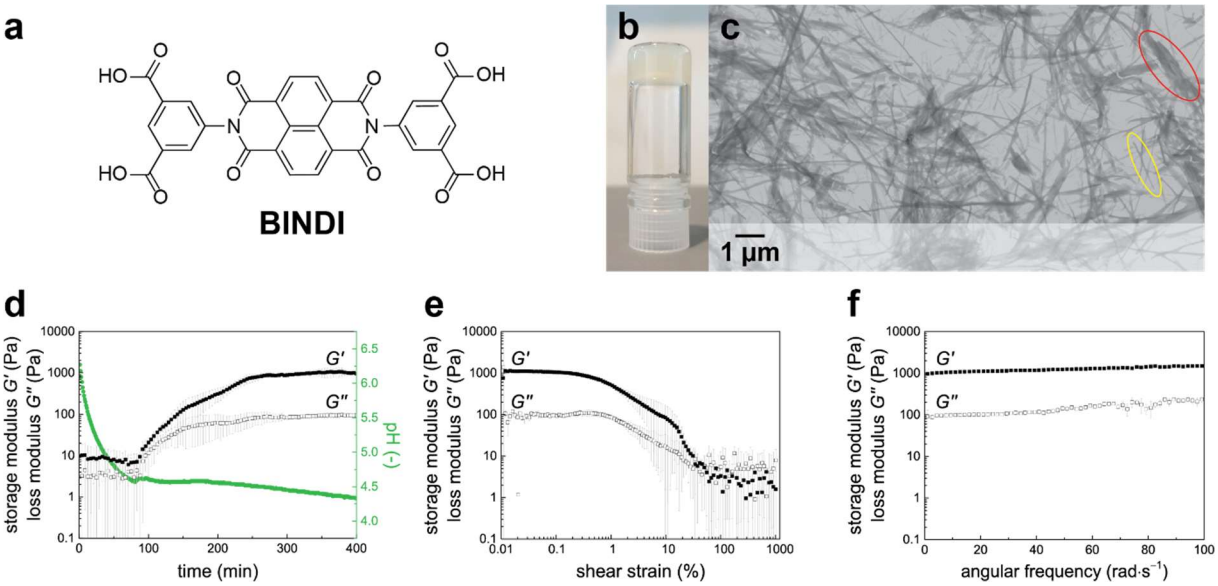

Figure 5.5 | Supramolecular BINDI hydrogel at 10 eq. GdL. (a) Molecular structure of the gelator **BINDI**. (b) Digital photograph of the inverted vial test. (c) STEM image of the fibrous nanostructure, drop-cast. (d) Kinetic rheological data of the gel at 25 °C (black) and pH measurement over time (green). (e) Strain sweep, revealing critical shear strains of 0.32 and 14.5 %. (f) Frequency sweep, showing frequency-independence of the gel. Full squares represent the storage modulus *G′*, hollow squares the loss modulus *G″*. Error bars represent the standard deviation over three measurements.

By STEM imaging (Figure 5.5c) we observe that the hydrogel is composed of around 50 nm thick fibrils (53 nm ± 23 nm, one example is highlighted in yellow in Figure 5.5c), but also fibrils that aggregate into fibers and bundles as thick as hundreds of nanometers (one example is highlighted in red in Figure 5.5c). The single fibers are larger than in the **Dy-BINDI** gel (Figure 5.1c). Macroscopically, the metal-free **BINDI** gel is more opaque than the previously shown gels of **M-BINDI**.

According to kinetic rheological measurements (black squares in Figure 5.5d), both the storage- and loss moduli *G′* and *G″* start to increase after 80 min, and reach a plateau after 270 min. The gelation appears to be a two-step process, as we observe two subsequent sigmoidal-like increases of the storage- and loss moduli *G′* and *G″* after around 80 and 160 min, respectively. Likewise, the shear strain sweep shows that the gel structure is destroyed in a bimodal process, with a first critical shear strain of 0.32 %, and a second of around 14.5 %, respectively (Figure **5.5**e). During the first step of gelation, the difference between the storage- and loss moduli *G′* and *G″* is less than an order of magnitude. Thus, the system is not considered a gel, but a viscous solution with pronounced solid-like and liquid-like properties. During the second step, the difference between *G′* and *G″* increases significantly, which indicates the formation of a gel. With time, the gel becomes stiffer until it reaches a plateau at around 1 kPa. Frequency-independence of the gel at a shear strain of 0.1 % confirms that measurements are performed within the linear viscoelastic region of the material (Figure 5.5f).

The pH evolution over time (green circles in Figure 5.5d) reveals that a plateau at pH 4.5 is reached after around 80 minutes. This value coincides well with the second pK_a if isophthalic acid, indicating that one of two electronically coupled carboxylates is protonated. After about 180 min, the pH decreases slowly by 0.2 within 200 min. The shift of the pH plateau by 1 from 4.5 in lanthanide-free **BINDI** gel to 3.5 in the **M-BINDI** gel (Figure 5.1d) is likely a result of coordination in **M-BINDI**. Upon chelation, the weakly basic carboxylates ($pK_b \approx 10$) are captured by the Lewis-acidic lanthanides, replacing either water ($pK_b \approx 16$) or chloride

($pK_b \approx 20$) ligands. Moreover, the complexation will alter the electronic state of the isophthalic acid moiety, in a similar way as would protonation.

Regarding the bimodal gelation process, we assume that in the first step of the assembly fibers are formed, which entangle and trap a part of the solvent. The network formation is then enhanced by a second process, resulting in a self-sustaining gel. As *G′* and *G″* start increasing when the first of two carboxylates per isophthalic acid moiety is protonated (pH 4.5), we assume that complementary hydrogen bonding of two acid groups is the main driving force of this first assembly. The development of the gel network up to a full inclusion of the solvent will then be completed by π-π stacking of the NDI cores (2nd process). With this reasoning, we find an analogy to the BTA network formation in solution, which was discussed in Chapter 4.

Just like for the **M-BINDI** gels, the magneto-response of the material was tested by magnetorheology. Strikingly, complete gelation was impeded upon exposure to a magnetic field of 0.78 T during the gelation phase (Figure 5.6a, black squares). What was first believed to be a failed experiment, could be reproduced reliably. While initially both storage- and loss moduli *G′* and *G″* increase fast in a bimodal curve, the gel seems to collapse at a stiffness of around 700 Pa after 160 minutes. In analogy to the **M-BINDI** gels, the gelation starts 60 % earlier as compared to gelation in no field (Figure 5.6a, red triangles), being reduced from around 80 to 50 min. Intrigued by this observation, the gelation was monitored at different field strengths. Neither at 0.52 T nor at 0.67 T, the rheological measurements could be reproduced reliably (blue and purple symbols in Figure 5.6b). Nevertheless, we can observe general trends, such as an acceleration of the gelation process in 0.67 T, (Figure 5.6b, light blue diamonds). In one of the three measurements, the gel collapses after around 240 min. Two out of three measurements in 0.52 T (Figure 5.6b, light green circles), show unchanged gelation kinetics as compared to 0 T. In the third curve, we find an accelerated gelation process reaching the final stiffness after around 180 min. At these field strengths, the system seems to be weakened by the magnetic field, allowing the smallest deviations of the measuring conditions (possibly mechanical vibrations or temperature) to influence the gelation process. Only at 0.78 T (black squares), the **BINDI** sample breaks down after 150 minutes and does not form a hydrogel.

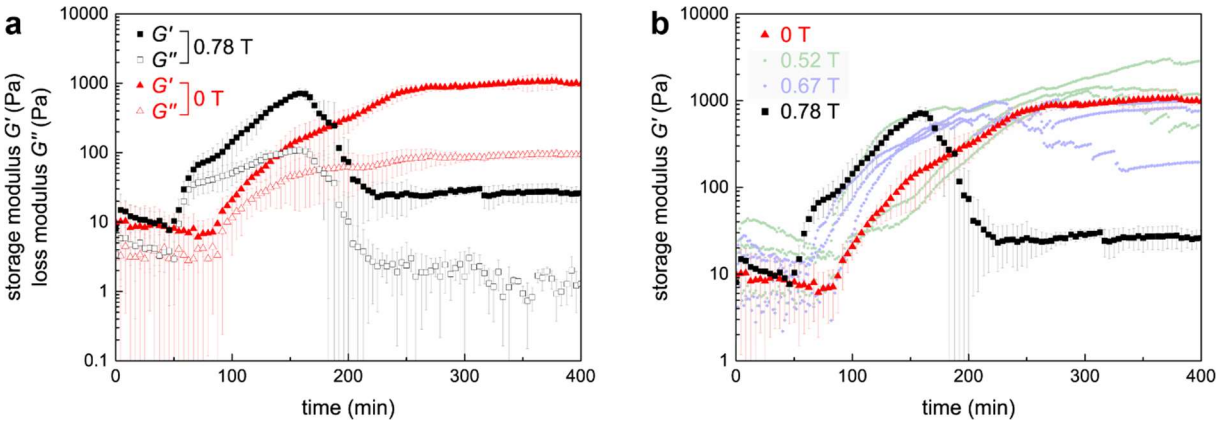

Figure 5.6 | Magnetoresponse of BINDI gels using 10 eq. GdL. (a) Kinetic rheological measurements of **BINDI** gels in the presence (black squares) and absence (red triangles) of a 0.78 T magnetic field. (b) Time dependent storage modulus *G′* of **Dy-BINDI** gels at 0.78 T (black squares), 0.67 T (light blue circles), 0.52 T (light green diamonds), and 0 T (red triangles). Full symbols represent the storage modulus *G′*, hollow symbols the loss modulus *G″*. Error bars represent the standard deviations over three measurements. Data in 0.67 T and 0.52 T are poorly reproducible and therefore represented as single runs.

While diamagnetic alignment in gels has been reported in strong fields (section 5.1), such a substantial impact of a weak magnetic field of 0.78 T was not expected. When comparing the kinetics at different fields, a trend towards faster gelation from 0.67 T becomes apparent. Therefore, we assume that the large, diamagnetically anisotropic π-system is—at least partly—aligned. This entropically favors further assembly and leads to an accelerated gelation process before the collapse.

Based on our rheological measurements alone, we cannot find a conclusive explanation for the observed collapse. It is possible that the fibers reach a critical size, at which their magnetic anisotropy will be large enough to make them align perpendicular to the field. In this case, the collapse would mark the transformation from a three-dimensional, entangled network structure of a self-sustaining material to unidirectionally aligned fibers. On the other hand, we might observe a local densification of the gel, similar to what we observe for **Gd-BTA** in Chapter 2. At a critical density of the system, we expect solvent expulsion, and thus a collapse of the gel.

Scattering experiments (SANS/SAXS) or real-time imaging of the gelation process in a uniform magnetic field could provide evidence to support our hypotheses. However, an experimental setup of a highly performing microscope with a magnetic field source seems tricky to implement. We were not able to observe any alignment by STEM imaging on gels which were formed in the magnetic field. Polarized optical microscopy did not show any birefringence. Due to the small and fine nature of the fibers and the low fluorescence of the NDI core, confocal imaging did not yield any revealing results. The use of fluorescent dyes like Thioflavin T or Congo Red may be helpful to overcome these difficulties.

5.5 Conclusions

We have presented two different supramolecular hydrogels based on the organic gelator **BINDI**. Through coordination of the carboxylate moieties of the gelator, paramagnetic lanthanide ions can be incorporated into the hydrogel. Upon exposure to uniform magnetic fields of up to 0.78 T, the gelation times of these gels can be reduced by up to 95 %, reaching a nearly identical final mechanical stiffness and strength. Even a weak field of 0.13 T, which is easily accessible in any research lab, can accelerate the gelation by around 14 %. The kinetic profiles can be tailored more precisely if the magnetic field is switched on at different times during gelation.

The acceleration of the gelation kinetics by up to 95 % most likely originates from partial alignment of assembled structures with the magnetic fields of 0.13 to 0.78 T. Alignment will promote faster gelation, as chain growth is entropically favored. In turn, longer chains will align more, which further promotes assembly. In this way, the co-dependency of alignment and chain growth provides positive feedback. By incorporating lanthanide ions in a supramolecular assembly, the ions do not act individually, but as a group with a collective magnetic moment. This amplification allows for magnetic manipulation in mild conditions (fields of 0.8 T, 298 K, in solution or hydrogel).

If diamagnetic La^{3+} is incorporated, the acceleration of the gelation kinetics is less pronounced, but still significant (up to 48 %). In this case, we assume diamagnetic alignment of the conjugated π-system perpendicular to the field.

In line with this reasoning, we have shown that the gelation kinetics of a metal-free **BINDI** hydrogel, which is formed at a higher concentration of the pH trigger GdL, can be accelerated similarly. Supramolecular hydrogels are formed in fields of up to 0.67 T. At 0.78 T, the gelation is accelerated at first, before the system gets disrupted and collapses.

In both systems the gel- and fiber morphologies as well as the mechanisms of gel formation remain to be elucidated in more detail. The indications given from the bulk properties are intriguing, and further microscopic or scattering experiments may help to understand the process on a nano- and microscopic level. Even though the observed phenomena cannot yet be explained satisfactorily, the control over the system that can be achieved by uniform magnetic fields is striking—especially when considering the weak fields and the low magnetic susceptibilities of the components. Notably, the gelation of a diamagnetic, organic supramolecular hydrogel can be entirely impeded.

5.6 Author contributions

Michaela Schicho performed the synthesis and rheological measurements. Ana María Fuentes Caparrós assisted in the conception, setup, and evaluation of the rheology experiments. Daniel Iglesias Asperilla performed STEM imaging. Thomas Hermans supervised the research.

5.7 Appendix

5.7.1 Materials and methods

All reagents were obtained from commercial sources (TCI, Sigma Aldrich, VWR) and used without further purification.

Nuclear magnetic resonance (NMR). Spectra were recorded in on a Bruker 400 MHz Ultrashield™ NMR spectrometer at 25 °C. Chemical shifts (δ) are given in ppm relative to tetramethylsilane (TMS).

Gel preparation.
lanthanide containing gel (**M-BINDI** gel): GdL (9.1 mg) was dissolved in a mixture of 0.85 mL demineralized water and 99 µL of 0.17 M aqueous $MCl_3 \cdot 6\ H_2O$. To this solution, 51 µL of a 0.17 M **BINDI** solution in 1 M NaOH was added and the mixture was homogenized.
lanthanide-free gel (**BINDI** gel): GdL (15.2 mg) was dissolved in 0.95 µL demineralized water and 51 µL of a 0.17 M **BINDI** solution in 1 M NaOH was added.

Infrared Spectroscopy (IR). FTIR spectra were collected in ATR mode on a Spectrum II spectrometer (Perkin-Elmer).

Rheology. Measurements were recorded on an MCR 302 Modular Compact Rheometer (Anton Paar) equipped with a PS-MRD magnetorheological cell, an PP/MRD/TI parallel plate, and a MAGNET-PHYSIK FH 54 Teslameter (Dr. Steingroever GmbH). All measurements were recorded using a PP20/MRD/TI parallel plate at a gap position of 1.000 mm and at 25 °C. Unless further specified, all measurements were recorded at a shear strain of 0.1 % and an angular frequency of 10 $rad \cdot s^{-1}$. For frequency sweeps, the angular frequency was increased linearly from 1 to 100 $rad \cdot s^{-1}$. For strain sweeps, the strain was increased logarithmically from 0.01 to 1000 %. For every measurement, 400 µL of a freshly prepared sample were pipetted on the rheometer.

Potentiometry. The pH evaluation of the samples was recorded using a SevenCompact pH meter S220 pH equipped with an LE422 electrode (both Mettler-Toledo).

Scanning Transmission Electron Microscopy (STEM). A small portion of hydrogel was drop-cast on a copper grid (300 mesh, carbon film). After drying at open air, the samples were imaged under vacuum in a Quanta FEG 250 (FEI) system operating at 30 kV. Fiber diameters were quantified from the obtained images using ImageJ (NIH) and are expressed as mean and standard deviation over 100 fibers.

5.7.2 Synthesis

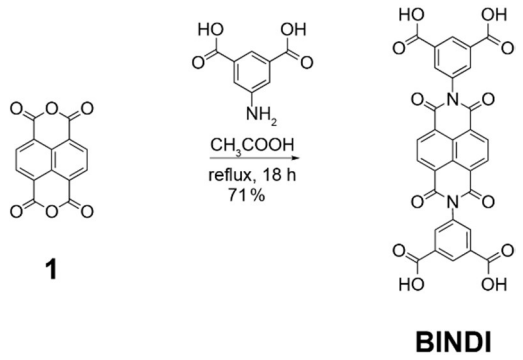

Figure 5.7 | Reaction scheme for the synthesis of BINDI.[35]

BINDI was prepared following a literature procedure.[35] 1,4,5,8-Naphthalene-tetracarboxyl dianhydride **1** (3.35 g, 12.5 mmol) was suspended in acetic acid (100 mL) and stirred at 25 °C for 30 mins. To the suspension, 5-aminoisophthalic acid (4.98 g, 27.5 mmol, 2.2 eq.) was added and the reaction mixture was refluxed for 18 h. The mixture was allowed to cool down to room temperature, and demineralized water (100 mL) was added. The precipitate was filtered off using a porosity 4 sintered filter and washed with acetic acid and ethanol. The crude product was dried in vacuo at 50 °C and recrystallized from DMF. The resulting compound was washed thoroughly with diethyl ether to yield the desired product as a yellow powder (5.26 g, 8.84 mmol, 71 %).

^{1}H-NMR (400 MHz, DMSO-d^{6}) δ(ppm): 13.48 (br s, 4 H, carboxylic acid), 8.74 (s, 4 H, NDI), 8.59 (t, 2 H, *p*-phenyl), 8.34 (d, 4 H, *o*-phenyl).

5.7.3 GdL hydrolysis

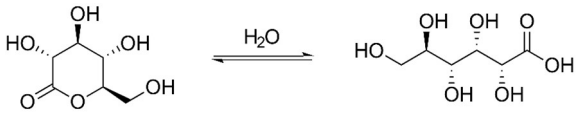

Figure 5.8 | Controlled pH decrease. Reaction scheme of GdL hydrolysis to gluconic acid.[21]

5.7.4 Infrared Spectroscopy

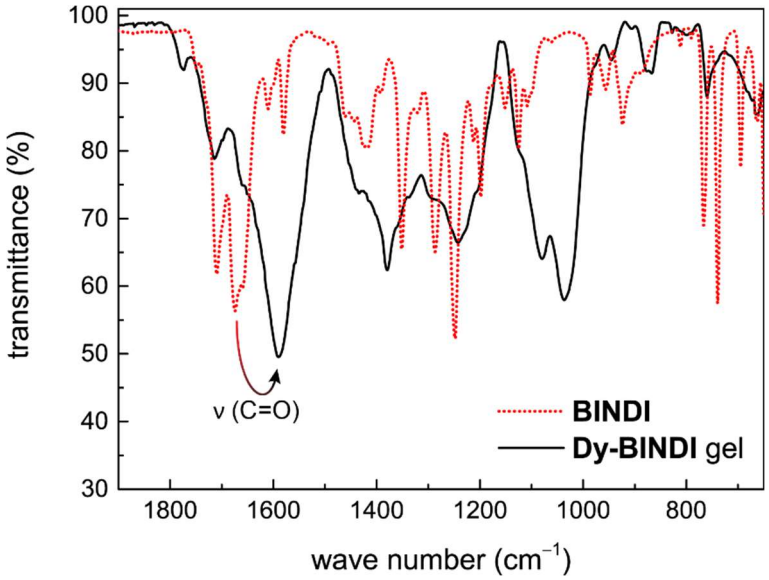

Figure 5.9 | Infrared spectroscopy. ATR-IR spectra of **BINDI** (red dotted line) and a **Dy-BINDI** gel (black full line).

5.7.5 Inverted vial test

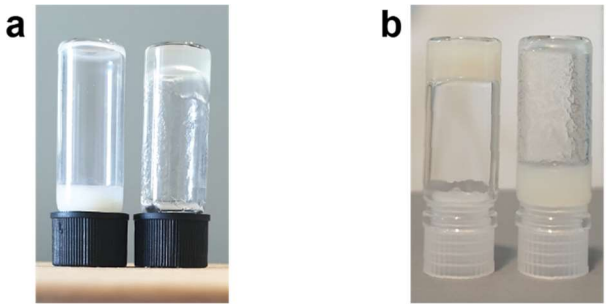

Figure 5.10 | Vial inversion. Digital photographs of inverted vials. (a) **Dy-BINDI**, 6 eq. GdL with 0 eq. (left, no gel) and 2 eq. (right, gel) $DyCl_3$. (b) **BINDI**, 10 eq. GdL, with 0 (left, gel) and 0.5 eq. (right, no gel) $DyCl_3$.

5.7.6 Rheology

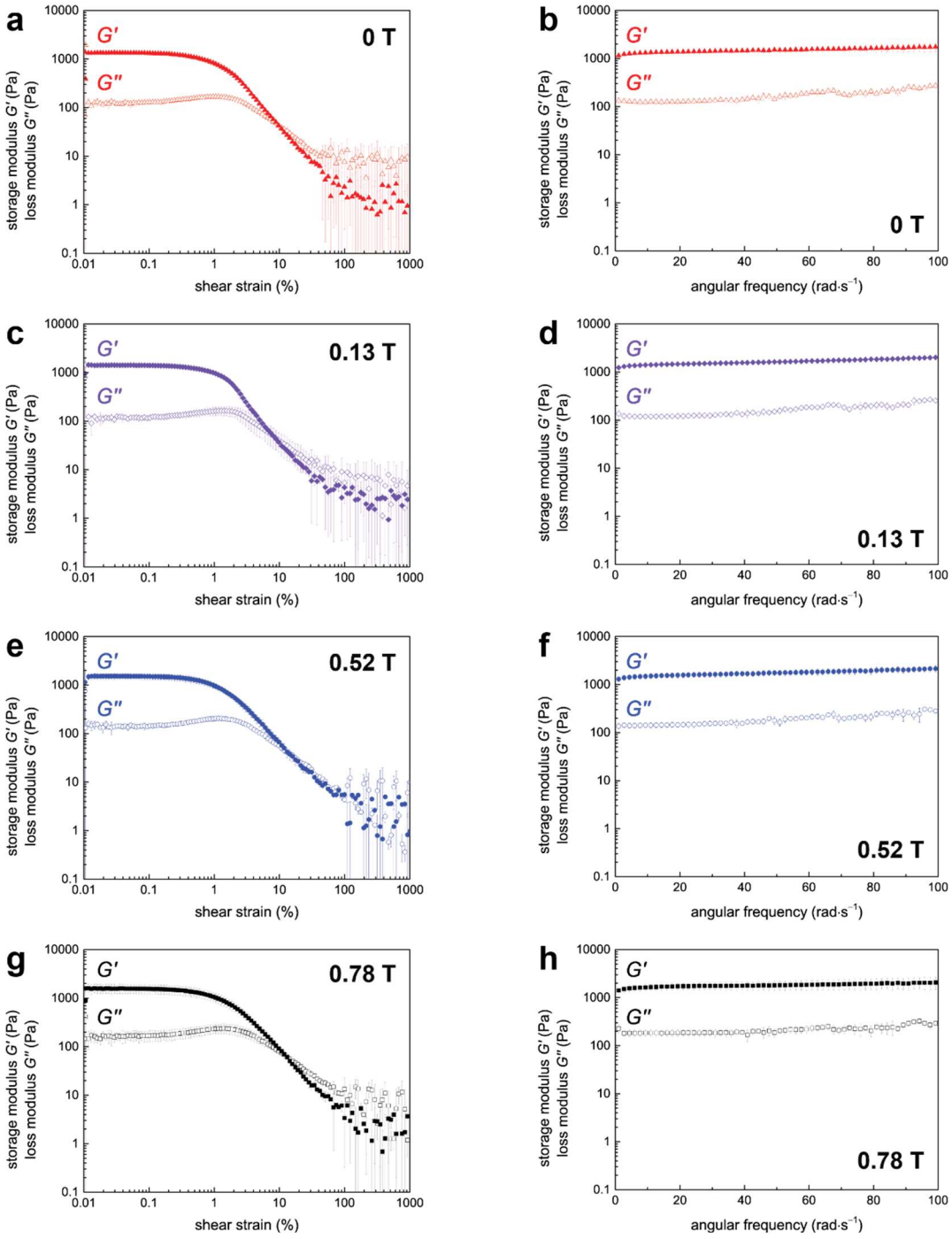

Figure 5.11 | Shear strain and angular frequency dependent rheological data at different fields. Strain sweeps (left) and frequency sweeps (right) of **Dy-BINDI** gels at 6 eq. GdL. (a,b) 0 T. (c,d) 0.13 T, (e,f) 0.52 T. (g,h) 0.78 T. Full squares represent the storage modulus G', hollow squares the loss modulus G''. Error bars represent standard deviations over three measurements.

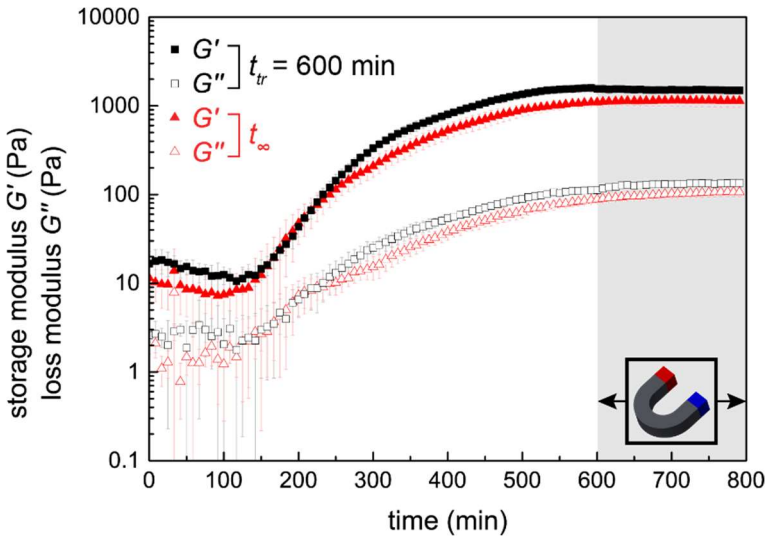

Figure 5.12 | Magnetic trigger after 600 minutes. Kinetic rheological data of **Dy-BINDI** gels at 6 eq. GdL, which were magnetically triggered by a 0.78 T magnetic field 600 min after gelation started (black squares) and without magnetic field (red triangles). Full symbols represent the storage modulus G', hollow symbols the loss modulus G''. Error bars represent the standard deviations over three measurements. The trigger time t_{tr} = 600 min are accentuated by the horseshoe illustration.

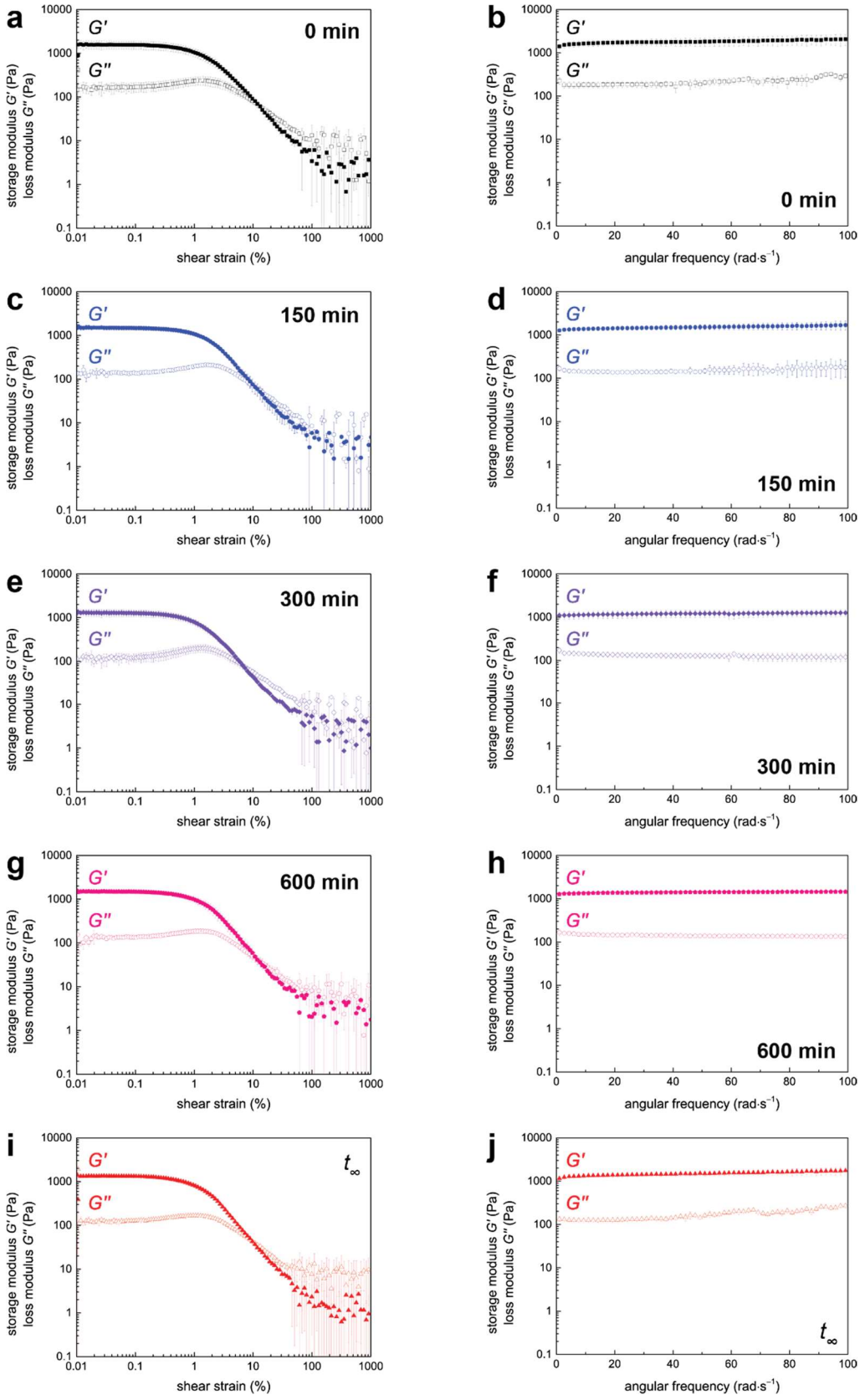

Figure 5.13 | Shear strain and angular frequency dependent rheological data at different trigger times. Strain sweeps (left) and frequency sweeps (right) of **Dy-BINDI** gels at 6 eq. GdL, in which the magnetic field was switched on at different times t_{tr}. (a,b) t_{tr} = 0 min. (c,d) t_{tr} = 150 min. (e,f) t_{tr} = 300 min. (g,h) t_{tr} = 600 min. (i,j) $t_{tr} = t_{\infty}$ (i.e. no trigger). Full symbols represent the storage modulus G', hollow symbols the loss modulus G''. Error bars represent standard deviations over three measurements.

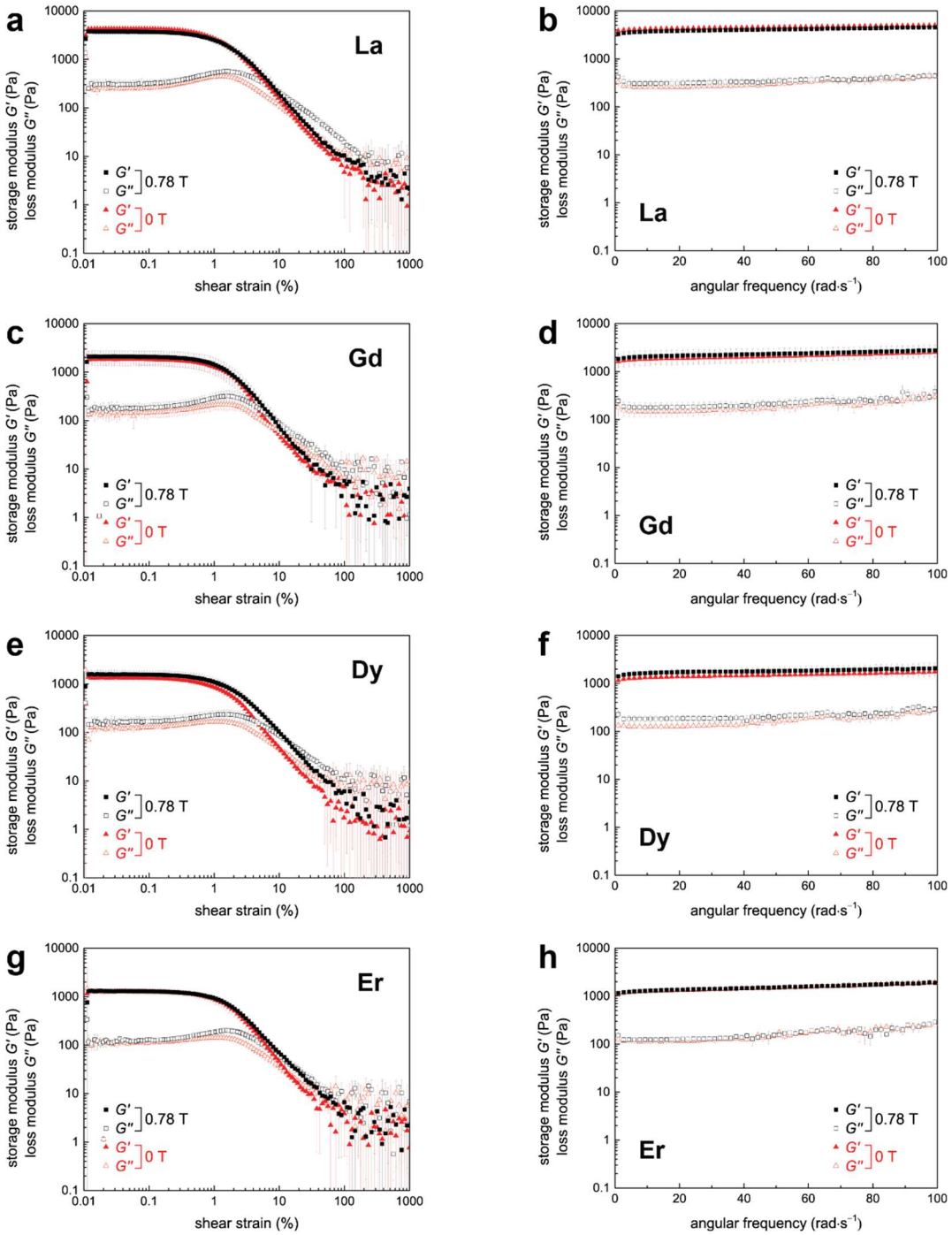

Figure 5.14 | Shear strain and angular frequency dependent rheological data for different ions. Strain sweeps (left) and frequency sweeps (right) of **M-BINDI** gels (6 eq. GdL), at 0 T (red triangles) and 0.78 T (black squares). (a,b) **M** = La. (c,d) **M** = Gd. (e,f) **M** = Dy. (g,h) **M** = Er. Full symbols represent the storage modulus G', hollow symbols the loss modulus G''. Error bars represent standard deviations over three measurements.

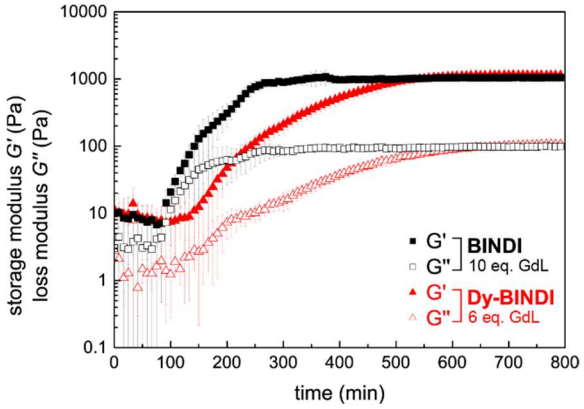

Figure 5.15 | Gelation kinetics of different BINDI-based gels. Kinetic rheological data of the lanthanide-free **BINDI** gel (10 eq. GdL, black squares), and **Dy-BINDI** (6 eq. GdL, red triangles). Full symbols represent the storage modulus *G′*, hollow symbols the loss modulus *G″*. Error bars represent standard deviations over three measurements.

5.7.7 pH measurements

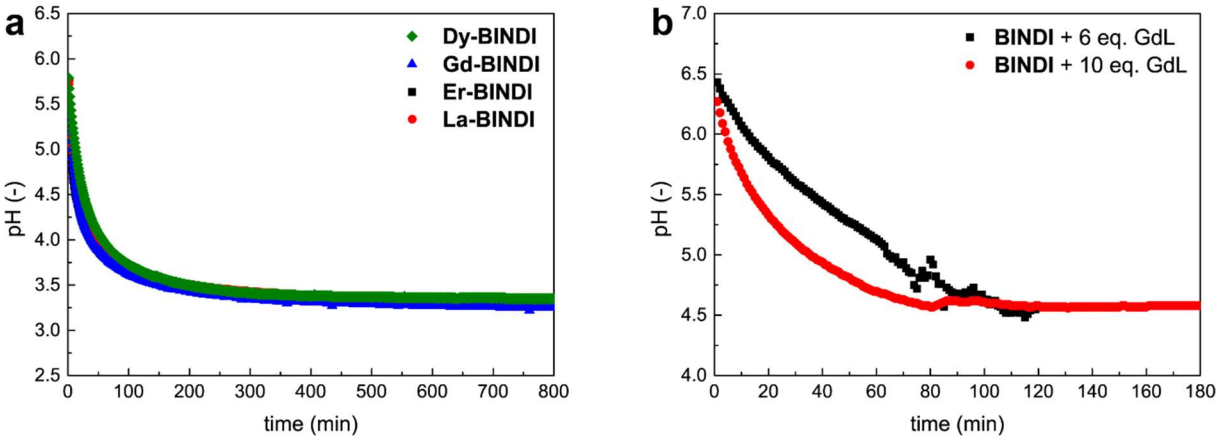

Figure 5.16 | pH evolution. (a) Time-dependent pH for the four **M-BINDI** gels (**M**=Dy, Gd, Er, La). (b) Time dependent pH of lanthanide-free **BINDI** gels at 6 eq. (black squares) and 10 eq. (red circles) GdL.

5.7.8 STEM imaging

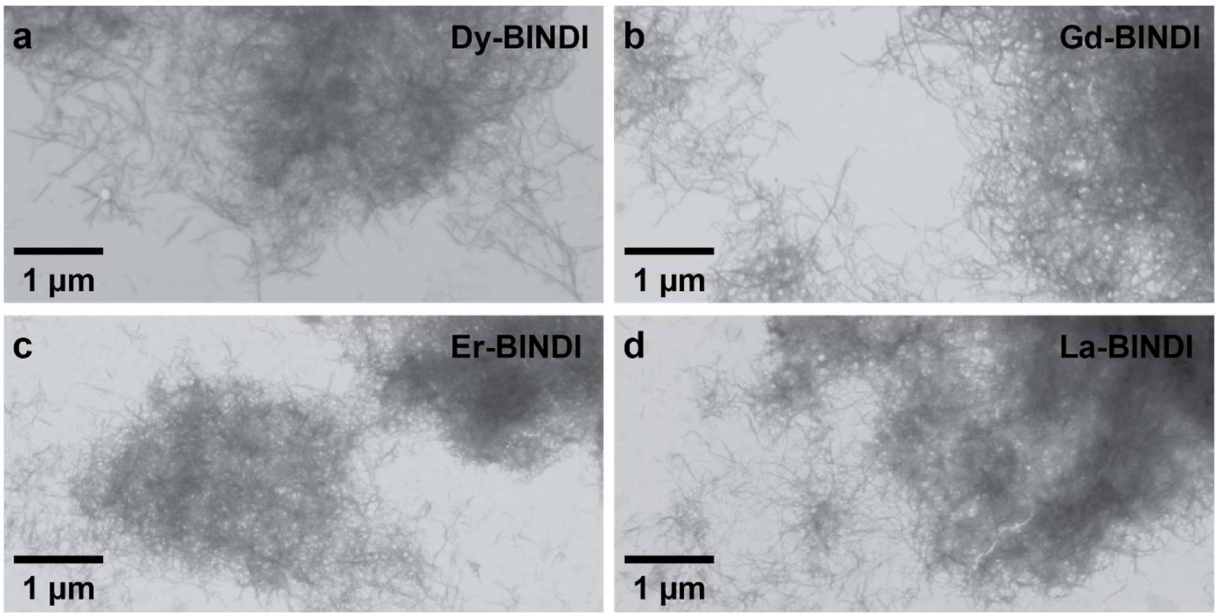

Figure 5.17 | STEM imaging. Fibrous nanostructure of **M-BINDI** gels, drop-cast. (a) **Dy-BINDI**. (b) **Gd-BINDI**. (c) **Er-BINDI**. (d) **La-BINDI**.

Table 5.4 | Fiber thickness. Average fiber thicknesses and standard deviations over 100 fibers.

gel	fiber thickness (nm)
Dy-BINDI	12 ± 5
Gd-BINDI	9 ± 3
Er-BINDI	12 ± 5
La-BINDI	11 ± 5

5.7.9 Proposed assembly processes

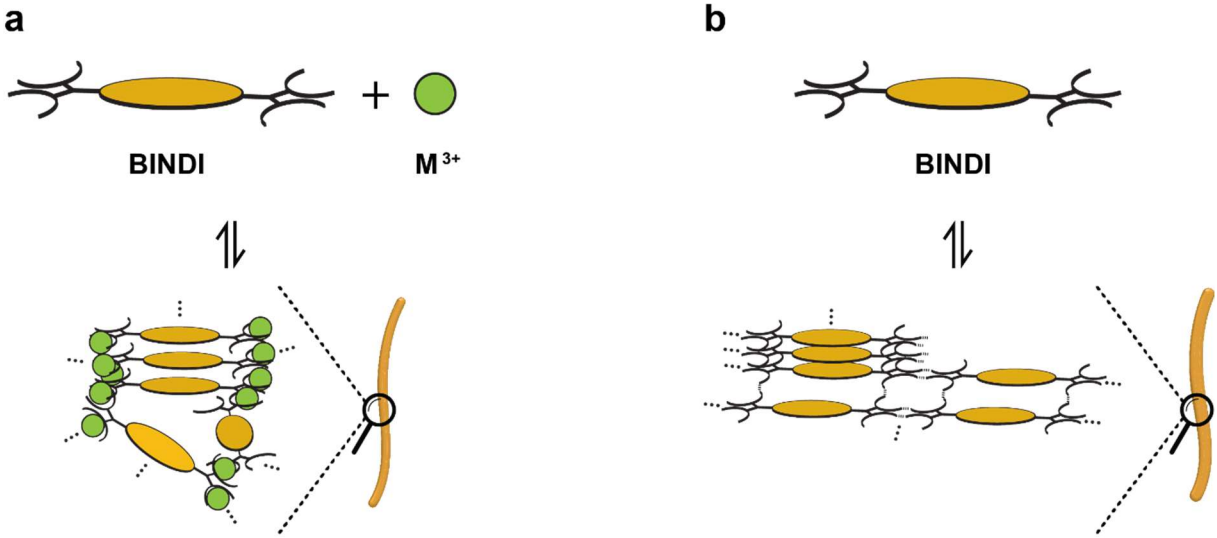

Figure 5.18 | Molecular assembly to nanofibers. Schematic illustrations of possible assembly processes of (a) **M-BINDI** hydrogels and (b) lanthanide-free **BINDI** hydrogels. **M-BINDI** gels are presumably more branched on a molecular level and dominated by coordination and π-π stacking. Lanthanide-free **BINDI** gels exhibit more directional hydrogen bonding between carboxylates and carboxylic acids, complementing the π-π interactions.

5.8 References

1. Matson, J. B. & Stupp, S. I. Self-Assembling Peptide Scaffolds for Regenerative Medicine. *Chem. Commun.* **48**, 26–33 (2012).
2. Stupp, S. I., Zha, R. H., Palmer, L. C., Cui, H. & Bitton, R. Self-Assembly of Biomolecular Soft Matter. *Faraday Discuss.* **166**, 9 (2013).
3. Webber, M. J., Berns, E. J. & Stupp, S. I. Supramolecular Nanofibers of Peptide Amphiphiles for Medicine. *Isr. J. Chem.* **53**, 530–554 (2013).
4. Wall, B. D., Diegelmann, S. R., Zhang, S., Dawidczyk, T. J., Wilson, W. L., Katz, H. E., Mao, H.-Q. & Tovar, J. D. Aligned Macroscopic Domains of Optoelectronic Nanostructures Prepared via Shear-Flow Assembly of Peptide Hydrogels. *Adv. Mater.* **23**, 5009–5014 (2011).
5. Besar, K., Ardoña, H. A. M., Tovar, J. D. & Katz, H. E. Demonstration of Hole Transport and Voltage Equilibration in Self-Assembled π-Conjugated Peptide Nanostructures Using Field-Effect Transistor Architectures. *ACS Nano* **9**, 12401–12409 (2015).
6. Sanders, A. M., Magnanelli, T. J., Bragg, A. E. & Tovar, J. D. Photoinduced Electron Transfer within Supramolecular Donor–Acceptor Peptide Nanostructures under Aqueous Conditions. *J. Am. Chem. Soc.* **138**, 3362–3370 (2016).
7. Leung, F. K., Kajitani, T., Stuart, M. C. A., Fukushima, T. & Feringa, B. L. Dual-Controlled Macroscopic Motions in a Supramolecular Hierarchical Assembly of Motor Amphiphiles. *Angew. Chem. Int. Ed.* **58**, 10985–10989 (2019).
8. Cao, B., Zhu, Y., Wang, L. & Mao, C. Controlled Alignment of Filamentous Supramolecular Assemblies of Biomolecules into Centimeter-Scale Highly Ordered Patterns by Using Nature-Inspired Magnetic Guidance. *Angew. Chem. Int. Ed.* **52**, 11750–11754 (2013).
9. Hu, L., Zhang, R. & Chen, Q. Synthesis and Assembly of Nanomaterials under Magnetic Fields. *Nanoscale* **6**, 14064–14105 (2014).
10. Wallace, M., Cardoso, A. Z., Frith, W. J., Iggo, J. A. & Adams, D. J. Magnetically Aligned Supramolecular Hydrogels. *Chem. Eur. J.* **20**, 16484–16487 (2014).
11. Shklyarevskiy, I. O., Jonkheijm, P., Christianen, P. C. M., Schenning, A. P. H. J., Del Guerzo, A., Desvergne, J.-P., Meijer, E. W. & Maan, J. C. Magnetic Alignment of Self-Assembled Anthracene Organogel Fibers. *Langmuir* **21**, 2108–2112 (2005).
12. Wu, Y., Hirai, Y., Tsunobuchi, Y., Tokoro, H., Eimura, H., Yoshio, M., Ohkoshi, S. & Kato, T. Supramolecular Approach to the Formation of Magneto-Active Physical Gels. *Chem. Sci.* **3**, 3007 (2012).
13. Veloso, S. R. S., Silva, J. F. G., Hilliou, L., Moura, C., Coutinho, P. J. G., Martins, J. A., Testa-Anta, M., Salgueiriño, V., Correa-Duarte, M. A., Ferreira, P. M. T. & Castanheira, E. M. S. Impact of Citrate and Lipid-Functionalized Magnetic Nanoparticles in Dehydropeptide Supramolecular Magnetogels: Properties, Design and Drug Release. *Nanomaterials* **11**, 16 (2020).
14. Löwik, D. W. P. M., Shklyarevskiy, I. O., Ruizendaal, L., Christianen, P. C. M., Maan, J. C. & van Hest, J. C. M. A Highly Ordered Material from Magnetically Aligned Peptide Amphiphile Nanofiber Assemblies. *Adv. Mater.* **19**, 1191–1195 (2007).
15. da Silva, F. F., de Menezes, F. L., da Luz, L. L. & Alves, S. Supramolecular Luminescent Hydrogels Based on β-Amino Acid and Lanthanide Ions Obtained by Self-Assembled Hydrothermal Reactions. *New J. Chem.* **38**, 893–896 (2014).
16. Kim, C., Kim, K. Y., Lee, J. H., Ahn, J., Sakurai, K., Lee, S. S. & Jung, J. H. Chiral Supramolecular Gels with Lanthanide Ions: Correlation between Luminescence and Helical Pitch. *ACS Appl. Mater. Interfaces* **9**, 3799–3807 (2017).
17. Ma, Q., Zhang, M., Xu, X., Meng, K., Yao, C., Zhao, Y., Sun, J., Du, Y. & Yang, D. Multiresponsive Supramolecular Luminescent Hydrogels Based on a Nucleoside/Lanthanide Complex. *ACS Appl. Mater. Interfaces* **11**, 47404–47412 (2019).
18. Chakraborty, P., Das, S., Mondal, S. & Nandi, A. K. Conducting Hydrogel of a Naphthalenetetracarboxylic Dianhydride Derivative and Polyaniline: Different Electronic Properties in Gel and Xerogel States. *CrystEngComm* **17**, 8093–8104 (2015).
19. Rardin, R. L., Tolman, W. B. & Lippard, S. J. Monodentate Carboxylate Complexes and the Carboxylate Shift: Implications for Polymetalloprotein Structure and Function. *New J. Chem.* **15**, 417–430 (1991).
20. Zhang, Y., Bhadbhade, M., Scales, N., Karatchevtseva, I., Price, J. R., Lu, K. & Lumpkin, G. R. Dysprosium Complexes with Mono-/Di-Carboxylate Ligands—From Simple Dimers to 2D and 3D Frameworks. *J. Solid State Chem.* **219**, 1–8 (2014).
21. Pocker, Y. & Green, Edmond. Hydrolysis of D-Glucono-delta-Lactone. I. General Acid-Base Catalysis, Solvent Deuterium Isotope Effects, and Transition State Characterization. *J. Am. Chem. Soc.* **95**, 113–119 (1973).
22. Jiang, S.-D. & Qin, S.-X. Prediction of the Quantized Axis of Rare-Earth Ions: The Electrostatic Model with Displaced Point Charges. *Inorg. Chem. Front.* **2**, 613–619 (2015).

23. Coey, J. M. D. *Magnetism and Magnetic Materials*. (Cambridge University Press, 2010).
24. Orhanović, Z., Pokrić, B., Füredi, H. & Branica, M. Precipitation and Hydrolysis of Metallic Ions. III. Studies on the Solubility of Yttrium and Some Rare Earth Hydroxides. *Croat. Chem. Acta* **38**, 269–273 (1966).
25. Bang, D.-Y., Lee, I.-K. & Lee, B.-M. Toxicological Characterization of Phthalic Acid. *Toxicol. Res.* **27**, 191–203 (2011).
26. Kalra, A., Tugcu, N., Cramer, S. M. & Garde, S. Salting-In and Salting-Out of Hydrophobic Solutes in Aqueous Salt Solutions. *J. Phys. Chem. B* **105**, 6380–6386 (2001).
27. Sander Langereis, de Lussanet, Q. G., van Genderen, M. H. P., Backes, W. H. & Meijer, E. W. Multivalent Contrast Agents Based on Gadolinium−Diethylenetriaminepentaacetic Acid-Terminated Poly(propylene imine) Dendrimers for Magnetic Resonance Imaging. *Macromolecules* **37**, 3084–3091 (2004).
28. Liu, S., Pietryka, J., Ellars, C. E. & Edwards, D. S. Comparison of Yttrium and Indium Complexes of DOTA-BA and DOTA-MBA: Models for ^{90} Y- and ^{111} In-Labeled DOTA−Biomolecule Conjugates. *Bioconjug. Chem.* **13**, 902–913 (2002).
29. Orbach, R., Mironi-Harpaz, I., Adler-Abramovich, L., Mossou, E., Mitchell, E. P., Forsyth, V. T., Gazit, E. & Seliktar, D. The Rheological and Structural Properties of Fmoc-Peptide-Based Hydrogels: The Effect of Aromatic Molecular Architecture on Self-Assembly and Physical Characteristics. *Langmuir* **28**, 2015–2022 (2012).
30. King, R. B., Crabtree, R. H., Lukehart, C. M., Atwood, D. A. & Scott, R. A. *Encyclopedia of Inorganic Chemistry*. (John Wiley & Sons, Ltd, 2006).
31. Ciferri, A. *Supramolecular Polymers*. (Taylor & Francis, 2005).
32. Helen, W., de Leonardis, P., Ulijn, R. V., Gough, J. & Tirelli, N. Mechanosensitive Peptide Gelation: Mode of Agitation Controls Mechanical Properties and Nano-Scale Morphology. *Soft Matter* **7**, 1732–1740 (2011).
33. Angelerou, M. G. F. Surface-Directed Modulation of Supramolecular Gel Properties. *Chem. Commun.* **52**, 4298–4300 (2016).
34. Hixon, K. R., Dunn, A. J., Flores, R., Minden-Birkenmaier, B. A., Kalaf, E. A. G., Shornick, L. P. & Sell, S. A. Using Electrospun Scaffolds to Promote Macrophage Phenotypic Modulation and Support Wound Healing. *Electrospinning* **1**, (2017).
35. Garai, B., Mallick, A. & Banerjee, R. Photochromic Metal–Organic Frameworks for Inkless and Erasable Printing. *Chem. Sci.* **7**, 2195–2200 (2016).

THIS PAGE IS INTENTIONALLY LEFT BLANK

Chapter 6. Overall conclusions and outlook

Since the development of supramolecular polymers in the 1980s, many aspects of their assembly processes and the resulting materials have been thoroughly studied and are well understood. There remains, however, room for further progress and extension of the field, in order to have applications of supramolecular materials to the same extent as seen currently for covalent polymers.[1]

This thesis is focused on the magnetic control of supramolecular polymers. In comparison with more conventional stimuli, the magnetic stimulus is intriguing, because it is non-invasive, non-destructive, easily tunable in intensity and direction over space and time, and tolerates a wide range of materials, conditions, and atmospheres. Nevertheless, it is poorly explored in the domain of supramolecular polymers. This is mainly because the magnetic energies and forces decrease with the size of the magnetic object and tend to be outcompeted by Brownian motion on a (supra)molecular level. The state of the art of this unconventional and multidisciplinary field of research is laid out in **Chapter 1**.

Alongside certain other recent reports (Chapter 1.3), we have shown that a targeted molecular design opens possibilities for magnetic manipulation in easily accessible fields (≤ 2 T.) The presented **Chapters 2–5** each focus on separate aspects with respect to the nature of the supramolecular system and the role of magnetism in the assembly process (Figure 6.1)

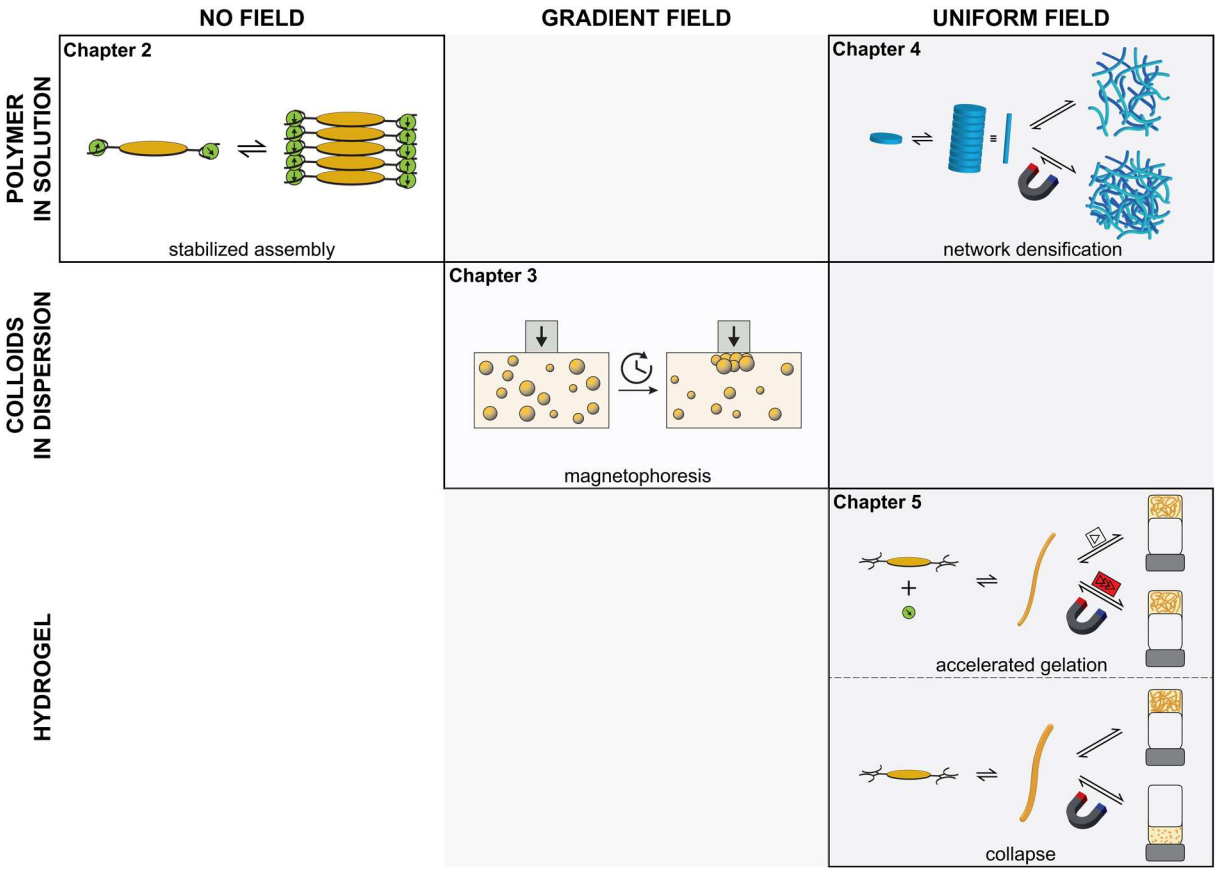

Figure 6.1 | Overview over the reported phenomena. Simplistic illustrations of the observations described in **Chapters 2–5**, categorized by the respective type of supramolecular system (lines) and magnetic field (columns).

No external field. Most fundamentally, **Chapter 2** has shown that the incorporation of paramagnetic lanthanide ions in a naphthalene diimide (NDI)-based assembler influences the enthalpy/entropy balance of its supramolecular polymerization. At an equal Gibbs free energy, the enthalpy is decreased by up to 60 % for a Dy^{3+}containing monomer with respect to an Y^{3+} containing analog. The trend we find over a scope of eight lanthanides clearly follows the magnetic moments of the ions, rather than possible variations due to the lanthanide contraction. Calorimetric studies such as ITC[2,3] or DSC[4] may be useful to confirm these unexpected results with an independent method. Calorimetry would be especially interesting in this case because it measures heat evolution directly.

It seems that the order provided by supramolecular assembly limits the degrees of freedom of the ions sufficiently to instill an additional, magnetically induced ordering, which is measurable for solutions at room temperature and above through spectroscopic studies. Magnetometry of the bulk material reveals antiferromagnetic coupling between the paramagnetic ions, with Curie-Weiss temperatures θ of –10 to –30 K. If we assume simple antiferromagnetism[5], these values correspond to the negative Néel temperatures $-T_N$ (T_N = 10 to 30 K). We would expect the antiferromagnetic ordering to vanish above T_N, which is more than 200 K below room temperature (298 K). Seeing an approximately linear trend of the enthalpy of assembly with the magnetic moment of the chelated ions at 298 K is thus particularly surprising.

If we regard the solid samples as maximally assembled polymer, we may use the SQUID measurements as a proxy for supramolecular packing. However, we need to consider that we have no information about the supramolecular order in the bulk material. The latter is obtained from lyophilization of aqueous solutions. In this process, the solutions are spontaneously frozen with liquid nitrogen (77 K), immobilizing the current state of the solution, which may be more or less assembled. Therefore, we assume that the molecular packing of the monomers may be less ordered in bulk than in solubilized assemblies. Moreover, SQUID magnetometry records the average magnetization over the sample and does not separate the monomeric and polymeric state. If our hypothesis is accurate, the antiferromagnetic coupling of the lanthanide ions should be well-pronounced in the assembly, but negligible or zero for monomers. To clarify these uncertainties, one needs to either analyze a purely polymeric sample, or ensure that the molecular packing of the sample is known. SQUID measurements of the material in its native solution state or the maximally ordered crystal state could clarify these uncertainties.

Crystalline **M-NDI** would additionally allow for X-Ray structure resolution, which would certainly help to grasp the assembly. So far, we were not able to obtain sufficiently large monocrystals. A larger batch size may facilitate crystallization.

Our finding is surprising and could help to elucidate other reported phenomena that were observed in lanthanide containing supramolecular assemblies.[6,7] It could provide a new approach towards a programmable and reversible interconversion of a paramagnetic system, which gets magnetized by an external field (monomeric state), to a field-inert antiferromagnet (assembled state).

Gradient field. In **Chapter 3**, the response of colloidal, lanthanide containing naphthalene diimide (NDI) derivatives in a binary water/THF system have been investigated. We find that the monomers assemble to µm-sized spherical colloids upon the increase of the THF proportion in the solvent mixture. The gradient field of a 0.5 cm commercial cube magnet is sufficient to

induce directed movement of the colloids towards the high-field region of the gradient field (magnetophoresis). At the surface of the magnet, they form an around 100 µm thick organic layer, which can be removed easily upon addition of water. By means of supramolecular polymerization, single molecules are aggregated to structures that are large enough to experience directed motion from small field gradients ($\leq 500\ T \cdot m^{-1}$).

The separation of magnetic particles from their solvent could open new pathways towards the recycling of rare earths, which remains a major economic and ecological challenge in today's era of technological development.[8] Our **M-NDI** system seems to qualify for the separation of magnetic lanthanides from a mixed solution of the latter and smaller ions (such as Na^+, K^+, or Mg^{2+}). Hypothetically, the large, multivalent lanthanides can be chelated selectively[9], assembled to colloids by adding a bad solvent, and removed from the mixture through magnetophoresis. If the accumulation of compound is collected and treated with acid for decomplexation, the ions and the ligand may be recovered after physical separation (by size exclusion or adsorption chromatography, for instance). For this approach to work in the separation of similarly sized ions, one would need to verify that **M-NDI**s self-sort into colloids of only a specific lanthanide (*i.e.*, not for example **Y-NDI** that co-assembles with **Dy-NDI**, which would impede separation).

Uniform field. Thirdly, and lastly, we have studied the effect of a uniform magnetic field of up to 2 T on two lanthanide-containing systems: (i) a benzenetricarboxamide (BTA)-based polymer network in solution (**Chapter 4**), and (ii) an NDI-based hydrogel (**Chapter 5**). For the supramolecular polymer network, we find evidence for a spontaneous change in the network topology from a rod-like structure to randomly branched clusters upon the application of a 2 T field. Moreover, the network density increases steadily by up to 35 % within 10–12 h due to minor alignment of the rods. Both the change in the network topology and the densification are reversible processes, and the system relaxes back to the initial state within one day.

The supramolecular gelation, on the other hand, represents an irreversible process. Upon the application of a 0.8 T field, the kinetics of gelation of a Dy^{3+}-containing hydrogel are significantly accelerated, resulting in a decrease of the half-time by 50 %. In an analogous diamagnetic hydrogel, the extended π-system of the assembled gelator gives rise to a diamagnetic response to the field. The gelation times are reduced less pronouncedly, but still significantly, by around 30 %.

In both the rod network (**Chapter 4**) and the hydrogel (**Chapter 5**), we expect slight alignment of rods or fibers, respectively. The alignment, may it be of para- or diamagnetic origin, favors supramolecular assembly entropically, and more assembled structures will align to a larger extent. By this mutual dependence, positive feedback is provided (Figure 6.2).[10]

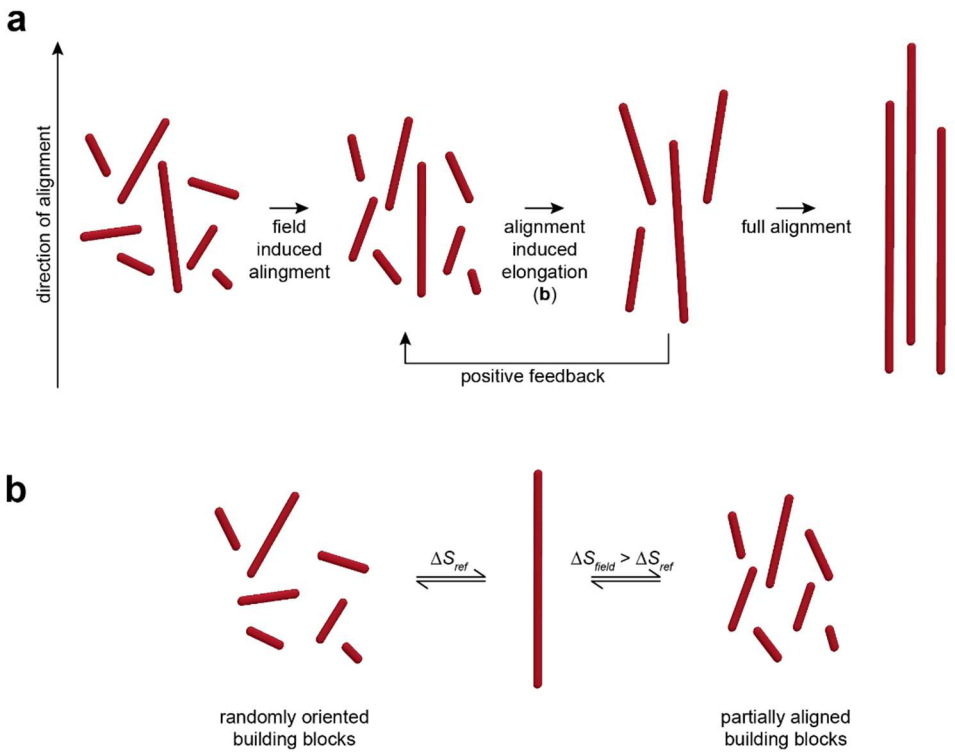

Figure 6.2 | Mutual dependence of alignment and chain growth. (a) Schematic illustration of self-assembled rods and their response to an aligning field.[10,11] (b) Schematic illustration to visualize the influence of (partial) alignment on the entropy of supramolecular assembly.

So far, we have not been able to prove alignment by microscopy or birefringence experiments. The assumed anisotropy may be detected indirectly by ^{98}Y-NMR (½ nuclear spin, 100% abundance) for a **Y-BINDI** gel, similar to previous work by Adams and coworkers.[12] Perhaps SQUID measurements could confirm alignment, if we find magnetic anisotropy in a gel incorporating and isotropic lanthanide (Gd^{3+}).

Although we have a theoretical explanation to describe the accelerated gelation qualitatively, the magnitude and precision of the response are remarkable and unexpected. If we consider the high charge of magnetic ions (up to 4 ions per 590 Da ligand in **M-BINDI** vs. 3 ions per 1.3 kDa ligand in **M-BTA**), the larger fibers (around 10 nm vs 3 nm) in the system, it is plausible that the gel responds stronger to the field than the BTA network. If we look at a single fiber of **Dy-BINDI** (10 nm diameter and 500 nm length, which is roughly what we observe in STEM imaging) the magnetic energy exceeds the thermal energy by a factor 10^7 ($\beta = E_{mag}/E_{therm} \approx 10^7$, rough estimation). Such a fiber is thus expected to react to the field. However, it is surprising that we observe an almost constant acceleration throughout the entire gelation process, starting from single ions. We assume that the latter may not be evenly distributed throughout the sample. Coordination seems to happen spontaneously, as we see precipitation when ligand and ions are first mixed. Homogenization is reached over a longer time scale, presumably following the pH decrease, which improves solubility and reduces electrostatic repulsion through charge compensation. The initial inhomogeneity of the sample may cause magneto-response of highly lanthanide-charged assemblies from the very beginning, whereas fibers with lower lanthanide content will react later, once they have reached a large enough fiber size. As the distribution is initially phase-separated (which was referred to as “inhomogeneity” before) but isotropic, we observe a macroscopically uniform gel.

In the lanthanide-free gel, on the other hand, we observe magneto-response of a purely diamagnetic system. For a significant response, stronger fields are required as compared to the paramagnetic gels. At 0.78 T, we observe an acceleration of the gelation process, which is in line with the observations in the BTA network (**Chapter 4**) and the paramagnetic gels. Yet, the collapse of the system is unique. At this point, we assume that the break-down is either caused by a rearrangement of the fibers from randomly oriented to aligned, or the expulsion of solvent due to a local densification of the fibers in the network. Further experiments, ideally *in-situ* imaging, are indispensable to identify the mechanism on a molecular or nanoscopic scale.

Aligned hydrogels find application in medical applications such as drug delivery[13] and regenerative medicine[14], or (opto-)electronics[15–17].[18] If our assumptions are correct, our system provides control over both the directionality and the kinetics of gelation using a single trigger. Given the access to highly developed magnetic setups used for MRI technology, even an *in-vivo* gelation of a biocompatible, aligned hydrogel could be envisioned on the long term.

All in all, this thesis presents a variety of different scenarios, in which magnetism can be exploited as a stimulus to manipulate supramolecular polymerization. The studies cover different types of magnetic fields (uniform, gradient, 0–2 T), monomer species (diamagnetic and paramagnetic), and supramolecular structures (solution polymers, colloids, hydrogels). Our approach to multiply the magnetic properties of single molecules or ions through their assembly to larger structures allows for magnetic control in experimentally simple setups. In the context of a poorly explored field, our work gives a general overview of the possibilities a magnetic stimulus can offer to control supramolecular systems.

Over the last years, it has been shown that supramolecular polymers qualify as dynamic functional materials for applications in sustainable processing and recycling, electronics, medicine and cosmetics.[1] To embed these achievements in society, it will be necessary to further complete our understanding of these systems, and to then convert experimental systems into large-scale and easy-to-handle processes. In this thesis, we have shed light on the use of magnetic fields to this end and found a number of counterintuitive effects. With further study, magnets can aid in the structuring of future supramolecular (bio)materials to achieve more complex functionalities.

References

1. Aida, T. & Meijer, E. W. Supramolecular Polymers – We've Come Full Circle. *Isr. J. Chem.* **60**, 33–47 (2020).
2. Syamala, P. P. N., Soberats, B., Görl, D., Gekle, S. & Würthner, F. Thermodynamic Insights into the Entropically Driven Self-Assembly of Amphiphilic Dyes in Water. *Chem. Sci.* **10**, 9358–9366 (2019).
3. Arnaud, A. & Bouteiller, L. Isothermal Titration Calorimetry of Supramolecular Polymers. *Langmuir* **20**, 6858–6863 (2004).
4. Bellot, M. & Bouteiller, L. Thermodynamic Description of Bis-urea Self-Assembly: Competition between Two Supramolecular Polymers. *Langmuir* **24**, 14176–14182 (2008).
5. Valenta, J., Honda, F., Vališka, M., Opletal, P., Kaštil, J., Míšek, M., Diviš, M., Sandratskii, L., Prchal, J. & Sechovský, V. Antiferromagnetism and Phase Transitions in Noncentrosymmetric UIrSi3. *Phys. Rev. B* **97**, 144423 (2018).
6. Sander Langereis, de Lussanet, Q. G., van Genderen, M. H. P., Backes, W. H. & Meijer, E. W. Multivalent Contrast Agents Based on Gadolinium−Diethylenetriaminepentaacetic Acid-Terminated Poly(propylene imine) Dendrimers for Magnetic Resonance Imaging. *Macromolecules* **37**, 3084–3091 (2004).
7. Polarz, S., Bährle, C., Landsmann, S. & Klaiber, A. Panoscopic Structures by Hierarchical Cascade Self-Assembly of Inorganic Surfactants with Magnetic Heads Containing Dysprosium Ions. *Angew. Chem. Int. Ed.* **52**, 13665–13670 (2013).
8. Binnemans, K. & Jones, P. T. Rare Earths and the Balance Problem. *J. Sustain. Metall.* **1**, 29–38 (2015).
9. Anderegg, G., Arnaud-Neu, F., Delgado, R., Felcman, J. & Popov, K. Critical Evaluation of Stability Constants of Metal Complexes of Complexones for Biomedical and Environmental Applications. *Pure Appl. Chem.* **77**, 1445–1495 (2005).
10. Ciferri, A. *Supramolecular Polymers*. (Taylor & Francis, 2005).
11. Turner, M. S. & Cates, M. E. Flow-Induced Phase Transitions in Rod-like Micelles. *J. Phys.: Condens.Matter* **4**, 3719–3741 (1992).
12. Draper, E. R., Wallace, M., Honecker, D. & Adams, D. J. Aligning Self-Assembled Perylene Bisimides in a Magnetic Field. *Chem. Commun.* **54**, 10977–10980 (2018).
13. Nguyen, L. H., Gao, M., Lin, J., Wu, W., Wang, J. & Chew, S. Y. Three-Dimensional Aligned Nanofibers-Hydrogel Scaffold for Controlled Non-Viral Drug/Gene Delivery to Direct Axon Regeneration in Spinal Cord Injury Treatment. *Sci. Rep.* **7**, 42212 (2017).
14. Dumont, C. M., Carlson, M. A., Munsell, M. K., Ciciriello, A. J., Strnadova, K., Park, J., Cummings, B. J., Anderson, A. J. & Shea, L. D. Aligned Hydrogel Tubes Guide Regeneration Following Spinal Cord Injury. *Acta Biomater.* **86**, 312–322 (2019).
15. Wall, B. D., Diegelmann, S. R., Zhang, S., Dawidczyk, T. J., Wilson, W. L., Katz, H. E., Mao, H.-Q. & Tovar, J. D. Supramolecular Materials: Aligned Macroscopic Domains of Optoelectronic Nanostructures Prepared via Shear-Flow Assembly of Peptide Hydrogels. *Adv. Mater.* **23**, 4967–4967 (2011).
16. Liu, M., Ishida, Y., Ebina, Y., Sasaki, T., Hikima, T., Takata, M. & Aida, T. An Anisotropic Hydrogel with Electrostatic Repulsion between Cofacially Aligned Nanosheets. *Nature* **517**, 68–72 (2015).
17. Tu, T., Sakurai, T., Seki, S., Ishida, Y. & Chan, Y. Towards Macroscopically Anisotropic Functionality: Oriented Metallo-supramolecular Polymeric Materials Induced by Magnetic Fields. *Angew. Chem. Int. Ed.* **133**, 1951–1956 (2021).
18. Leung, F. K., Kajitani, T., Stuart, M. C. A., Fukushima, T. & Feringa, B. L. Dual-Controlled Macroscopic Motions in a Supramolecular Hierarchical Assembly of Motor Amphiphiles. *Angew. Chem. Int. Ed.* **58**, 10985–10989 (2019).

Acknowledgements / Remerciements / Danksagung

On these last pages, I would like to take the opportunity to thank all the people who have participated to this work, and who have been supporting me along the way. It goes without saying that this thesis would not have been possible without your efforts.

First of all, I would like to thank Pr. Thomas Hermans for his supervision and the opportunity to perform this work in his group. Even though the past three years have been full of challenges, I would not want to miss the experience I have made in this inspiring international and multidisciplinary environment. Your incentive has given me the courage to leave my scientific comfort zone.

I would like to thank Pr. David González Rodríguez, Pr. Silvia Marchesan, and Pr. Sylvie Ferlay-Charitat for accepting to be part of my jury, and to evaluate this thesis with your expertise.

A special thanks goes to Georges Formon, who has been my fellow PhD student on paper, but has acted more as a Postdoc in reality. From the beginning to the end of my time in this lab, which is long after his contract had ended, he has given me kind advice and guidance. You are the king of modelling, and you deserve to have a super cute dog!

I thank Ana-Mari Fuentes Capparós for her help and collaboration in our hydrogel project. It is astonishing to see what a difference it makes to work hand in hand with a dedicated and supportive accomplice. These last few months we have been working together has made lab life a little more colorful, and a little brighter.

Alessandra Tassoni, Serena de Piccoli, Chunfeng Chen, and Lucas Giacchetti, my colleagues and, more importantly, friends from my beginnings in this lab. I am truly thankful for having had you by my side along this tough journey, in all the highs and lows (and very lows). I would like to thank all former and current members of the group, Takuji Adachi, Peter Dunne, Nina Matoussevitch, Nishant Singh, Arvind Dev, Anastasiia Sharko, Florencia Sacarelli, Tianheng Xu, Álvaro López-Acosta, Jennifer Ciesielski, Mohammadreza Zolala, Jorge Valera, Daniel Iglesias Asperilla, and Oleksandr Shyshov. Every one of you has participated to this work at some point along the way. More than that, I would like to thank you all for the friendly atmosphere in the lab, and all the personal, scientific, and culinary support you have offered me until today. I hope to even the score someday.

Merci à toute l'équipe de Qfluidics, Lucas Giacchetti (encore), Caroline Thébault, Thomas Biellmann et Vincent Marichez, pour votre partage d'expertise et tout le matériel mis à ma disposition. Vous êtes très aimants comme collègues ! Merci particulièrement à Lucas et Caroline, pour les corrections des parties en français, votre support moral, et les bonnes bouffes équilibrées.

Je remercie Cyril Antheaume de m'avoir aidé à caractériser mes composés avec son expertise en RMN et spectrométrie de masse. Merci également à Fanny Richard pour son temps et son aide avec les mesures de ITC.

J'aimerais remercier le personnel permanent de l'ISIS, de l'ILB, et de l'ED222, administratif et logistique. Vos efforts nous permettent de travailler dans des conditions optimales. Je remercie Annia Bertrand et Soumia Hnini pour leur aide avec toutes les procédures administratives et leur gentillesse au quotidien.

Merci les poteaux, Dorian, Nicolas, Vivien, Lucas (encore), Abdou, Pichois et Manoly, pour les soirées, les restos, les pétanques et les tarots, et tous les autres moments partagés entre amis. J'avoue que c'est devenu de plus en plus rare de me retrouver avec vous, mais avec cette thèse terminée j'espère reprendre l'ancien rythme.

Merci à mes colocataires, les actuels et les anciens, Alexia, Jérôme, Sophie et Benoît, d'avoir fait de notre appart un endroit de rire, de bonheur et de repos (même pendant les périodes de confinement et de télétravail intensif).

Ich danke dir, liebe Lisa Chen, für dein ständig offenes Ohr, deinen Zuspruch, dein Verständnis und deinen Rat in allen Lebenslagen. Liebe Julia und Natty, danke für die Gründung unserer kleinen Selbsthilfegruppe. Hoffentlich brauchen wir sie bald nicht mehr!

Vielen Dank an meine Familie, für eure blinde Unterstützung auf verschiedensten Wegen. Ganz besonders dafür, dass ihr mich immer wieder daran erinnert, dass es im Leben um mehr geht als um Abschlüsse und Ergebnisse.

Finalement je remercie Pier, mon partenaire de vie, de (petit) crime et de gourmandise. C'est grâce à toi que j'ai pu sortir de cette période intense en bonne santé mentale.

Michaela SCHICHO

Magnetic Control over Supramolecular Polymerization

Résumé

Cette thèse vise à obtenir un aperçu général sur les possibilités qu'un stimulus magnétique peut offrir pour contrôler des systèmes supramoléculaires. L'objectif final est d'identifier les modes d'action magnétiques pouvant contribuer à l'ensemble des interactions supramoléculaires. Pour cela, quatre systèmes sont présentés, chacun se focalisant sur un aspect différent.

Nos études démontrent que l'incorporation d'ions magnétiques de lanthanides dans la structure moléculaire de monomères à base de naphthalène affecte la thermodynamique de leur assemblage. Sous forme de colloïdes microscopiques, l'application d'un gradient de champ magnétique permet de diriger leur mouvement dans l'espace (magnétophorèse). Un réseau supramoléculaire, ayant également comme base un monomère décoré d'ions magnétiques, subit un changement de topologie lors de l'exposition à un champ uniforme. De la même manière, la gélification d'un hydrogel supramoléculaire peut être accélérée.

Compte tenu de la nouveauté du sujet, les connaissances acquises servent de base solide pour de futurs études, qui peuvent s'étendre de la chimie supramoléculaire aux matériaux intelligents.

Mots-clés : Auto-assemblage, polymérisation supramoléculaire, magnétisme, magnéto-sensibilité, magnétophorèse, lanthanides.

Résumé en anglais

This thesis aims to provide a general overview over the possibilities a magnetic stimulus can offer to control supramolecular systems. Its final goal is to identify, whether magnetic interactions can complete the toolbox of non-covalent interactions in supramolecular self-assembly. To this end, four systems have been studied, which all focus on a separate aspect.

Our studies show that the incorporation of magnetic lanthanide ions into the molecular structure of a naphthalene-based monomer influences the thermodynamics of their supramolecular polymerization. If assembled to microscopic colloids, their movement can be directed by the application of a gradient magnetic field (magnetophoresis). Moreover, we find that a supramolecular network of lanthanide-decorated monomers undergoes a change in topology upon the application of a uniform magnetic field. Similarly, the gelation of a supramolecular hydrogel can be accelerated.

Considering the novelty of the field, the obtained findings lay a solid foundation for future studies. These may range from fundamental supramolecular polymerization to the development of smart materials.

Keywords: Self-assembly, supramolecular polymerization, magnetism, magneto-response, magnetophoresis, lanthanides.